Université Joseph Fourier – Grenoble – France
Ecole Doctorale Terre – Univers – Environnement
Observatoire des Sciences de l'Univers de Grenoble
Laboratoire de Géophysique Interne et de Tectonophysique

Thèse

présentée à
L'Université Joseph Fourier - Grenoble I - France
pour obtenir le grade de
Docteur de l'Université Joseph Fourier,
spécialité « Terre – Univers – Environnement »

par
Aloé SCHLAGENHAUF

Identification des forts séismes passés sur les failles normales actives de la région Lazio-Abruzzo (Italie Centrale) par 'datations cosmogéniques' (^{36}Cl) de leurs escarpements

---

ANNEXES

Thèse soutenue publiquement le 30 Septembre 2009 devant le jury composé de :

P. Galli	Protezione Civile, Roma, Italie	Rapporteur
G. Hilley	Université de Stanford, Etats-Unis	Rapporteur
M. Campillo	Université J. Fourier, LGIT, Grenoble	Président du Jury
P. Tapponnier	Earth Observatory of Singapore	Examinateur
Y. Gaudemer	Université Paris 7, IPGP, Paris	Examinateur
J. Malavieille	Géosciences Montpellier	Examinateur
L. Benedetti	CEREGE, Aix-en-Provence	Directeur de thèse
I. Manighetti	LGIT, Grenoble	Directeur de thèse

Annexe I
(du chapitre 3)

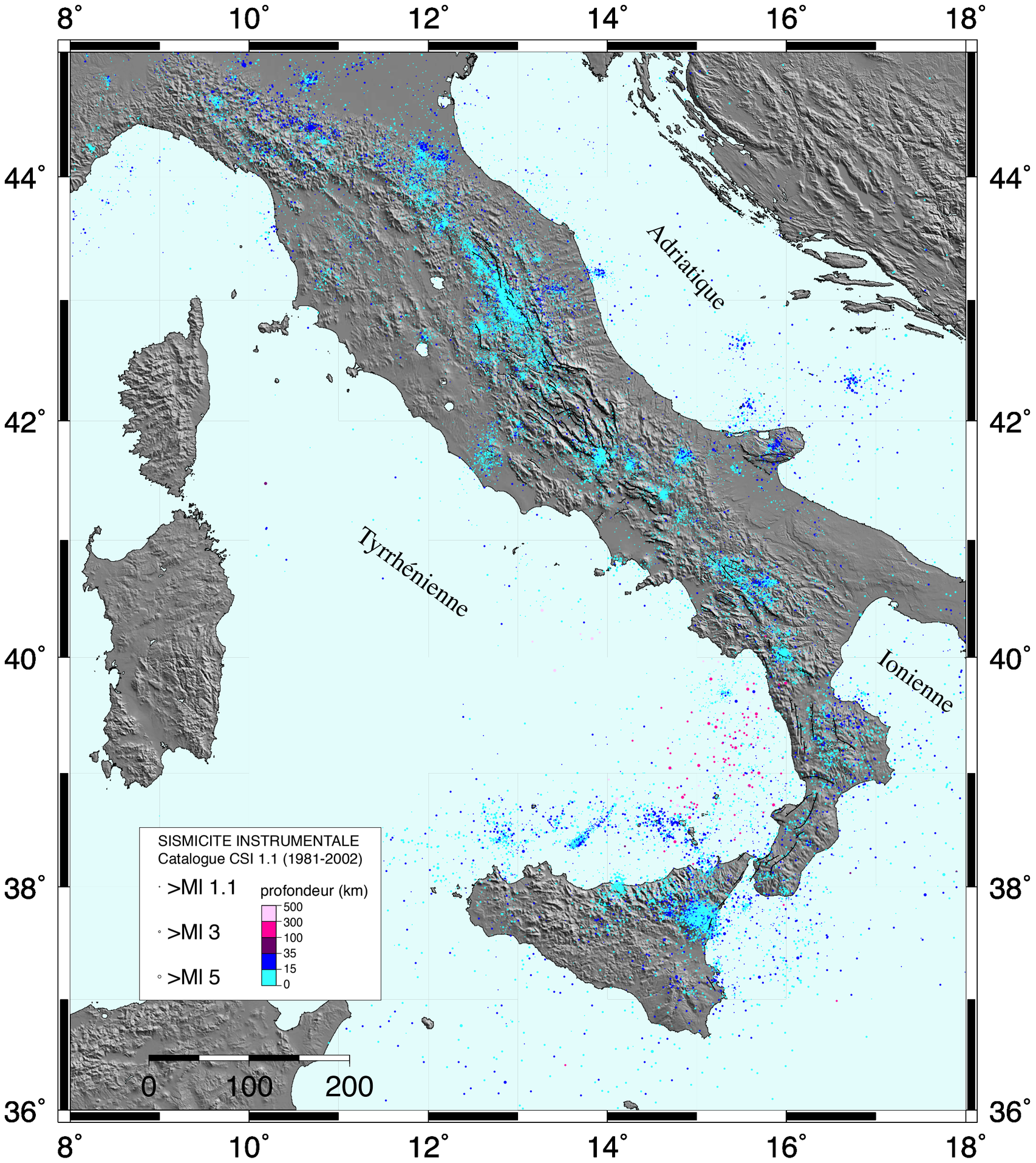

- Annexe I - A. Schlagenhauf, thèse, 2009

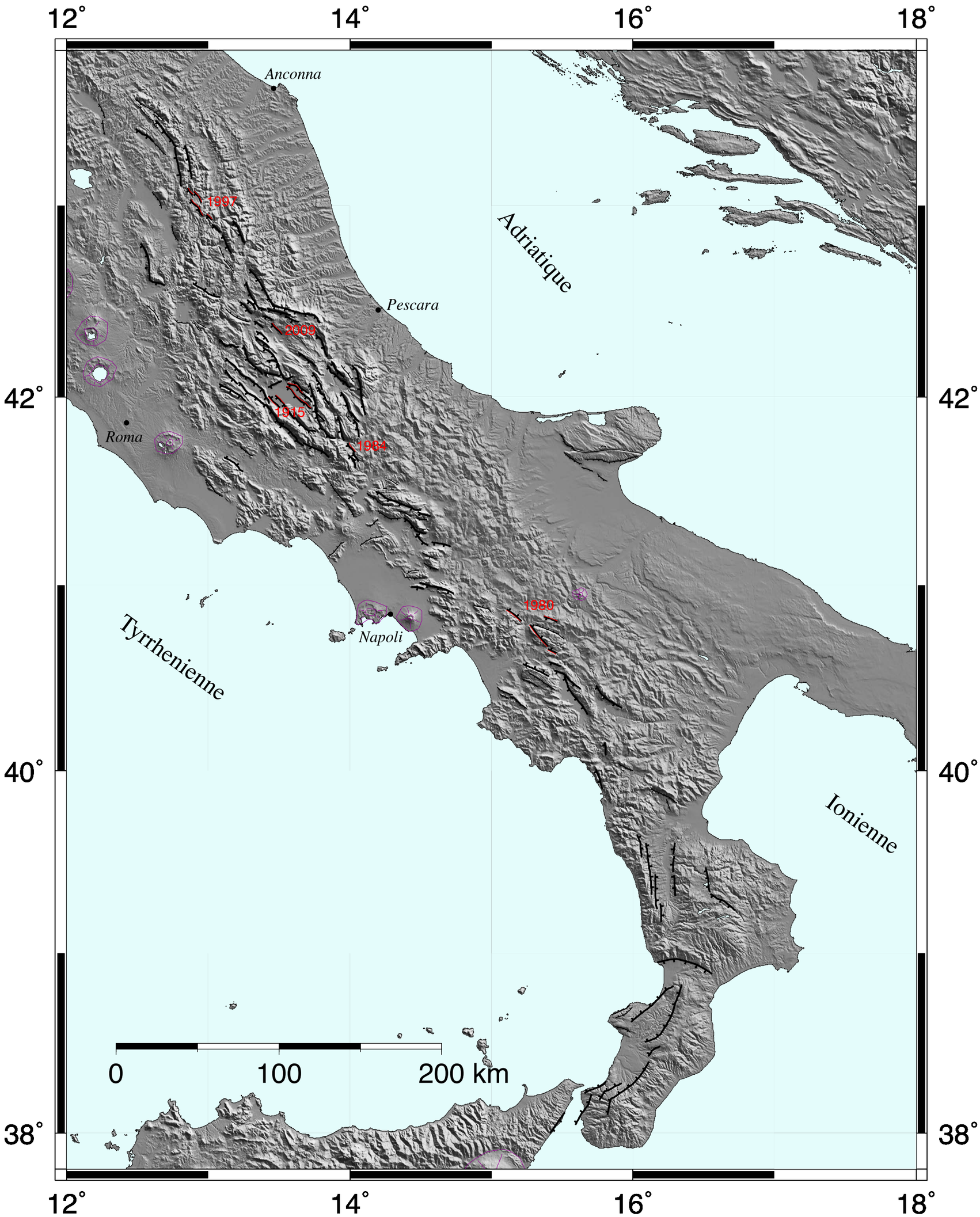
12°
14°
16°
18°
42°
40°
38°
Anconna
Pescara
Roma
Napoli
Adriatique
Tyrrhenienne
Ionienne
1997
2009
1915
1984
1980
0
100
200 km

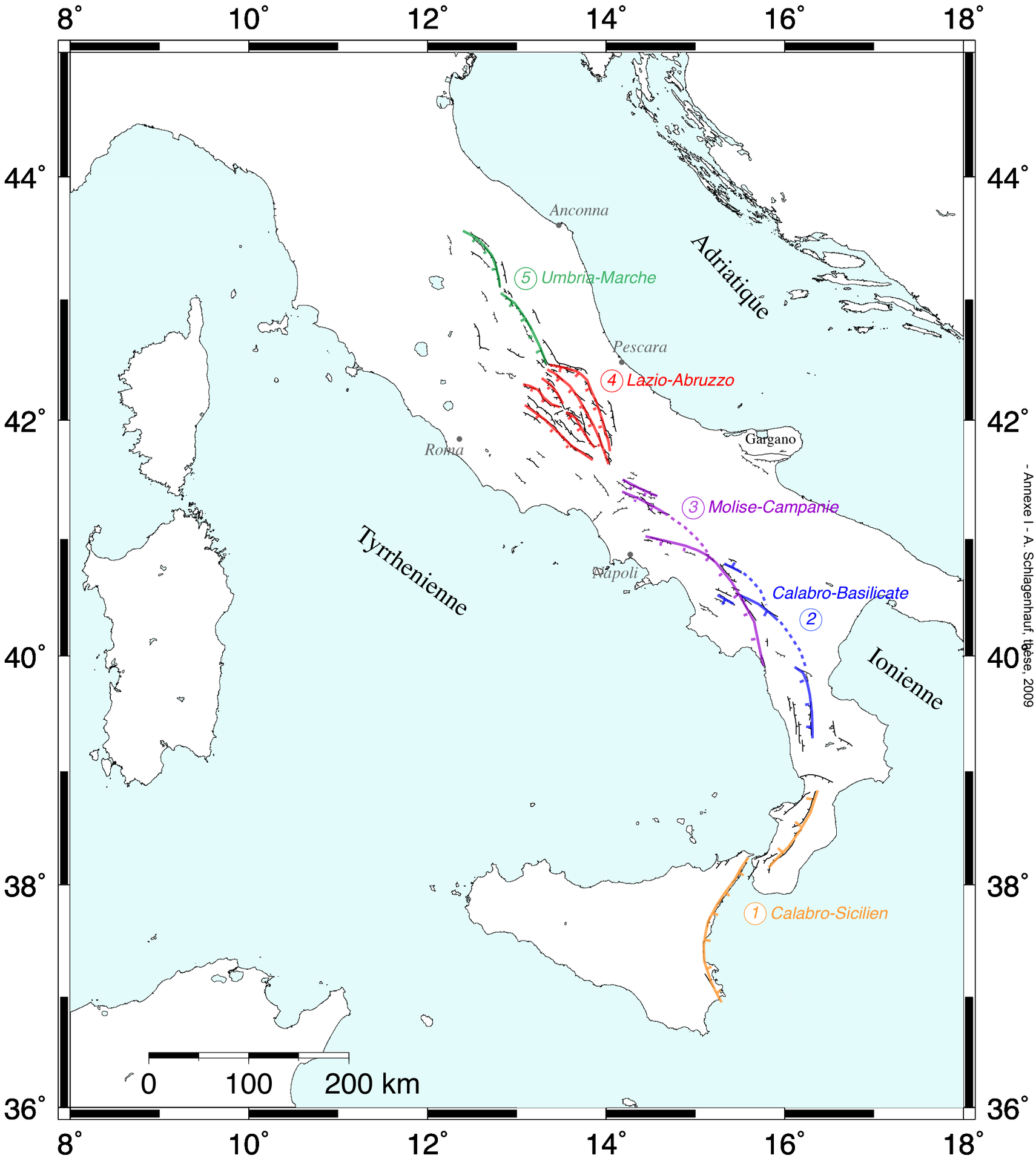
8°
10°
12°
14°
16°
18°
44°
42°
40°
38°
36°
Anconna
Adriatique
5 Umbria-Marche
Pescara
4 Lazio-Abruzzo
Roma
Gargano
3 Molise-Campanie
Tyrrhenienne
Napoli
Calabro-Basilicate
2
Ionienne
1 Calabro-Sicilien
0
100
200 km

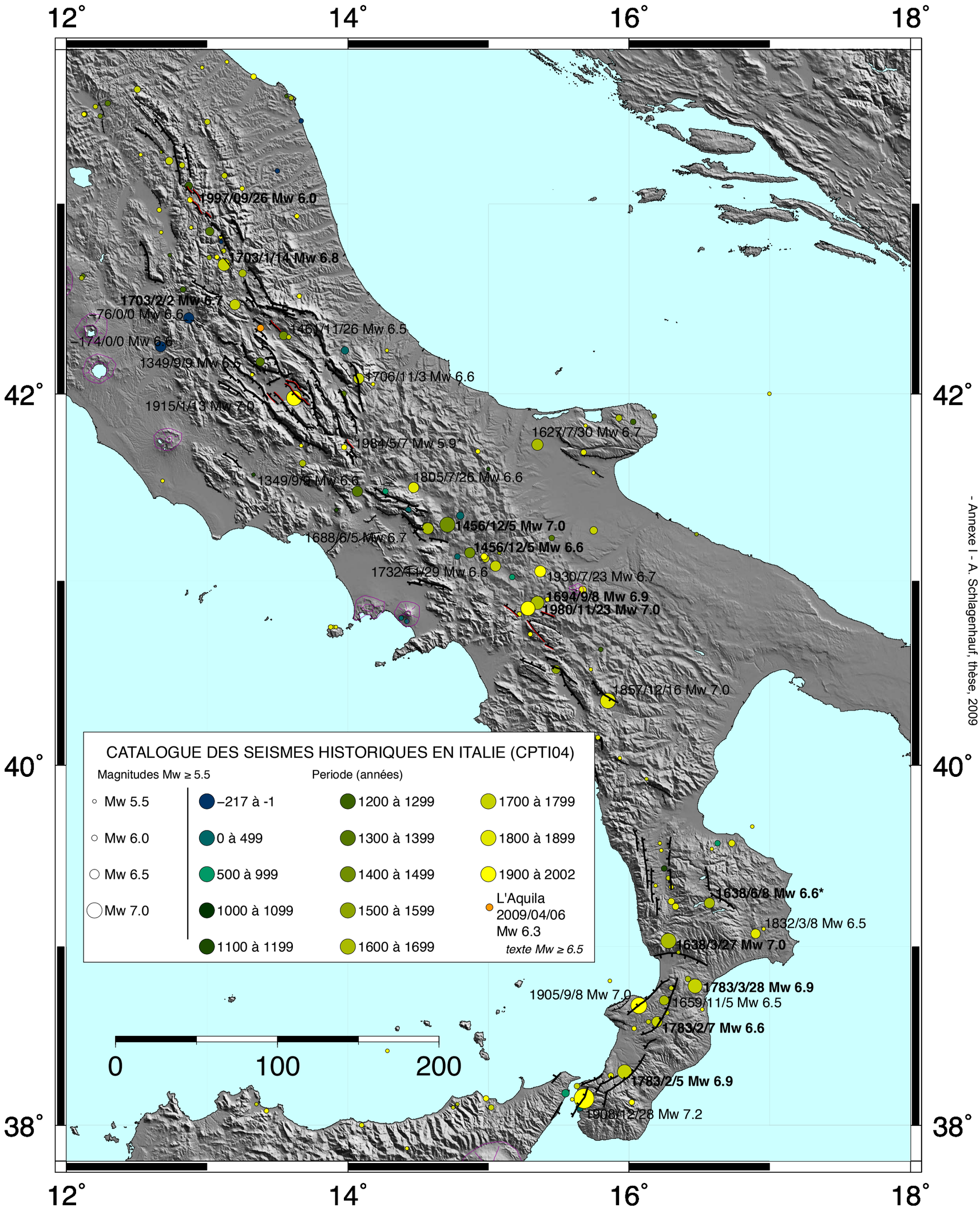
12°
14°
16°
18°
42°
40°
38°
1997/09/26 Mw 6.0
1703/1/14 Mw 6.8
1703/2/2 Mw 6.7
-76/0/0 Mw 6.6
1461/11/26 Mw 6.5
-174/0/0 Mw 6.6
1349/9/9 Mw 6.6
1706/11/3 Mw 6.6
1915/1/13 Mw 7.0
1627/7/30 Mw 6.7
1984/5/7 Mw 5.9*
1349/9/6 Mw 6.6
1805/7/26 Mw 6.6
1456/12/5 Mw 7.0
1688/6/5 Mw 6.7
1456/12/5 Mw 6.6
1732/11/29 Mw 6.6
1930/7/23 Mw 6.7
1694/9/8 Mw 6.9
1980/11/23 Mw 7.0
1857/12/16 Mw 7.0
CATALOGUE DES SEISMES HISTORIQUES EN ITALIE (CPTI04)
Magnitudes Mw ≥ 5.5
Mw 5.5
Mw 6.0
Mw 6.5
Mw 7.0
Periode (années)
-217 à -1
0 à 499
500 à 999
1000 à 1099
1100 à 1199
1200 à 1299
1300 à 1399
1400 à 1499
1500 à 1599
1600 à 1699
1700 à 1799
1800 à 1899
1900 à 2002
L'Aquila 2009/04/06 Mw 6.3
texte Mw ≥ 6.5
1638/6/8 Mw 6.6*
1832/3/8 Mw 6.5
1638/3/27 Mw 7.0
1783/3/28 Mw 6.9
1905/9/8 Mw 7.0
1659/11/5 Mw 6.5
1783/2/7 Mw 6.6
1783/2/5 Mw 6.9
1908/12/28 Mw 7.2
0
100
200

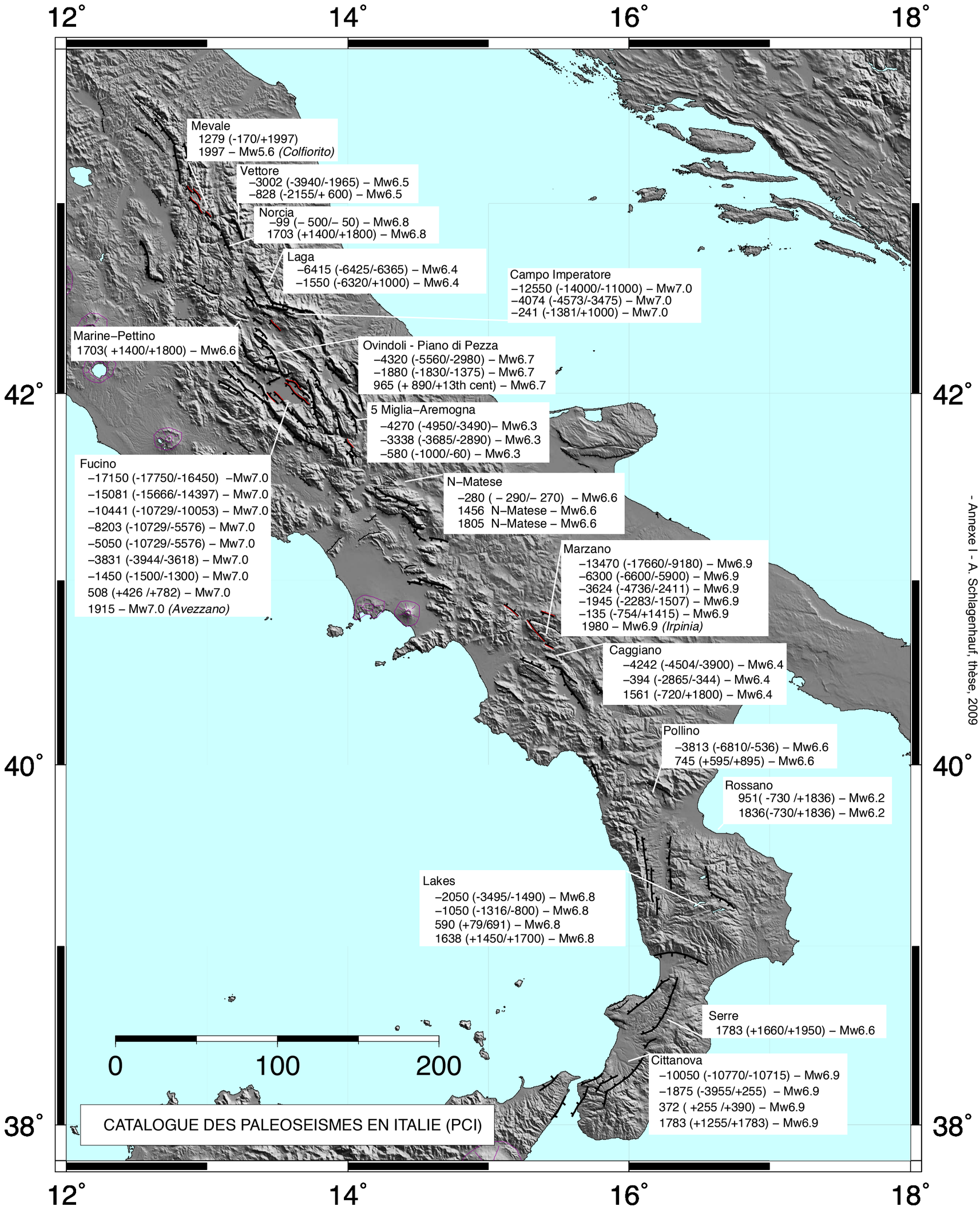
12°
14°
16°
18°
42°
40°
38°
Mevale
1279 (-170/+1997)
1997 – Mw5.6 (Colfiorito)
Vettore
–3002 (-3940/-1965) – Mw6.5
–828 (-2155/+ 600) – Mw6.5
Norcia
–99 (– 500/– 50) – Mw6.8
1703 (+1400/+1800) – Mw6.8
Laga
–6415 (-6425/-6365) – Mw6.4
–1550 (-6320/+1000) – Mw6.4
Campo Imperatore
–12550 (-14000/-11000) – Mw7.0
–4074 (-4573/-3475) – Mw7.0
–241 (-1381/+1000) – Mw7.0
Marine–Pettino
1703(+1400/+1800) – Mw6.6
Ovindoli - Piano di Pezza
–4320 (-5560/-2980) – Mw6.7
–1880 (-1830/-1375) – Mw6.7
965 (+ 890/+13th cent) – Mw6.7
5 Miglia–Aremogna
–4270 (-4950/-3490)– Mw6.3
–3338 (-3685/-2890) – Mw6.3
–580 (-1000/-60) – Mw6.3
Fucino
–17150 (-17750/-16450) –Mw7.0
–15081 (-15666/-14397) – Mw7.0
–10441 (-10729/-10053) – Mw7.0
–8203 (-10729/-5576) – Mw7.0
–5050 (-10729/-5576) – Mw7.0
–3831 (-3944/-3618) – Mw7.0
–1450 (-1500/-1300) – Mw7.0
508 (+426 /+782) – Mw7.0
1915 – Mw7.0 (Avezzano)
N–Matese
–280 (– 290/– 270) – Mw6.6
1456 N–Matese – Mw6.6
1805 N–Matese – Mw6.6
Marzano
–13470 (-17660/-9180) – Mw6.9
–6300 (-6600/-5900) – Mw6.9
–3624 (-4736/-2411) – Mw6.9
–1945 (-2283/-1507) – Mw6.9
–135 (-754/+1415) – Mw6.9
1980 – Mw6.9 (Irpinia)
Caggiano
–4242 (-4504/-3900) – Mw6.4
–394 (-2865/-344) – Mw6.4
1561 (-720/+1800) – Mw6.4
Pollino
–3813 (-6810/-536) – Mw6.6
745 (+595/+895) – Mw6.6
Rossano
951(-730 /+1836) – Mw6.2
1836(-730/+1836) – Mw6.2
Lakes
–2050 (-3495/-1490) – Mw6.8
–1050 (-1316/-800) – Mw6.8
590 (+79/691) – Mw6.8
1638 (+1450/+1700) – Mw6.8
Serre
1783 (+1660/+1950) – Mw6.6
Cittanova
–10050 (-10770/-10715) – Mw6.9
–1875 (-3955/+255) – Mw6.9
372 (+255 /+390) – Mw6.9
1783 (+1255/+1783) – Mw6.9
0
100
200
CATALOGUE DES PALEOSEISMES EN ITALIE (PCI)

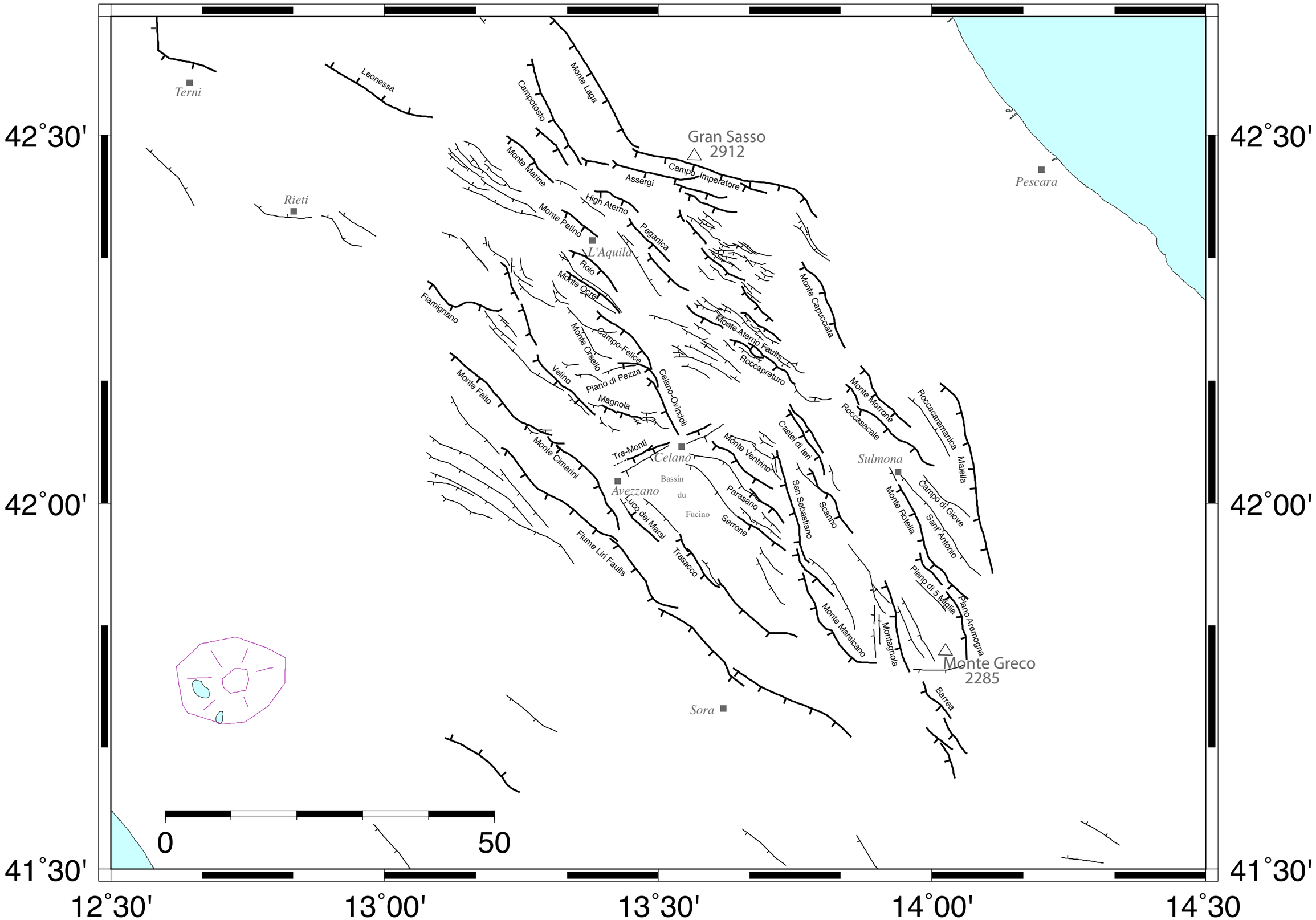
12°30'
13°00'
13°30'
14°00'
14°30
42°30'
42°00'
41°30'
Terni
Rieti
L'Aquila
Pescara
Celano
Avezzano
Sulmona
Sora
Gran Sasso
2912
Monte Greco
2285
Leonessa
Campotosto
Monte Laga
Campo Imperatore
Assergi
Monte Marine
High Aterno
Monte Petino
Paganica
Roio
Monte Ocre
Fiamignano
Monte Orsello
Campo-Felice
Monte Capucciata
Monte Aterno Faults
Roccapreturo
Velino
Piano di Pezza
Magnola
Monte Faito
Celano-Ovindoli
Monte Morrone
Roccasacale
Roccacaramanica
Maiella
Tre-Monti
Monte Cimarini
Bassin
du
Fucino
Lucq dei Marsi
Parasano
Serrone
Monte Ventrino
Castel di Ieri
San Sebastiano
Scanno
Monte Rotella
Campo di Giove
Sant'Antonio
Piano di 5 Miglia
Piano Aremogna
Monte Marsicano
Montagnola
Barrea
Fiume Liri Faults
Trasacco
0
50

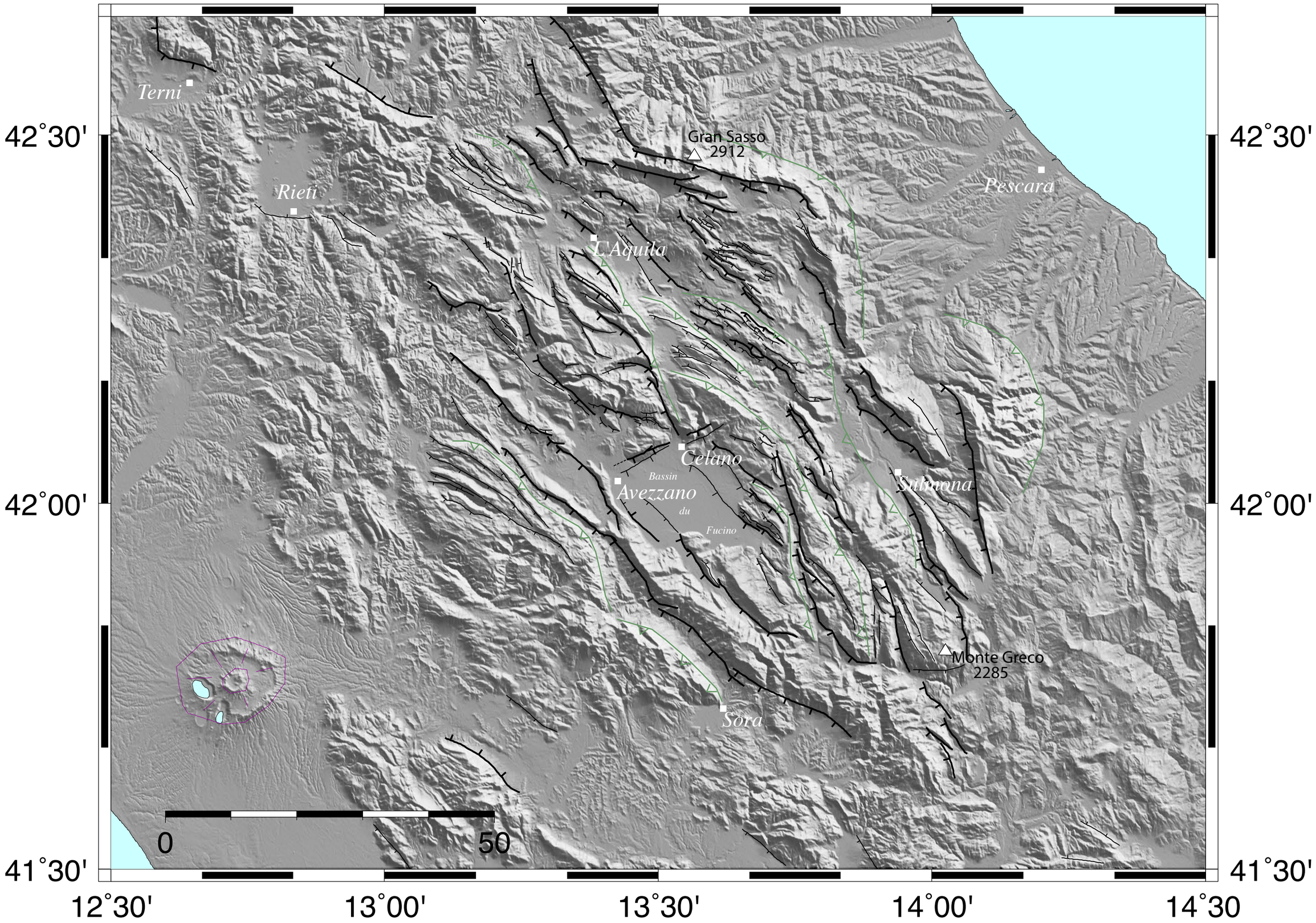
12°30'
13°00'
13°30'
14°00'
14°30
42°30'
42°00'
41°30'
Terni
Rieti
Gran Sasso
2912
L'Aquila
Pescara
Celano
Bassin
Avezzano
du
Fucino
Sulmona
Monte Greco
2285
Sora
0
50

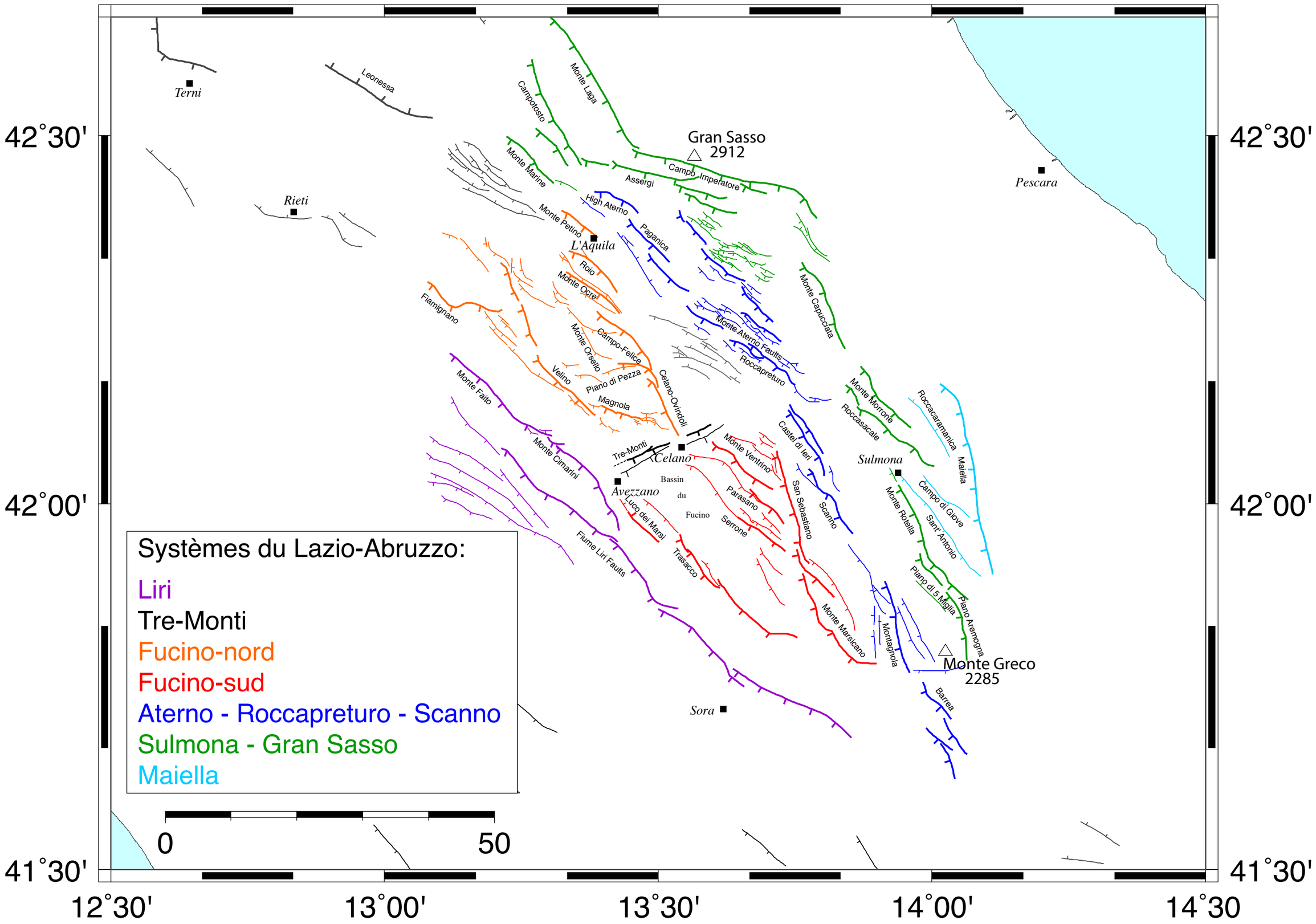
12°30'
13°00'
13°30'
14°00'
14°30
42°30'
42°00'
41°30'
Terni
Rieti
L'Aquila
Pescara
Celano
Avezzano
Sora
Sulmona
Gran Sasso
2912
Monte Greco
2285
Bassin
du
Fucino
Leonessa
Campotosto
Monte Laga
Monte Marine
Assergi
Campo Imperatore
High Aterno
Monte Petino
Paganica
Roio
Monte Ocre
Fiamignano
Monte Orsello
Campo-Felice
Velino
Piano di Pezza
Magnola
Celano-Ovindoli
Monte Faito
Monte Cimarini
Tre-Monti
Monte Ventrino
Parasano
Serrone
Lucoi dei Marsi
Trasacco
Fiume Liri Faults
Castel di Ieri
San Sebastiano
Scanno
Monte Marsicano
Monte Capucciata
Monte Aterno Faults
Roccapreturo
Monte Morrone
Roccasacale
Roccacaramanica
Maiella
Monte Rotella
Campo di Giove
Sant' Antonio
Piano di 5 Miglia
Piano Aremogna
Montagnola
Barrea
Systèmes du Lazio-Abruzzo:
Liri
Tre-Monti
Fucino-nord
Fucino-sud
Aterno - Roccapreturo - Scanno
Sulmona - Gran Sasso
Maiella
0
50

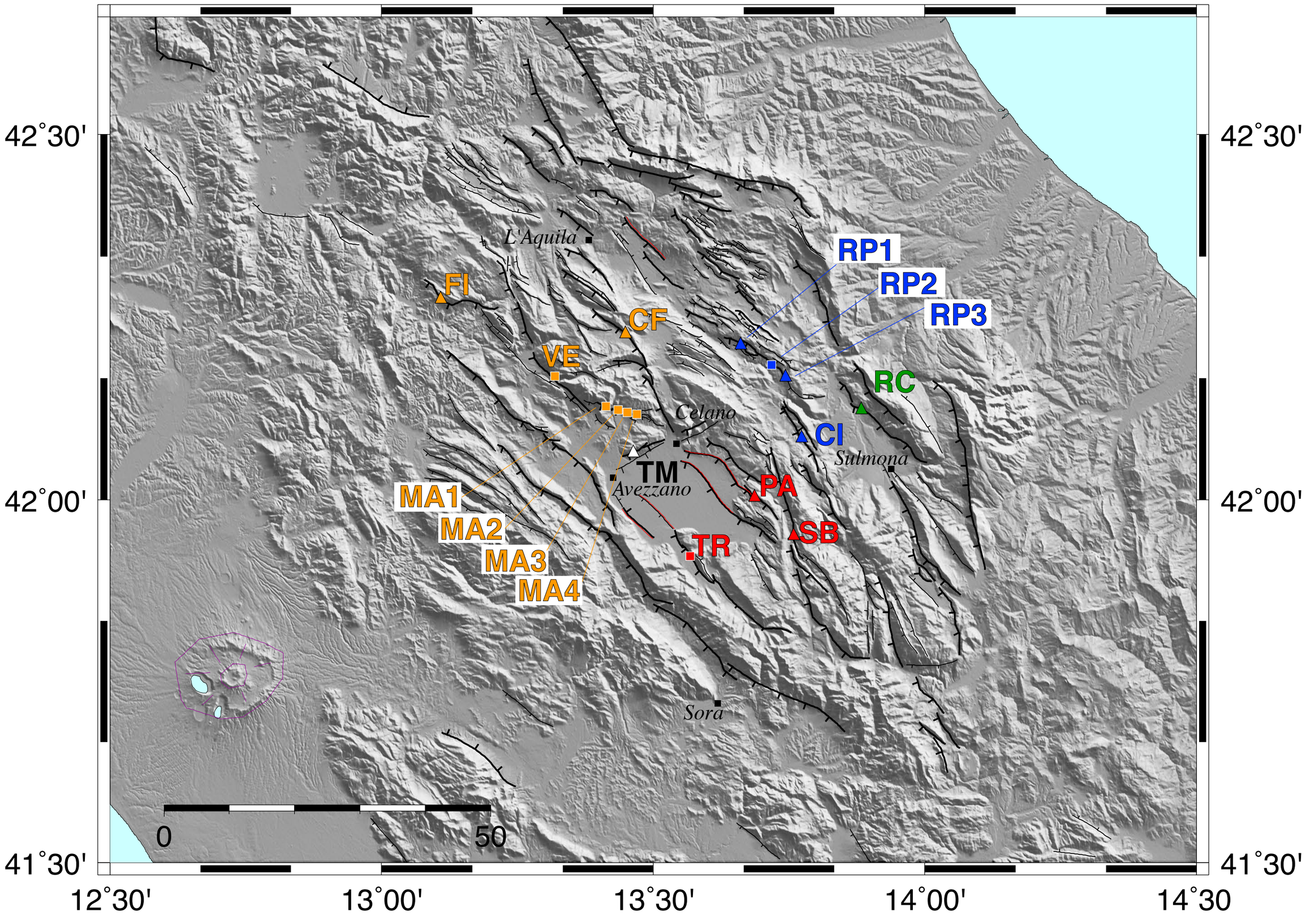
12°30'
13°00'
13°30'
14°00'
14°30
42°30'
42°00'
41°30'
L'Aquila
Celano
Sulmona
Avezzano
Sora
FI
CF
VE
MA1
MA2
MA3
MA4
RP1
RP2
RP3
RC
CI
TM
PA
SB
TR
0
50

Annexe II
(du chapitre 4)

APPENDIX

A Topographic shielding of normal fault sites

Equations below are only valid for calculation of the fast neutron flux which is not energy dependent.

The cosmic ray flux intensity arriving from the sky in the direction given by the inclination θ (positive upwards) and the azimuth ϕ is generally given by :

$$I(\theta, \phi) = I_o \sin^m \theta \tag{A.1}$$

for $\theta > 0$ and $I(\theta, \phi) = 0$ for $\theta < 0$. I_o is the maximum intensity and m is an empirical constant, generally taken to be equal to 2.3 (e.g. Lal, 1958 ; Nishiizumi et al., 1989). If the sample exposed is not shielded, it will receive the maximum possible flux given by :

$$\Phi_{max} = \int_0^{2\pi} \int_0^{\pi/2} I_o \sin^m \theta \cos\theta \, d\theta \, d\phi = \frac{2\pi I_o}{m+1} \tag{A.2}$$

In the presence of a shielding topography, the cosmic ray flux Φ will be reduced by a shielding factor $S = \Phi/\Phi_{max}$. If the topography is described by a relationship between its vertical angle θ_{topo} (as seen from the sampling site) and the azimuth ϕ, the remaining flux will be :

$$\Phi = \int_0^{2\pi} \int_{\theta_{topo}(\phi)}^{\pi/2} I_o \sin^m \theta \cos\theta \, d\theta \, d\phi \tag{A.3}$$

and the shielding factor S is given by :

$$S = \frac{m+1}{2\pi} \int_0^{2\pi} \int_{\theta_{topo}(\phi)}^{\pi/2} \sin^m \theta \cos\theta \, d\theta \, d\phi \tag{A.4}$$

Equation A.4 can lead to a closed form in the rare cases where the $\theta_{topo}(\phi)$ relationship is simple. Otherwise, is has to be numerically integrated.

A simple dipping fault plane

Generally, the fault scarp can be modelled in a first approximation as a semi-infinite plane of dip β. If the azimuth ϕ is taken to be 0 (or π) in the fault direction and $\pi/2$ in the direction of maximum scarp slope, the relationship between θ_{topo} and ϕ is given by :

$$\theta_{topo}(\phi) = \text{atan}(\tan\beta \sin\phi), \ 0 \leqslant \phi \leqslant \pi \tag{A.5a}$$

$$\theta_{topo}(\phi) = 0, \ \pi \leqslant \phi \leqslant 2\pi \tag{A.5b}$$

Equation A.5a is simply the expression of the apparent slope of the scarp in the azimuth ϕ. The resulting shielding factor $S(\beta)$ is given by :

$$S(\beta) = \frac{1}{2} + \frac{m+1}{2\pi} \int_0^{\pi} \int_{\text{atan}(\tan\beta \sin\phi)}^{\pi/2} \sin^m \theta \cos\theta \, d\theta \, d\phi \tag{A.6}$$

If there is a significant topography across the valley, its shielding effect must be included here, in the $\pi \leqslant \phi \leqslant 2\pi$ domain, by replacing the $1/2$ term by an expression similar to equation (A.4) but for $\pi \leqslant \phi \leqslant 2\pi$.

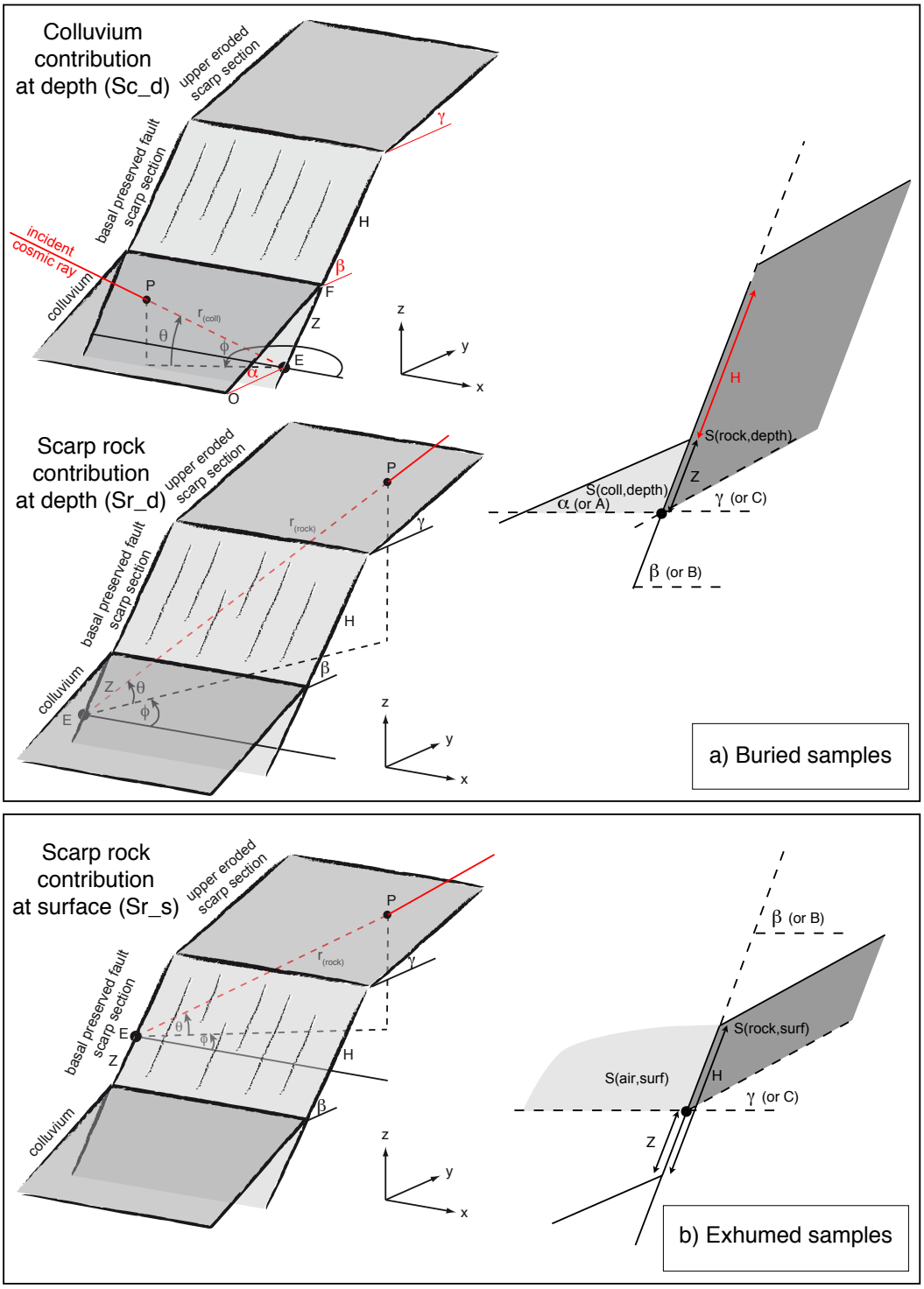

FIGURE A.1 - Schematic representation of the geometry of a normal fault scarp and associated colluvial wedge, and resulting shielding. α is colluvial wedge dip, β the basal scarplet dip, and γ the dip of the upper part of the fault escarpment. H is the actual height of the basal scarplet. When γ and β are different, a) buried samples receive cosmic rays passing through the colluvium ('colluvium contribution' of the flux), and cosmic rays passing through the scarp rock ('rock contribution' of the flux), b) the exhumed samples receive cosmic rays traveling through the air, plus cosmic rays passing through the rock.

Colluvial wedge

As the samples have been buried beneath a colluvial wedge before being exhumed by an earthquake, it is necessary to take into account the partial shielding created by this wedge. As for the fault scarp, we assume that it can be modelled by a semi-infinite plane of dip α. At any point beneath the colluvial wedge, the cosmic ray flux intensity coming from the direction (θ, ϕ) will be attenuated from its surface value by a factor $\exp(-d/\lambda)$ where d is the distance travelled throuth the colluvium by the incoming particle and λ the true attenuation length of the corresponding particle flux. In the case of fast neutrons, $\lambda \approx 208$ g.cm^{-1} (e.g. Gosse and Phillips, 2001).
If the target is at a distance Z (positive downwards) beneath the colluvium-fault intersection (Figure 4 in the main text), the distance d travelled through the colluvium by a particle coming from the direction (θ, ϕ) is given by :

$$d_- = \frac{Z \sin(\beta - \alpha)}{\sin\theta \cos\alpha - \cos\theta \sin\alpha \sin\phi} \text{ if } 0 \leqslant \phi \leqslant \pi \tag{A.7a}$$

$$d_+ = \frac{Z \sin(\beta - \alpha)}{\sin\theta \cos\alpha + \cos\theta \sin\alpha \sin\phi} \text{ if } \pi \leqslant \phi \leqslant 2\pi \tag{A.7b}$$

Our expression of d differs from that given by Dunne et al. (1999, eq. 12) as we use a different depth Z. Combining the shielding provided by the fault scarp of slope β and the attenuation due to the colluvial wedge of slope α, the resulting flux at Z is :

$$\begin{aligned}\Phi(Z, \alpha, \beta) = &\int_0^{\pi} \int_{\text{atan}(\tan\beta \sin\phi)}^{\pi/2} I_o e^{-d_-/\lambda} \sin^m\theta \cos\theta \, d\theta \, d\phi \\ &+ \int_{\pi}^{2\pi} \int_0^{\pi/2} I_o e^{-d_+/\lambda} \sin^m\theta \cos\theta \, d\theta \, d\phi\end{aligned} \tag{A.8}$$

In the actual calculation, the distances d_-, d_+, and the attenuation length λ have to be expressed in the same units, e.g. cm or g.cm^{-2}. The ratio between Φ and $\Phi_{\max}$ can then be used as a scaling factor $S_d(Z, \alpha, \beta)$ for the production rate (Dunne et al. 1999) beneath the colluvial wedge. The Matlab® program (see Electronic Supplement 1) `scdepth.m` computes $S_d(Z, \alpha, \beta)$.

Plotting S as a function of Z for given values of α and β shows (Figures A.2.a,b,c) that it is reasonable to approximate the scaling factor by an exponential decay of the form :

$$S_d(Z, \alpha, \beta) \approx S_Z \exp(-Z/\Lambda_Z) \tag{A.9}$$

where Λ_Z is an apparent attenuation length. In order to facilitate the comparison with the work of Dunne et al. (1999), we calculate the scaling factor as a function of z, the distance measured perpendicularly to the colluvial upper surface, which is related to Z by $z = Z \sin(\beta - \alpha)$. The scaling factor can also be approximated by an exponential decay in z of the form $S_d(z) = S_z \exp(-z/\Lambda_z)$ where Λ_z is the apparent attenuation length relevant to the z direction, perpendicular to the colluvial outer surface. In the case of a flat colluvium and no scarp, $\alpha = \beta = 0$, we find that setting the true attenuation length $\lambda = 208$ g.cm^{-2} gives $\Lambda_z \approx 157$ g.cm^{-2}, which is close to the classical value of 160 g.cm^{-2} used in vertical profiles (e.g. Gosse and Phillips, 2001). Other calculated values of $s_{o,f}$ and Λ_f are given in Figures A.2c,d for given α and β related to Figures 5a,b of the main text.

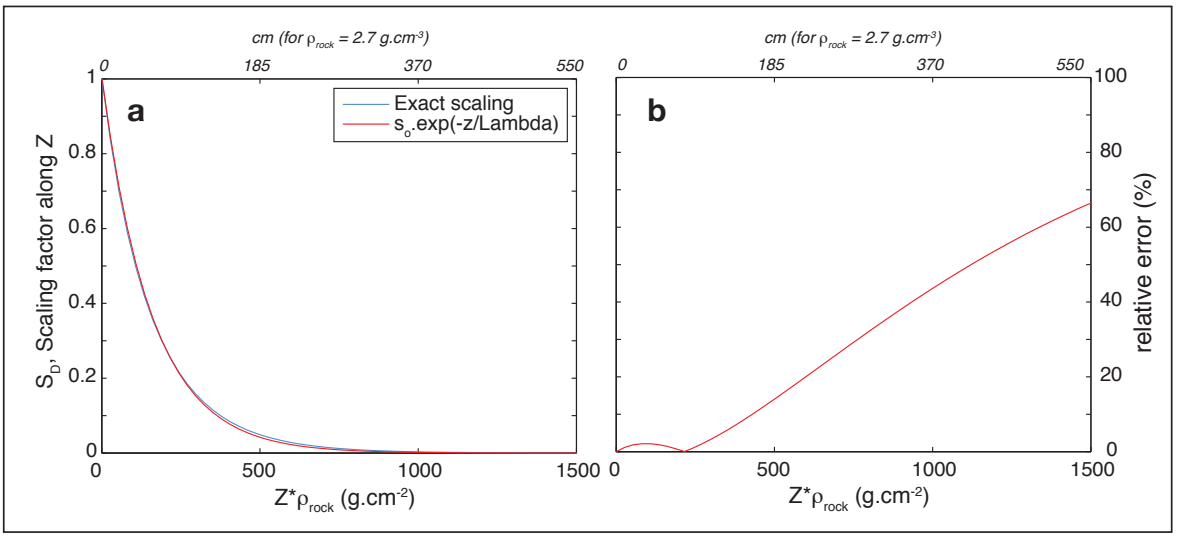

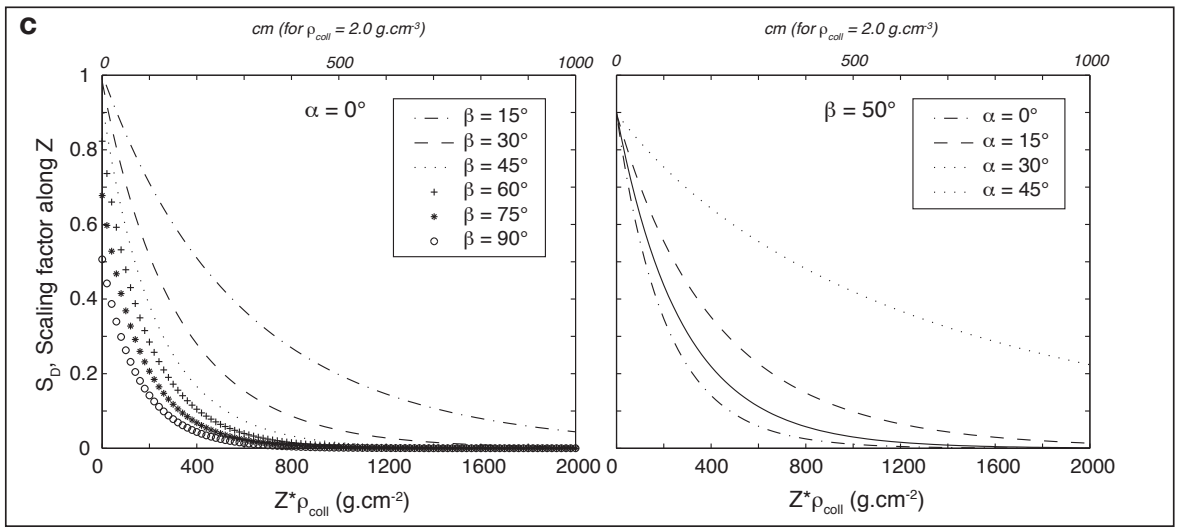

d

1) variations of β (α = 0°):

β	15°	30°	45°	60°	75°	90°
so_f_depth	0.9876	0.9679	0.9120	0.8114	0.6680	0.5015
Λ_f_depth	157.35	159.70	162.80	164.80	163.65	157.65

2) variations of α (β = 50°):

α	0°	15°	30°	45°
so_f_depth	0.8836	0.8836	0.8836	0.8836
Λ_f_depth	163.70	162.70	149.25	116.70

for ρrock = 2.7 and ρcoll = 2.0 (g.cm-3)

FIGURE A.2 - Fast neutron attenuation at depth. a) Comparison of exact scaling and its fit by an exponential with the fitexp.m Matlab® code ($S = s_o.exp(-Z/\Lambda_f)$. Corresponding values of z in cm at the top are given for $\rho_{rock} = 2.7$. b) Relative error between the two previous curves. c) Scaling with depth for different values of β and α, and d) corresponding values of s_o and Λ_f.

Change in dip of the fault escarpment

It has been observed that, above the steep scarplet, the mountain front has a gentler slope. Samples located near the top of the scarplet will receive not only particles from the atmosphere directly above them but also particles who will have travelled through the upper surface (Figure A.1). Again, if we take the scarp and the mountain front above as planar surfaces of slopes β and γ respectively, the particle flux arriving at the sample from the direction (θ, ϕ) will be attenuated by a factor $\exp(-d/\lambda)$ where d is the distance travelled through the footwall rock from the entry point to the sample and λ is the true attenuation length. If the scarp height is H and the position of the sample on the scarp surface is measured by Z (positive upwards), then d is given by :

$$d = \frac{(H - Z)\sin(\beta - \gamma)}{\sin\theta\cos\gamma - \cos\theta\sin\gamma\sin\phi} \tag{A.10}$$

The net contribution of these particles to the flux reaching the sample will then be :

$$\Phi = \int_0^{\pi} \int_0^{\mathrm{atan}(\tan\beta\sin\phi)} I_o \mathrm{e}^{-d/\lambda} \sin^m\theta\cos\theta\, d\theta\, d\phi \tag{A.11}$$

In fact, the lower limit of the inner integral may not be 0 but $\mathrm{atan}(\tan\gamma\sin\phi)$, the apparent slope of the upper surface in the direction ϕ, as the distance d becomes infinite for $\theta <= \mathrm{atan}(\tan\gamma\sin\phi)$ and attenuation is complete.

The total flux received by the sample can then be calculated and leads to the following scaling factor $S_s(Z, H, \beta, \gamma)$:

$$\begin{aligned} S_s(Z, H, \beta, \gamma) = \frac{1}{2} &+ \frac{m+1}{2\pi} \int_0^{\pi} \int_{\mathrm{atan}(\tan\beta\sin\phi)}^{\pi/2} \sin^m\theta\cos\theta\, d\theta\, d\phi \\ &+ \frac{m+1}{2\pi} \int_0^{\pi} \int_{\mathrm{atan}(\tan\gamma\sin\phi)}^{\mathrm{atan}(\tan\beta\sin\phi)} \mathrm{e}^{-d/\lambda} \sin^m\theta\cos\theta\, d\theta\, d\phi \end{aligned} \tag{A.12}$$

The Matlab® program (see Electronic Supplement 1) `scsurf.m` computes $S_s(Z, H, \beta, \gamma)$. This time, the scaling factor $S_s(Z, H, \beta, \gamma)$ should be modelled, for given values of H, β, and γ, as the sum of a constant term and of an exponential, reflecting the contributions of particles reaching directly the sample and particles having travelled through the upper surface of the fault scarp, respectively.

If the scarplet height H is small enough, it may become necessary to combine the effects of the colluvial wedge and of the upper surface to calculate the scaling factor for samples located at relatively shallow depths beneath the colluvial wedge (in fact, the Matlab® program `scdepth.m` mentioned above includes the presence of an upper slope).

In the presence of erosion

In the presence of erosion, a sample now at the surface will have been partially shielded from the surface flux by a layer of rock of decreasing thickness. It is therefore necessary to calculate the flux reaching a sample beneath the scarp surface. Assuming for the moment that the scarp surface is an infinite plane of slope β, if e is the rock thickness between the (future) sample and the scarp surface (Figure A.3a), the distance travelled by a particle coming from the direction (θ, ϕ) is :

$$d_- = \frac{e}{\sin\theta\cos\beta - \cos\theta\sin\beta\sin\phi} \text{ if } 0 \leqslant \phi \leqslant \pi \tag{A.13a}$$

$$d_+ = \frac{e}{\sin\theta\cos\beta + \cos\theta\sin\beta\sin\phi} \text{ if } \pi \leqslant \phi \leqslant 2\pi \tag{A.13b}$$

The corresponding scaling factor is :

$$S_r(e,\beta) = \frac{m+1}{2\pi}\int_0^{\pi}\int_{\mathrm{atan}(\tan\beta\sin\phi)}^{\pi/2} \mathrm{e}^{-d_-/\lambda}\sin^m\theta\cos\theta\,d\theta\,d\phi + \frac{m+1}{2\pi}\int_{\pi}^{2\pi}\int_0^{\pi/2}\mathrm{e}^{-d_+/\lambda}\sin^m\theta\cos\theta\,d\theta d\phi \tag{A.14}$$

The Matlab® program (see Electronic Supplement 1) `scrock.m` computes $S_r(e,\beta)$. For a given scarp slope β, the scaling factor $S_r(e)$ is also well approximated by an exponential decay of the form :

$$S_r(e,\beta) \approx S_e\exp(-e/\Lambda_e) \tag{A.15}$$

Colluvium + upper surface + erosion

If we wish to model the erosion of a scarp of slope β and height H, above a colluvial wedge of slope α and below an upper surface of slope γ, the same methodology as in the above cases should be used : (1) calculating first the distance d between the entry point at the Earth's surface and the target at depth as a function of the incoming direction (θ,ϕ), (2) integrating the attenuated flux intensity over the $(0\leqslant\phi\leqslant 2\pi, 0\leqslant\theta\leqslant\pi/2)$ domain, skipping regions from which no flux is coming by adjusting the integration limits for θ as we did above.

It is easy to see that the expression of d as a function of the target position given by Z and e (Figure A.3a) becomes very complex as several regions have to be considered and that the integration of the flux intensity becomes cumbersome, if not painful. It will be very difficult to easily express the corresponding scaling factor $S_t(Z,e)$ as a function of Z and e. As, however, this scaling factor should vary smoothly with Z and e, we believe that it is reasonable to assume that S_t can be expressed as the product of two scaling factors, one accounting for the shape of the scarp itself and being a function of Z, and one accounting for the thickness e of footwall rock separating the target form the scarp surface :

$$S_t(Z,e) = f(Z)g(e) \tag{A.16}$$

At the surface of the scarp ($e=0$), $S_t(Z,0)$ should be equal to the scaling factors S_d or S_s we have calculated above in equations (A.9) and (A.12). Above the colluvial wedge and far enough from the top of the scarp surface, $S_t(Z,e)$ should be equal to $S_r(e)$. The solution is to take :

$$S(Z,e) = S_r(e)\bar{S}(Z) \tag{A.17}$$

where $\bar{S}(Z)$ is either $S_d(Z)$ or $S_s(Z)$, depending on the location of the target, normalized to the (identical) value they take at the colluvium-fault scarp limit (Figure A3.a). This ensures that the effect of the scarp slope β is not taken into account twice. With this normalization, $\bar{S}(Z)$ decrease exponentially from 1 towards 0 for increasing depths beneath the colluvium, while it increases slightly towards the top of the scarp, reflecting the increasing contribution of particles entering through the upper surface (Figure A.3b).

B Matlab® code description

The production rate P

Production rates are calculated using the full description of the production sources from Schimmelpfennig et al. (2009 ; after Gosse and Phillips, 2001). Both `clrock.m` and `clcoll.m` have equivalent equations. They differ only by the fact that `clcoll.m` also takes into account the colluvial wedge mean chemical composition : it calculates the production rate in the sample (scarp rock composition) buried under a thickness z of colluvium having its proper chemical composition.
Thickness factors (Q_x ; with x standing for each production source) from Gosse and Phillips (2001) are only valid for samples at the surface vicinity. We re-calculated the thickness factors to express them as a function of depth. The new thickness factors are defined at the sample center, or thickness half, named

th_2 (in 'e' direction) and are the following (using Schimmelpfennig et al., 2009 nomenclature) :

For spallation :

$$Q_{sp} = 1 + \frac{1}{6}\left(\frac{th_2}{\Lambda_{f,e}}\right)^2 \tag{B.1}$$

For direct capture of slow negative muons :

$$Q_{\mu} = 1 + \frac{1}{6}\left(\frac{th_2}{\Lambda_{\mu}}\right)^2 \tag{B.2}$$

For epithermal neutrons :

$$\begin{aligned} Q_{eth} = \frac{1}{P_{eth}} \quad & \left[\phi^*_{eth}\left(\frac{f_{eth}}{\Lambda_{eth}}\right)(1-p(E_{th}))\exp\left(\frac{-e}{\Lambda_{f,e}}\right)\left(1+\frac{1}{6}\left(\frac{th_2}{\Lambda_{f,e}}\right)^2\right)\right. \\ & + (1+R_{\mu}R_{eth})(F\Delta\phi)^*_{eth}\left(\frac{f_{eth}}{\Lambda_{eth}}\right)(1-p(E_{th}))\exp\left(\frac{-e}{L_{eth}}\right)\left(1+\frac{1}{6}\left(\frac{th_2}{L_{eth}}\right)^2\right) \\ & \left. + R_{\mu}\phi^*_{eth}\left(\frac{f_{eth}}{\Lambda_{eth}}\right)(1-p(E_{th}))\exp\left(\frac{-e}{\Lambda_{\mu}}\right)\left(1+\frac{1}{6}\left(\frac{th_2}{\Lambda_{\mu}}\right)^2\right)\right] \end{aligned} \tag{B.3}$$

For thermal neutrons :

$$\begin{aligned} Q_{th} = \frac{1}{P_{th}} \quad & \left[\phi^*_{th}\left(\frac{f_{th}}{\Lambda_{th}}\right)\exp\left(\frac{-e}{\Lambda_{f,e}}\right)\left(1+\frac{1}{6}\left(\frac{th_2}{\Lambda_{f,e}}\right)^2\right)\right. \\ & + (1+R^{'}_{\mu})(\Im\Delta\phi)^*_{eth}\left(\frac{f_{th}}{\Lambda_{th}}\right)\exp\left(\frac{-e}{L_{eth}}\right)\left(1+\frac{1}{6}\left(\frac{th_2}{L_{eth}}\right)^2\right) \\ & + (1+R^{'}_{\mu}R_{th})(\Im\Delta\phi)^*_{th}\left(\frac{f_{th}}{\Lambda_{th}}\right)\exp\left(\frac{-e}{L_{th}}\right)\left(1+\frac{1}{6}\left(\frac{th_2}{L_{th}}\right)^2\right) \\ & \left. + R^{'}_{\mu}\phi^*_{th}\left(\frac{f_{th}}{\Lambda_{th}}\right)\exp\left(\frac{-e}{\Lambda_{\mu}}\right)\left(1+\frac{1}{6}\left(\frac{th_2}{\Lambda_{\mu}}\right)^2\right)\right] \end{aligned} \tag{B.4}$$

Apparent attenuation length for fast neutrons is calculated as explained above in part 1 of the Appendix using either `scdepth.m`, `scsurf.m`, or `scrock.m` depending of sample position in Z direction (Figure 5 of the main text). As slow muons flux is energy dependent (e.g. Gosse and Phillips, 2001) the same calculation of the apparent attenuation length of slow muons cannot be achieved as for fast neutron. We use the 1500 g.cm^{-2} defined for a flat surface (e.g. Gosse and Phillips, 2001, p 1504).

The number of atoms N

The equation governing the evolution of the number N of ^{36}Cl atoms is :

$$\frac{dN}{dt} = -\lambda_{36}N + P \tag{B.5}$$

where λ_{36} is the decay constant of ^{36}Cl and P is the production rate. In certain conditions, equation (B.5) can be solved analytically. Here we want to model the evolution of a fault scarp whose geometry changes repeatedly with time, we wish also to study the influence of a variable magnetic field on the production rate, and to account for possible erosion of the scarp surface. This has lead us to solve equation (B.5) numerically by dividing the time span of the scarp evolution into small increments of time and writing :

$$N(t+\Delta t) = N(t) + [P(t) - \lambda_{36}N(t)] \times \Delta t \tag{B.6}$$

These time increments are small enough, typically 100 years, to ensure that the magnetic field and hence its effects on the production rate through the elevation-latitude correcting factors $S_{\mathrm{el,f}}$ for fast neutrons and $S_{\mathrm{el},\mu}$ for muons, can be considered constant. In that, we follow the method used for instance by Dunai (2001), Pigati and Lifton (2004), Lifton et al. (2005) and Lifton et al. (2008). The changes in geometry, either by earthquake slip or erosion are accounted for by calculating the scaling factor $S(Z(t), e(t))$. For instance, if the erosion rate is ε, the thickness e of rock between the sample and the scarp surface varies as :

$$e(t + \Delta t) = e(t) - \varepsilon \times \Delta t \tag{B.7}$$

Changes in Z occur every time there is an earthquake, so that $Z(t)$ values are updated much less frequently than $e(t)$ values. Finally, each segment of the fault scarp has its own exhumation history. This has lead us to write a Matlab® program, named `modelscarp.m` (see Electronic Supplement 1 and Figure B.1), whose main structure is based on the nesting of three loops : one for each of the segments, one for the number of earthquakes prior to the exhumation of the current segment (once it is exhumed, the actual Z values of a segment have no influence the production rate), and one for the small time increments Δt. Before these loops, the program calculates the number of ^{36}Cl atoms at the end of the pre-exposition time.

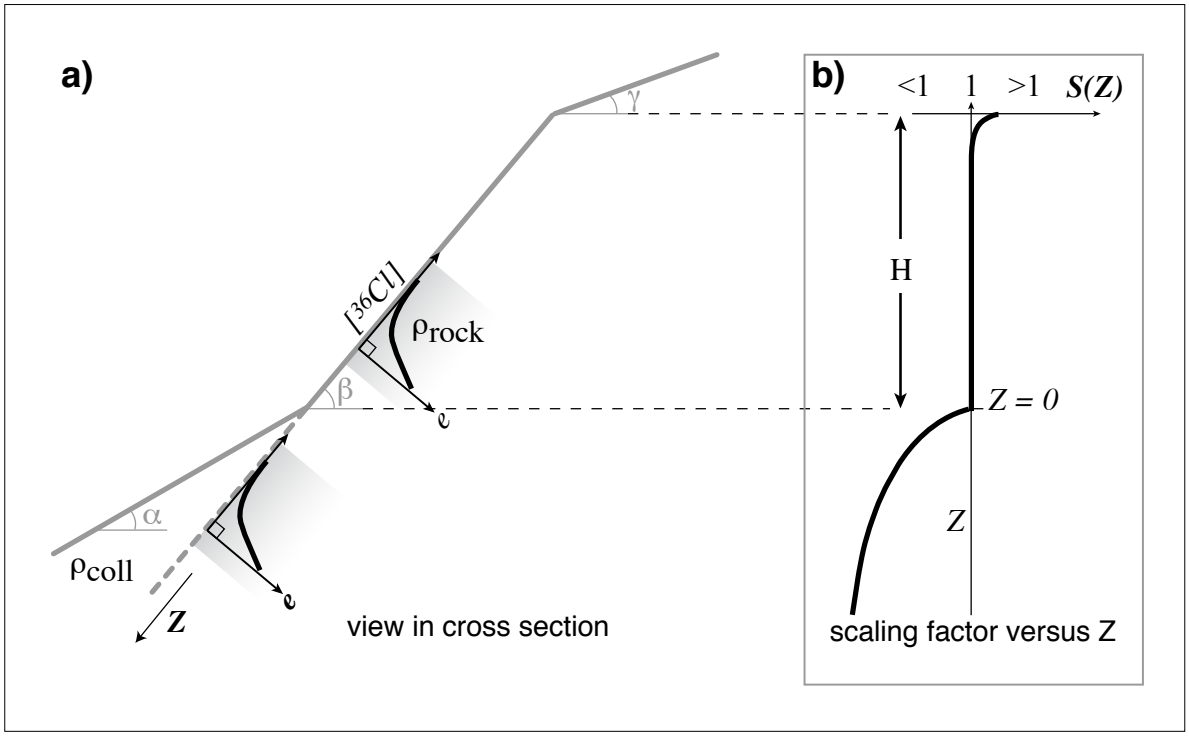

FIGURE A.3 - The attenuations along 'e' and 'Z' directions are separated : a) the [^{36}Cl] profile due to rock attenuation is calculated for a surface of dip β in the direction e perpendicular, b) a scaling factor $S(Z)$, which is only applied to the cosmogenic part of the production, is introduced. It accounts for both attenuation at depth ($S(Z) < 1$) and increased flux at the vicinity of γ ($S(Z)$). It is calculated by scaling the cosmogenic production at surface far from γ (at Z = 0, for β infinite).

FIGURE B.1 - Schematic representation of the Matlab® `modelscarp.m` program given in Electronic Supplement 1. In orange, parameters that need to be modified for each site by the users. *EQ* stands for Earthquake ; *f* for neutrons ; μ for muons ; *j* for the sample ; *i* for the earthquake number ; *t* for the time step ; *rock* for the sample chemical composition ; *coll* for the mean colluvial wedge composition ; P_{cosmo} for the cosmogenic production ; P_{rad} for the radiogenic production ; *epsilon* for the erosion rate (in mm/yr).

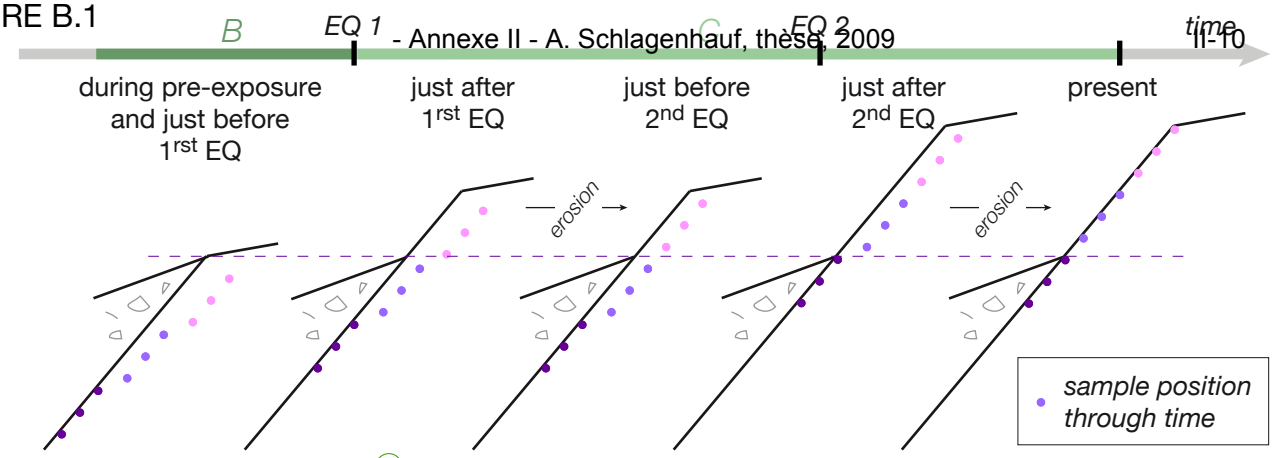

modelscarp.m (Matlab® code):

A - Initialization

CONSTANTS DECLARATION: α, β, γ, ρ_{rock}, ρ_{coll}, H_{final} (per site)
$\Psi^{36}Cl\_Ca,0$ (function of Earth magnetic field description used)

CONSTANTS LOADING: λ_{36}, Λ_f, $S_{el,f}(t)$, $S_{el,\mu}(t)$

SURFACE SCALING (along $z \geq 0$) — $S(z \geq 0)$ equal to 1 if β infinite ; $S(z) \geq 1$ (for $z \geq 0$) if H, γ
scsurf.m

DEPTH SCALING (along $z \leq 0$) after each EQ(i) — $S(z,H_i) \leq 1$ (for $z \leq 0$) ; loop on H_i
$S(z \leq 0, H_i)$ fitted whith fitexp.m —> $so_{f,d,i}$ and $\Lambda_{f,d,i}$ (d: depth)
scdepth.m

ROCK SCALING (along $e \leq 0$) — calculates $S_e(e)$ (for $e \leq 0$) independently of position on z
$S_e(e)$ fitted whith fitexp.m —> $so_{f,e}$ and $\Lambda_{f,e}$
scrock.m

VARIABLES INITIALIZATION — Initial samples (j) positions along e —> $e_0(j)$

B - Calculation of ^{36}Cl depth profile after pre-exposure *(all samples buried under the colluvium)*

sample (j) / time (t):
clrock.m (rock(j), $e_0(j)$, $\Lambda_{f,e}$, $so_{f,e}$, $S_{el,f}(t)$, $S_{el,\mu}(t)$) —> $P_{cosmo}(j)$ and $P_{rad}(j)$ at $e_0(j)$
clcoll.m(coll(j), rock(j), $\Lambda_{f,d,i=0}$, $so_{f,d,i=0}$, $S_{el,f}(t)$, $S_{el,\mu}(t)$) / clcoll.m (.., z=0,..) —> $S_{coll,cosmo}(j)$ (scalling)
$P_{tot,pre\text{-}exp}(j) = P_{rad}(j) + P_{cosmo}(j) * S_{coll,cosmo}(j) - \lambda_{36} * P_{tot,pre\text{-}exp}(j,t-1) * t$
—> $P_{tot,pre\text{-}exp}(j)$ *depth*

C - Calculation of ^{36}Cl depth and surface profiles during seismic phase

earthquake (i) / sample (j) / time (t):
clrock.m (rock(j), $e_0(j)$, $\Lambda_{f,e}$, $so_{f,e}$, $S_{el,f}(t)$, $S_{el,\mu}(t)$) —> $P_{cosmo}(j)$ and $P_{rad}(j)$ at e(j)
clcoll.m(coll(j), rock(j), $\Lambda_{f,d,i=0}$, $so_{f,d,i=0}$, $S_{el,f}(t)$, $S_{el,\mu}(t)$) / clcoll.m (.., z=0,..) —> $S_{coll,cosmo}(j)$ (scalling)
$P_{tot,depth}(j) = P_{rad}(j) + P_{cosmo}(j) * S_{coll,cosmo}(j) - \lambda_{36} * P_{tot}(j,t-1) * t$
depth

earthquake (i) / sample (j) / time (t):
clrock.m (rock(j), e(j,t), $\Lambda_{f,e}$, $so_{f,e}$, $S_{el,f}(t)$, $S_{el,\mu}(t)$) —> $P_{cosmo}(j)$ and $P_{rad}(j)$ at e(j,t)
(scsurf.m) $S(j) / S(z=0)$ —> $S_{surf,cosmo}(j)$ (scalling)
$P_{tot,depth}(j) = P_{rad}(j) + P_{cosmo}(j) * S_{surf,cosmo}(j) - \lambda_{36} * P_{tot}(j,t-1) * t$
$e(j,t+1) = e(j,t) - \varepsilon * t$
—> $P_{tot,EQ}(j)$ *surface*

$P(j) = P_{tot,pre\text{-}exp}(j) + P_{tot,EQ}(j)$

Matlab® command window:

```
data = load('datarock.txt');          66 columns * x lines (x samples)
coll = load('datacolluvium.txt');     62 columns * 1 line (mean colluvium composition)   ] dataset loading
EL = load('datamagfield.txt');         4 columns * t lines

modelscarp(data,coll,age,slip,preexp,EL,epsilon)                                          calculation
```

Legend of Electronic Supplement 1 – Schlagenhauf et al., 2009

For a new sampling site:

1- Create the 3 input files as the ones given for Magnola MA3 site (text format with tabulations – no coma, use points for decimal separator):

- 'datarock.txt': 66 columns by x lines (x : number of samples) ; see Tables 1 and 2 of main text
- 'datacolluvium.txt': 62 columns by 1 line (mean colluvium composition) ; see Table 1 of main text
- 'datamagfield.txt': 4 columns by t lines (variations of scaling factors $S_{el,s}$ and $S_{el,\mu}$);
  from 1rst to 4th column: time period (yrs) – time steps (yrs) - $S_{el,s}$ - $S_{el,\mu}$
  example (for a variable magnetic field):

0	0	2.744	1.784
100	100	2.706	1.78
200	100	2.763	1.786
300	100	2.825	1.792
400	100	2.777	1.787
500	100	2.692	1.778
600	100	2.302	1.732
700	100	2.102	1.697
800	100	2.33	1.736
900	100	2.482	1.756
1000	100	2.733	1.783

2- Modify the Matlab® code *modelscarp.m (*actual values are the one corresponding to MA3 Magnola site):

- alpha (degrees): colluvium wedge dip
- beta (degrees): preserved scarp dip
- gamma (degrees): upper eroded scarp dip
- Hfinal: final height (present height) of the fault scarp of dip β (m)
- rho_coll: colluvial wedge mean density
- rho_rock: scarp rock mean density
- Psi_36Cl_Ca_0: spallation production rate of ^{36}Cl at surface from ^{40}Ca corresponding to the description of magnetic field used (ex: 48.8 at ^{36}Cl/g Ca /yr, from Stone et al., 1996 using a constant magnetic field).

3- In the Matlab® command window:

```
data = load('datarockMA3.txt');
coll = load('datacolluviumMA3.txt');
EL = load('datamagfieldMA3Stone2000.txt');
age = [7200 4900 4000 3400 1500 0]; % Earthquakes ages (years), here last event is at t=0 to model the buried samples
slip = [190 205 160 360 200 400]; % Corresponding earthquakes displacements (cm ; 400 cm for the buried samples)
preexp = 1900; % pre-exposure duration (years)
epsilon = 0; % erosion rate (mm/yr)
modelscarp(data,coll,age,slip,preexp,EL,epsilon)
```

Output: *it can take a few minutes to run*. *A* Figure window of Matlab will appear displaying the results. Black dots are the [^{36}Cl] concentrations with horizontals bars for the corresponding uncertainties. Blue open dots are the modelled [^{36}Cl] concentrations. Blue line represent the position of each discontinuities associated with each modelled event.

"Modelscarp" folder contains: all the Matlab® codes for earthquake recovering using ^{36}Cl cosmogenic isotope on active normal fault scarps, and all input files for MA3 site on the Magnola Fault.

modelscarp.m is the main routine iterating the other six (see Appendix for more details).

- *clcoll.m* and *clrock.m* calculate production of ^{36}Cl in a sample buried under colluvium or at surface, respectively,
- *scdepth.m, scsurf.m* calculate the scaling of the samples along *Z* when buried or at surface, respectively,
- *scrock.m* calculates the scaling along direction *e*,
- *fitexp.m* calculates the fit by an exponential form of the 3 scaling factors described above to derived the attenuation length Λ.

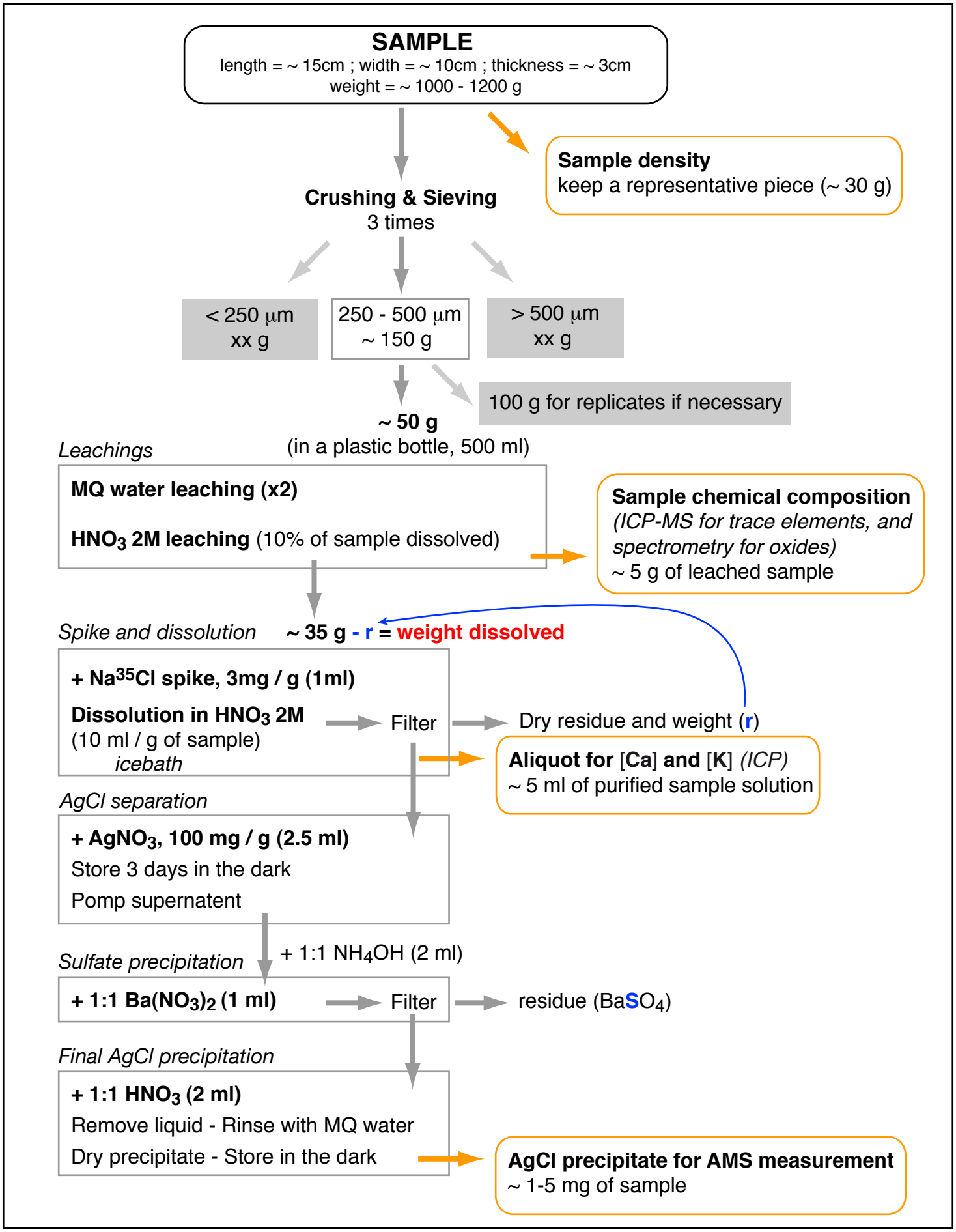

Sample chemical preparation for Cl extraction in limestone rocks
(modified after Stone et al., 1996)

Electronic Supplement 3 – Schlagenhauf et al. 2009

Equations for [Cl] and [^{36}Cl] concentrations calculations, from AMS ratios.
The example is given for a ^{35}Cl-spiked sample.

More details can be found in Desilets et al., 2006
[Desilets, D., Zreda, M., Almasi, P.F., Elmore, D., 2006. Determination of cosmogenic ^{36}Cl in rocks by isotope dilution: innovations, validation and error propagation. Chemical Geology 233, 185-195]

AMS ratios: $\left(\frac{^{36}Cl}{^{35}Cl(or\,^{37}Cl)}\right)_{sample,AMS}$ and $\left(\frac{^{36}Cl}{^{35}Cl(or\,^{37}Cl)}\right)_{blk,i,AMS}$; $\left(\frac{^{35}Cl}{^{37}Cl}\right)_{sample,AMS}$ and $\left(\frac{^{35}Cl}{^{37}Cl}\right)_{blk,i,AMS}$

[Cl_{nat}] calculation:

$m_{Cl,spike} = [Cl_{spike}] \times m_{spike} \times 0.001$ (g)

with $[Cl_{spike}]$ the spike concentration in Cl (mg/g)
m_{spike} the spike mass (g)

$n_{Cl,spike} = m_{Cl,spike} \times N_{av} / M_{spike}$ (at.)

with N_{av} the Avogadro number ($6.022.10^{23}$ mol^{-1})
M_{spike} the molar mass of the spike (%$_{35Cl}$ x M_{35Cl} + %$_{37Cl}$ x M_{37Cl})
M_{35Cl} = 34.9689 g.mol^{-1} and M_{37Cl} = 36.9659 g.mol^{-1}

Isotopic dilution equations to calculate $n_{Cl_{nat,sample}}$ *:*

Cl_{nat} ratio: $R_{Cl_{nat}} = \frac{\%^{35}Cl_{nat}}{\%^{37}Cl_{nat}} = \frac{75.77}{24.23} = 3.127$

Spike ratio: $R_{spike} = \frac{\%^{35}Cl_{spike}}{\%^{37}Cl_{spike}}$ *(known)*

Sample ratio from AMS: $R_{sample,AMS} = \left(\frac{^{35}Cl}{^{37}Cl}\right)_{sample,AMS} = \frac{n_{^{35}Cl_{spike}} + n_{^{35}Cl_{nat,sample}}}{n_{^{37}Cl_{spike}} + n_{^{37}Cl_{nat,sample}}}$

with $n_{^{35}Cl_{spike}} = n_{Cl_{spike}} \times \%_{^{35}Cl_{spike}}$ and $n_{^{37}Cl_{spike}} = n_{Cl_{spike}} \times \%_{^{37}Cl_{spike}}$

$n_{^{35}Cl_{nat,sample}} = n_{Cl_{nat,sample}} \times \%_{^{35}Cl_{nat}}$ and $n_{^{37}Cl_{nat,sample}} = n_{Cl_{nat,sample}} \times \%_{^{37}Cl_{nat}}$

$$R_{sample} = \frac{(n_{Cl_{spike}} \times \%_{^{35}Cl_{spike}}) + (n_{Cl_{nat,sample}} \times \%_{^{35}Cl_{nat}})}{(n_{Cl_{spike}} \times \%_{^{37}Cl_{spike}}) + (n_{Cl_{nat,sample}} \times \%_{^{37}Cl_{nat}})}$$

for the sample: $$n_{Cl_{nat,sample}} = n_{Cl_{spike}} \times \left(\frac{\%_{^{35}Cl_{spike}} - \left(\frac{^{35}Cl}{^{37}Cl}\right)_{sample,AMS} \times \%_{^{37}Cl_{spike}}}{\left(\frac{^{35}Cl}{^{37}Cl}\right)_{sample,AMS} \times \%_{^{37}Cl_{nat}} - \%_{^{35}Cl_{nat}}} \right)$$

and for the blank: $n_{Cl_{nat},blk,i} = n_{Cl_{spike}} \times \left(\frac{\%_{^{35}Cl_{spike}} - \left(\frac{^{35}Cl}{^{37}Cl}\right)_{blk,i,AMS} \times \%_{^{37}Cl_{spike}}}{\left(\frac{^{35}Cl}{^{37}Cl}\right)_{blk,i,AMS} \times \%_{^{37}Cl_{nat}} - \%_{^{35}Cl_{nat}}} \right)$

So, the blank corrected sample number of mole is: $n_{Cl_{nat}corr} = n_{Cl_{nat},sample} - n_{Cl_{nat},blk,i}$

Finally, $[Cl_{nat}]_{sample} = \frac{n_{Cl_{nat}corr} \times M_{Cl_{nat}} \times 10^6}{N_{av} \times m_{sample}}$ (ppm)

[^{36}Cl] calculation:

For a ^{35}Cl spike: $\left(\frac{^{36}Cl}{^{35}Cl}\right)_{sample,AMS} = \frac{n_{^{36}Cl_{sample}}}{n_{^{35}Cl_{sample}}} \quad \Leftrightarrow \quad n_{^{36}Cl_{sample}} = \left(\frac{^{36}Cl}{^{35}Cl}\right)_{sample,AMS} \times n_{^{35}Cl_{sample}}$

with $n_{^{35}Cl_{sample}} = n_{^{35}Cl_{spike}} + n_{^{35}Cl_{nat,sample}} \quad \Leftrightarrow \quad n_{^{35}Cl_{sample}} = \left(n_{Cl_{spike}} \times \%_{^{35}Cl_{spike}}\right) + \left(n_{Cl_{nat,sample}} \times \%_{35_{Cl,nat}}\right)$

for the sample: $n_{^{36}Cl_{sample}} = \left(\frac{^{36}Cl}{^{35}Cl}\right)_{sample,AMS} \times \left[\left(n_{Cl_{spike}} \times \%_{^{35}Cl_{spike}}\right) + \left(n_{Cl_{nat,sample}} \times \%_{35_{Cl,nat}}\right)\right]$

and for the blank: $n_{^{36}Cl_{blk,i}} = \left(\frac{^{36}Cl}{^{35}Cl}\right)_{blk,i,AMS} \times \left[\left(n_{Cl_{spike}} \times \%_{^{35}Cl_{spike}}\right) + \left(n_{Cl_{nat,blk,i}} \times \%_{35_{Cl,nat}}\right)\right]$

So, the blank corrected number of mole in the sample is: $n_{^{36}Cl_{sample,corr}} = n_{^{36}Cl_{sample}} - n_{^{36}Cl_{blk,i}}$

Finally, $[^{36}Cl] = \frac{n_{^{36}Cl_{sample,corr}}}{m_{sample}}$ (at.g^{-1})

And the uncertainty on the calculated [^{36}Cl] concentration is:

$$\Delta\left[^{36}Cl\right] = \left[^{36}Cl\right] \times \sqrt{\left(\frac{\Delta^{36}Cl/^{35}Cl}{^{36}Cl/^{35}Cl}\right)^2 + \left(\frac{\Delta^{35}Cl/^{37}Cl}{^{35}Cl/^{37}Cl}\right)^2}$$

---

blk,i: blank associated to chemistry series *i*
sample: sample prepared in the series *i*
Cl_{nat}: natural chlorine (75.77% ^{35}Cl; 24.23% ^{35}Cl)
m_{sample}: sample weight

Electronic Supplement 4 - Schlagenhauf et al. 2009

Scaling factors for fast neutrons ($S_{el,s}$) and slow muons($S_{el,\mu}$) according to different Earth paleomagnetic models

a - Stone (2000)

Spallation rate at latitude λ and elevation z (normalized to its value at 60° latitude and at standard sea level pressure) :

$$\boxed{S_{el,s}(P) = a + b\exp\left(\frac{-P}{150}\right) + cP + dP^2 + eP^3} \tag{a.1}$$

with a, b, c, d, e : scaling coefficients function of latitude from 0 to $> 60°$ with a 10° step (see Stone, 2000), and P : Pressure (hPa) - (from Lal., 1991) :

$$P(z) = P_s \exp\left[-\frac{g_o M}{R\xi}\left(\ln T_s - \ln(T_s - \xi z)\right)\right] \tag{a.2}$$

P_s : Sea level pressure = 1013.25 hPa ; M : Molar weight of air
T_s : Sea level temperature = 288.15 K ; g_o : acceleration of gravity
ξ : adiabatic lapse rate = 0.0065 K.m $^{-1}$; R : gaz constant
} $\frac{g_o M}{R} = 0.03417$ K.m^{-1}

Slow muon capture at latitude λ and elevation z :

$$\boxed{S_{el,\mu}(P) = M_{\lambda,1013.25}\exp\frac{(1013.25 - P)}{242}} \tag{a.3}$$

with the attenuation length of muons in the air = 242,
and $M_{\lambda,1013.25}$: scaling coefficients for latitudes from 0 to $> 60°$ with a 10° step (see Stone, 2000).

b - Dunai (2001)

Spallation rate at latitude λ, longitude θ and elevation z :

$$\boxed{S_{el,s} = \frac{\sum N_i}{i} \text{ ; with } N_{(z,Rc,t)} = N_{(1030,Rc,f)}\exp\frac{z_{(h)}}{\Lambda_{(Rc)}}} \tag{b.1}$$

$N_{(1030,Rc,f)}$: neutron flux at sea level,
$z_{(h)}$; difference in atmospheric depth,
$\Lambda_{(Rc)}$: attenuation coefficient.

- with $N_{1030,Rc} = Y + \dfrac{A}{\left[1 + \exp\frac{-(R_c - X)}{B}\right]^C}$; and A, B, C, X, Y scaling coefficients (see Dunai, 2001)

(b.2)

Depending on the age of the site, R_c is calculated following one of the two equations below :

⋆ > 10-20 ka (using Yang et al., 2000 and Guyodo and Valet, 1999 record of dipole moment) :

$$R_c(t) = \frac{M(t)\mu_o c}{16\pi R^2} \tag{b.3}$$

$M(t)$: dipole moment over time (Am^2) ; 0-11ka : Yang et al., 2000 ; > 11 ka : Guyodo and Valet, 1999 ;
μ_o : permeability of free space = $1.2566.10^{-6}$
c : speed of light = $2.99.10^8$ (m/s) ;
R : Earth radius = $6.37.10^6$ (m)

⋆ 0 - 11 ka (using Ohno and Hamano record of dipole moment, 1993) :

$$R_c(t) = \frac{R}{4}\frac{H(t)c}{(1+0.25\tan^2 I(t))^{3/2}} \tag{b.4}$$

$H(t)$: horizontal field strength over time,
$I(t)$: inclination of the site over time.

$$H(t) = \frac{M(t)\mu_o \sin\theta(t)}{4\pi R^3} \tag{b.5}$$

$M(t)$: dipole moment over time (values from Ohno and Hamano, 1993),
$\theta(t)$: paleocolatitude over time, $\cos\theta(t) = \sin\lambda_s \sin\lambda_N(t) + \cos\lambda_s \cos\lambda_N(t)\cos(\theta_N(t) - \theta_s)$,
λ_s : present geographic latitude of the site,
$\lambda_N(t)$: paleolatitude of the North geomagnetic pole over time (values from Ohno and Hamano, 1993),
θ_s : present geographic longitude of the site,
$\theta_N(t)$: paleolongitude of the North geomagnetic pole over time (values from Ohno and Hamano, 1993).

$$I(t) = I_{(REF,measured)}(t) - I_{(REF,expected)} + I_{(s,expected)} \tag{b.6}$$

$I_{(REF,measured)}(t)$: paleoinclination at the reference site over time,
$\tan(I_{(REF,expected)}) = 2\tan\lambda_{(REF)}$: paleoinclination at reference site if field would be a pure axial dipole,
$I_{(s,expected)} = 2\tan\lambda_{(s)}$: paleoinclination of the site if field would be a pure axial dipole.

• with $z_{(h)} = \dfrac{10}{g_o}(P_o - P_h)$; and P_o= 1013.25 mbar ; P_h : atmospheric pressure (mbar) (b.7)

$$P_h = P_o\left[1 - \beta_o\frac{z}{T_o}\right]^{\left(\frac{g_o}{R_d\beta_o}\right)} \tag{b.8}$$

β_o : temperature decrease with z = 0.0065 K/m,
z : altitude (m) ; T_o : Temperature at sea level = 288.15 K,
g_o : acceleration due to gravity = 9.80665 $m.s^{-2}$; R_d : gas constant = 287.05 (J/kg/K).

• with $\Lambda(R_c) = y + \dfrac{a}{\left[1+\exp\frac{-(R_c-x)}{b}\right]^c}$; and a, b, c, x, y scaling coefficients (see Dunai, 2001) (b.9)

Slow muon capture at latitude λ and elevation z (time independent) :

$$\boxed{S_{el,\mu} = N_{(1030,\mu)}\exp\frac{z(h)}{\Lambda_\mu}} \tag{b.10}$$

$z_{(h)}$; difference in atmospheric depth (see equation b.7),
$\Lambda_\mu = 247$ (g.cm^{-2}) : muon attenuation length in atmosphere,
$N_{(1013.25,\mu)}$: neutron flux at sea level.

$$\text{with } N_{1013.25,\mu} = Y + \frac{A}{\left[1+\exp\frac{-(I-X)}{B}\right]^C} \quad \text{; and A, B, C, X, Y scaling coefficients for muons (see Dunai, 2001)} \tag{b.11}$$

$\tan(I) = 2\tan(\lambda)$: inclination (time independent).

c - Pigati and Lifton (2004), using Desilets and Zreda (2003)

Spallation rate at latitude λ, longitude θ and elevation z :

$$\boxed{S_{el,s} = \left[\frac{J}{J_o}\right]_{(f,lat)} \left[\frac{J_x}{J_{1033}}\right]_{(f,alt)}} \tag{c.1}$$

- with $\left[\frac{J}{J_o}\right]_{(f,lat)} = 1 - \exp(-\alpha_f R_c^{-k_f})$ (equation from Desilets and Zreda, 2003) (c.2)

J : cosmic-ray flux at site,
J_o : cosmic ray flux at Sea Level and High Latitude (SLHL),
alt stands for altitude and *lat* for latitude,
$\alpha_f = 10.275$ and $k_f = 0.9615$: fitting parameters for neutrons.

$$R_c = \sum_{i=6}^{i=0} \left[e_i + f_i \left(\frac{M}{M_o}\right)\right] \theta(t)^i \text{ (equation from Desilets and Zreda, 2003)} \tag{c.3}$$

M : geomagnetic field intensity (or dipole moment) at time t (A.m^{-2}) from : 0-11 ka, Yang et al. (2000) and >11 ka, Guyodo and Valet (SINT800, 1999),
$M_o = 8.075.10^{22}$ (Am^{-2}) : modern geomagnetic field intensity (in 1945),
$\theta(t)$: geomagnetic paleolatitude over time (see above in part (b) for equation) : 0-2 ka, Merrill and McElhinny (1983), Champion (1980) and 2-11 ka, Ohno and Hamano (1993).

- with $\left[\frac{J_x}{J_{1033}}\right]_{(f,alt)} = \exp\left[\frac{x_2 - x_1}{\Lambda_{(eff,f,x)}}\right]$ (equation from Desilets and Zreda, 2003) (c.4)

$x_2 = 1033$ (g.cm^{-2}) : atmospheric depth at sea level,
x_1 : atmospheric depth at site of interest (g.cm^{-2}).
$\Lambda_{(eff,f,x)}$: effective attenuation length for high energy (spallogenic) neutrons (g.cm^{-2}).

$$x_1 = \left[\frac{10P_o}{g_o}\right]\left[\frac{T_o}{T_o+\beta_o z}\right]^{\left(\frac{g_o M}{1000 R \beta_o}\right)} \tag{c.5}$$

$P_o = 1013.25$ (hPa) : Sea level pressure,
$g_o = 9.8$ (m.s^{-2}) : gravitational constant,
$T_o = 288.15$ (K) : Sea level temperature,
$\beta_o = -0.0065$ (K.m^{-1}) : adiabatic lapse rate,
$M = 28.96$ (g.mol^{-1}) : mean molecular weight of atmosphere,
$R = 8.31451$ (m.mol^{-1}K^{-1}) : gas constant.

$$\Lambda_{(eff,f,x)} = \frac{x_2 - x_1}{\left[\begin{array}{l} n\big(1+exp(-a{R_c}^{-k})\big)^{-1}(x_2-x_1) + 1/2(b_0+b_1R_c+b_2{R_c}^2)({x_2}^2-{x_1}^2)+ \\ 1/3(b_3+b_4R_c+b_5{R_c}^2)({x_2}^3-{x_1}^3) + 1/4(b_6+b_7R_c+b_8{R_c}^2)({x_2}^4-{x_1}^4) \end{array}\right]} \tag{c.6}$$

n, a, k, b_1 to b_8 : fitting parameters from Desilets and Zreda (2003).

Slow muon capture at latitude λ longitude θ and elevation z :

$$\boxed{S_{el,\mu} = \left[\frac{J}{J_o}\right]_{(\mu,alt)}\left[\frac{J_x}{J_{1033}}\right]_{(\mu,lat)}} \tag{c.7}$$

- with $\left[\frac{J}{J_o}\right]_{(\mu,alt)} = 1 - \exp(-\alpha_\mu R_c^{-k_\mu})$ (equation from Desilets and Zreda, 2003) (c.8)

α_μ and k_μ : fitting parameters for muons.

- with $\left[\frac{J_x}{J_{1033}}\right]_{(\mu,lat)} = \exp\left[\frac{x_2 - x_1}{\Lambda_{(eff,\mu,x)}}\right]$ (equation from Desilets and Zreda, 2003) (c.9)

$$\text{and } \Lambda_{(eff,\mu,x)} = 233 + 3.68R_c \tag{c.10}$$

d - Lifton et al. (2005)

Spallation rate at latitude λ, longitude θ and elevation z :

$$\boxed{S_{el,s} = \exp\left[\ln(Flux, sp)\right]} \tag{d.1}$$

$$\text{with } \ln(Flux, sp) = c_1\ln(x_1 S) - S\exp\left[\frac{c_2 S}{(R_c+5S)^{2S}}\right] + c_3(x_1)^{c_4} + c_5[x_1(R_c+4S)]^{c_6} + c_7(R_c+4S)^{c_8} \tag{d.2}$$

x_1 : atmospheric depth at site of interest (see equation c.5 in part (c)),
S : sunspot modulation (over time) from Solanki et al. (2004),
c_1 to c_6 : spallogenic coefficients (Lifton et al., 2005).

$$\text{and } R_c = d_1 \frac{M}{M_o} \cos^{d_2} \theta(t) \text{ (Cutoff rigidity)} \tag{d.3}$$

M : geomagnetic field intensity (or dipole moment) at time t ($A.m^{-2}$) from : 0-11 ka, Yang et al. (2000) and >11 ka, Guyodo and Valet (SINT800, 1999),
$M_o = 8.075.10^{22}$ (Am^{-2}) : modern geomagnetic field intensity (in 1945),
$\theta(t)$: geomagnetic paleolatitude over time (see above in part (b) for equation) : 0-2 ka, Merrill and McElhinny (1983) and 2-11 ka, Ohno and Hamano (1993),
$d_1 = 15.765$ and $d_2 = 3.800$: scaling coefficients.

Slow muon capture at latitude λ longitude θ and elevation z :

$$\boxed{S_{el,\mu} = \exp\left[\ln(Flux, sm)\right]} \tag{d.4}$$

$$\text{with } \ln(Flux, sm) = a_1 + a_2 x_1 + a_3 {x_1}^2 + a_4 x_1 R_c + a_5 R_c + a_6 {R_c}^2 \tag{d.5}$$

x_1 : atmospheric depth at site of interest (see equation (c.5)),
R_c : Cutoff rigidity over time (equation (d.3)),
a_1 to a_6 : coefficients for slow muons (Lifton et al., 2005).

e - Pigati and Lifton (2004) modified using Desilets et al. (2006)

Same equations as part (c), but $\Lambda_{(eff,f,x)}$ calculated using new fitting parameters (n, a, k, b_1 to b_8) from Desilets et al. (2006).

f - Lifton et al. (2008)

Same equations as Lifton et al. (2005, part (d)) but R_c :

⋆ 0 - 7 ka : R_c values extracted from R_c grids from Korte and Constable (2005a,b ; 5° latitude and 15° longitude grid spacing),

⋆ ≥ 7 ka : R_c calculation based on mean field over the entire 0 - 7 ka period

$$R_c = \frac{M}{M_o} \sum_{i=1}^{6} d_{2i-1} \cos^i \left(\theta(t) + \frac{d_{2i}}{M/M_o} \right) \tag{f.1}$$

M : geomagnetic field intensity (or dipole moment) at time t ($A.m^{-2}$) from : 0-11 ka, Yang et al. (2000) and >11 ka, Guyodo and Valet (SINT800, 1999),
$M_o = 8.075.10^{22}$ (Am^{-2}) : modern geomagnetic field intensity (in 1945),
$\theta(t)$: geomagnetic paleolatitude over time (see above in part (b) for equation) : 0-2 ka, Merrill and McElhinny (1983) and 2-11 ka, Ohno and Hamano (1993),
d_1 to d_{12} : coefficients for R_c calculation.

References

D.E Champion, 1980, Holocene geomagnetic secular variation in the western United States : implication for global geomagnetic field, *Open-File Rep. (U.S. Geol. Surv.)*, 80-824, 314.

D. Desilets and M. Zreda, 2003, Spatial and temporal distribution of secondary cosmic-ray nucleon intensities and applications to in situ cosmogenic dating, *Earth and Planetary Science Letters*, Vol. 206, pp 21-42.

D. Desilets, M. Zreda, and T. Prabu, 2006, Extended scaling factors for in situ cosmogenic nuclides : new measurements at low latitude, *Earth and Planetary Science Letters*, Vol. 246, pp 265-276.

T.J. Dunai, 2001, Influence of secular variation of the geomagnetic field on production rates of in situ produced cosmogenic isotopes, *Earth and Planetary Science Letters*, Vol. 193, pp 197-212.

W. Elsasser, E.P. Ney, and J.R. Winckler, 1956, Cosmic-ray intensity and geomagnetism, *Nature*, Vol. 178, pp 1226-1227.

Y. Guyodo and J.P. Valet, 1999, Global changes in intensity of the Earth's magnetic field during the past 800 kyr, *Nature*, Vol. 399, pp 249-252.

M. Korte and C.G. Constable, 2005a, Continuous geomagnetic field models for the past 7 millennia : 2. CALS7K, *Geochem., Geophys., Geosyst.*, Vol. 6, DOI :10.1029/2004GC000801.

M. Korte and C.G. Constable, 2005b, The geomagentic dipole moment over the last 7000 years - new results form a global model, *Earth and Planetary Science Letters*, Vol. 236, pp 348-358.

D. Lal, 1991, Cosmic ray labeling of erosion surfaces : In situ nuclide production rates and erosion models, *Earth and Planetary Science Letters*, Vol. 104, pp 424-439.

N.A. Lifton, J.W. Bieber, J.M. Clem, M.L. Duldig, P. Evenson, J.E. Humble and R. Pyle, 2005, Addressing solar modulation and long-term uncertainties in scaling secondary cosmic rays for in situ cosmogenic nuclide applications, *Earth and Planetary Science Letters*, Vol. 239, pp 140-161.

N.A. Lifton, D.F. Smart and M.A. Shea, 2008, scaling time-integrated in situ cosmogenic nuclide production rates using a continuous geomagnetic model, *Earth and Planetary Science Letters*, Vol. 268, pp 190-201.

R.T. Merrill and M.W. McElhinny, 1983, The Earth's magnetic field : Its history, origin and planetary perspective, *Academic Press, London*, 401 pp.

M. Ohno and Y. Hamano, 1993, Global analysis of the geomagnetic field : time variation of the dipole moment and the geomagnetic pole in the Holocene, *J. Geomag. Geoelectr.*, Vol. 45, pp 1455-1466.

S. Pigati and N.A. Lifton, 2004, Geomagnetic effects on time-integrated cosmogenic nuclide production with emphasis on in situ 14C and 10Be, *Earth and Planetary Science Letters*, Vol. 226, pp 193-205.

S.K. Solanki, I.G. Usoskin, B. Kromer, M. Schussler and J. Beer, 2004, Unusual activity of the Sun during recent decades compared to the previous 11,000 years, *Nature*, Vol. 431, pp 1084-1087.

J.O. Stone, 2000, Air pressure and cosmogenic isotope production, *Journal of Geophysical Research*, Vol. 105, No. B10, pp 23,753-23,759.

S. Yang, H. Odah and J. Shaw, 2000, Variations in the geomagnetic dipole moment over the last 12 000 years, *Geophys. J. Int.*, Vol. 140, pp 158-162.

Electronic Supplement 5 - Schlagenhauf et al. 2009

	[Cl]nat	[36Cl]	uncertainty on [36Cl]
MA3c-18	11,1	1,40E+05	3,34E+03
MA3c-18R	11,4	1,45E+05	3,59E+03
MA3c-18 mean	***11,2***	***1,43E+05***	***2,79E+03***
MA3c-28	12,9	1,25E+05	3,14E+03
MA3C-28R	13,1	1,27E+05	3,76E+03
MA3c-28 mean	***13,0***	***1,26E+05***	***1,02E+03***
MA3c-42	10,8	1,05E+05	2,61E+03
MA3c-42R	11,1	1,05E+05	3,20E+03
MA3c-42 mean	***10,9***	***1,05E+05***	***3,64E+02***

Replicates values from Magnola MA3c data-set (samples below the colluvium).

	1	2	3	4	5	6	7	8	9
	As	Ba	Be	Bi	Cd	Ce	Co	Cr	Cs
Sample name	ppm	ppm	ppm	ppm	ppm	ppm	ppm	ppm	ppm
MA3c - S1	4.162	120.6	1.724	0.191	1.087	37.14	5.989	26.82	3.697
MA3c - S2	8.421	221.0	2.748	0.335	1.465	63.26	9.904	49.34	6.626
MA3c - S4	5.608	153.7	1.949	0.217	1.085	43.16	7.314	33.04	4.373
MA3c - S8	3.924	130.5	1.577	0.199	0.660	36.71	5.470	20.67	4.998
MA3c - S10	0	41.27	0	0	0.422	9.897	2.653	8.241	1.303
MA3c - Soil mean	*4.423*	*133.4*	*1.600*	*0.188*	*0.944*	*38.03*	*6.266*	*27.62*	*4.199*
MA3c-P1	0	2.534	0	0	0.391	0.426	1.203	0	0
MA3c-P2	0	7.110	0	0	0.339	0.451	1.130	0	0
MA3c-P4	0	0	0	0	0.360	0.359	1.214	0	0
MA3c-P8	0	14.82	0	0	0.480	4.135	1.664	0	0.598
MA3c-P10	0	12.86	0	0	0.366	2.623	1.617	0	0.350
MA3c -Pebbles mean	*0*	*7.465*	*0*	*0*	*0.387*	*1.599*	*1.366*	*0*	*0.190*

10	11	12	13	14	15	16	17	18	19
Cu	Dy	Er	Eu	Ga	Gd	Ge	Hf	Ho	In
ppm	ppm	ppm	ppm	ppm	ppm	ppm	ppm	ppm	ppm
15.74	1.963	1.094	0.586	5.574	2.413	0.473	1.674	0.388	0
21.86	3.264	1.746	0.982	10.37	3.933	0.836	2.862	0.615	0
15.62	2.259	1.221	0.673	7.070	2.715	0.576	1.89	0.435	0
8.956	1.713	0.898	0.556	4.394	2.223	0.402	1.625	0.324	0
0	0.602	0.338	0.18	1.481	0.692	0.145	0.498	0.117	0
12.43	*1.960*	*1.059*	*0.595*	*5.778*	*2.395*	*0.486*	*1.71*	*0.376*	*0*
0	0.123	0.069	0.036	0	0.128	0	0.025	0.025	0
0	0.134	0.086	0.027	0	0.121	0	0	0.029	0
0	0.130	0.086	0.029	0	0.131	0	0.020	0.029	0
0	0.414	0.218	0.139	0.512	0.487	0	0.194	0.078	0
0	0.240	0.147	0.071	0.366	0.303	0	0.117	0.050	0
0	*0.208*	*0.121*	*0.06*	*0.176*	*0.234*	*0*	*0.071*	*0.042*	*0*

20	21	22	23	24	25	26	27	28	29
La	Lu	Mo	Nb	Nd	Ni	Pb	Pr	Rb	Sb
ppm	ppm	ppm	ppm	ppm	ppm	ppm	ppm	ppm	ppm
20.43	0.167	0	7.465	15.62	20.67	11.88	4.333	31.86	0.325
32.61	0.265	0.649	12.67	25.70	29.60	21.54	6.997	61.88	0.509
22.81	0.179	0	8.225	17.90	23.97	14.13	4.881	42.08	0.373
20.06	0.133	0	6.382	15.21	19.28	11.77	4.219	30.69	0.352
5.831	0.051	0	1.780	4.608	14.55	3.382	1.247	10.05	0
20.348	*0.159*	*0.13*	*7.304*	*15.808*	*21.614*	*12.54*	*4.335*	*35.312*	*0.312*
1.346	0.010	0	0.059	0.951	10.05	0	0.260	0	0
0.886	0.012	0	0.053	0.627	9.672	0	0.162	0.368	0
1.176	0.012	0	0	0.856	10.21	0	0.231	0.303	0
4.864	0.032	0	0.683	3.722	10.72	1.801	1.011	5.409	0
2.290	0.023	0	0.410	1.879	11.41	1.250	0.496	2.966	0
2.112	*0.018*	*0*	*0.241*	*1.607*	*10.412*	*0.61*	*0.432*	*1.809*	*0*

30	31	32	33	34	35	36	37	38	39
Sm	Sn	Sr	Ta	Tb	Th	Tm	U	V	W
ppm	ppm	ppm	ppm	ppm	ppm	ppm	ppm	ppm	ppm
2.873	1.143	145.7	0.528	0.359	6.849	0.159	1.174	32.12	0.653
4.760	1.932	130.3	0.891	0.567	12.06	0.254	1.775	60.01	1.206
3.351	1.401	138.9	0.588	0.392	7.813	0.171	1.256	41.91	0.849
2.728	1.067	122.0	0.418	0.310	8.572	0.130	1.021	30.18	0.633
0.847	0.457	96.89	0.129	0.102	1.978	0.048	0.486	10.82	0
2.912	*1.2*	*126.758*	*0.511*	*0.346*	*7.454*	*0.152*	*1.142*	*35.008*	*0.668*
0.160	0	148.9	0	0.018	0.062	0.010	0.231	0	0
0.118	0	155.9	0	0.019	0.047	0.012	0.383	0	0
0.143	0	154.1	0	0.020	0.036	0.012	0.407	0	0
0.660	0	122.5	0.048	0.070	1.010	0.032	0.383	4.952	0
0.373	0	106.3	0.029	0.042	0.515	0.020	0.223	2.975	0
0.291	*0*	*137.54*	*0.015*	*0.034*	*0.334*	*0.017*	*0.325*	*1.585*	*0*

40	41	42	43	44	45	46	47	48	49
Y	Yb	Zn	Zr	SiO2 (Si)	Al2O3 (Al)	Fe2O3 (Fe)	MnO (Mn)	MgO (Mg)	CaO (Ca)
ppm	ppm	ppm	ppm	%	%	%	%	%	%
13.41	1.046	42.40	73.07	9.915	4.575	1.722	0.036	0.785	43.54
20.94	1.705	73.40	124.3	19.07	8.355	3.228	0.065	1.115	33.46
14.64	1.198	50.42	81.76	12.56	5.525	2.167	0.045	0.901	40.76
10.56	0.869	33.92	74.15	9.294	4.024	1.551	0.031	0.722	45.15
4.260	0.317	15.41	20.73	3.098	1.246	0.515	0.011	0.43	52.23
12.762	*1.027*	*43.11*	*74.802*	*10.787*	*4.745*	*1.837*	*0.038*	*0.791*	*43.03*
1.157	0.07	0	1.358	0	0	0	0.004	0.55à	55.21
1.385	0.078	9.205	0	0	0	0	0.006	0.543	55.41
1.443	0.077	8.114	0	0	0	0	0.004	0.556	55.18
3.089	0.202	8.739	9.120	0.943	0.458	0.202	0.007	0.509	54.15
1.962	0.135	0	5.759	0.604	0.297	0.130	0.004	0.389	54.31
1.807	*0.112*	*5.212*	*3.247*	*0.309*	*0.151*	*0.066*	*0.005*	*0.499*	*54.85*

50	51	52	53	54	55	56	57	58
Na2O(Na)	K2O(K)	TiO2(Ti)	P2O5(P)	B	Li	H2Otot (H)	Stot (S)	CO2 tot (C)
%	%	%	%	ppm	ppm	%	%	%
0	0.370	0.213	0.286	11.00	15.00	3.790	0.040	37.92
0.151	0.762	0.386	0.342	23.00	27.60	6.020	0.060	31.91
0.094	0.497	0.259	0.256	17.00	17.70	4.470	0.040	36.10
0.078	0.413	0.192	0.216	11.00	11.30	3.050	0.020	36.56
0	0.146	0.064	0.106	6.000	3.900	1.280	0.020	41.58
0.065	*0.438*	*0.223*	*0.241*	*13.6*	*15.1*	*3.722*	*0.036*	*36.814*
0	0	0	0.061	2.000	1.000	0.230	0.020	44.18
0	0	0	0.143	2.000	0.900	0.240	0.010	44.16
0	0	0	0.086	2.000	1.000	0.240	0.020	44.17
0	0.084	0.024	0.079	2.000	2.000	0.430	0.010	43.16
0	0	0.017	0.044	2.000	1.600	0.490	0.010	43.42
0	*0.017*	*0.008*	*0.083*	*2*	*1.3*	*0.326*	*0.014*	*43.818*

Chemical composition of five samples from the colluvial wedge at MA3 site (Magnola Fault) and corresponding mean compositions. See Figure 15 for position of the samples. Pebbles and soil were analyzed separately. Note that when using the 'most concentrated' sample S2 as mean composition of the colluvial wedge, production rate is similar to the one modeled with the mean composition over the five samples.

Electronic Supplement 7 - Schlagenhauf et al. 2009

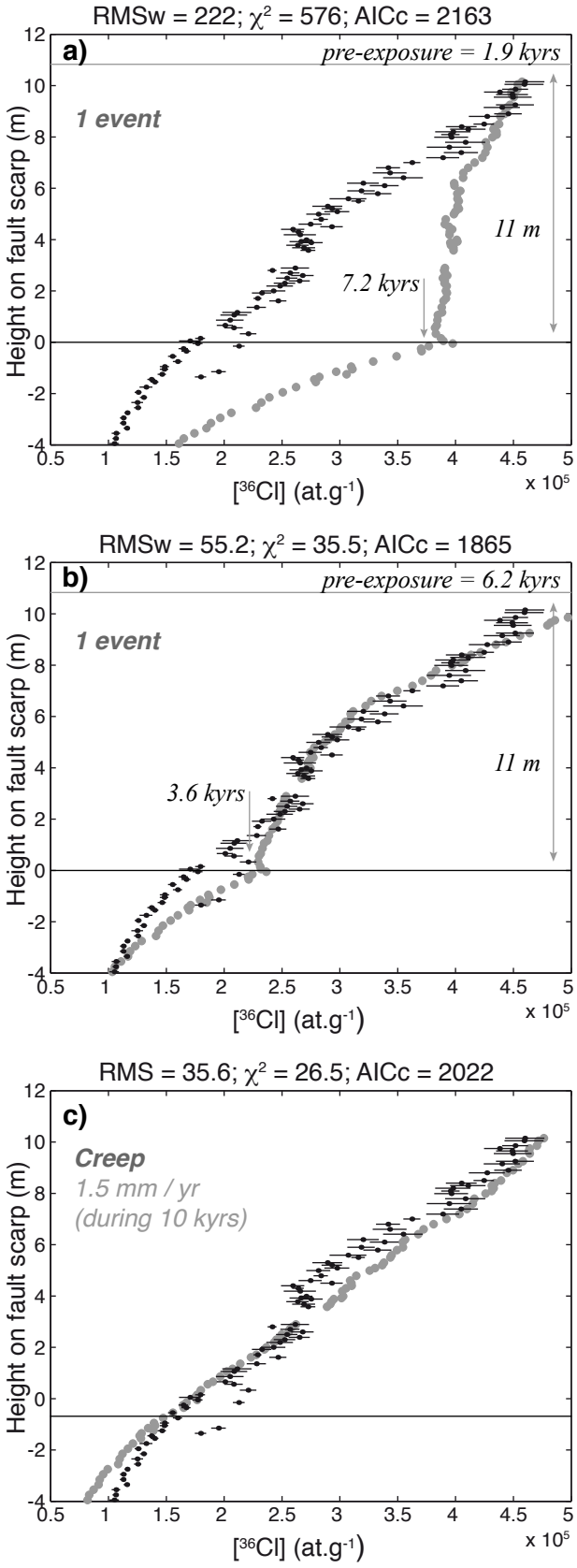

Magnola fault data set (MA3 site). Samples below z = 0 are those from the buried scarp under the colluvium. a,b) Bests fits for a unique event (one earthquake or a landslide). a) Fit of the topmost segment, one event of 10 meters 7.2 kyrs ago (with pre-exposure fixed at 1.9 kyrs as Fig. 18a). b) Best fit of the complete data set with an event of same displacement 3.6 kyrs ago (pre-exposure parameter free: best fit for 6.2 kyrs). c) Modeling creep on the fault. Best fit is obtained for slip-rate of 1.5 mm/yr over 10 kyrs. In all cases, fit is not satisfactory.

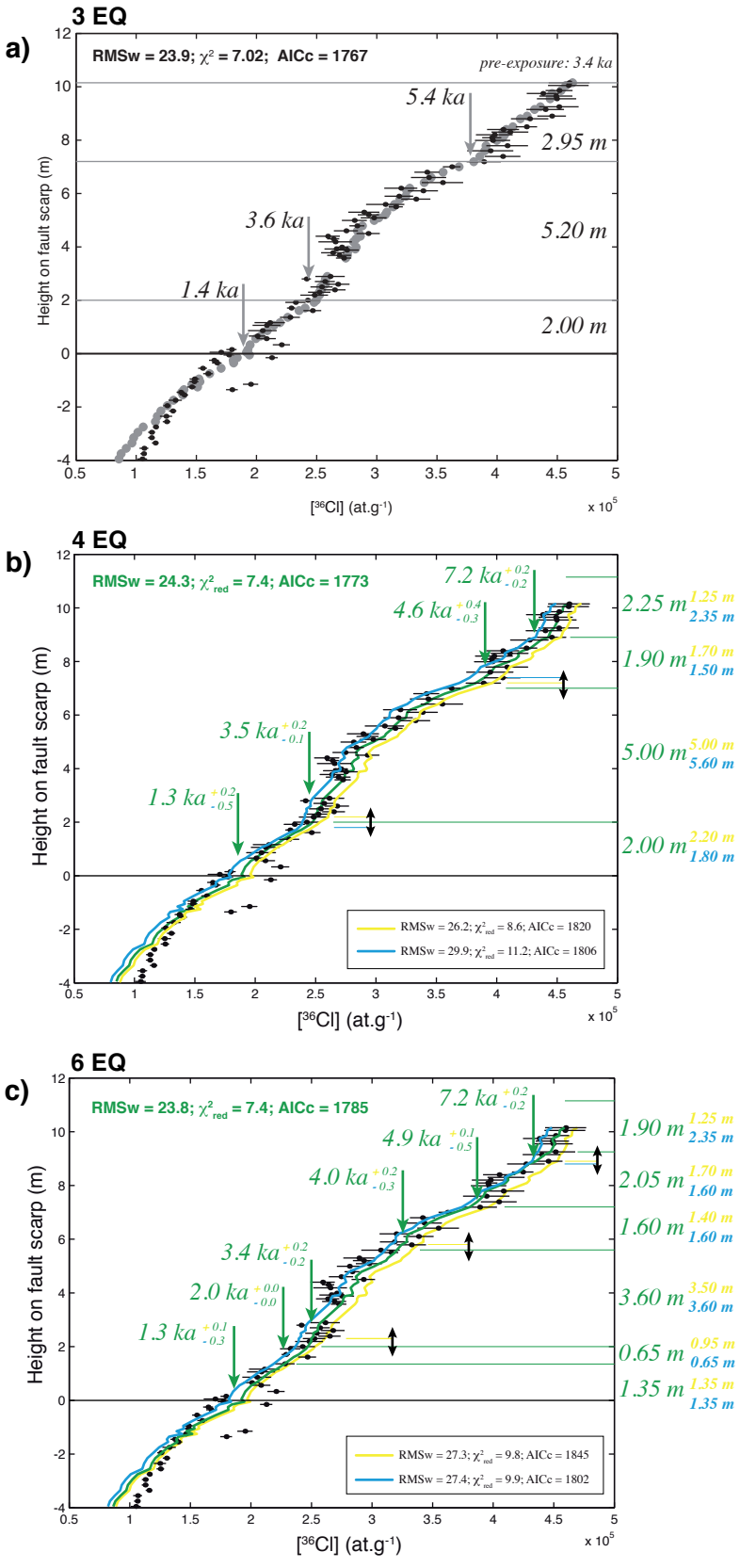

Best fit of the Magnola data set from MA3 site (black dots and respective uncertainties as horizontal lines) by 3, 4 and 6 large slip exhumations. Models have been calculated with no erosion and for a constant Earth's magnetic field.

a) 3 events model. The data best-fit function is in grey. Earthquake ages and displacements are indicated.

b-c) 4 and 6 events models. The data best-fit function is in green, while fitting the data uncertainties produce the yellow and blue curves. Double arrows indicate the uncertainties on the displacements. Earthquake ages are indicated together with their uncertainties.

Annexe III

(du chapitre 5)

RECAPITULATIF SITES ABRUZZES (ITALIE)

FAILLE	Nom du site	NOUVEAU NOM	date éch.	rho_rock	rho_coll	alpha	beta	gamma	H	altitude	latitude	longitude	EL_f Stone 2000	EL_mu Stone 2000	H echantillons
Magnola	M1	**MA3**	2003	2.7	1.5 (mesuré)	30°	45°	30°	20m	1255m +/- 5m	N42.11900	E013.44800	2.750	1.703	10.15 + 4.0 m
	M1c		Mai 2007												
Magnola	A1c (W)	**MA1**	Sept. 2005	2.67	1.5 ?	25°	40°	35°	15m	1265m +/- 5m	N42.12800	E013.41371	2.771	1.711	8.10 m
Magnola	A4c (E)	**MA4**	Sept. 2005	2.64	1.5 ?	30°	42°	30°	7m	1300m +/- 10m	N42.11840	E013.46135	2.846	1.737	7.00 m
Magnola	A6c	**MA2**	Avril 2006	2.67	1.5 ?	35°	50°	35°	8.6m	1200m +/- 5m	N42.12400	E013.42737	2.636	1.662	8.55 m
Velino	**VE**		Mai 2007	2.71	1.5 ?	30°	40°	35°	9.50	1014m +/-5m	N42.16858	E013.31302	2.281	1.531	7.01 m
Campo Felice	**CF**		Mai 2007	2.66	1.5 ?	30°	55°	45°	17m	1595m +/-5m	N42.22832	E013.4437	3.558	1.974	8.85 m
Fiamignano	**FI**		Mai 2007	2.68	1.5 ?	12°	63°/40°	38°	10m	1178m +/-5m	N42.27208	E013.11618	2.597	1.648	7.10 m
Tre Monti	**TM**		Mai 2007	2.67	1.5 ?	20°	72°	35°	3.5m	970m +/-5m	N42.06505	E013.4627	2.200	1.499	2.70 m
Trasacco	**TR**		Mai 2007	2.64	1.5 ? - 2.0 ?	25°	65°	25°	4.7m	800m +/-5m	N41.92805	E013.56700	1.916	1.386	4.45 m
Parasano	**PA**		Mai 2007	2.64	1.5 ?	25°	55°	35°	4.5m	1270m +/-5m	N41.99613	E013.70275	2.777	1.713	3.30 m
San Sebastiano	**SB**		Mai 2007	2.62	1.5 ?	25°	62°	35°	8.5m	1214m +/-5m	N41.94667	E013.76185	2.658	1.671	4.45 m
Roccapreturo	A2R (W)	**RP1**	Avril 2006	2.69	1.5 ?	20°	60°	35°	10m	795m +/- 5m	N42.21846	E013.65015	1.915	1.386	7.35 m
Roccapreturo	A1R	**RP2**	Avril 2006	2.66	1.5 ?	25°	55°	35°	10.25m	805m +/-10m	N42.19143	E013.71244	1.930	1.392	10.20 m
Roccapreturo	A3R (E)	**RP3**	Avril 2006	2.65	1.5 ?	25°	60°	40°	10m	783m +/-7m	N42.18127	E013.72890	1.896	1.378	5.35 m
Castel di Ieri	**CI**		Mai 2007	2.64	1.5 ?	15°	45°	40°	4m	570 +/- 5 m	N42.1057	E013.90263	1.601	1.253	3.0 m
Roccacasale	**RC**		Mai 2007	2.68	1.5 ?	30°	55°	25°	5.7m	392m +/-5m	N42.12515	E013.88250	1.366	1.147	4.70 m

Faille de Fiamignano

Panorama de la faille de Fiamignano (vue vers le nord)

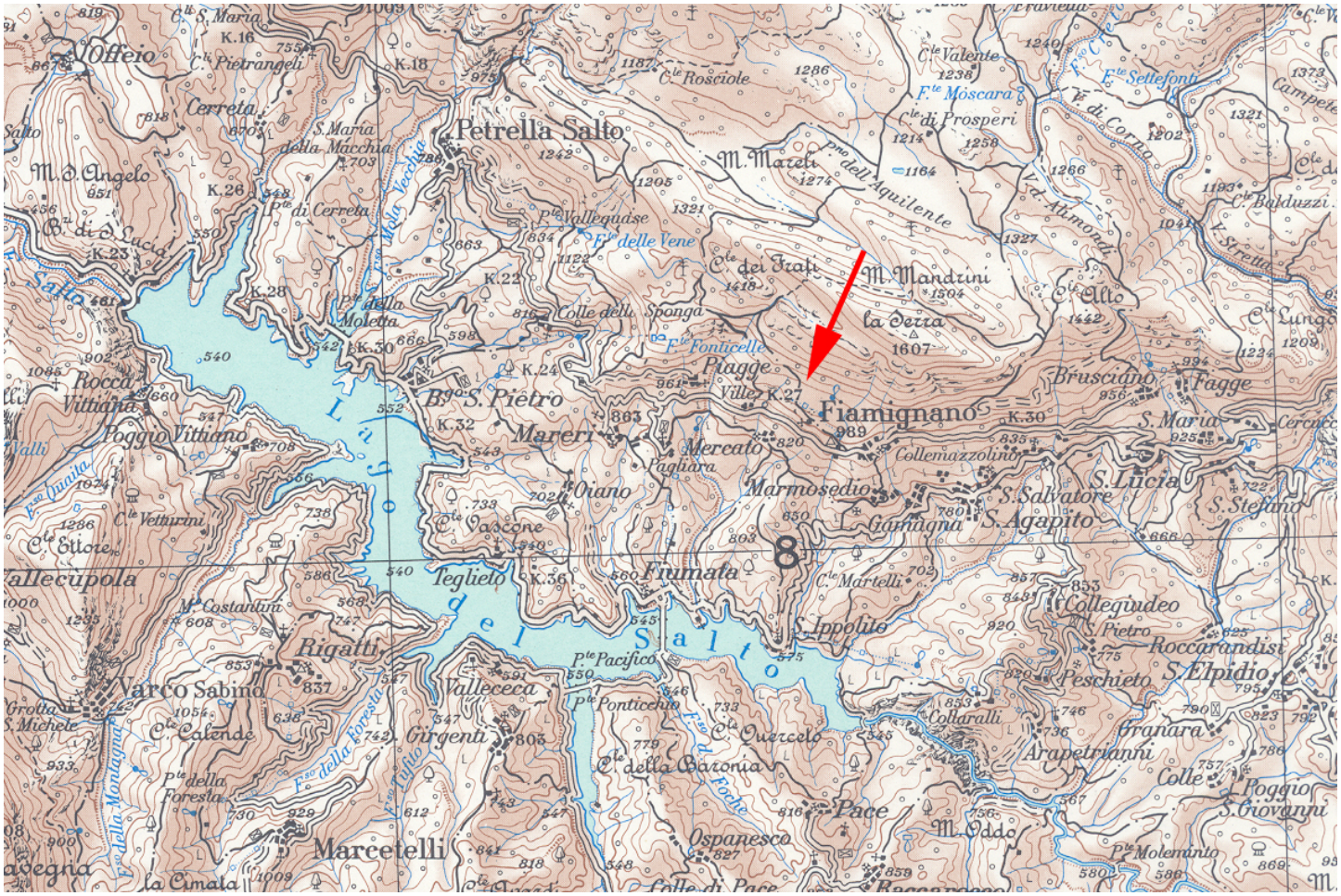

Extrait de la feuille n°145 (AVEZZANO) au 1:100 000ème, IGM

Faille de Fiamignano - Site FI-A

Mission Mai 2007
GPS FI-A: alt. 1178 m ± 5m ; N42.27208 - E013.11618
Ecrantage : seulement le plan de faille, à la base **115 SW 63** (1m de hauteur), au dessus **115 SW 40**
Nbre échantillons : 95 (FI-1 à FI-95)
+ 2 échantillons au dessus : **FI-TOP1** (alt. 1188 m ± 5m ; γ = 38°)
FI-TOP2 (alt. 1191 m ± 5m ; γ = 38°)
+ **FI-COL** (alt. 1176 m ± 5m ; α = 12°)
α = 12° ; β = 63° puis 40° ; γ = 38°
H = 10 m

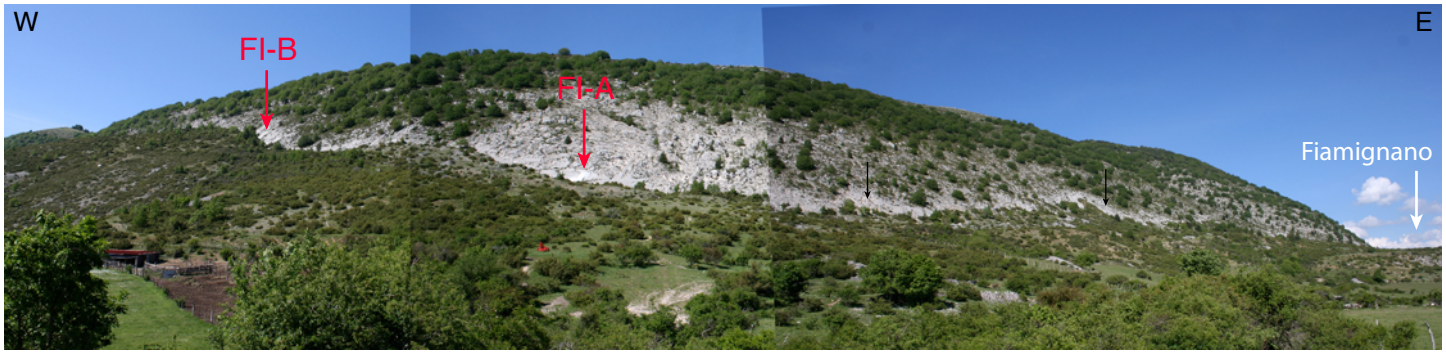

Vue vers le nord des sites FI (A et B) au nord-ouest du village de Fiamignano

Site principal FI-A
(échantillons FI-1 à FI-95)

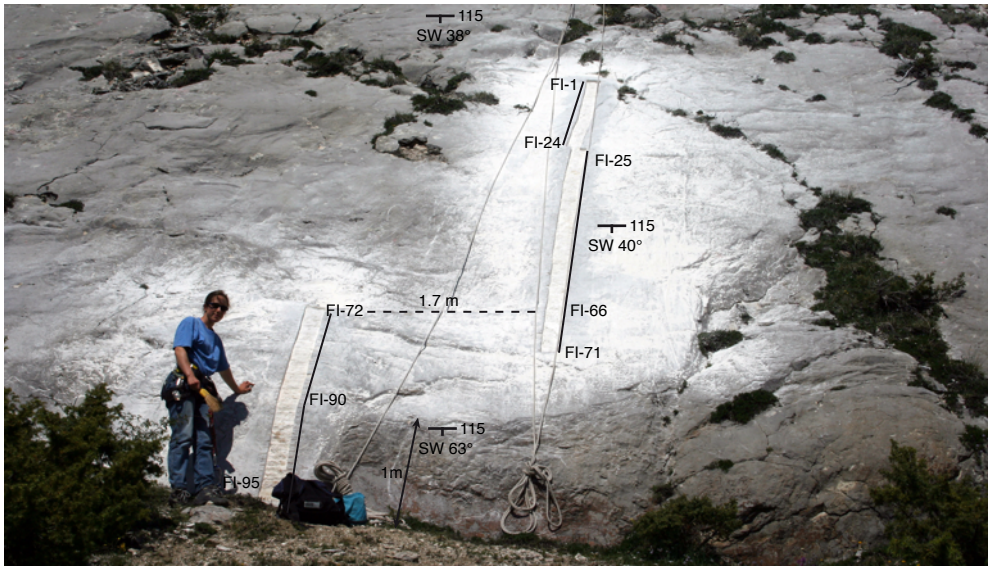

Faille de Fiamignano - Site FI-B

Mission Mai 2007
GPS FI-B: alt. 1200 m ± 5m ; N42.27378 - E013.11400
Ecrantage : seulement le plan de faille **135 SW 40**
Nbre échantillons : 15 (FI-100 à FI-115)

α = 20° ; β = 40° ; γ = 38°
H = 7 m

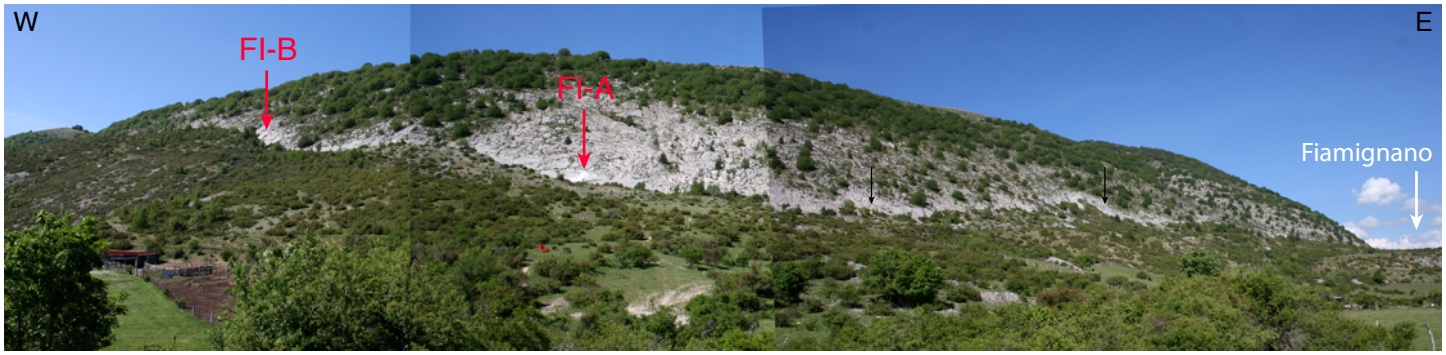

Vue vers le nord des sites FI (A et B) au nord-ouest du village de Fiamignano

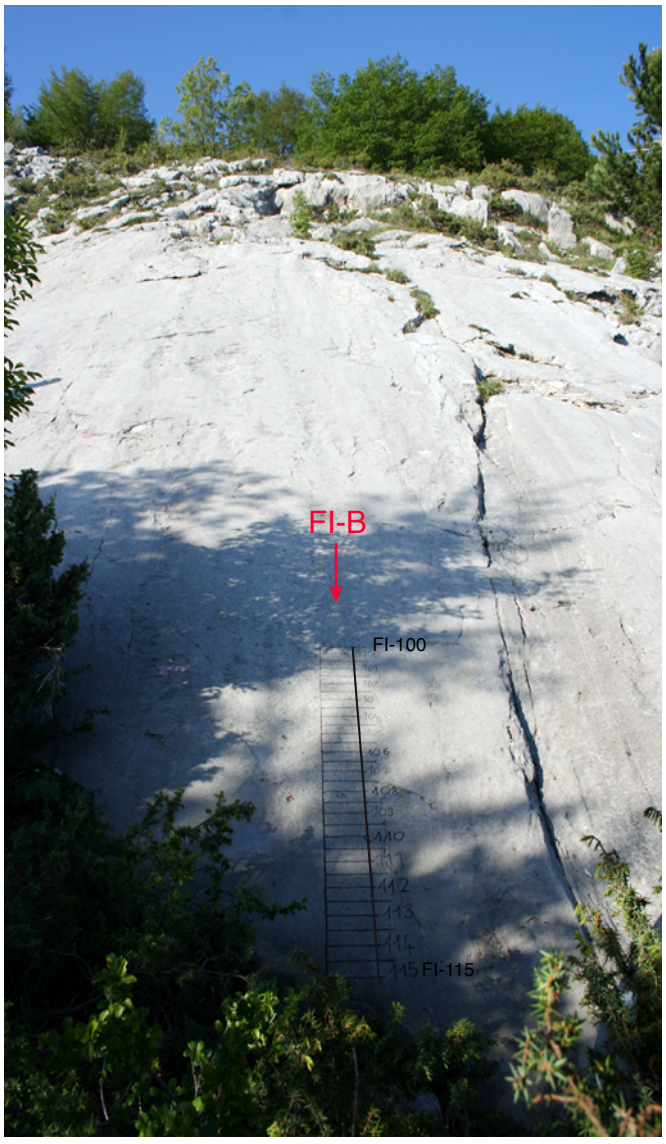

Site secondaire FI-B
(échantillons FI-100 à FI-105)

Faille de Campo Felice

Mission Mai 2007
GPS : alt. 1595 m ± 5m ; N42.22832 - E013.44370
Ecrantage : seulement le plan de faille **105 S 55**
Nbre échantillons : 77 (CF-1 à CF-77)
+ 1 échantillon au dessus : **CF-TOP** (alt. 1612 m ± 5m ; γ = 45°)
+ **CF-COL** (alt. 1590 m ± 5m ; α = 30°)
α = 30° ; β = 55° γ = 45°
H = 17 m

Panorama de la faille de Campo Felice (vue vers le nord)

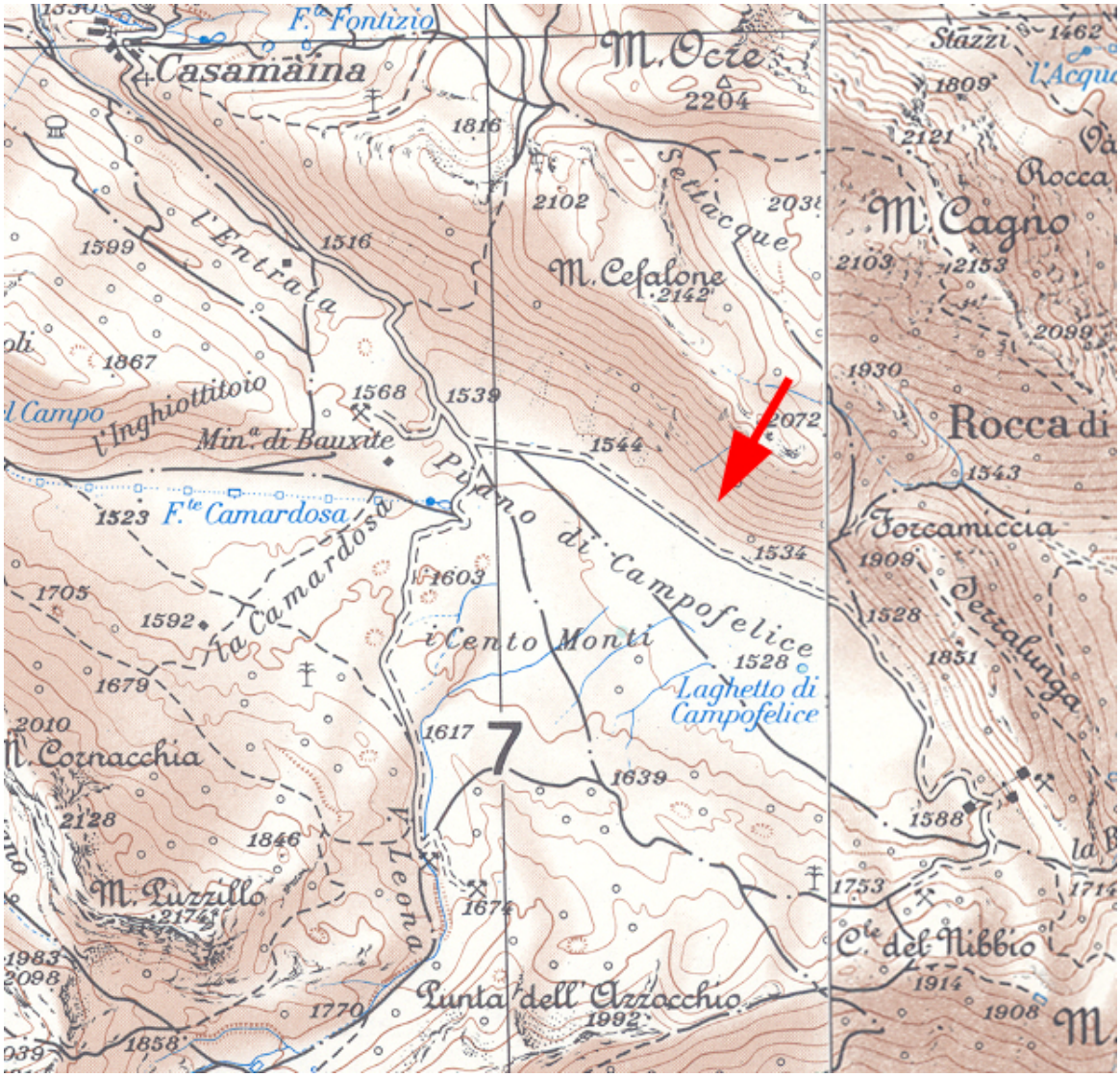

Extrait des feuilles n°145 (AVEZZANO) et n°146 (SULMONA) au 1:100 000ème, IGM

Site CF

Faille de Campo Felice, localisation du site d'échantillonnage CF

SiteCF

Faille du Mont Velino - Site VE

Site au dessus du village de Cartore
Mission Mai 2007
GPS : alt. 1014 m ± 5m ; N42.16858 - E013.31302
Ecrantage : seulement le plan de faille **130 SW 40**
Nbre échantillons : 76 (VE-1 à VE-77 ; *pas de VE-40*)
+ 2 échantillons au dessus : **VE-TOP1** (alt. 1023 m ± 5m ; γ = 35°)
VE-TOP2 (alt. 1022.5 m ± 5m ; γ = 35°)
+ **VE-COL** (alt. 1011 m ± 5m ; α = 30°)
α = 30° ± 3°; β = 40° ± 2° ; γ = 35° ± 5°
H = 9.5 m

Faille du Mont Velino vue depuis le village de Cartore (vue vers le nord)

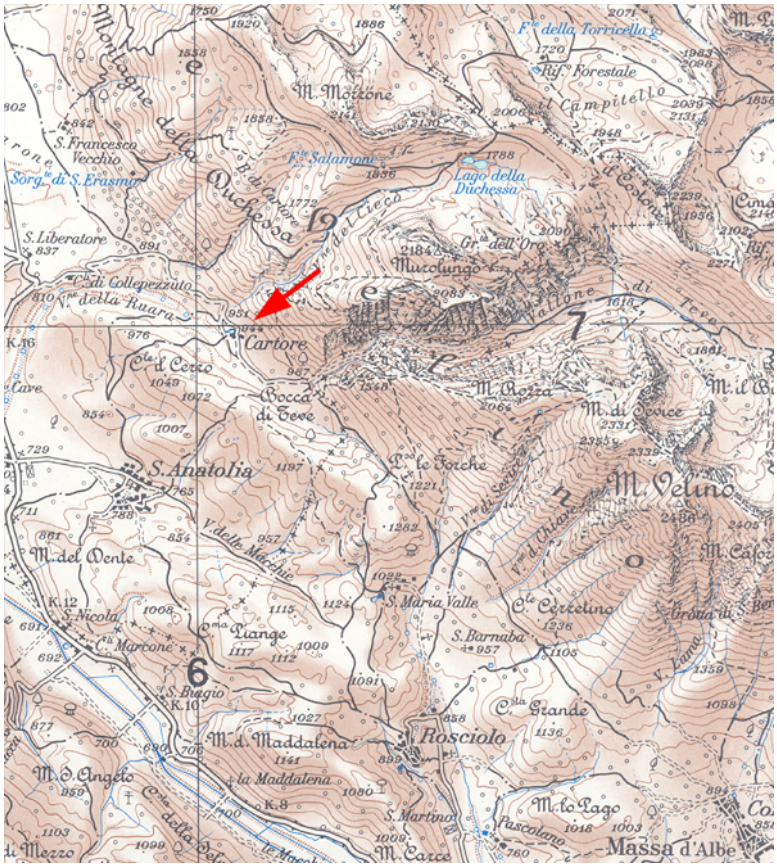

Extrait de la feuille n°145 (AVEZZANO) au 1:100 000ème, IGM

Site VE

Faille de la Magnola

Panorama de la faille de la Magnola vue depuis la route au sud du village de Forme (vue vers le nord)

Panorama de la faille de la Magnola vue depuis le village de Forme (vue vers le nord)

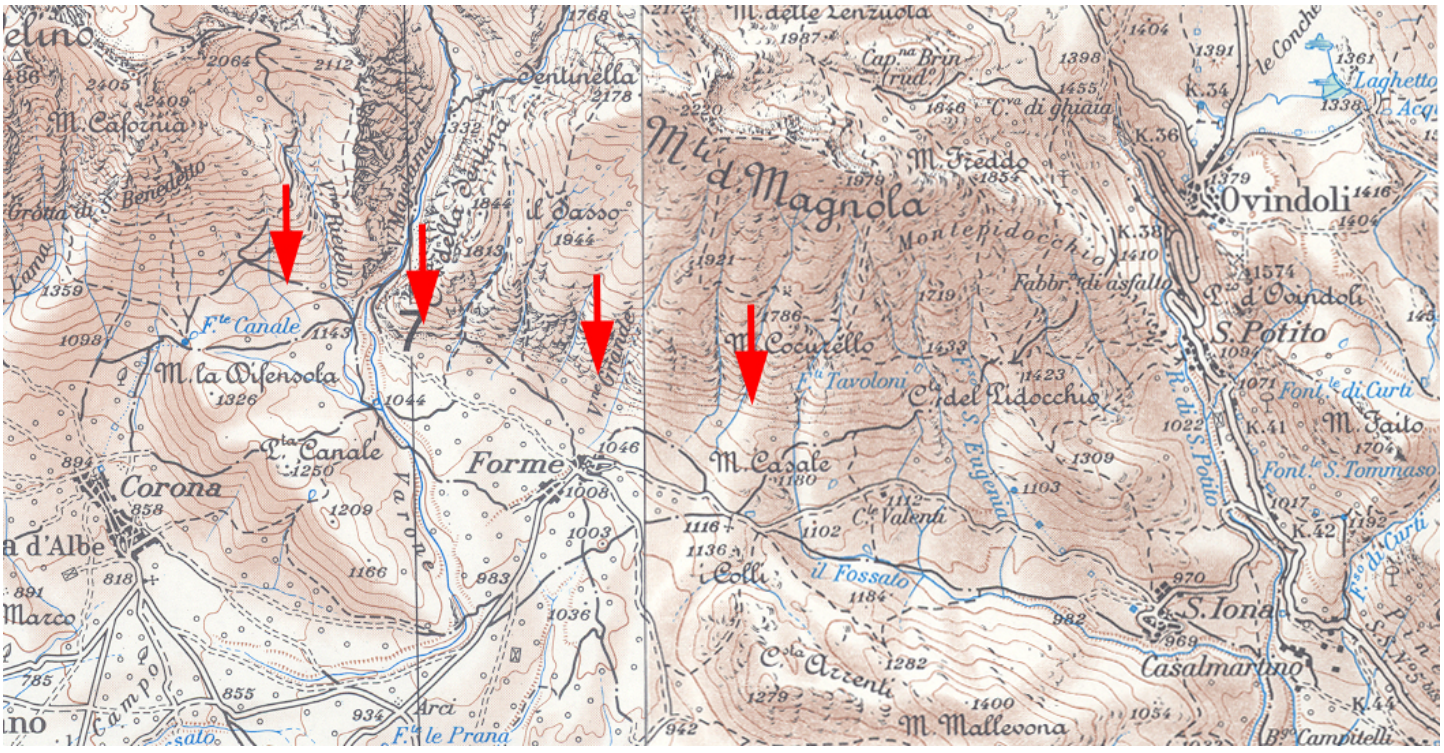

Extrait des feuilles n°145 (AVEZZANO) et n°146 (SULMONA) au 1:100 000ème, IGM

Faille de la Magnola - Site MA1

Terminaison Ouest de la faille de la Magnola (à l'ouest de la Vallée Majelama)
Mission Sept. 2005
GPS : alt. 1265 m ± 5m ; N42.12800 - E013.41371
Ecrantage : seulement le plan de faille **110 S 42**
Nbre échantillons : 70 (A1c-1 à A1c-70)
+ 1 échantillon au dessus : **A1c-TOP** (alt. 1305 m ± 5m ; γ = 35°)
α = 25° ± 3° ; β = 40° ± 2° ; γ = 35° ± 5°
H = 15 m

Vue vers le nord de l'extrémité ouest de la faille de la Magnola et localisation du site MA1

Site MA1 (anciemment nommé A1c)

Faille de la Magnola - Site MA2

(à l'est de la Vallée Majelama)
Mission Avril 2006
GPS : alt. 1200 m ± 5m ; N42.12400 - E013.42737
Ecrantage : seulement le plan de faille **100 S 50**
Nbre échantillons : 74 (A6c-1 à A6c-74)
$\alpha = 35° \pm 3°$; $\beta = 50° \pm 2°$; $\gamma = 35° \pm 5°$
H = 8.6 m

Vue vers le nord de la faille de la Magnola (à l'est de la vallée Majelama) et localisation du site MA2

Site MA2 (anciennement nommé A6c)

Faille de la Magnola - Site MA3

Site central de la faille de la Magnola (au dessus du village de Forme)
Echantillonnage "MAG" lors de la thèse de L. Palumbo ; "M1c" mission Mai 2007
GPS : alt. 1255 m ± 5m ; N42.11900 - E013.44800
Ecrantage : seulement le plan de faille **110 S 45**
Nbre échantillons : 65 (MAG-1 à MAG-65)
+ échantillons du scarp sous le colluvion: **42** (M1c-1 à M1c-42)
+ cailloux dans le colluvion : **14** (M1S-1 à M1S-14)
+ ^{14}C : **2** échantillons (M1carb-1 = 31.6 ± 0.5 ka ; M1carb-2 = 38.8 ± 1.2 ka)
$\alpha = 30° \pm 3°$; $\beta = 45° \pm 2°$; $\gamma = 30° \pm 5°$
H = 20 m

Vue vers le nord de la partie centrale de la faille de la Magnola et localisation du site MA3

Site MA3 (anciennement nommé M1)

Faille de la Magnola - SITE A4c

Terminaison Est de la faille de la Magnola
Mission Sept. 2005
GPS : alt. 1300 m ± 10m ; N42.11840 - E013.46135
Ecrantage : seulement le plan de faille **97 S 42**
Nbre échantillons : 64 (A4c-1 à A4c-64)
$\alpha = 30° \pm 3°$; $\beta = 42° \pm 2°$; $\gamma = 30° \pm 5°$
H = 7 m

Vue vers le nord de la terminaison Est de la faille de la Magnola et localisation du site MA4

Site MA4 (anciemment nommé A4c)

Faille de Tre Monti - Site TM

Site au dessus du hameau de San Pelino Vecchio
Mission Mai 2007
GPS : alt. 970 m ± 5m ; N42.06505 - E013.46270
Ecrantage : seulement le plan de faille **65 SSE 72**
Nbre échantillons : 27 (TM-1 à TM-27)
+ 1 échantillon au dessus : **TM-TOP** (alt. 977 m ± 5m ; γ = 35°)
+ **TM-COL** (alt. 968 m ± 5m ; α = 20°)
α = 20° ; β = 72° γ = 35°
H = 3.5 m

Faille de Tre Monti vue depuis le le bassin du Fucino (vue vers le nord)

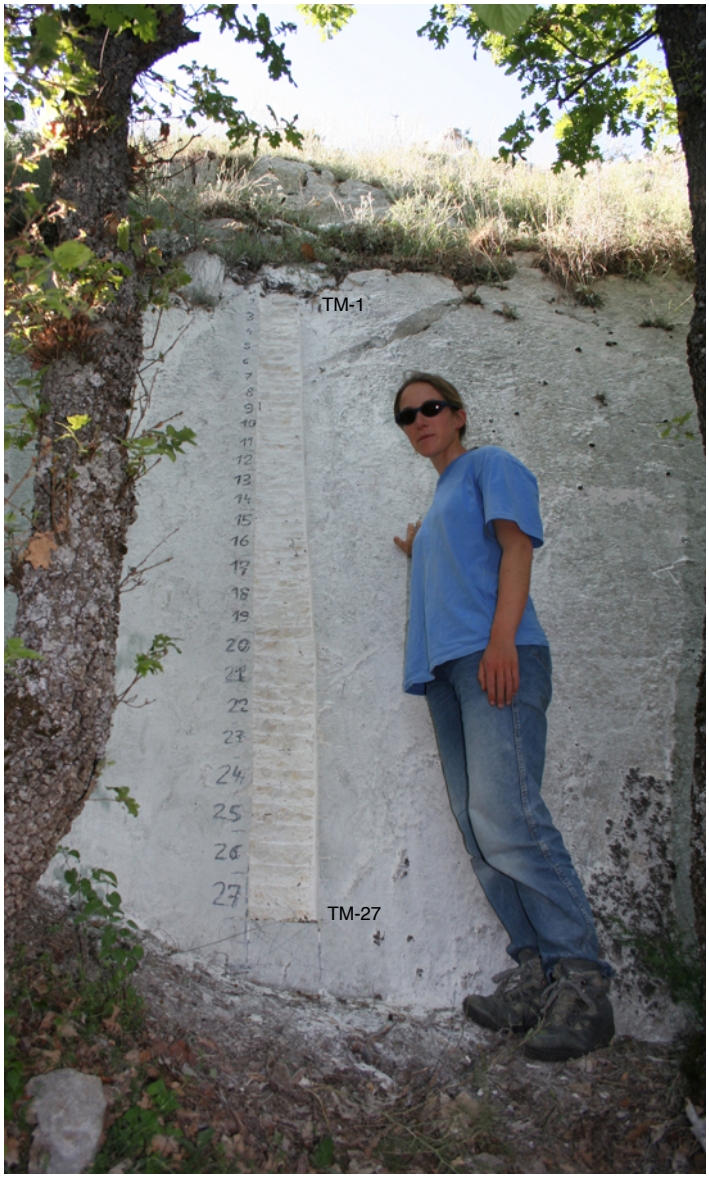

Extrait des feuilles n°145 (AVEZZANO) et n°146 (SULMONA) au 1:100 000ème, IGM

Site TM
La base sur 60 cm de hauteur a un aspect plus lisse tout au long de la faille de Tre Monti. Stries normales-dextres.

Faille de Trasacco (site TR)

Au sud-est du village de Trasacco
Mission Mai 2007
GPS : alt. 800 m ± 5m ; N41.92805 - E013.56700
Ecrantage : seulement le plan de faille **110 S 65**
Nbre échantillons : 45 (TR-1 à TR-45)
+ 1 échantillon au dessus : **TR-TOP** (alt. 810 m ± 5m ; γ = 25°)
+ **9** échantillons du colluvion exhumé (à 20 m à l'est du site principal, 90cm exhumés, 50cm à l'avant du scarp principal : TR-C1 à TR-C9)

α = 25° ± 3° ; β = 65° ± 2° ; γ = 25° ± 5°
H = 4.7 m

Faille de Trasacco (vue vers le nord)

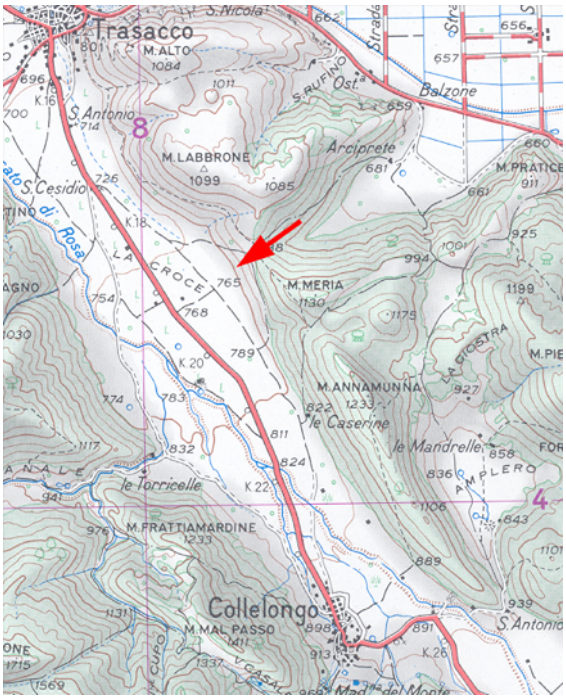

Extrait de la feuille n°152 (SORA) au 1:100 000ème, IGM

Site TR

Site TR. A cet endroit, le colluvion induré est décallé verticalement de 30cm, 2m devant le plan principal

TR-C1 à TR-C9 : Colluvion induré exhumé (90cm de hauteur, 50cm devant le plan principal)

Faille de Parasano (site PA)

Mission Mai 2007
GPS : alt. 1270 m ± 5m ; N41.99613- E013.70275
Ecrantage : seulement le plan de faille **125 SW 55**
Nbre échantillons : 33 (PA-1 à PA-33)

$\alpha = 25°$; $\beta = 55°$ $\gamma = 35°$
H = 4.5 m

Faille de San Sebastiano (site SB)

Mission Mai 2007
GPS : alt. 1214 m ± 5m ; N41.94667- E013.76185
Ecrantage : seulement le plan de faille **0 W 62**
Nbre échantillons : 45 (SB-1 à SB-45)

α = 25° ; β = 62° γ = 35°
H = 8.5 m

Faille de Castel di Ieri (site CI)

Mission Mai 2007
GPS : alt. 570 m ± 5m ; N42.1057 - E013.90263
Ecrantage : seulement le plan de faille **135 SW 45**
Nbre échantillons : 29 (CI-1 à CI-29)
+ CI-TOP : à 10. 5 m de la base
+ CI-col : à 4 m de la base

α = 15° ; β = 45° γ = 40°
H = 4 m

Faille de Roccapreturo - site RP1

Mission Avril 2006 (ancien nom du site : A2R)
GPS : alt. 795 m ± 5 m ; N42.21846 - E013.65015
Ecrantage : seulement le plan de faille **125 SW 60**
Nbre échantillons : 71 (A2R-1 à A2R-71)

(pas de A2R-49!)

$\alpha = 20° \pm 3°$; $\beta = 60° \pm 2°$; $\gamma = 35° \pm 5°$
H = 10 m

Faille de Roccapreturo - site RP2

Site à ~2km à l'est du village de Roccapreturo
Mission Avril 2006 (ancien nom du site : A1R)
GPS : alt. 805 m ± 10m ; N42.19143 - E013.71244
Ecrantage : seulement le plan de faille **125 SW 55**
Nbre échantillons (deux verticales) : 75 à droite (A1R-1 à A1R-75)
et **25 à gauche** (A1R-76 à A1R-100)

$\alpha = 25° \pm 3°$; $\beta = 55° \pm 2°$; $\gamma = 35° \pm 5°$
H = 10.2 m

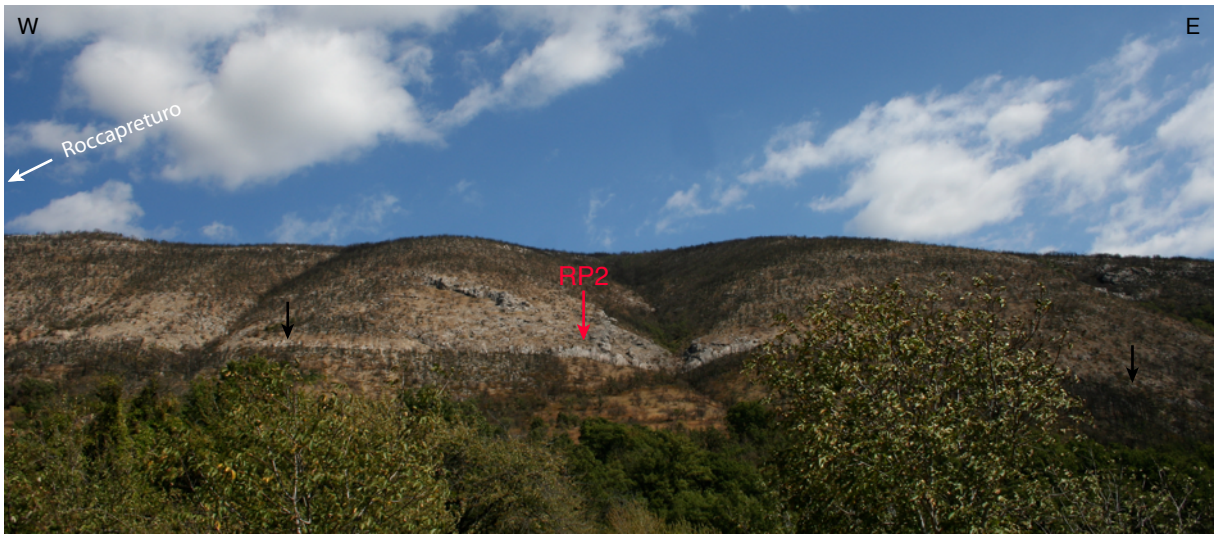

Faille du Roccapreturo vue vers le nord

Site RP2 sur la faille de Roccapreturo (anciennement nommé A1R)

Faille de Roccapreturo - site RP3

Mission Avril 2006 (ancien nom du site : A3R)
GPS : alt. 783 m ± 5 m ; N42.18127 - E013.72890
Ecrantage : seulement le plan de faille **115 S 60**
Nbre échantillons : 53 (A3R-1 à A3R-53)

α = 25° ± 3° ; β = 60° ± 2° ; γ = 40° ± 5°
H = 10 m

Faille de Roccacasale - site RC

Mission Mai 2007
GPS : alt. 392 m ± 5 m ; N42.12515 - E013.88250
Ecrantage : seulement le plan de faille **120 S 55**
Nbre échantillons : 47 (RC-1 à RC-47)

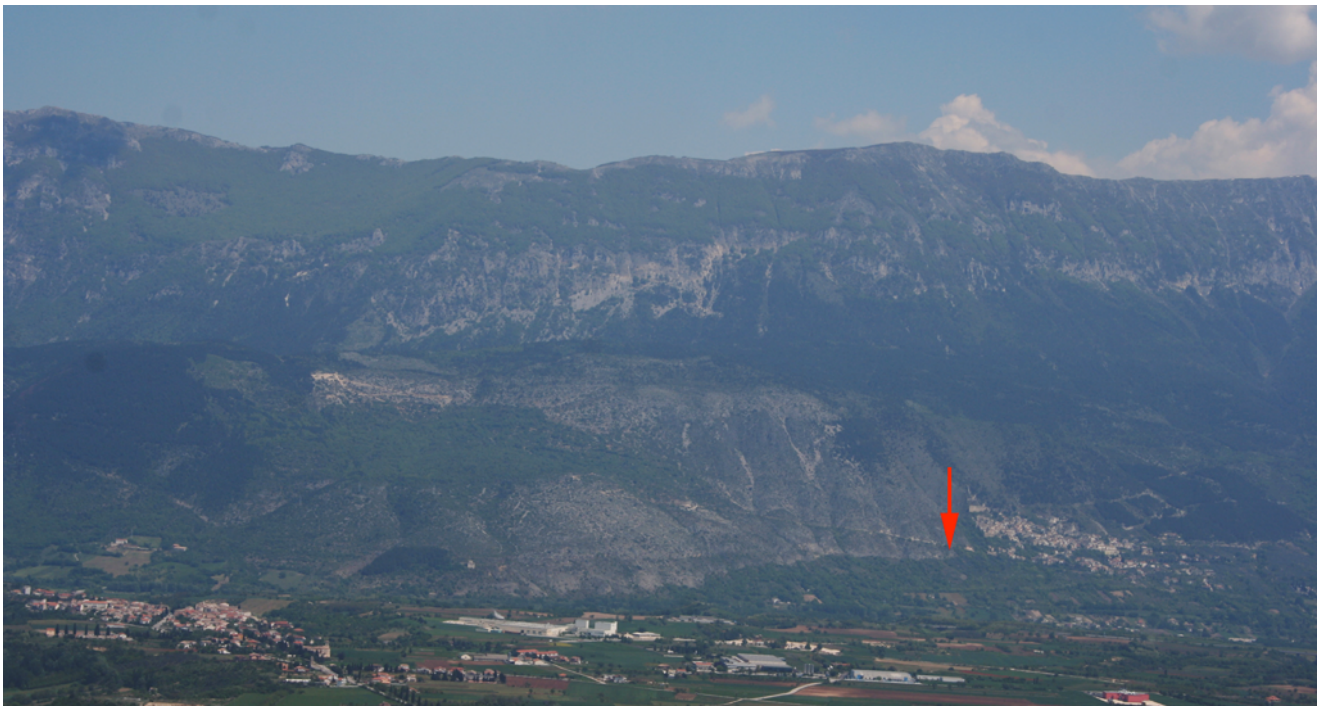

SITE	nom blk.	atom Clnat	atom 36Cl	spike name
MA3	**B3**MAG 01	5,65E+17	1,40E+05	13/02/2003
Palumbo et al	**B4**MAG 01	8,44E+17	2,12E+05	13/02/2003
2004	**B6**MAG 01	5,86E+17	1,36E+05	13/02/2003
(M1)	**B7**MAG 01	8,58E+17	4,05E+05	13/02/2003
	moy MA3 =	**7,13E+17**	***2,23E+05***	
MA3c	BLK M1c 1-20	2,71E+17	1,92E+05	25/09/2007
(M1c)	BLK M1c 21-42	2,67E+17	1,66E+05	25/09/2007
	moy MA3c =	**2,69E+17**	***1,79E+05***	
MA1	A1c-BL3	6,55E+17	1,72E+05	13/01/2006
	AG-BL1	2,42E+17	3,09E+05	14/02/2006
	BLK 22/02/07	4,76E+17	3,67E+05	30/11/2006
	BLK 28/03/07	2,43E+17	2,54E+05	30/11/2006
	BLK 07/03/07	2,79E+17	2,33E+05	30/11/2006
	BLK A1C-2K/54TK	2,28E+17	*1,79E+05*	25/09/2007
(A1c)	BLK A1C-42/70	2,76E+17	2,98E+05	30/11/2006
	moy MA1 =	***3,43E+17***	***2,59E+05***	
MA4	A4c-BL 1	6,05E+17	3,89E+05	13/01/2006
	BLK 22/02/07	4,76E+17	3,67E+05	30/11/2006
	BLK 07/03/07	2,79E+17	2,33E+05	30/11/2006
	BLK mai 08	1,38E+17	2,13E+05	28/04/2008
(A4c)	*moy MA4=*	***3,74E+17***	***3,01E+05***	
MA2	AG-BL1	2,42E+17	3,09E+05	14/02/2006
	BLK A6c-3/12	2,44E+17	4,48E+05	27/04/2007
	BLK A6c-31/47	2,25E+17	4,00E+05	27/04/2007
	BLK A6c-28/03/07	2,43E+17	2,54E+05	30/11/2006
	BLK A6C-64/73	2,68E+17	2,38E+05	30/11/2006
	BLK A6C-13/30	9,23E+16	4,27E+05	27/04/2007
(A6c)	*moy MA2 =*	***2,19E+17***	***3,46E+05***	
VE	BLK VE42-61	2,42E+17	1,73E+05	25/09/2007
	BLK VE1-20	2,74E+17	1,97E+05	25/09/2007
	BLK VE-21/41	4,03E+17	1,71E+05	25/09/2007
	moy VE =	***3,06E+17***	***1,81E+05***	
TR	BLK TR-21/40	2,15E+17	1,87E+05	10/12/2007
	BLK TR-01/20	1,63E+17	2,01E+05	10/12/2007
	moy TR =	**1,89E+17**	**1,94E+05**	

Récapitulatif des valeurs des blancs de chimie sur les sites. Entre paranthèse est indiqué l'ancien nom du site lorsqu'il a été simplifié dans le manuscrit.

nom ech.	[Cl]nat	[36Cl]	uncertitude sur [36Cl]	uncert. %
pas de réplicat sur MA3				
MA3c (M1c)				
M1C-18	11,120	1,40E+05	3,34E+03	
M1C-18R	11,364	1,45E+05	3,59E+03	
M1C-18 mean	***11,242***	***1,43E+05***	***2,79E+03***	1,96
M1C-28	12,908	1,25E+05	3,14E+03	
M1C-28R	13,074	1,27E+05	3,76E+03	
M1C-28 mean	***12,991***	***1,26E+05***	***1,02E+03***	0,81
M1C-42	10,833	1,05E+05	2,61E+03	
M1C-42R	11,077	1,05E+05	3,20E+03	
M1C-42 mean	***10,878***	***1,05E+05***	***3,64E+02***	0,35
MA1 (A1c)				
A1c-54TK	0,887	2,80E+05	8,90E+03	
A1c-54T	0,788	2,77E+05	7,32E+03	
A1c-54T mean	***0,837***	***2,79E+05***	***1,77E+03***	0,63
A1c-54sinK	1,237	3,00E+05	8,35E+03	
A1c-54sin	1,129	2,85E+05	1,45E+04	
A1c-54sin mean	***1,183***	***2,92E+05***	***7,47E+03***	2,56
A1c-1	0,994	5,68E+05	8,05E+02	
A1c-1R	1,071	5,52E+05	1,00E+04	
A1c-1 mean	***1,032***	***5,60E+05***	***7,98E+03***	1,42
A1c-8	1,357	5,09E+05	1,00E+04	
A1c-8K	0,844	5,01E+05	9,25E+03	
A1c-8 mean	***1,100***	***5,05E+05***	***3,58E+03***	0,71
A1c-9	0,870	4,65E+05	8,28E+03	
A1c-9R	0,413	4,56E+05	1,59E+04	
A1c-9 mean	***0,642***	***4,60E+05***	***4,47E+03***	0,97
A1c-10	0,792	4,74E+05	1,12E+04	
A1c-10R	0,364	4,51E+05	1,16E+04	
A1c-10 mean	***0,578***	***4,62E+05***	***1,15E+04***	2,49
A1c-12	0,812	4,33E+05	2,04E+04	
A1c-12K	0,710	4,40E+05	1,59E+04	
A1c-12 mean	***0,761***	***4,37E+05***	***3,57E+03***	0,82
A1c-20	0,787	4,48E+05	1,69E+04	
A1c-20K	0,590	3,94E+05	1,04E+04	
A1c-20 mean	***0,688***	***4,21E+05***	***2,67E+04***	6,34
A1c-28	0,848	3,52E+05	8,06E+03	
A1c-28K	0,844	3,58E+05	9,63E+03	
A1c-28 mean	***0,846***	***3,55E+05***	***3,04E+03***	0,86
A1c-24	2,105	4,04E+05	1,15E+04	
A1C-24K	1,028	3,93E+05	8,06E+03	
A1c-24 mean	***1,566***	***3,98E+05***	***5,29E+03***	1,33
A1c-32	1,442	3,80E+05	9,79E+03	
A1c-32K	1,381	3,57E+05	7,42E+03	
A1c-32 mean	***1,412***	***3,69E+05***	***1,14E+04***	3,10
A1c-38	0,380	3,43E+05	6,58E+03	
A1c-38R	0,646	3,55E+05	1,15E+04	
A1c-38 mean	***0,513***	***3,49E+05***	***6,13E+03***	1,76
A1c-44	0,208	3,16E+05	9,35E+03	
A1c-44K	0,407	3,20E+05	7,50E+03	
A1c-44 mean	***0,307***	***3,18E+05***	***1,58E+03***	0,50
A1c-69	3,042	2,59E+05	4,70E+03	
A1c-69R	3,072	2,78E+05	5,57E+03	
A1c-69 mean	***3,057***	***2,69E+05***	***9,50E+03***	3,54
MA4 (A4c)				
A4c-3	8,925	1,01E+06	1,82E+04	
A4c-3R	8,196	9,79E+05	1,74E+04	
A4c-3 mean	***8,561***	***9,94E+05***	***1,45E+04***	1,46
A4c-63	7,508	3,70E+05	6,53E+03	
A4c-63R	7,588	3,71E+05	6,55E+03	
A4c-63 mean	***7,548***	***3,70E+05***	***5,12E+02***	0,14
A4C-10	9,080	9,26E+05	2,19E+04	
A4C-10R	8,783	9,39E+05	2,86E+04	
A4C-10 mean	***8,932***	***9,32E+05***	***6,31E+03***	0,68
A4c-56	2,675	3,83E+05	9,12E+03	
A4c-56R	2,877	3,97E+05	7,67E+03	
A4c-56 mean	***2,776***	***3,90E+05***	***6,92E+03***	1,77
A4c-43	12,758	5,18E+05	9,48E+03	
A4c-43R	13,002	5,41E+05	9,70E+03	
A4c-43 mean	***12,880***	***5,30E+05***	***1,20E+04***	2,26
A4c-35	5,329	6,02E+05	1,10E+04	
A4c-35R	5,381	6,15E+05	1,77E+04	
A4c-35 mean	***5,355***	***6,08E+05***	***6,34E+03***	1,04
A4c-11	9,198	9,23E+05	1,64E+04	
A4c-11R	8,200	9,33E+05	1,71E+04	
A4c-11 mean	***8,699***	***9,28E+05***	***5,10E+03***	0,55
MA2 (A6c)				
A6c-72	4,598	3,45E+05	9,91E+03	
A6c-72R	4,809	3,75E+05	1,30E+04	
A6c-72 mean	***4,704***	***3,60E+05***	***1,50E+04***	4,16
A6c-42	9,780	6,25E+05	1,51E+04	
A6c-42R	10,440	6,72E+05	1,66E+04	
A6c-42 mean	***10,110***	***6,49E+05***	***2,32E+04***	3,58
A6c-74	5,687	3,73E+05	8,78E+03	
A6C-74R	5,299	3,46E+05	8,20E+03	
A6c-74 mean	***5,493***	***3,60E+05***	***1,33E+04***	3,71
A6c-30	8,196	7,30E+05	1,77E+04	
A6C-30R	8,536	7,53E+05	1,04E+04	
A6c-30 mean	***8,366***	***7,41E+05***	***1,16E+04***	1,56
A6c-01	7,380	1,15E+06	2,73E+04	
A6C-01R	7,126	1,07E+06	1,92E+04	
A6c-01 mean	***7,253***	***1,11E+06***	***4,21E+04***	3,79
VE				
VE-77	5,121	2,49E+05	6,59E+03	
VE-77R	5,212	2,38E+05	6,55E+03	
VE-77 mean	***5,167***	***2,43E+05***	***5,65E+03***	2,32
VE-29	3,658	3,69E+05	8,49E+03	
VE-29R	3,818	3,88E+05	8,48E+03	
VE-29 mean	***3,738***	***3,79E+05***	***9,39E+03***	2,48

Récapitulatif des réplicats de chimie. Entre paranthèse est indiqué l'ancien nom du site lorsqu'il a été simplifié dans le manuscrit.

	1	2	3	4	5	6	7	8	9	10	11	12	13	14	15	16	17	18	19	20	21	22
SITE VE	As	Ba	Be	Bi	Cd	Ce	Co	Cr	Cs	Cu	Dy	Er	Eu	Ga	Gd	Ge	Hf	Ho	In	La	Lu	Mo
om échantillo	ppm	ppm	ppm	ppm	ppm	ppm	ppm	ppm	ppm	ppm	ppm	ppm	ppm	ppm	ppm	ppm	ppm	ppm	ppm	ppm	ppm	ppm
VE-77mean	0.0	6.31	0.0	0.02	0.03	0.91	1.9	0.0	0.05	0.0	0.07	0.04	0.02	0.02	0.07	0.0	0	0.01	0.0	0.49	0.0	0.0
VE-76	0.0	6.31	0.0	0.02	0.03	0.91	1.9	0.0	0.05	0.0	0.07	0.04	0.02	0.02	0.07	0.0	0	0.01	0.0	0.49	0.0	0.0
VE-75	0.0	6.31	0.0	0.02	0.03	0.91	1.9	0.0	0.05	0.0	0.07	0.04	0.02	0.02	0.07	0.0	0	0.01	0.0	0.49	0.0	0.0
VE-74	0.0	6.31	0.0	0.02	0.03	0.91	1.9	0.0	0.05	0.0	0.07	0.04	0.02	0.02	0.07	0.0	0	0.01	0.0	0.49	0.0	0.0
VE-73	0.0	6.31	0.0	0.02	0.03	0.91	1.9	0.0	0.05	0.0	0.07	0.04	0.02	0.02	0.07	0.0	0	0.01	0.0	0.49	0.0	0.0
VE-71	0.0	6.31	0.0	0.02	0.03	0.91	1.9	0.0	0.05	0.0	0.07	0.04	0.02	0.02	0.07	0.0	0	0.01	0.0	0.49	0.0	0.0
VE-69	0.0	6.31	0.0	0.02	0.03	0.91	1.9	0.0	0.05	0.0	0.07	0.04	0.02	0.02	0.07	0.0	0	0.01	0.0	0.49	0.0	0.0
VE-67	0.0	6.31	0.0	0.02	0.03	0.91	1.9	0.0	0.05	0.0	0.07	0.04	0.02	0.02	0.07	0.0	0	0.01	0.0	0.49	0.0	0.0
VE-65	0.0	6.31	0.0	0.02	0.03	0.91	1.9	0.0	0.05	0.0	0.07	0.04	0.02	0.02	0.07	0.0	0	0.01	0.0	0.49	0.0	0.0
VE-64	0.0	6.31	0.0	0.02	0.03	0.91	1.9	0.0	0.05	0.0	0.07	0.04	0.02	0.02	0.07	0.0	0	0.01	0.0	0.49	0.0	0.0
VE-63	0.0	6.31	0.0	0.02	0.03	0.91	1.9	0.0	0.05	0.0	0.07	0.04	0.02	0.02	0.07	0.0	0	0.01	0.0	0.49	0.0	0.0
VE-62	0.0	6.31	0.0	0.02	0.03	0.91	1.9	0.0	0.05	0.0	0.07	0.04	0.02	0.02	0.07	0.0	0	0.01	0.0	0.49	0.0	0.0
VE-61	0.0	6.31	0.0	0.02	0.03	0.91	1.9	0.0	0.05	0.0	0.07	0.04	0.02	0.02	0.07	0.0	0	0.01	0.0	0.49	0.0	0.0
VE-60	0.0	6.31	0.0	0.02	0.03	0.91	1.9	0.0	0.05	0.0	0.07	0.04	0.02	0.02	0.07	0.0	0	0.01	0.0	0.49	0.0	0.0
VE-59	0.0	6.31	0.0	0.02	0.03	0.91	1.9	0.0	0.05	0.0	0.07	0.04	0.02	0.02	0.07	0.0	0	0.01	0.0	0.49	0.0	0.0
VE-58	0.0	6.31	0.0	0.02	0.03	0.91	1.9	0.0	0.05	0.0	0.07	0.04	0.02	0.02	0.07	0.0	0	0.01	0.0	0.49	0.0	0.0
VE-57	0.0	6.31	0.0	0.02	0.03	0.91	1.9	0.0	0.05	0.0	0.07	0.04	0.02	0.02	0.07	0.0	0	0.01	0.0	0.49	0.0	0.0
VE-55	0.0	6.31	0.0	0.02	0.03	0.91	1.9	0.0	0.05	0.0	0.07	0.04	0.02	0.02	0.07	0.0	0	0.01	0.0	0.49	0.0	0.0
VE-54	0.0	6.31	0.0	0.02	0.03	0.91	1.9	0.0	0.05	0.0	0.07	0.04	0.02	0.02	0.07	0.0	0	0.01	0.0	0.49	0.0	0.0
VE-53	0.0	6.31	0.0	0.02	0.03	0.91	1.9	0.0	0.05	0.0	0.07	0.04	0.02	0.02	0.07	0.0	0	0.01	0.0	0.49	0.0	0.0
VE-52	0.0	6.31	0.0	0.02	0.03	0.91	1.9	0.0	0.05	0.0	0.07	0.04	0.02	0.02	0.07	0.0	0	0.01	0.0	0.49	0.0	0.0
VE-51	0.0	6.31	0.0	0.02	0.03	0.91	1.9	0.0	0.05	0.0	0.07	0.04	0.02	0.02	0.07	0.0	0	0.01	0.0	0.49	0.0	0.0
VE-49	0.0	6.31	0.0	0.02	0.03	0.91	1.9	0.0	0.05	0.0	0.07	0.04	0.02	0.02	0.07	0.0	0	0.01	0.0	0.49	0.0	0.0
VE-48	0.0	6.31	0.0	0.02	0.03	0.91	1.9	0.0	0.05	0.0	0.07	0.04	0.02	0.02	0.07	0.0	0	0.01	0.0	0.49	0.0	0.0
VE-47	0.0	6.31	0.0	0.02	0.03	0.91	1.9	0.0	0.05	0.0	0.07	0.04	0.02	0.02	0.07	0.0	0	0.01	0.0	0.49	0.0	0.0
VE-46	0.0	6.31	0.0	0.02	0.03	0.91	1.9	0.0	0.05	0.0	0.07	0.04	0.02	0.02	0.07	0.0	0	0.01	0.0	0.49	0.0	0.0
VE-45	0.0	6.31	0.0	0.02	0.03	0.91	1.9	0.0	0.05	0.0	0.07	0.04	0.02	0.02	0.07	0.0	0	0.01	0.0	0.49	0.0	0.0
VE-44	0.0	6.31	0.0	0.02	0.03	0.91	1.9	0.0	0.05	0.0	0.07	0.04	0.02	0.02	0.07	0.0	0	0.01	0.0	0.49	0.0	0.0
VE-43	0.0	6.31	0.0	0.02	0.03	0.91	1.9	0.0	0.05	0.0	0.07	0.04	0.02	0.02	0.07	0.0	0	0.01	0.0	0.49	0.0	0.0
VE-42	0.0	6.31	0.0	0.02	0.03	0.91	1.9	0.0	0.05	0.0	0.07	0.04	0.02	0.02	0.07	0.0	0	0.01	0.0	0.49	0.0	0.0
VE-41	0.0	6.31	0.0	0.02	0.03	0.91	1.9	0.0	0.05	0.0	0.07	0.04	0.02	0.02	0.07	0.0	0	0.01	0.0	0.49	0.0	0.0
VE-39	0.0	6.31	0.0	0.02	0.03	0.91	1.9	0.0	0.05	0.0	0.07	0.04	0.02	0.02	0.07	0.0	0	0.01	0.0	0.49	0.0	0.0
VE-38	0.0	6.31	0.0	0.02	0.03	0.91	1.9	0.0	0.05	0.0	0.07	0.04	0.02	0.02	0.07	0.0	0	0.01	0.0	0.49	0.0	0.0
VE-37	0.0	6.31	0.0	0.02	0.03	0.91	1.9	0.0	0.05	0.0	0.07	0.04	0.02	0.02	0.07	0.0	0	0.01	0.0	0.49	0.0	0.0
VE-36	0.0	6.31	0.0	0.02	0.03	0.91	1.9	0.0	0.05	0.0	0.07	0.04	0.02	0.02	0.07	0.0	0	0.01	0.0	0.49	0.0	0.0
VE-35	0.0	6.31	0.0	0.02	0.03	0.91	1.9	0.0	0.05	0.0	0.07	0.04	0.02	0.02	0.07	0.0	0	0.01	0.0	0.49	0.0	0.0
VE-33	0.0	6.31	0.0	0.02	0.03	0.91	1.9	0.0	0.05	0.0	0.07	0.04	0.02	0.02	0.07	0.0	0	0.01	0.0	0.49	0.0	0.0
VE-32	0.0	6.31	0.0	0.02	0.03	0.91	1.9	0.0	0.05	0.0	0.07	0.04	0.02	0.02	0.07	0.0	0	0.01	0.0	0.49	0.0	0.0
VE-31	0.0	6.31	0.0	0.02	0.03	0.91	1.9	0.0	0.05	0.0	0.07	0.04	0.02	0.02	0.07	0.0	0	0.01	0.0	0.49	0.0	0.0
VE-30	0.0	6.31	0.0	0.02	0.03	0.91	1.9	0.0	0.05	0.0	0.07	0.04	0.02	0.02	0.07	0.0	0	0.01	0.0	0.49	0.0	0.0
VE-29mean	0.0	6.31	0.0	0.02	0.03	0.91	1.9	0.0	0.05	0.0	0.07	0.04	0.02	0.02	0.07	0.0	0	0.01	0.0	0.49	0.0	0.0
VE-28	0.0	6.31	0.0	0.02	0.03	0.91	1.9	0.0	0.05	0.0	0.07	0.04	0.02	0.02	0.07	0.0	0	0.01	0.0	0.49	0.0	0.0
VE-27	0.0	6.31	0.0	0.02	0.03	0.91	1.9	0.0	0.05	0.0	0.07	0.04	0.02	0.02	0.07	0.0	0	0.01	0.0	0.49	0.0	0.0
VE-26	0.0	6.31	0.0	0.02	0.03	0.91	1.9	0.0	0.05	0.0	0.07	0.04	0.02	0.02	0.07	0.0	0	0.01	0.0	0.49	0.0	0.0
VE-25	0.0	6.31	0.0	0.02	0.03	0.91	1.9	0.0	0.05	0.0	0.07	0.04	0.02	0.02	0.07	0.0	0	0.01	0.0	0.49	0.0	0.0
VE-24	0.0	6.31	0.0	0.02	0.03	0.91	1.9	0.0	0.05	0.0	0.07	0.04	0.02	0.02	0.07	0.0	0	0.01	0.0	0.49	0.0	0.0
VE-23	0.0	6.31	0.0	0.02	0.03	0.91	1.9	0.0	0.05	0.0	0.07	0.04	0.02	0.02	0.07	0.0	0	0.01	0.0	0.49	0.0	0.0
VE-22	0.0	6.31	0.0	0.02	0.03	0.91	1.9	0.0	0.05	0.0	0.07	0.04	0.02	0.02	0.07	0.0	0	0.01	0.0	0.49	0.0	0.0
VE-21mean	0.0	6.31	0.0	0.02	0.03	0.91	1.9	0.0	0.05	0.0	0.07	0.04	0.02	0.02	0.07	0.0	0	0.01	0.0	0.49	0.0	0.0
VE-20	0.0	6.31	0.0	0.02	0.03	0.91	1.9	0.0	0.05	0.0	0.07	0.04	0.02	0.02	0.07	0.0	0	0.01	0.0	0.49	0.0	0.0
VE-19mean	0.0	6.31	0.0	0.02	0.03	0.91	1.9	0.0	0.05	0.0	0.07	0.04	0.02	0.02	0.07	0.0	0	0.01	0.0	0.49	0.0	0.0
VE-18	0.0	6.31	0.0	0.02	0.03	0.91	1.9	0.0	0.05	0.0	0.07	0.04	0.02	0.02	0.07	0.0	0	0.01	0.0	0.49	0.0	0.0
VE-17mean	0.0	6.31	0.0	0.02	0.03	0.91	1.9	0.0	0.05	0.0	0.07	0.04	0.02	0.02	0.07	0.0	0	0.01	0.0	0.49	0.0	0.0
VE-16new	0.0	6.31	0.0	0.02	0.03	0.91	1.9	0.0	0.05	0.0	0.07	0.04	0.02	0.02	0.07	0.0	0	0.01	0.0	0.49	0.0	0.0
VE-15mean	0.0	6.31	0.0	0.02	0.03	0.91	1.9	0.0	0.05	0.0	0.07	0.04	0.02	0.02	0.07	0.0	0	0.01	0.0	0.49	0.0	0.0
VE-13mean	0.0	6.31	0.0	0.02	0.03	0.91	1.9	0.0	0.05	0.0	0.07	0.04	0.02	0.02	0.07	0.0	0	0.01	0.0	0.49	0.0	0.0
VE-12	0.0	6.31	0.0	0.02	0.03	0.91	1.9	0.0	0.05	0.0	0.07	0.04	0.02	0.02	0.07	0.0	0	0.01	0.0	0.49	0.0	0.0
VE-11mean	0.0	6.31	0.0	0.02	0.03	0.91	1.9	0.0	0.05	0.0	0.07	0.04	0.02	0.02	0.07	0.0	0	0.01	0.0	0.49	0.0	0.0
VE-09mean	0.0	6.31	0.0	0.02	0.03	0.91	1.9	0.0	0.05	0.0	0.07	0.04	0.02	0.02	0.07	0.0	0	0.01	0.0	0.49	0.0	0.0
VE-08	0.0	6.31	0.0	0.02	0.03	0.91	1.9	0.0	0.05	0.0	0.07	0.04	0.02	0.02	0.07	0.0	0	0.01	0.0	0.49	0.0	0.0
VE-07n	0.0	6.31	0.0	0.02	0.03	0.91	1.9	0.0	0.05	0.0	0.07	0.04	0.02	0.02	0.07	0.0	0	0.01	0.0	0.49	0.0	0.0
VE-06	0.0	6.31	0.0	0.02	0.03	0.91	1.9	0.0	0.05	0.0	0.07	0.04	0.02	0.02	0.07	0.0	0	0.01	0.0	0.49	0.0	0.0
VE-05mean	0.0	6.31	0.0	0.02	0.03	0.91	1.9	0.0	0.05	0.0	0.07	0.04	0.02	0.02	0.07	0.0	0	0.01	0.0	0.49	0.0	0.0
VE-04	0.0	6.31	0.0	0.02	0.03	0.91	1.9	0.0	0.05	0.0	0.07	0.04	0.02	0.02	0.07	0.0	0	0.01	0.0	0.49	0.0	0.0
VE-03mean	0.0	6.31	0.0	0.02	0.03	0.91	1.9	0.0	0.05	0.0	0.07	0.04	0.02	0.02	0.07	0.0	0	0.01	0.0	0.49	0.0	0.0
VE-02	0.0	6.31	0.0	0.02	0.03	0.91	1.9	0.0	0.05	0.0	0.07	0.04	0.02	0.02	0.07	0.0	0	0.01	0.0	0.49	0.0	0.0
VE-01mean	0.0	6.31	0.0	0.02	0.03	0.91	1.9	0.0	0.05	0.0	0.07	0.04	0.02	0.02	0.07	0.0	0	0.01	0.0	0.49	0.0	0.0

23	24	25	26	27	28	29	30	31	32	33	34	35	36	37	38	39	40	41	42	43	44	45
Nb	Nd	Ni	Pb	Pr	Rb	Sb	Sm	Sn	Sr	Ta	Tb	Th	Tm	U	V	W	Y	Yb	Zn	Zr	SiO2 (Si)	Al2O3 (Al)
ppm	ppm	ppm	ppm	ppm	ppm	ppm	ppm	ppm	ppm	ppm	ppm	ppm	ppm	ppm	ppm	ppm	ppm	ppm	ppm	ppm	%	%
0.13	0.43	21.38	0.43	0.11	1.11	0.0	0.08	0.05	152.01	0.01	0.01	0.11	0.0	0.38	2.89	0.0	0.29	0.04	0.0	1.65	0.16	0.13

46	47	48	49	50	51	52	53	54	55	56	57	58	59	60	61	62	63	64	65	66
Fe2O3 (Fe)	MnO (Mn)	MgO (Mg)	CaO (Ca)	Na2O(Na)	K2O(K)	TiO2(Ti)	P2O5(P)	B	Li	H2Otot (H)	Stot (S)	CO2 tot (C)	O,rock	O,water	Cl nat AMS	Ca ICP	Z (position sur le scarp)	Thickness sample	[36Cl] AMS	uncertainty
%	%	%	%	%	%	%	%	ppm	ppm	%	%	%			ppm	ppm	cm	cm	at/g.rock	
0.07	0.0	0.65	55.75	0.0	0.0	0.01	0.0	2.0	0.99	0.29	0.02	43.77	0.0	0.0	5.25	380626	3	3.7	243273	6010
0.07	0.0	0.65	55.75	0.0	0.0	0.01	0.0	2.0	0.99	0.29	0.02	43.77	0.0	0.0	4.67	383741	10	3.5	250243	4421
0.07	0.0	0.65	55.75	0.0	0.0	0.01	0.0	2.0	0.99	0.29	0.02	43.77	0.0	0.0	5.65	384666	20	3.5	267334	6410
0.07	0.0	0.65	55.75	0.0	0.0	0.01	0.0	2.0	0.99	0.29	0.02	43.77	0.0	0.0	4.67	409582	30	3.2	258838	6595
0.07	0.0	0.65	55.75	0.0	0.0	0.01	0.0	2.0	0.99	0.29	0.02	43.77	0.0	0.0	3.84	380814	40	3	262230	6829
0.07	0.0	0.65	55.75	0.0	0.0	0.01	0.0	2.0	0.99	0.29	0.02	43.77	0.0	0.0	5.93	392767	60	3.3	271365	6290
0.07	0.0	0.65	55.75	0.0	0.0	0.01	0.0	2.0	0.99	0.29	0.02	43.77	0.0	0.0	6.9	381115	80	3.3	276166	6354
0.07	0.0	0.65	55.75	0.0	0.0	0.01	0.0	2.0	0.99	0.29	0.02	43.77	0.0	0.0	4.55	383735	100	3.3	281508	6487
0.07	0.0	0.65	55.75	0.0	0.0	0.01	0.0	2.0	0.99	0.29	0.02	43.77	0.0	0.0	3.85	396680	120	3.5	290359	6674
0.07	0.0	0.65	55.75	0.0	0.0	0.01	0.0	2.0	0.99	0.29	0.02	43.77	0.0	0.0	3.68	384921	130	3.5	294968	5212
0.07	0.0	0.65	55.75	0.0	0.0	0.01	0.0	2.0	0.99	0.29	0.02	43.77	0.0	0.0	3.32	371727	141	3.5	298124	5603
0.07	0.0	0.65	55.75	0.0	0.0	0.01	0.0	2.0	0.99	0.29	0.02	43.77	0.0	0.0	2.79	384310	151	3.5	301051	6420
0.07	0.0	0.65	55.75	0.0	0.0	0.01	0.0	2.0	0.99	0.29	0.02	43.77	0.0	0.0	2.78	387039	161	3	290094	6683
0.07	0.0	0.65	55.75	0.0	0.0	0.01	0.0	2.0	0.99	0.29	0.02	43.77	0.0	0.0	3.17	371121	171	3	305362	6331
0.07	0.0	0.65	55.75	0.0	0.0	0.01	0.0	2.0	0.99	0.29	0.02	43.77	0.0	0.0	3.57	370577	181	3.5	285949	6597
0.07	0.0	0.65	55.75	0.0	0.0	0.01	0.0	2.0	0.99	0.29	0.02	43.77	0.0	0.0	3.03	393867	191	3	297066	7935
0.07	0.0	0.65	55.75	0.0	0.0	0.01	0.0	2.0	0.99	0.29	0.02	43.77	0.0	0.0	4.08	379063	201	3.3	312197	7541
0.07	0.0	0.65	55.75	0.0	0.0	0.01	0.0	2.0	0.99	0.29	0.02	43.77	0.0	0.0	5.05	388872	221	3	312499	7252
0.07	0.0	0.65	55.75	0.0	0.0	0.01	0.0	2.0	0.99	0.29	0.02	43.77	0.0	0.0	3.89	377289	231	3	305652	6256
0.07	0.0	0.65	55.75	0.0	0.0	0.01	0.0	2.0	0.99	0.29	0.02	43.77	0.0	0.0	5.37	376068	241	3.5	305250	7090
0.07	0.0	0.65	55.75	0.0	0.0	0.01	0.0	2.0	0.99	0.29	0.02	43.77	0.0	0.0	5.28	389280	251	3	331975	6800
0.07	0.0	0.65	55.75	0.0	0.0	0.01	0.0	2.0	0.99	0.29	0.02	43.77	0.0	0.0	5.3	388380	261	2.5	323813	9941
0.07	0.0	0.65	55.75	0.0	0.0	0.01	0.0	2.0	0.99	0.29	0.02	43.77	0.0	0.0	4.9	382178	281	3	336063	9442
0.07	0.0	0.65	55.75	0.0	0.0	0.01	0.0	2.0	0.99	0.29	0.02	43.77	0.0	0.0	3.92	384874	291	3	330886	6788
0.07	0.0	0.65	55.75	0.0	0.0	0.01	0.0	2.0	0.99	0.29	0.02	43.77	0.0	0.0	3.89	381503	302	3	349707	11755
0.07	0.0	0.65	55.75	0.0	0.0	0.01	0.0	2.0	0.99	0.29	0.02	43.77	0.0	0.0	3.22	387957	312	3	323695	6684
0.07	0.0	0.65	55.75	0.0	0.0	0.01	0.0	2.0	0.99	0.29	0.02	43.77	0.0	0.0	5.15	371541	322	2.8	345849	8026
0.07	0.0	0.65	55.75	0.0	0.0	0.01	0.0	2.0	0.99	0.29	0.02	43.77	0.0	0.0	6.09	375201	332	3	342156	6988
0.07	0.0	0.65	55.75	0.0	0.0	0.01	0.0	2.0	0.99	0.29	0.02	43.77	0.0	0.0	7.24	395587	342	3	355592	9715
0.07	0.0	0.65	55.75	0.0	0.0	0.01	0.0	2.0	0.99	0.29	0.02	43.77	0.0	0.0	7.6	380426	352	2.8	347228	8518
0.07	0.0	0.65	55.75	0.0	0.0	0.01	0.0	2.0	0.99	0.29	0.02	43.77	0.0	0.0	6.01	386504	362	2	344035	7972
0.07	0.0	0.65	55.75	0.0	0.0	0.01	0.0	2.0	0.99	0.29	0.02	43.77	0.0	0.0	5.5	388286	372	3	345148	8575
0.07	0.0	0.65	55.75	0.0	0.0	0.01	0.0	2.0	0.99	0.29	0.02	43.77	0.0	0.0	4.7	390236	381	3.3	373889	6640
0.07	0.0	0.65	55.75	0.0	0.0	0.01	0.0	2.0	0.99	0.29	0.02	43.77	0.0	0.0	5.5	383682	391	2.8	373201	9901
0.07	0.0	0.65	55.75	0.0	0.0	0.01	0.0	2.0	0.99	0.29	0.02	43.77	0.0	0.0	3.7	384505	401	3.3	371358	9477
0.07	0.0	0.65	55.75	0.0	0.0	0.01	0.0	2.0	0.99	0.29	0.02	43.77	0.0	0.0	4.16	392527	411	3	367715	8465
0.07	0.0	0.65	55.75	0.0	0.0	0.01	0.0	2.0	0.99	0.29	0.02	43.77	0.0	0.0	4.65	378960	431	3	374392	8614
0.07	0.0	0.65	55.75	0.0	0.0	0.01	0.0	2.0	0.99	0.29	0.02	43.77	0.0	0.0	4.61	416000	441	2.8	374608	12145
0.07	0.0	0.65	55.75	0.0	0.0	0.01	0.0	2.0	0.99	0.29	0.02	43.77	0.0	0.0	3.93	393748	451	3.3	357616	8245
0.07	0.0	0.65	55.75	0.0	0.0	0.01	0.0	2.0	0.99	0.29	0.02	43.77	0.0	0.0	3.15	395353	461	3	367941	6624
0.07	0.0	0.65	55.75	0.0	0.0	0.01	0.0	2.0	0.99	0.29	0.02	43.77	0.0	0.0	3.89	392975	471	3	388559	22231
0.07	0.0	0.65	55.75	0.0	0.0	0.01	0.0	2.0	0.99	0.29	0.02	43.77	0.0	0.0	6.75	396263	482	2.5	390576	6897
0.07	0.0	0.65	55.75	0.0	0.0	0.01	0.0	2.0	0.99	0.29	0.02	43.77	0.0	0.0	6.82	373204	492	3	414749	9545
0.07	0.0	0.65	55.75	0.0	0.0	0.01	0.0	2.0	0.99	0.29	0.02	43.77	0.0	0.0	6.71	390701	501	2.7	393725	8366
0.07	0.0	0.65	55.75	0.0	0.0	0.01	0.0	2.0	0.99	0.29	0.02	43.77	0.0	0.0	8.14	382472	511	3	406083	9435
0.07	0.0	0.65	55.75	0.0	0.0	0.01	0.0	2.0	0.99	0.29	0.02	43.77	0.0	0.0	7.48	398319	521	2.7	409963	7249
0.07	0.0	0.65	55.75	0.0	0.0	0.01	0.0	2.0	0.99	0.29	0.02	43.77	0.0	0.0	7.27	398477	531	2.5	427419	10200
0.07	0.0	0.65	55.75	0.0	0.0	0.01	0.0	2.0	0.99	0.29	0.02	43.77	0.0	0.0	6.79	404685	541	2.5	441048	13578
0.07	0.0	0.65	55.75	0.0	0.0	0.01	0.0	2.0	0.99	0.29	0.02	43.77	0.0	0.0	9.44	388954	551	3	470506	5283
0.07	0.0	0.65	55.75	0.0	0.0	0.01	0.0	2.0	0.99	0.29	0.02	43.77	0.0	0.0	8.02	404789	561	3	443263	7843
0.07	0.0	0.65	55.75	0.0	0.0	0.01	0.0	2.0	0.99	0.29	0.02	43.77	0.0	0.0	8.07	402744	571	3	469192	1667
0.07	0.0	0.65	55.75	0.0	0.0	0.01	0.0	2.0	0.99	0.29	0.02	43.77	0.0	0.0	6.08	402948	581	3	435924	8347
0.07	0.0	0.65	55.75	0.0	0.0	0.01	0.0	2.0	0.99	0.29	0.02	43.77	0.0	0.0	6.55	403989	591	3	449818	3062
0.07	0.0	0.65	55.75	0.0	0.0	0.01	0.0	2.0	0.99	0.29	0.02	43.77	0.0	0.0	7.41	398719	601	3	453718	8701
0.07	0.0	0.65	55.75	0.0	0.0	0.01	0.0	2.0	0.99	0.29	0.02	43.77	0.0	0.0	7.89	399356	611	3	486368	11301
0.07	0.0	0.65	55.75	0.0	0.0	0.01	0.0	2.0	0.99	0.29	0.02	43.77	0.0	0.0	7.99	403535	630	2	499714	12261
0.07	0.0	0.65	55.75	0.0	0.0	0.01	0.0	2.0	0.99	0.29	0.02	43.77	0.0	0.0	8.96	384338	640	2.5	484225	9261
0.07	0.0	0.65	55.75	0.0	0.0	0.01	0.0	2.0	0.99	0.29	0.02	43.77	0.0	0.0	9.87	401307	650	2.5	512288	12999
0.07	0.0	0.65	55.75	0.0	0.0	0.01	0.0	2.0	0.99	0.29	0.02	43.77	0.0	0.0	11.72	393725	671	3	542468	9575
0.07	0.0	0.65	55.75	0.0	0.0	0.01	0.0	2.0	0.99	0.29	0.02	43.77	0.0	0.0	12.69	400025	681	2.8	498289	9529
0.07	0.0	0.65	55.75	0.0	0.0	0.01	0.0	2.0	0.99	0.29	0.02	43.77	0.0	0.0	14.6	392300	691	2.7	577073	15662
0.07	0.0	0.65	55.75	0.0	0.0	0.01	0.0	2.0	0.99	0.29	0.02	43.77	0.0	0.0	12.94	400376	701	2.5	527627	10079
0.07	0.0	0.65	55.75	0.0	0.0	0.01	0.0	2.0	0.99	0.29	0.02	43.77	0.0	0.0	11.81	399842	711	2.5	547735	6567
0.07	0.0	0.65	55.75	0.0	0.0	0.01	0.0	2.0	0.99	0.29	0.02	43.77	0.0	0.0	11.08	394226	721	2.5	524027	11721
0.07	0.0	0.65	55.75	0.0	0.0	0.01	0.0	2.0	0.99	0.29	0.02	43.77	0.0	0.0	10.95	407687	731	3	559367	13818
0.07	0.0	0.65	55.75	0.0	0.0	0.01	0.0	2.0	0.99	0.29	0.02	43.77	0.0	0.0	10.55	394902	741	3.3	548834	10605
0.07	0.0	0.65	55.75	0.0	0.0	0.01	0.0	2.0	0.99	0.29	0.02	43.77	0.0	0.0	13.23	405518	751	2.7	595590	27619

	1	2	3	4	5	6	7	8	9	10	11	12	13	14	15	16	17	18	19	20	21	22
SITE MA1	As	Ba	Be	Bi	Cd	Ce	Co	Cr	Cs	Cu	Dy	Er	Eu	Ga	Gd	Ge	Hf	Ho	In	La	Lu	Mo
nom échantillor	ppm	ppm	ppm	ppm	ppm	ppm	ppm	ppm	ppm	ppm	ppm	ppm	ppm	ppm	ppm	ppm	ppm	ppm	ppm	ppm	ppm	ppm
colluvion approx a la roche moy	0.0	4.847	0.037	0.0	0.324	0.361	1.984	0.337	0.013	0.0	0.097	0.078	0.017	0.0	0.08	0.0	0.004	0.024	0.0	0.572	0.012	0.0
A1c-70	0.0	4.847	0.037	0.0	0.324	0.361	1.984	0.337	0.013	0.0	0.097	0.078	0.017	0.0	0.08	0.0	0.004	0.024	0.0	0.572	0.012	0.0
A1c-69mean	0.0	4.847	0.037	0.0	0.324	0.361	1.984	0.337	0.013	0.0	0.097	0.078	0.017	0.0	0.08	0.0	0.004	0.024	0.0	0.572	0.012	0.0
A1c-68	0.0	4.847	0.037	0.0	0.324	0.361	1.984	0.337	0.013	0.0	0.097	0.078	0.017	0.0	0.08	0.0	0.004	0.024	0.0	0.572	0.012	0.0
A1c-66	0.0	4.847	0.037	0.0	0.324	0.361	1.984	0.337	0.013	0.0	0.097	0.078	0.017	0.0	0.08	0.0	0.004	0.024	0.0	0.572	0.012	0.0
A1c-65	0.0	4.847	0.037	0.0	0.324	0.361	1.984	0.337	0.013	0.0	0.097	0.078	0.017	0.0	0.08	0.0	0.004	0.024	0.0	0.572	0.012	0.0
A1c-64	0.0	4.847	0.037	0.0	0.324	0.361	1.984	0.337	0.013	0.0	0.097	0.078	0.017	0.0	0.08	0.0	0.004	0.024	0.0	0.572	0.012	0.0
A1c-P1-63	0.0	4.847	0.037	0.0	0.324	0.361	1.984	0.337	0.013	0.0	0.097	0.078	0.017	0.0	0.08	0.0	0.004	0.024	0.0	0.572	0.012	0.0
A1c-62	0.0	4.847	0.037	0.0	0.324	0.361	1.984	0.337	0.013	0.0	0.097	0.078	0.017	0.0	0.08	0.0	0.004	0.024	0.0	0.572	0.012	0.0
A1c-61	0.0	4.847	0.037	0.0	0.324	0.361	1.984	0.337	0.013	0.0	0.097	0.078	0.017	0.0	0.08	0.0	0.004	0.024	0.0	0.572	0.012	0.0
A1c-60	0.0	4.847	0.037	0.0	0.324	0.361	1.984	0.337	0.013	0.0	0.097	0.078	0.017	0.0	0.08	0.0	0.004	0.024	0.0	0.572	0.012	0.0
A1c-58	0.0	4.847	0.037	0.0	0.324	0.361	1.984	0.337	0.013	0.0	0.097	0.078	0.017	0.0	0.08	0.0	0.004	0.024	0.0	0.572	0.012	0.0
A1c-57	0.0	4.847	0.037	0.0	0.324	0.361	1.984	0.337	0.013	0.0	0.097	0.078	0.017	0.0	0.08	0.0	0.004	0.024	0.0	0.572	0.012	0.0
A1c-56	0.0	4.847	0.037	0.0	0.324	0.361	1.984	0.337	0.013	0.0	0.097	0.078	0.017	0.0	0.08	0.0	0.004	0.024	0.0	0.572	0.012	0.0
A1C-55	0.0	4.847	0.037	0.0	0.324	0.361	1.984	0.337	0.013	0.0	0.097	0.078	0.017	0.0	0.08	0.0	0.004	0.024	0.0	0.572	0.012	0.0
A1c-54T mean	0.0	4.847	0.037	0.0	0.324	0.361	1.984	0.337	0.013	0.0	0.097	0.078	0.017	0.0	0.08	0.0	0.004	0.024	0.0	0.572	0.012	0.0
A1c-P2-53	0.0	4.847	0.037	0.0	0.324	0.361	1.984	0.337	0.013	0.0	0.097	0.078	0.017	0.0	0.08	0.0	0.004	0.024	0.0	0.572	0.012	0.0
A1c-52	0.0	4.847	0.037	0.0	0.324	0.361	1.984	0.337	0.013	0.0	0.097	0.078	0.017	0.0	0.08	0.0	0.004	0.024	0.0	0.572	0.012	0.0
A1c-51	0.0	4.847	0.037	0.0	0.324	0.361	1.984	0.337	0.013	0.0	0.097	0.078	0.017	0.0	0.08	0.0	0.004	0.024	0.0	0.572	0.012	0.0
A1c-50	0.0	4.847	0.037	0.0	0.324	0.361	1.984	0.337	0.013	0.0	0.097	0.078	0.017	0.0	0.08	0.0	0.004	0.024	0.0	0.572	0.012	0.0
A1c-49	0.0	4.847	0.037	0.0	0.324	0.361	1.984	0.337	0.013	0.0	0.097	0.078	0.017	0.0	0.08	0.0	0.004	0.024	0.0	0.572	0.012	0.0
A1c-48	0.0	4.847	0.037	0.0	0.324	0.361	1.984	0.337	0.013	0.0	0.097	0.078	0.017	0.0	0.08	0.0	0.004	0.024	0.0	0.572	0.012	0.0
A1c-46	0.0	4.847	0.037	0.0	0.324	0.361	1.984	0.337	0.013	0.0	0.097	0.078	0.017	0.0	0.08	0.0	0.004	0.024	0.0	0.572	0.012	0.0
A1c-45	0.0	4.847	0.037	0.0	0.324	0.361	1.984	0.337	0.013	0.0	0.097	0.078	0.017	0.0	0.08	0.0	0.004	0.024	0.0	0.572	0.012	0.0
A1c-44 mean	0.0	4.847	0.037	0.0	0.324	0.361	1.984	0.337	0.013	0.0	0.097	0.078	0.017	0.0	0.08	0.0	0.004	0.024	0.0	0.572	0.012	0.0
A1c-42	0.0	4.847	0.037	0.0	0.324	0.361	1.984	0.337	0.013	0.0	0.097	0.078	0.017	0.0	0.08	0.0	0.004	0.024	0.0	0.572	0.012	0.0
A1c-41	0.0	4.847	0.037	0.0	0.324	0.361	1.984	0.337	0.013	0.0	0.097	0.078	0.017	0.0	0.08	0.0	0.004	0.024	0.0	0.572	0.012	0.0
A1c-40	0.0	4.847	0.037	0.0	0.324	0.361	1.984	0.337	0.013	0.0	0.097	0.078	0.017	0.0	0.08	0.0	0.004	0.024	0.0	0.572	0.012	0.0
A1c-38 mean	0.0	4.847	0.037	0.0	0.324	0.361	1.984	0.337	0.013	0.0	0.097	0.078	0.017	0.0	0.08	0.0	0.004	0.024	0.0	0.572	0.012	0.0
A1c-37	0.0	4.847	0.037	0.0	0.324	0.361	1.984	0.337	0.013	0.0	0.097	0.078	0.017	0.0	0.08	0.0	0.004	0.024	0.0	0.572	0.012	0.0
A1c-36	0.0	4.847	0.037	0.0	0.324	0.361	1.984	0.337	0.013	0.0	0.097	0.078	0.017	0.0	0.08	0.0	0.004	0.024	0.0	0.572	0.012	0.0
A1c-34	0.0	4.847	0.037	0.0	0.324	0.361	1.984	0.337	0.013	0.0	0.097	0.078	0.017	0.0	0.08	0.0	0.004	0.024	0.0	0.572	0.012	0.0
A1c-33	0.0	4.847	0.037	0.0	0.324	0.361	1.984	0.337	0.013	0.0	0.097	0.078	0.017	0.0	0.08	0.0	0.004	0.024	0.0	0.572	0.012	0.0
A1c-32 mean	0.0	4.847	0.037	0.0	0.324	0.361	1.984	0.337	0.013	0.0	0.097	0.078	0.017	0.0	0.08	0.0	0.004	0.024	0.0	0.572	0.012	0.0
A1c-30	0.0	4.847	0.037	0.0	0.324	0.361	1.984	0.337	0.013	0.0	0.097	0.078	0.017	0.0	0.08	0.0	0.004	0.024	0.0	0.572	0.012	0.0
A1c-29	0.0	4.847	0.037	0.0	0.324	0.361	1.984	0.337	0.013	0.0	0.097	0.078	0.017	0.0	0.08	0.0	0.004	0.024	0.0	0.572	0.012	0.0
A1c-28 mean	0.0	4.847	0.037	0.0	0.324	0.361	1.984	0.337	0.013	0.0	0.097	0.078	0.017	0.0	0.08	0.0	0.004	0.024	0.0	0.572	0.012	0.0
A1c-26	0.0	4.847	0.037	0.0	0.324	0.361	1.984	0.337	0.013	0.0	0.097	0.078	0.017	0.0	0.08	0.0	0.004	0.024	0.0	0.572	0.012	0.0
A1c-25	0.0	4.847	0.037	0.0	0.324	0.361	1.984	0.337	0.013	0.0	0.097	0.078	0.017	0.0	0.08	0.0	0.004	0.024	0.0	0.572	0.012	0.0
A1c-24 mean	0.0	4.847	0.037	0.0	0.324	0.361	1.984	0.337	0.013	0.0	0.097	0.078	0.017	0.0	0.08	0.0	0.004	0.024	0.0	0.572	0.012	0.0
A1C-23	0.0	4.847	0.037	0.0	0.324	0.361	1.984	0.337	0.013	0.0	0.097	0.078	0.017	0.0	0.08	0.0	0.004	0.024	0.0	0.572	0.012	0.0
A1c-22	0.0	4.847	0.037	0.0	0.324	0.361	1.984	0.337	0.013	0.0	0.097	0.078	0.017	0.0	0.08	0.0	0.004	0.024	0.0	0.572	0.012	0.0
A1c-21	0.0	4.847	0.037	0.0	0.324	0.361	1.984	0.337	0.013	0.0	0.097	0.078	0.017	0.0	0.08	0.0	0.004	0.024	0.0	0.572	0.012	0.0
A1c-20 mean	0.0	4.847	0.037	0.0	0.324	0.361	1.984	0.337	0.013	0.0	0.097	0.078	0.017	0.0	0.08	0.0	0.004	0.024	0.0	0.572	0.012	0.0
A1C-19	0.0	4.847	0.037	0.0	0.324	0.361	1.984	0.337	0.013	0.0	0.097	0.078	0.017	0.0	0.08	0.0	0.004	0.024	0.0	0.572	0.012	0.0
A1c-18	0.0	4.847	0.037	0.0	0.324	0.361	1.984	0.337	0.013	0.0	0.097	0.078	0.017	0.0	0.08	0.0	0.004	0.024	0.0	0.572	0.012	0.0
A1c-17	0.0	4.847	0.037	0.0	0.324	0.361	1.984	0.337	0.013	0.0	0.097	0.078	0.017	0.0	0.08	0.0	0.004	0.024	0.0	0.572	0.012	0.0
A1c-16	0.0	4.847	0.037	0.0	0.324	0.361	1.984	0.337	0.013	0.0	0.097	0.078	0.017	0.0	0.08	0.0	0.004	0.024	0.0	0.572	0.012	0.0
A1c-14	0.0	4.847	0.037	0.0	0.324	0.361	1.984	0.337	0.013	0.0	0.097	0.078	0.017	0.0	0.08	0.0	0.004	0.024	0.0	0.572	0.012	0.0
A1c-13	0.0	4.847	0.037	0.0	0.324	0.361	1.984	0.337	0.013	0.0	0.097	0.078	0.017	0.0	0.08	0.0	0.004	0.024	0.0	0.572	0.012	0.0
A1c-12 mean	0.0	4.847	0.037	0.0	0.324	0.361	1.984	0.337	0.013	0.0	0.097	0.078	0.017	0.0	0.08	0.0	0.004	0.024	0.0	0.572	0.012	0.0
A1C-11	0.0	4.847	0.037	0.0	0.324	0.361	1.984	0.337	0.013	0.0	0.097	0.078	0.017	0.0	0.08	0.0	0.004	0.024	0.0	0.572	0.012	0.0
A1c-10 mean	0.0	4.847	0.037	0.0	0.324	0.361	1.984	0.337	0.013	0.0	0.097	0.078	0.017	0.0	0.08	0.0	0.004	0.024	0.0	0.572	0.012	0.0
A1c-9 mean	0.0	4.847	0.037	0.0	0.324	0.361	1.984	0.337	0.013	0.0	0.097	0.078	0.017	0.0	0.08	0.0	0.004	0.024	0.0	0.572	0.012	0.0
A1c-8 mean	0.0	4.847	0.037	0.0	0.324	0.361	1.984	0.337	0.013	0.0	0.097	0.078	0.017	0.0	0.08	0.0	0.004	0.024	0.0	0.572	0.012	0.0
A1c-6	0.0	4.847	0.037	0.0	0.324	0.361	1.984	0.337	0.013	0.0	0.097	0.078	0.017	0.0	0.08	0.0	0.004	0.024	0.0	0.572	0.012	0.0
A1c-5	0.0	4.847	0.037	0.0	0.324	0.361	1.984	0.337	0.013	0.0	0.097	0.078	0.017	0.0	0.08	0.0	0.004	0.024	0.0	0.572	0.012	0.0
A1c-4	0.0	4.847	0.037	0.0	0.324	0.361	1.984	0.337	0.013	0.0	0.097	0.078	0.017	0.0	0.08	0.0	0.004	0.024	0.0	0.572	0.012	0.0
A1C-03	0.0	4.847	0.037	0.0	0.324	0.361	1.984	0.337	0.013	0.0	0.097	0.078	0.017	0.0	0.08	0.0	0.004	0.024	0.0	0.572	0.012	0.0
A1c-2	0.0	4.847	0.037	0.0	0.324	0.361	1.984	0.337	0.013	0.0	0.097	0.078	0.017	0.0	0.08	0.0	0.004	0.024	0.0	0.572	0.012	0.0
A1c-1mean	0.0	4.847	0.037	0.0	0.324	0.361	1.984	0.337	0.013	0.0	0.097	0.078	0.017	0.0	0.08	0.0	0.004	0.024	0.0	0.572	0.012	0.0

23	24	25	26	27	28	29	30	31	32	33	34	35	36	37	38	39	40	41	42	43	44	45
Nb	Nd	Ni	Pb	Pr	Rb	Sb	Sm	Sn	Sr	Ta	Tb	Th	Tm	U	V	W	Y	Yb	Zn	Zr	SiO2 (Si)	Al2O3 (Al)
ppm	ppm	ppm	ppm	ppm	ppm	ppm	ppm	ppm	ppm	ppm	ppm	ppm	ppm	ppm	ppm	ppm	ppm	ppm	ppm	ppm	%	%
0.008	0.342	21.187	49.416	0.08	0.1	0.0	0.068	0.0	183.122	0.0	0.013	0.009	0.011	0.351	1.221	0.0	1.524	0.073	0.0	0.179	0.0	0.015

46	47	48	49	50	51	52	53	54	55	56	57	58	59	60	61	62	63	64	65	66
Fe2O3 (Fe)	MnO (Mn)	MgO (Mg)	CaO (Ca)	Na2O(Na)	K2O(K)	TiO2(Ti)	P2O5(P)	B	Li	H2Otot (H)	Stot (S)	CO2 tot (C)	O,rock	O,water	Cl nat AMS	Ca ICP	Z (position sur le scarp)	Thickness sample	[36Cl] AMS	uncertainty
%	%	%	%	%	%	%	%	ppm	ppm	%	%	%			ppm	ppm	cm	cm	at/g.rock	
																moyenne repliqué	moyenne site			
0.0	0.001	0.549	54.818	0.0	0.0	0.001	0.007	1.0	0.811	0.56	0.016	44.249	0.0	0.0	1.18	385564				
0.0	0.001	0.549	54.818	0.0	0.0	0.001	0.007	1.0	0.811	0.56	0.016	44.249	0.0	0.0	2.68	387982	17	3	257805	5889
0.0	0.001	0.549	54.818	0.0	0.0	0.001	0.007	1.0	0.811	0.56	0.016	44.249	0.0	0.0	3.06	385564	27	3	268529	9495
0.0	0.001	0.549	54.818	0.0	0.0	0.001	0.007	1.0	0.811	0.56	0.016	44.249	0.0	0.0	2.45	378742	37	3	260354	6033
0.0	0.001	0.549	54.818	0.0	0.0	0.001	0.007	1.0	0.811	0.56	0.016	44.249	0.0	0.0	2.91	384440	57	2	268382	8127
0.0	0.001	0.549	54.818	0.0	0.0	0.001	0.007	1.0	0.811	0.56	0.016	44.249	0.0	0.0	3.14	385564	67	1	274533	4984
0.0	0.001	0.549	54.818	0.0	0.0	0.001	0.007	1.0	0.811	0.56	0.016	44.249	0.0	0.0	3.62	383306	78	2	276525	6404
0.0	0.001	0.549	54.818	0.0	0.0	0.001	0.007	1.0	0.811	0.56	0.016	44.249	0.0	0.0	3.74	385564	89 2.5		286894	5083
0.0	0.001	0.549	54.818	0.0	0.0	0.001	0.007	1.0	0.811	0.56	0.016	44.249	0.0	0.0	1.19	379925	99	2	280470	6493
0.0	0.001	0.549	54.818	0.0	0.0	0.001	0.007	1.0	0.811	0.56	0.016	44.249	0.0	0.0	0.52	385564	110	2	280362	5865
0.0	0.001	0.549	54.818	0.0	0.0	0.001	0.007	1.0	0.811	0.56	0.016	44.249	0.0	0.0	0.34	388792	120	2	290988	10848
0.0	0.001	0.549	54.818	0.0	0.0	0.001	0.007	1.0	0.811	0.56	0.016	44.249	0.0	0.0	0.26	393260	140 2.5		289789	10182
0.0	0.001	0.549	54.818	0.0	0.0	0.001	0.007	1.0	0.811	0.56	0.016	44.249	0.0	0.0	1	385564	150	1	301092	5938
0.0	0.001	0.549	54.818	0.0	0.0	0.001	0.007	1.0	0.811	0.56	0.016	44.249	0.0	0.0	0.96	399673	160 3.5		303973	7962
0.0	0.001	0.549	54.818	0.0	0.0	0.001	0.007	1.0	0.811	0.56	0.016	44.249	0.0	0.0	0.64	394667	170	2	298236	7773
0.0	0.001	0.549	54.818	0.0	0.0	0.001	0.007	1.0	0.811	0.56	0.016	44.249	0.0	0.0	0.84	385564	179 0.3		278605	1768
0.0	0.001	0.549	54.818	0.0	0.0	0.001	0.007	1.0	0.811	0.56	0.016	44.249	0.0	0.0	3.54	385564	190 2.5		292869	5188
0.0	0.001	0.549	54.818	0.0	0.0	0.001	0.007	1.0	0.811	0.56	0.016	44.249	0.0	0.0	2.19	382231	200 3.5		297552	70547
0.0	0.001	0.549	54.818	0.0	0.0	0.001	0.007	1.0	0.811	0.56	0.016	44.249	0.0	0.0	1.66	385564	209	4	311247	6137
0.0	0.001	0.549	54.818	0.0	0.0	0.001	0.007	1.0	0.811	0.56	0.016	44.249	0.0	0.0	0.17	403358	222	3	305190	7048
0.0	0.001	0.549	54.818	0.0	0.0	0.001	0.007	1.0	0.811	0.56	0.016	44.249	0.0	0.0	0.16	385564	232	2	320141	7889
0.0	0.001	0.549	54.818	0.0	0.0	0.001	0.007	1.0	0.811	0.56	0.016	44.249	0.0	0.0	0.27	380692	242	3	301995	6968
0.0	0.001	0.549	54.818	0.0	0.0	0.001	0.007	1.0	0.811	0.56	0.016	44.249	0.0	0.0	0.28	388721	262	3	314382	7247
0.0	0.001	0.549	54.818	0.0	0.0	0.001	0.007	1.0	0.811	0.56	0.016	44.249	0.0	0.0	0.12	385564	273	3	313412	6182
0.0	0.001	0.549	54.818	0.0	0.0	0.001	0.007	1.0	0.811	0.56	0.016	44.249	0.0	0.0	0.31	375844	283	1	317951	1583
0.0	0.001	0.549	54.818	0.0	0.0	0.001	0.007	1.0	0.811	0.56	0.016	44.249	0.0	0.0	0.23	386548	303	3	331260	7654
0.0	0.001	0.549	54.818	0.0	0.0	0.001	0.007	1.0	0.811	0.56	0.016	44.249	0.0	0.0	0.17	385564	313	1	330562	6517
0.0	0.001	0.549	54.818	0.0	0.0	0.001	0.007	1.0	0.811	0.56	0.016	44.249	0.0	0.0	0.29	385564	323	2	338860	15098
0.0	0.001	0.549	54.818	0.0	0.0	0.001	0.007	1.0	0.811	0.56	0.016	44.249	0.0	0.0	0.51	385564	344 2.5		349018	6127
0.0	0.001	0.549	54.818	0.0	0.0	0.001	0.007	1.0	0.811	0.56	0.016	44.249	0.0	0.0	0.21	385564	353	1	345434	7124
0.0	0.001	0.549	54.818	0.0	0.0	0.001	0.007	1.0	0.811	0.56	0.016	44.249	0.0	0.0	1.38	385564	363	2	353964	9539
0.0	0.001	0.549	54.818	0.0	0.0	0.001	0.007	1.0	0.811	0.56	0.016	44.249	0.0	0.0	0.59	385564	384	2	350428	14767
0.0	0.001	0.549	54.818	0.0	0.0	0.001	0.007	1.0	0.811	0.56	0.016	44.249	0.0	0.0	0.4	385564	394 1.5		371107	7313
0.0	0.001	0.549	54.818	0.0	0.0	0.001	0.007	1.0	0.811	0.56	0.016	44.249	0.0	0.0	1.41	364357	404	2	368569	11436
0.0	0.001	0.549	54.818	0.0	0.0	0.001	0.007	1.0	0.811	0.56	0.016	44.249	0.0	0.0	1.4	385564	424	2	370344	14149
0.0	0.001	0.549	54.818	0.0	0.0	0.001	0.007	1.0	0.811	0.56	0.016	44.249	0.0	0.0	0.64	385564	433 1.5		353416	7750
0.0	0.001	0.549	54.818	0.0	0.0	0.001	0.007	1.0	0.811	0.56	0.016	44.249	0.0	0.0	0.85	374550	443	2	354636	3040
0.0	0.001	0.549	54.818	0.0	0.0	0.001	0.007	1.0	0.811	0.56	0.016	44.249	0.0	0.0	1.22	385564	463 1.5		363379	14292
0.0	0.001	0.549	54.818	0.0	0.0	0.001	0.007	1.0	0.811	0.56	0.016	44.249	0.0	0.0	1.09	385564	474 1.5		375265	7398
0.0	0.001	0.549	54.818	0.0	0.0	0.001	0.007	1.0	0.811	0.56	0.016	44.249	0.0	0.0	1.57	373821	484	2	398214	5291
0.0	0.001	0.549	54.818	0.0	0.0	0.001	0.007	1.0	0.811	0.56	0.016	44.249	0.0	0.0	0.78	390743	494 2.5		386180	9877
0.0	0.001	0.549	54.818	0.0	0.0	0.001	0.007	1.0	0.811	0.56	0.016	44.249	0.0	0.0	0.94	385564	525 2.5		407166	11862
0.0	0.001	0.549	54.818	0.0	0.0	0.001	0.007	1.0	0.811	0.56	0.016	44.249	0.0	0.0	0.38	385564	535 1.5		406517	7217
0.0	0.001	0.549	54.818	0.0	0.0	0.001	0.007	1.0	0.811	0.56	0.016	44.249	0.0	0.0	0.69	386455	545	2	421208	26720
0.0	0.001	0.549	54.818	0.0	0.0	0.001	0.007	1.0	0.811	0.56	0.016	44.249	0.0	0.0	0.14	400444	555 1.5		403828	10468
0.0	0.001	0.549	54.818	0.0	0.0	0.001	0.007	1.0	0.811	0.56	0.016	44.249	0.0	0.0	0.62	385564	565 2.5		421259	8880
0.0	0.001	0.549	54.818	0.0	0.0	0.001	0.007	1.0	0.811	0.56	0.016	44.249	0.0	0.0	1.92	385564	578	1	433112	7700
0.0	0.001	0.549	54.818	0.0	0.0	0.001	0.007	1.0	0.811	0.56	0.016	44.249	0.0	0.0	2.53	385564	587	2	442875	10795
0.0	0.001	0.549	54.818	0.0	0.0	0.001	0.007	1.0	0.811	0.56	0.016	44.249	0.0	0.0	0.81	385564	607 2.5		447781	9437
0.0	0.001	0.549	54.818	0.0	0.0	0.001	0.007	1.0	0.811	0.56	0.016	44.249	0.0	0.0	0.49	385564	618	2	447151	7930
0.0	0.001	0.549	54.818	0.0	0.0	0.001	0.007	1.0	0.811	0.56	0.016	44.249	0.0	0.0	0.76	380526	628 2.5		436897	3567
0.0	0.001	0.549	54.818	0.0	0.0	0.001	0.007	1.0	0.811	0.56	0.016	44.249	0.0	0.0	0.58	393275	638	2	466201	10622
0.0	0.001	0.549	54.818	0.0	0.0	0.001	0.007	1.0	0.811	0.56	0.016	44.249	0.0	0.0	0.58	385564	663 2.5		462236	11509
0.0	0.001	0.549	54.818	0.0	0.0	0.001	0.007	1.0	0.811	0.56	0.016	44.249	0.0	0.0	0.64	385564	674	2	460048	4465
0.0	0.001	0.549	54.818	0.0	0.0	0.001	0.007	1.0	0.811	0.56	0.016	44.249	0.0	0.0	1.1	386097	706 2.5		504976	3582
0.0	0.001	0.549	54.818	0.0	0.0	0.001	0.007	1.0	0.811	0.56	0.016	44.249	0.0	0.0	1.59	385564	725 2.5		507106	13886
0.0	0.001	0.549	54.818	0.0	0.0	0.001	0.007	1.0	0.811	0.56	0.016	44.249	0.0	0.0	1.22	385564	755	3	542742	9617
0.0	0.001	0.549	54.818	0.0	0.0	0.001	0.007	1.0	0.811	0.56	0.016	44.249	0.0	0.0	1.89	385564	765	2	555218	15300
0.0	0.001	0.549	54.818	0.0	0.0	0.001	0.007	1.0	0.811	0.56	0.016	44.249	0.0	0.0	0.88	398167	785 1.5		554123	10168
0.0	0.001	0.549	54.818	0.0	0.0	0.001	0.007	1.0	0.811	0.56	0.016	44.249	0.0	0.0	2.05	385564	795 1.5		562833	21419
0.0	0.001	0.549	54.818	0.0	0.0	0.001	0.007	1.0	0.811	0.56	0.016	44.249	0.0	0.0	1.03	385564	805 1.5		560436	7982

	1	2	3	4	5	6	7	8	9	10	11	12	13	14	15	16	17	18	19	20	21	22
SITE MA2	As	Ba	Be	Bi	Cd	Ce	Co	Cr	Cs	Cu	Dy	Er	Eu	Ga	Gd	Ge	Hf	Ho	In	La	Lu	Mo
nom échantillon	ppm	ppm	ppm	ppm	ppm	ppm	ppm	ppm	ppm	ppm	ppm	ppm	ppm	ppm	ppm	ppm	ppm	ppm	ppm	ppm	ppm	ppm
	0	1,39318182	0,04436364	0	0,238	0,22690909	1,82927273	0	0	0	0,06781818	0,05090909	0,01172727	0	0,05563636	0	0	0,01663636	0	0,29281818	0,00845455	0
	0	1,39	0,04	0	0,24	0,23	1,83	0	0	0	0,07	0,05	0,01	0	0,06	0	0	0,02	0	0,29	0,01	0
coll aprox à la roche	0.0	1.39	0.04	0.0	0.24	0.23	1.83	0.0	0.0	0.0	0.07	0.05	0.01	0.0	0.06	0.0	0.0	0.02	0.0	0.29	0.01	0.0
A6c-74 mean	0.0	1.39	0.04	0.0	0.24	0.23	1.83	0.0	0.0	0.0	0.07	0.05	0.01	0.0	0.06	0.0	0.0	0.02	0.0	0.29	0.01	0.0
A6C-73	0.0	1.39	0.04	0.0	0.24	0.23	1.83	0.0	0.0	0.0	0.07	0.05	0.01	0.0	0.06	0.0	0.0	0.02	0.0	0.29	0.01	0.0
A6c-72 mean	0.0	1.39	0.04	0.0	0.24	0.23	1.83	0.0	0.0	0.0	0.07	0.05	0.01	0.0	0.06	0.0	0.0	0.02	0.0	0.29	0.01	0.0
A6C-71	0.0	1.39	0.04	0.0	0.24	0.23	1.83	0.0	0.0	0.0	0.07	0.05	0.01	0.0	0.06	0.0	0.0	0.02	0.0	0.29	0.01	0.0
A6c-70	0.0	1.39	0.04	0.0	0.24	0.23	1.83	0.0	0.0	0.0	0.07	0.05	0.01	0.0	0.06	0.0	0.0	0.02	0.0	0.29	0.01	0.0
A6C-69	0.0	1.39	0.04	0.0	0.24	0.23	1.83	0.0	0.0	0.0	0.07	0.05	0.01	0.0	0.06	0.0	0.0	0.02	0.0	0.29	0.01	0.0
A6c-68	0.0	1.39	0.04	0.0	0.24	0.23	1.83	0.0	0.0	0.0	0.07	0.05	0.01	0.0	0.06	0.0	0.0	0.02	0.0	0.29	0.01	0.0
A6C-67	0.0	1.39	0.04	0.0	0.24	0.23	1.83	0.0	0.0	0.0	0.07	0.05	0.01	0.0	0.06	0.0	0.0	0.02	0.0	0.29	0.01	0.0
A6c-66	0.0	1.39	0.04	0.0	0.24	0.23	1.83	0.0	0.0	0.0	0.07	0.05	0.01	0.0	0.06	0.0	0.0	0.02	0.0	0.29	0.01	0.0
A6C-65	0.0	1.39	0.04	0.0	0.24	0.23	1.83	0.0	0.0	0.0	0.07	0.05	0.01	0.0	0.06	0.0	0.0	0.02	0.0	0.29	0.01	0.0
A6c-64	0.0	1.39	0.04	0.0	0.24	0.23	1.83	0.0	0.0	0.0	0.07	0.05	0.01	0.0	0.06	0.0	0.0	0.02	0.0	0.29	0.01	0.0
A6C-63	0.0	1.39	0.04	0.0	0.24	0.23	1.83	0.0	0.0	0.0	0.07	0.05	0.01	0.0	0.06	0.0	0.0	0.02	0.0	0.29	0.01	0.0
A6c-62	0.0	1.39	0.04	0.0	0.24	0.23	1.83	0.0	0.0	0.0	0.07	0.05	0.01	0.0	0.06	0.0	0.0	0.02	0.0	0.29	0.01	0.0
A6C-61	0.0	1.39	0.04	0.0	0.24	0.23	1.83	0.0	0.0	0.0	0.07	0.05	0.01	0.0	0.06	0.0	0.0	0.02	0.0	0.29	0.01	0.0
A6c-60	0.0	1.39	0.04	0.0	0.24	0.23	1.83	0.0	0.0	0.0	0.07	0.05	0.01	0.0	0.06	0.0	0.0	0.02	0.0	0.29	0.01	0.0
A6C-59	0.0	1.39	0.04	0.0	0.24	0.23	1.83	0.0	0.0	0.0	0.07	0.05	0.01	0.0	0.06	0.0	0.0	0.02	0.0	0.29	0.01	0.0
A6c-58	0.0	1.39	0.04	0.0	0.24	0.23	1.83	0.0	0.0	0.0	0.07	0.05	0.01	0.0	0.06	0.0	0.0	0.02	0.0	0.29	0.01	0.0
A6C-57	0.0	1.39	0.04	0.0	0.24	0.23	1.83	0.0	0.0	0.0	0.07	0.05	0.01	0.0	0.06	0.0	0.0	0.02	0.0	0.29	0.01	0.0
A6C-56N	0.0	1.39	0.04	0.0	0.24	0.23	1.83	0.0	0.0	0.0	0.07	0.05	0.01	0.0	0.06	0.0	0.0	0.02	0.0	0.29	0.01	0.0
A6C-55	0.0	1.39	0.04	0.0	0.24	0.23	1.83	0.0	0.0	0.0	0.07	0.05	0.01	0.0	0.06	0.0	0.0	0.02	0.0	0.29	0.01	0.0
A6c-54	0.0	1.39	0.04	0.0	0.24	0.23	1.83	0.0	0.0	0.0	0.07	0.05	0.01	0.0	0.06	0.0	0.0	0.02	0.0	0.29	0.01	0.0
A6C-53	0.0	1.39	0.04	0.0	0.24	0.23	1.83	0.0	0.0	0.0	0.07	0.05	0.01	0.0	0.06	0.0	0.0	0.02	0.0	0.29	0.01	0.0
A6c-52	0.0	1.39	0.04	0.0	0.24	0.23	1.83	0.0	0.0	0.0	0.07	0.05	0.01	0.0	0.06	0.0	0.0	0.02	0.0	0.29	0.01	0.0
A6C-51	0.0	1.39	0.04	0.0	0.24	0.23	1.83	0.0	0.0	0.0	0.07	0.05	0.01	0.0	0.06	0.0	0.0	0.02	0.0	0.29	0.01	0.0
A6c-50	0.0	1.39	0.04	0.0	0.24	0.23	1.83	0.0	0.0	0.0	0.07	0.05	0.01	0.0	0.06	0.0	0.0	0.02	0.0	0.29	0.01	0.0
A6C-49	0.0	1.39	0.04	0.0	0.24	0.23	1.83	0.0	0.0	0.0	0.07	0.05	0.01	0.0	0.06	0.0	0.0	0.02	0.0	0.29	0.01	0.0
A6c-48	0.0	1.39	0.04	0.0	0.24	0.23	1.83	0.0	0.0	0.0	0.07	0.05	0.01	0.0	0.06	0.0	0.0	0.02	0.0	0.29	0.01	0.0
A6C-47MEAN	0.0	1.39	0.04	0.0	0.24	0.23	1.83	0.0	0.0	0.0	0.07	0.05	0.01	0.0	0.06	0.0	0.0	0.02	0.0	0.29	0.01	0.0
A6c-46MEAN	0.0	1.39	0.04	0.0	0.24	0.23	1.83	0.0	0.0	0.0	0.07	0.05	0.01	0.0	0.06	0.0	0.0	0.02	0.0	0.29	0.01	0.0
A6C-45	0.0	1.39	0.04	0.0	0.24	0.23	1.83	0.0	0.0	0.0	0.07	0.05	0.01	0.0	0.06	0.0	0.0	0.02	0.0	0.29	0.01	0.0
A6c-44	0.0	1.39	0.04	0.0	0.24	0.23	1.83	0.0	0.0	0.0	0.07	0.05	0.01	0.0	0.06	0.0	0.0	0.02	0.0	0.29	0.01	0.0
A6C-43	0.0	1.39	0.04	0.0	0.24	0.23	1.83	0.0	0.0	0.0	0.07	0.05	0.01	0.0	0.06	0.0	0.0	0.02	0.0	0.29	0.01	0.0
A6c-42 mean	0.0	1.39	0.04	0.0	0.24	0.23	1.83	0.0	0.0	0.0	0.07	0.05	0.01	0.0	0.06	0.0	0.0	0.02	0.0	0.29	0.01	0.0
A6C-41	0.0	1.39	0.04	0.0	0.24	0.23	1.83	0.0	0.0	0.0	0.07	0.05	0.01	0.0	0.06	0.0	0.0	0.02	0.0	0.29	0.01	0.0
A6c-40	0.0	1.39	0.04	0.0	0.24	0.23	1.83	0.0	0.0	0.0	0.07	0.05	0.01	0.0	0.06	0.0	0.0	0.02	0.0	0.29	0.01	0.0
A6C-39	0.0	1.39	0.04	0.0	0.24	0.23	1.83	0.0	0.0	0.0	0.07	0.05	0.01	0.0	0.06	0.0	0.0	0.02	0.0	0.29	0.01	0.0
A6c-38	0.0	1.39	0.04	0.0	0.24	0.23	1.83	0.0	0.0	0.0	0.07	0.05	0.01	0.0	0.06	0.0	0.0	0.02	0.0	0.29	0.01	0.0
A6C-37	0.0	1.39	0.04	0.0	0.24	0.23	1.83	0.0	0.0	0.0	0.07	0.05	0.01	0.0	0.06	0.0	0.0	0.02	0.0	0.29	0.01	0.0
A6c-36	0.0	1.39	0.04	0.0	0.24	0.23	1.83	0.0	0.0	0.0	0.07	0.05	0.01	0.0	0.06	0.0	0.0	0.02	0.0	0.29	0.01	0.0
A6C-35	0.0	1.39	0.04	0.0	0.24	0.23	1.83	0.0	0.0	0.0	0.07	0.05	0.01	0.0	0.06	0.0	0.0	0.02	0.0	0.29	0.01	0.0
A6c-34	0.0	1.39	0.04	0.0	0.24	0.23	1.83	0.0	0.0	0.0	0.07	0.05	0.01	0.0	0.06	0.0	0.0	0.02	0.0	0.29	0.01	0.0
A6C-33	0.0	1.39	0.04	0.0	0.24	0.23	1.83	0.0	0.0	0.0	0.07	0.05	0.01	0.0	0.06	0.0	0.0	0.02	0.0	0.29	0.01	0.0
A6c-32	0.0	1.39	0.04	0.0	0.24	0.23	1.83	0.0	0.0	0.0	0.07	0.05	0.01	0.0	0.06	0.0	0.0	0.02	0.0	0.29	0.01	0.0
A6c-30 mean	0.0	1.39	0.04	0.0	0.24	0.23	1.83	0.0	0.0	0.0	0.07	0.05	0.01	0.0	0.06	0.0	0.0	0.02	0.0	0.29	0.01	0.0
A6C-29	0.0	1.39	0.04	0.0	0.24	0.23	1.83	0.0	0.0	0.0	0.07	0.05	0.01	0.0	0.06	0.0	0.0	0.02	0.0	0.29	0.01	0.0
A6c-28	0.0	1.39	0.04	0.0	0.24	0.23	1.83	0.0	0.0	0.0	0.07	0.05	0.01	0.0	0.06	0.0	0.0	0.02	0.0	0.29	0.01	0.0
A6C-27	0.0	1.39	0.04	0.0	0.24	0.23	1.83	0.0	0.0	0.0	0.07	0.05	0.01	0.0	0.06	0.0	0.0	0.02	0.0	0.29	0.01	0.0
A6c-26	0.0	1.39	0.04	0.0	0.24	0.23	1.83	0.0	0.0	0.0	0.07	0.05	0.01	0.0	0.06	0.0	0.0	0.02	0.0	0.29	0.01	0.0
A6C-25	0.0	1.39	0.04	0.0	0.24	0.23	1.83	0.0	0.0	0.0	0.07	0.05	0.01	0.0	0.06	0.0	0.0	0.02	0.0	0.29	0.01	0.0
A6c-24	0.0	1.39	0.04	0.0	0.24	0.23	1.83	0.0	0.0	0.0	0.07	0.05	0.01	0.0	0.06	0.0	0.0	0.02	0.0	0.29	0.01	0.0
A6C-23	0.0	1.39	0.04	0.0	0.24	0.23	1.83	0.0	0.0	0.0	0.07	0.05	0.01	0.0	0.06	0.0	0.0	0.02	0.0	0.29	0.01	0.0
A6c-22	0.0	1.39	0.04	0.0	0.24	0.23	1.83	0.0	0.0	0.0	0.07	0.05	0.01	0.0	0.06	0.0	0.0	0.02	0.0	0.29	0.01	0.0
A6c-20	0.0	1.39	0.04	0.0	0.24	0.23	1.83	0.0	0.0	0.0	0.07	0.05	0.01	0.0	0.06	0.0	0.0	0.02	0.0	0.29	0.01	0.0
A6C-21MEAN	0.0	1.39	0.04	0.0	0.24	0.23	1.83	0.0	0.0	0.0	0.07	0.05	0.01	0.0	0.06	0.0	0.0	0.02	0.0	0.29	0.01	0.0
A6C-19MEAN	0.0	1.39	0.04	0.0	0.24	0.23	1.83	0.0	0.0	0.0	0.07	0.05	0.01	0.0	0.06	0.0	0.0	0.02	0.0	0.29	0.01	0.0
A6C-17MEAN	0.0	1.39	0.04	0.0	0.24	0.23	1.83	0.0	0.0	0.0	0.07	0.05	0.01	0.0	0.06	0.0	0.0	0.02	0.0	0.29	0.01	0.0
A6C-15MEAN	0.0	1.39	0.04	0.0	0.24	0.23	1.83	0.0	0.0	0.0	0.07	0.05	0.01	0.0	0.06	0.0	0.0	0.02	0.0	0.29	0.01	0.0
A6c-14	0.0	1.39	0.04	0.0	0.24	0.23	1.83	0.0	0.0	0.0	0.07	0.05	0.01	0.0	0.06	0.0	0.0	0.02	0.0	0.29	0.01	0.0
A6C-13	0.0	1.39	0.04	0.0	0.24	0.23	1.83	0.0	0.0	0.0	0.07	0.05	0.01	0.0	0.06	0.0	0.0	0.02	0.0	0.29	0.01	0.0
A6C-12	0.0	1.39	0.04	0.0	0.24	0.23	1.83	0.0	0.0	0.0	0.07	0.05	0.01	0.0	0.06	0.0	0.0	0.02	0.0	0.29	0.01	0.0
A6C-11MEAN	0.0	1.39	0.04	0.0	0.24	0.23	1.83	0.0	0.0	0.0	0.07	0.05	0.01	0.0	0.06	0.0	0.0	0.02	0.0	0.29	0.01	0.0
A6C-10	0.0	1.39	0.04	0.0	0.24	0.23	1.83	0.0	0.0	0.0	0.07	0.05	0.01	0.0	0.06	0.0	0.0	0.02	0.0	0.29	0.01	0.0
A6C-09	0.0	1.39	0.04	0.0	0.24	0.23	1.83	0.0	0.0	0.0	0.07	0.05	0.01	0.0	0.06	0.0	0.0	0.02	0.0	0.29	0.01	0.0
A6C-8	0.0	1.39	0.04	0.0	0.24	0.23	1.83	0.0	0.0	0.0	0.07	0.05	0.01	0.0	0.06	0.0	0.0	0.02	0.0	0.29	0.01	0.0
A6C-07	0.0	1.39	0.04	0.0	0.24	0.23	1.83	0.0	0.0	0.0	0.07	0.05	0.01	0.0	0.06	0.0	0.0	0.02	0.0	0.29	0.01	0.0
A6C-6	0.0	1.39	0.04	0.0	0.24	0.23	1.83	0.0	0.0	0.0	0.07	0.05	0.01	0.0	0.06	0.0	0.0	0.02	0.0	0.29	0.01	0.0
A6C-05	0.0	1.39	0.04	0.0	0.24	0.23	1.83	0.0	0.0	0.0	0.07	0.05	0.01	0.0	0.06	0.0	0.0	0.02	0.0	0.29	0.01	0.0
A6C-4	0.0	1.39	0.04	0.0	0.24	0.23	1.83	0.0	0.0	0.0	0.07	0.05	0.01	0.0	0.06	0.0	0.0	0.02	0.0	0.29	0.01	0.0
A6C-03	0.0	1.39	0.04	0.0	0.24	0.23	1.83	0.0	0.0	0.0	0.07	0.05	0.01	0.0	0.06	0.0	0.0	0.02	0.0	0.29	0.01	0.0
A6C-2MEAN	0.0	1.39	0.04	0.0	0.24	0.23	1.83	0.0	0.0	0.0	0.07	0.05	0.01	0.0	0.06	0.0	0.0	0.02	0.0	0.29	0.01	0.0
A6c-1MEAN	0.0	1.39	0.04	0.0	0.24	0.23	1.83	0.0	0.0	0.0	0.07	0.05	0.01	0.0	0.06	0.0	0.0	0.02	0.0	0.29	0.01	0.0

23	24	25	26	27	28	29	30	31	32	33	34	35	36	37	38	39	40	41	42	43	44	45
Nb	Nd	Ni	Pb	Pr	Rb	Sb	Sm	Sn	Sr	Ta	Tb	Th	Tm	U	V	W	Y	Yb	Zn	Zr	SiO2 (Si)	Al2O3 (Al)
ppm	ppm	ppm	ppm	ppm	ppm	ppm	ppm	ppm	ppm	ppm	ppm	ppm	ppm	ppm	ppm	ppm	ppm	ppm	ppm	ppm	%	%
0	0,21545455	18,5681818	5,87033636	0,04881818	0	0	0,04545455	0	129,936364	0	0,00872727	0,00454545	0,00763636	0,16581818	0	0	0,89127273	0,05118182	0	0	0	0,00390909
0	0,22	18,57	5,87	0,05	0	0	0,05	0	129,94	0	0,01	0	0,01	0,17	0	0	0,89	0,05	0	0	0	0
0.0	**0.22**	**18.57**	**5.87**	**0.05**	**0.0**	**0.0**	**0.05**	**0.0**	**129.94**	**0.0**	**0.01**	**0.0**	**0.01**	**0.17**	**0.0**	**0.0**	**0.89**	**0.05**	**0.0**	**0.0**	**0.0**	**0.0**
0.0	0.22	18.57	5.87	0.05	0.0	0.0	0.05	0.0	129.94	0.0	0.01	0.0	0.01	0.17	0.0	0.0	0.89	0.05	0.0	0.0	0.0	0.0

46	47	48	49	50	51	52	53	54	55	56	57	58	59	60	61	62	63	64	65	66
Fe2O3 (Fe)	MnO (Mn)	MgO (Mg)	CaO (Ca)	Na2O(Na)	K2O(K)	TiO2(Ti)	P2O5(P)	B	Li	H2Otot (H)	Stot (S)	CO2 tot (C)	O,rock	O,water	Cl nat AMS	Ca ICP	Z (position sur le scarp)	Thickness sample	[36Cl] AMS	uncertainty
%	%	%	%	%	%	%	%	ppm	ppm	%	%	%			ppm	ppm	cm	cm	at/g.rock	
0	0,001	0,32718182	55,838	0	0	0	0,05590909	2	0,89090909	0,19454545	0,01	43,8681818								
0	0	0,33	55,84	0	0	0	0,06	2	0,89	0,19	0,01	43,87								
0.0	**0**	**0.33**	**55.84**	**0.0**	**0.0**	**0.0**	**0.06**	**2**	**0.89**	**0.19**	**0.01**	**43.87**	**0.0**	**0.0**	**9.23**	**387639**				
0.0	0	0.33	55.84	0.0	0.0	0.0	0.06	2	0.89	0.19	0.01	43.87	0.0	0.0	5.49	381823	5	3.5	359704	13345
0.0	0	0.33	55.84	0.0	0.0	0.0	0.06	2	0.89	0.19	0.01	43.87	0.0	0.0	6.41	380816	14	4.25	355658	6284
0.0	0	0.33	55.84	0.0	0.0	0.0	0.06	2	0.89	0.19	0.01	43.87	0.0	0.0	4.70	384881	24	3.5	359892	14972
0.0	0	0.33	55.84	0.0	0.0	0.0	0.06	2	0.89	0.19	0.01	43.87	0.0	0.0	7.31	389379	34	3.3	371298	10740
0.0	0	0.33	55.84	0.0	0.0	0.0	0.06	2	0.89	0.19	0.01	43.87	0.0	0.0	8.27	384228	44	3.5	378203	9574
0.0	0	0.33	55.84	0.0	0.0	0.0	0.06	2	0.89	0.19	0.01	43.87	0.0	0.0	8.78	379380	54	3.4	375324	6629
0.0	0	0.33	55.84	0.0	0.0	0.0	0.06	2	0.89	0.19	0.01	43.87	0.0	0.0	9.03	384046	64	3.4	398267	9504
0.0	0	0.33	55.84	0.0	0.0	0.0	0.06	2	0.89	0.19	0.01	43.87	0.0	0.0	9.26	383228	74	3.8	399308	8713
0.0	0	0.33	55.84	0.0	0.0	0.0	0.06	2	0.89	0.19	0.01	43.87	0.0	0.0	8.26	375275	84	3.65	398393	9494
0.0	0	0.33	55.84	0.0	0.0	0.0	0.06	2	0.89	0.19	0.01	43.87	0.0	0.0	7.75	379661	92	3	413779	7311
0.0	0	0.33	55.84	0.0	0.0	0.0	0.06	2	0.89	0.19	0.01	43.87	0.0	0.0	8.08	379322	125	3.1	433235	10390
0.0	0	0.33	55.84	0.0	0.0	0.0	0.06	2	0.89	0.19	0.01	43.87	0.0	0.0	11.15	378731	136	3.5	457888	13327
0.0	0	0.33	55.84	0.0	0.0	0.0	0.06	2	0.89	0.19	0.01	43.87	0.0	0.0	10.14	382925	146	3.35	453813	10934
0.0	0	0.33	55.84	0.0	0.0	0.0	0.06	2	0.89	0.19	0.01	43.87	0.0	0.0	9.27	374113	156	3	472868	8347
0.0	0	0.33	55.84	0.0	0.0	0.0	0.06	2	0.89	0.19	0.01	43.87	0.0	0.0	8.81	380641	165	3.5	468026	11260
0.0	0	0.33	55.84	0.0	0.0	0.0	0.06	2	0.89	0.19	0.01	43.87	0.0	0.0	9.67	386952	175	2.75	512128	9123
0.0	0	0.33	55.84	0.0	0.0	0.0	0.06	2	0.89	0.19	0.01	43.87	0.0	0.0	9.53	385680	185	3.6	479717	11514
0.0	0	0.33	55.84	0.0	0.0	0.0	0.06	2	0.89	0.19	0.01	43.87	0.0	0.0	11.22	387087	196	3.4	512206	9046
0.0	0	0.33	55.84	0.0	0.0	0.0	0.06	2	0.89	0.19	0.01	43.87	0.0	0.0	11.24	395687	207	3.4	532539	14456
0.0	0	0.33	55.84	0.0	0.0	0.0	0.06	2	0.89	0.19	0.01	43.87	0.0	0.0	11.42	382764	217	3.5	528552	11608
0.0	0	0.33	55.84	0.0	0.0	0.0	0.06	2	0.89	0.19	0.01	43.87	0.0	0.0	11.63	385473	226	3.4	532635	12747
0.0	0	0.33	55.84	0.0	0.0	0.0	0.06	2	0.89	0.19	0.01	43.87	0.0	0.0	10.97	396361	236	3.2	540116	12038
0.0	0	0.33	55.84	0.0	0.0	0.0	0.06	2	0.89	0.19	0.01	43.87	0.0	0.0	11.68	379271	246	3.25	548701	12953
0.0	0	0.33	55.84	0.0	0.0	0.0	0.06	2	0.89	0.19	0.01	43.87	0.0	0.0	12	380470	256	2.85	557177	10068
0.0	0	0.33	55.84	0.0	0.0	0.0	0.06	2	0.89	0.19	0.01	43.87	0.0	0.0	10.99	386157	266	2.9	549953	10144
0.0	0	0.33	55.84	0.0	0.0	0.0	0.06	2	0.89	0.19	0.01	43.87	0.0	0.0	10.91	395563	277	2.9	561389	10130
0.0	0	0.33	55.84	0.0	0.0	0.0	0.06	2	0.89	0.19	0.01	43.87	0.0	0.0	9.42	395057	287	2.9	562081	13643
0.0	0	0.33	55.84	0.0	0.0	0.0	0.06	2	0.89	0.19	0.01	43.87	0.0	0.0	10.44	385716	297	3	630573	9912
0.0	0	0.33	55.84	0.0	0.0	0.0	0.06	2	0.89	0.19	0.01	43.87	0.0	0.0	8.95	389388	307	3.35	591916	39163
0.0	0	0.33	55.84	0.0	0.0	0.0	0.06	2	0.89	0.19	0.01	43.87	0.0	0.0	10.24	393149	317	2.65	594991	10748
0.0	0	0.33	55.84	0.0	0.0	0.0	0.06	2	0.89	0.19	0.01	43.87	0.0	0.0	10.41	404045	327	3.25	619496	17117
0.0	0	0.33	55.84	0.0	0.0	0.0	0.06	2	0.89	0.19	0.01	43.87	0.0	0.0	12.03	375638	337	3.9	630394	11391
0.0	0	0.33	55.84	0.0	0.0	0.0	0.06	2	0.89	0.19	0.01	43.87	0.0	0.0	10.11	392791	357	3.1	648573	23214
0.0	0	0.33	55.84	0.0	0.0	0.0	0.06	2	0.89	0.19	0.01	43.87	0.0	0.0	9.46	398072	367	3	681796	12330
0.0	0	0.33	55.84	0.0	0.0	0.0	0.06	2	0.89	0.19	0.01	43.87	0.0	0.0	10.04	389325	378	3	663874	14606
0.0	0	0.33	55.84	0.0	0.0	0.0	0.06	2	0.89	0.19	0.01	43.87	0.0	0.0	11.77	397043	386	4	679544	12108
0.0	0	0.33	55.84	0.0	0.0	0.0	0.06	2	0.89	0.19	0.01	43.87	0.0	0.0	8.17	397483	455	2.75	708165	23117
0.0	0	0.33	55.84	0.0	0.0	0.0	0.06	2	0.89	0.19	0.01	43.87	0.0	0.0	7.3	387210	465	3.25	689464	12120
0.0	0	0.33	55.84	0.0	0.0	0.0	0.06	2	0.89	0.19	0.01	43.87	0.0	0.0	7.03	387363	475	4	688784	22969
0.0	0	0.33	55.84	0.0	0.0	0.0	0.06	2	0.89	0.19	0.01	43.87	0.0	0.0	7.71	387215	486	3.1	692902	11411
0.0	0	0.33	55.84	0.0	0.0	0.0	0.06	2	0.89	0.19	0.01	43.87	0.0	0.0	8.31	386545	496	2.75	708238	26186
0.0	0	0.33	55.84	0.0	0.0	0.0	0.06	2	0.89	0.19	0.01	43.87	0.0	0.0	8.44	378415	506	2	727787	12904
0.0	0	0.33	55.84	0.0	0.0	0.0	0.06	2	0.89	0.19	0.01	43.87	0.0	0.0	8.87	398794	516	2.9	705561	17098
0.0	0	0.33	55.84	0.0	0.0	0.0	0.06	2	0.89	0.19	0.01	43.87	0.0	0.0	8.37	388753	536	2	741471	11599
0.0	0	0.33	55.84	0.0	0.0	0.0	0.06	2	0.89	0.19	0.01	43.87	0.0	0.0	9.55	395904	546	2.75	748226	12700
0.0	0	0.33	55.84	0.0	0.0	0.0	0.06	2	0.89	0.19	0.01	43.87	0.0	0.0	8.36	371766	556	3	732543	17678
0.0	0	0.33	55.84	0.0	0.0	0.0	0.06	2	0.89	0.19	0.01	43.87	0.0	0.0	9.11	397560	566	3.7	738176	12510
0.0	0	0.33	55.84	0.0	0.0	0.0	0.06	2	0.89	0.19	0.01	43.87	0.0	0.0	11.25	375331	576	2.7	773378	15170
0.0	0	0.33	55.84	0.0	0.0	0.0	0.06	2	0.89	0.19	0.01	43.87	0.0	0.0	11.41	392919	586	3.5	768812	13000
0.0	0	0.33	55.84	0.0	0.0	0.0	0.06	2	0.89	0.19	0.01	43.87	0.0	0.0	11.09	402643	596	3	790238	19872
0.0	0	0.33	55.84	0.0	0.0	0.0	0.06	2	0.89	0.19	0.01	43.87	0.0	0.0	9.94	387459	606	3	788967	13255
0.0	0	0.33	55.84	0.0	0.0	0.0	0.06	2	0.89	0.19	0.01	43.87	0.0	0.0	9.15	386424	616	3	770119	27158
0.0	0	0.33	55.84	0.0	0.0	0.0	0.06	2	0.89	0.19	0.01	43.87	0.0	0.0	8.31	384482	636	3.2	804358	18465
0.0	0	0.33	55.84	0.0	0.0	0.0	0.06	2	0.89	0.19	0.01	43.87	0.0	0.0	9.76	383968	626	3	827942	18662
0.0	0	0.33	55.84	0.0	0.0	0.0	0.06	2	0.89	0.19	0.01	43.87	0.0	0.0	10.02	391639	645	3.3	868283	7474
0.0	0	0.33	55.84	0.0	0.0	0.0	0.06	2	0.89	0.19	0.01	43.87	0.0	0.0	8.41	388027	666	3	864390	5110
0.0	0	0.33	55.84	0.0	0.0	0.0	0.06	2	0.89	0.19	0.01	43.87	0.0	0.0	8.21	395682	687	3	902075	42608
0.0	0	0.33	55.84	0.0	0.0	0.0	0.06	2	0.89	0.19	0.01	43.87	0.0	0.0	8.63	393257	701	3.1	837880	27611
0.0	0	0.33	55.84	0.0	0.0	0.0	0.06	2	0.89	0.19	0.01	43.87	0.0	0.0	9.78	381548	713	3	890034	14405
0.0	0	0.33	55.84	0.0	0.0	0.0	0.06	2	0.89	0.19	0.01	43.87	0.0	0.0	6.94	405097	723	3	877031	17333
0.0	0	0.33	55.84	0.0	0.0	0.0	0.06	2	0.89	0.19	0.01	43.87	0.0	0.0	7.89	393775	733	3	917613	46425
0.0	0	0.33	55.84	0.0	0.0	0.0	0.06	2	0.89	0.19	0.01	43.87	0.0	0.0	8.87	377756	743	3.3	921669	19575
0.0	0	0.33	55.84	0.0	0.0	0.0	0.06	2	0.89	0.19	0.01	43.87	0.0	0.0	8.41	391732	753	3	919955	14227
0.0	0	0.33	55.84	0.0	0.0	0.0	0.06	2	0.89	0.19	0.01	43.87	0.0	0.0	6.74	406057	764	3.5	896109	16225
0.0	0	0.33	55.84	0.0	0.0	0.0	0.06	2	0.89	0.19	0.01	43.87	0.0	0.0	8.24	390318	774	3	969304	16337
0.0	0	0.33	55.84	0.0	0.0	0.0	0.06	2	0.89	0.19	0.01	43.87	0.0	0.0	7.56	396440	783	3	966462	17587
0.0	0	0.33	55.84	0.0	0.0	0.0	0.06	2	0.89	0.19	0.01	43.87	0.0	0.0	7.77	384021	793	2.9	981893	15275
0.0	0	0.33	55.84	0.0	0.0	0.0	0.06	2	0.89	0.19	0.01	43.87	0.0	0.0	7.32	386120	800	3	1007410	17867
0.0	0	0.33	55.84	0.0	0.0	0.0	0.06	2	0.89	0.19	0.01	43.87	0.0	0.0	7.8	383205	832	3	1022673	14854
0.0	0	0.33	55.84	0.0	0.0	0.0	0.06	2	0.89	0.19	0.01	43.87	0.0	0.0	7.8	383709	842	3	1041659	24979
0.0	0	0.33	55.84	0.0	0.0	0.0	0.06	2	0.89	0.19	0.01	43.87	0.0	0.0	7.37	383584	852	3.5	1121587	49218

	1	2	3	4	5	6	7	8	9	10	11	12	13	14	15	16	17	18	19	20	21	22
SITE MA4	As	Ba	Be	Bi	Cd	Ce	Co	Cr	Cs	Cu	Dy	Er	Eu	Ga	Gd	Ge	Hf	Ho	In	La	Lu	Mo
nom échantillon	ppm	ppm	ppm	ppm	ppm	ppm	ppm	ppm	ppm	ppm	ppm	ppm	ppm	ppm	ppm	ppm	ppm	ppm	ppm	ppm	ppm	ppm
A4C-64	0.0	3.16	0.0	0.0	0.32	0.24	2.01	0.0	0.0	0.79	0.08	0.06	0.01	0.0	0.06	0.0	0.0	0.02	0.0	0.42	0.01	0.0
A4c-63 mean	0.0	3.16	0.0	0.0	0.32	0.24	2.01	0.0	0.0	0.79	0.08	0.06	0.01	0.0	0.06	0.0	0.0	0.02	0.0	0.42	0.01	0.0
A4C-62	0.0	3.16	0.0	0.0	0.32	0.24	2.01	0.0	0.0	0.79	0.08	0.06	0.01	0.0	0.06	0.0	0.0	0.02	0.0	0.42	0.01	0.0
A4c-61	0.0	3.16	0.0	0.0	0.32	0.24	2.01	0.0	0.0	0.79	0.08	0.06	0.01	0.0	0.06	0.0	0.0	0.02	0.0	0.42	0.01	0.0
A4C-60	0.0	3.16	0.0	0.0	0.32	0.24	2.01	0.0	0.0	0.79	0.08	0.06	0.01	0.0	0.06	0.0	0.0	0.02	0.0	0.42	0.01	0.0
A4c-59	0.0	3.16	0.0	0.0	0.32	0.24	2.01	0.0	0.0	0.79	0.08	0.06	0.01	0.0	0.06	0.0	0.0	0.02	0.0	0.42	0.01	0.0
A4C-58	0.0	3.16	0.0	0.0	0.32	0.24	2.01	0.0	0.0	0.79	0.08	0.06	0.01	0.0	0.06	0.0	0.0	0.02	0.0	0.42	0.01	0.0
A4c-57	0.0	3.16	0.0	0.0	0.32	0.24	2.01	0.0	0.0	0.79	0.08	0.06	0.01	0.0	0.06	0.0	0.0	0.02	0.0	0.42	0.01	0.0
A4c-56 mean	0.0	3.16	0.0	0.0	0.32	0.24	2.01	0.0	0.0	0.79	0.08	0.06	0.01	0.0	0.06	0.0	0.0	0.02	0.0	0.42	0.01	0.0
A4c-55	0.0	3.16	0.0	0.0	0.32	0.24	2.01	0.0	0.0	0.79	0.08	0.06	0.01	0.0	0.06	0.0	0.0	0.02	0.0	0.42	0.01	0.0
A4C-54	0.0	3.16	0.0	0.0	0.32	0.24	2.01	0.0	0.0	0.79	0.08	0.06	0.01	0.0	0.06	0.0	0.0	0.02	0.0	0.42	0.01	0.0
A4c-53	0.0	3.16	0.0	0.0	0.32	0.24	2.01	0.0	0.0	0.79	0.08	0.06	0.01	0.0	0.06	0.0	0.0	0.02	0.0	0.42	0.01	0.0
A4C-52	0.0	3.16	0.0	0.0	0.32	0.24	2.01	0.0	0.0	0.79	0.08	0.06	0.01	0.0	0.06	0.0	0.0	0.02	0.0	0.42	0.01	0.0
A4C-50	0.0	3.16	0.0	0.0	0.32	0.24	2.01	0.0	0.0	0.79	0.08	0.06	0.01	0.0	0.06	0.0	0.0	0.02	0.0	0.42	0.01	0.0
A4c-49	0.0	3.16	0.0	0.0	0.32	0.24	2.01	0.0	0.0	0.79	0.08	0.06	0.01	0.0	0.06	0.0	0.0	0.02	0.0	0.42	0.01	0.0
A4C-48	0.0	3.16	0.0	0.0	0.32	0.24	2.01	0.0	0.0	0.79	0.08	0.06	0.01	0.0	0.06	0.0	0.0	0.02	0.0	0.42	0.01	0.0
A4c-47	0.0	3.16	0.0	0.0	0.32	0.24	2.01	0.0	0.0	0.79	0.08	0.06	0.01	0.0	0.06	0.0	0.0	0.02	0.0	0.42	0.01	0.0
A4C-46	0.0	3.16	0.0	0.0	0.32	0.24	2.01	0.0	0.0	0.79	0.08	0.06	0.01	0.0	0.06	0.0	0.0	0.02	0.0	0.42	0.01	0.0
A4c-45	0.0	3.16	0.0	0.0	0.32	0.24	2.01	0.0	0.0	0.79	0.08	0.06	0.01	0.0	0.06	0.0	0.0	0.02	0.0	0.42	0.01	0.0
A4C-44	0.0	3.16	0.0	0.0	0.32	0.24	2.01	0.0	0.0	0.79	0.08	0.06	0.01	0.0	0.06	0.0	0.0	0.02	0.0	0.42	0.01	0.0
A4c-43 mean	0.0	3.16	0.0	0.0	0.32	0.24	2.01	0.0	0.0	0.79	0.08	0.06	0.01	0.0	0.06	0.0	0.0	0.02	0.0	0.42	0.01	0.0
A4C-42	0.0	3.16	0.0	0.0	0.32	0.24	2.01	0.0	0.0	0.79	0.08	0.06	0.01	0.0	0.06	0.0	0.0	0.02	0.0	0.42	0.01	0.0
A4C-40	0.0	3.16	0.0	0.0	0.32	0.24	2.01	0.0	0.0	0.79	0.08	0.06	0.01	0.0	0.06	0.0	0.0	0.02	0.0	0.42	0.01	0.0
A4c-39	0.0	3.16	0.0	0.0	0.32	0.24	2.01	0.0	0.0	0.79	0.08	0.06	0.01	0.0	0.06	0.0	0.0	0.02	0.0	0.42	0.01	0.0
A4C-38	0.0	3.16	0.0	0.0	0.32	0.24	2.01	0.0	0.0	0.79	0.08	0.06	0.01	0.0	0.06	0.0	0.0	0.02	0.0	0.42	0.01	0.0
A4C-37	0.0	3.16	0.0	0.0	0.32	0.24	2.01	0.0	0.0	0.79	0.08	0.06	0.01	0.0	0.06	0.0	0.0	0.02	0.0	0.42	0.01	0.0
A4C-36	0.0	3.16	0.0	0.0	0.32	0.24	2.01	0.0	0.0	0.79	0.08	0.06	0.01	0.0	0.06	0.0	0.0	0.02	0.0	0.42	0.01	0.0
A4c-35 mean	0.0	3.16	0.0	0.0	0.32	0.24	2.01	0.0	0.0	0.79	0.08	0.06	0.01	0.0	0.06	0.0	0.0	0.02	0.0	0.42	0.01	0.0
A4c-34	0.0	3.16	0.0	0.0	0.32	0.24	2.01	0.0	0.0	0.79	0.08	0.06	0.01	0.0	0.06	0.0	0.0	0.02	0.0	0.42	0.01	0.0
A4C-32	0.0	3.16	0.0	0.0	0.32	0.24	2.01	0.0	0.0	0.79	0.08	0.06	0.01	0.0	0.06	0.0	0.0	0.02	0.0	0.42	0.01	0.0
A4c-31	0.0	3.16	0.0	0.0	0.32	0.24	2.01	0.0	0.0	0.79	0.08	0.06	0.01	0.0	0.06	0.0	0.0	0.02	0.0	0.42	0.01	0.0
A4C-30	0.0	3.16	0.0	0.0	0.32	0.24	2.01	0.0	0.0	0.79	0.08	0.06	0.01	0.0	0.06	0.0	0.0	0.02	0.0	0.42	0.01	0.0
A4C-29	0.0	3.16	0.0	0.0	0.32	0.24	2.01	0.0	0.0	0.79	0.08	0.06	0.01	0.0	0.06	0.0	0.0	0.02	0.0	0.42	0.01	0.0
A4C-28	0.0	3.16	0.0	0.0	0.32	0.24	2.01	0.0	0.0	0.79	0.08	0.06	0.01	0.0	0.06	0.0	0.0	0.02	0.0	0.42	0.01	0.0
A4c-27	0.0	3.16	0.0	0.0	0.32	0.24	2.01	0.0	0.0	0.79	0.08	0.06	0.01	0.0	0.06	0.0	0.0	0.02	0.0	0.42	0.01	0.0
A4C-26	0.0	3.16	0.0	0.0	0.32	0.24	2.01	0.0	0.0	0.79	0.08	0.06	0.01	0.0	0.06	0.0	0.0	0.02	0.0	0.42	0.01	0.0
A4C-25	0.0	3.16	0.0	0.0	0.32	0.24	2.01	0.0	0.0	0.79	0.08	0.06	0.01	0.0	0.06	0.0	0.0	0.02	0.0	0.42	0.01	0.0
A4C-24	0.0	3.16	0.0	0.0	0.32	0.24	2.01	0.0	0.0	0.79	0.08	0.06	0.01	0.0	0.06	0.0	0.0	0.02	0.0	0.42	0.01	0.0
A4c-23	0.0	3.16	0.0	0.0	0.32	0.24	2.01	0.0	0.0	0.79	0.08	0.06	0.01	0.0	0.06	0.0	0.0	0.02	0.0	0.42	0.01	0.0
A4C-22	0.0	3.16	0.0	0.0	0.32	0.24	2.01	0.0	0.0	0.79	0.08	0.06	0.01	0.0	0.06	0.0	0.0	0.02	0.0	0.42	0.01	0.0
A4C-21	0.0	3.16	0.0	0.0	0.32	0.24	2.01	0.0	0.0	0.79	0.08	0.06	0.01	0.0	0.06	0.0	0.0	0.02	0.0	0.42	0.01	0.0
A4C-20	0.0	3.16	0.0	0.0	0.32	0.24	2.01	0.0	0.0	0.79	0.08	0.06	0.01	0.0	0.06	0.0	0.0	0.02	0.0	0.42	0.01	0.0
A4c-19	0.0	3.16	0.0	0.0	0.32	0.24	2.01	0.0	0.0	0.79	0.08	0.06	0.01	0.0	0.06	0.0	0.0	0.02	0.0	0.42	0.01	0.0
A4C-18	0.0	3.16	0.0	0.0	0.32	0.24	2.01	0.0	0.0	0.79	0.08	0.06	0.01	0.0	0.06	0.0	0.0	0.02	0.0	0.42	0.01	0.0
A4c-17	0.0	3.16	0.0	0.0	0.32	0.24	2.01	0.0	0.0	0.79	0.08	0.06	0.01	0.0	0.06	0.0	0.0	0.02	0.0	0.42	0.01	0.0
A4C-16	0.0	3.16	0.0	0.0	0.32	0.24	2.01	0.0	0.0	0.79	0.08	0.06	0.01	0.0	0.06	0.0	0.0	0.02	0.0	0.42	0.01	0.0
A4c-15	0.0	3.16	0.0	0.0	0.32	0.24	2.01	0.0	0.0	0.79	0.08	0.06	0.01	0.0	0.06	0.0	0.0	0.02	0.0	0.42	0.01	0.0
A4C-14	0.0	3.16	0.0	0.0	0.32	0.24	2.01	0.0	0.0	0.79	0.08	0.06	0.01	0.0	0.06	0.0	0.0	0.02	0.0	0.42	0.01	0.0
A4c-13	0.0	3.16	0.0	0.0	0.32	0.24	2.01	0.0	0.0	0.79	0.08	0.06	0.01	0.0	0.06	0.0	0.0	0.02	0.0	0.42	0.01	0.0
A4C-12	0.0	3.16	0.0	0.0	0.32	0.24	2.01	0.0	0.0	0.79	0.08	0.06	0.01	0.0	0.06	0.0	0.0	0.02	0.0	0.42	0.01	0.0
A4c-11 mean	0.0	3.16	0.0	0.0	0.32	0.24	2.01	0.0	0.0	0.79	0.08	0.06	0.01	0.0	0.06	0.0	0.0	0.02	0.0	0.42	0.01	0.0
A4C-10 mean	0.0	3.16	0.0	0.0	0.32	0.24	2.01	0.0	0.0	0.79	0.08	0.06	0.01	0.0	0.06	0.0	0.0	0.02	0.0	0.42	0.01	0.0
A4c-9	0.0	3.16	0.0	0.0	0.32	0.24	2.01	0.0	0.0	0.79	0.08	0.06	0.01	0.0	0.06	0.0	0.0	0.02	0.0	0.42	0.01	0.0
A4C-8	0.0	3.16	0.0	0.0	0.32	0.24	2.01	0.0	0.0	0.79	0.08	0.06	0.01	0.0	0.06	0.0	0.0	0.02	0.0	0.42	0.01	0.0
A4c-7	0.0	3.16	0.0	0.0	0.32	0.24	2.01	0.0	0.0	0.79	0.08	0.06	0.01	0.0	0.06	0.0	0.0	0.02	0.0	0.42	0.01	0.0
A4C-6	0.0	3.16	0.0	0.0	0.32	0.24	2.01	0.0	0.0	0.79	0.08	0.06	0.01	0.0	0.06	0.0	0.0	0.02	0.0	0.42	0.01	0.0
A4c-5	0.0	3.16	0.0	0.0	0.32	0.24	2.01	0.0	0.0	0.79	0.08	0.06	0.01	0.0	0.06	0.0	0.0	0.02	0.0	0.42	0.01	0.0
A4C-4	0.0	3.16	0.0	0.0	0.32	0.24	2.01	0.0	0.0	0.79	0.08	0.06	0.01	0.0	0.06	0.0	0.0	0.02	0.0	0.42	0.01	0.0
A4c-3 mean	0.0	3.16	0.0	0.0	0.32	0.24	2.01	0.0	0.0	0.79	0.08	0.06	0.01	0.0	0.06	0.0	0.0	0.02	0.0	0.42	0.01	0.0
A4C-2	0.0	3.16	0.0	0.0	0.32	0.24	2.01	0.0	0.0	0.79	0.08	0.06	0.01	0.0	0.06	0.0	0.0	0.02	0.0	0.42	0.01	0.0
A4c-1	0.0	3.16	0.0	0.0	0.32	0.24	2.01	0.0	0.0	0.79	0.08	0.06	0.01	0.0	0.06	0.0	0.0	0.02	0.0	0.42	0.01	0.0

23	24	25	26	27	28	29	30	31	32	33	34	35	36	37	38	39	40	41	42	43	44	45
Nb	Nd	Ni	Pb	Pr	Rb	Sb	Sm	Sn	Sr	Ta	Tb	Th	Tm	U	V	W	Y	Yb	Zn	Zr	SiO2 (Si)	Al2O3 (Al)
ppm	ppm	ppm	ppm	ppm	ppm	ppm	ppm	ppm	ppm	ppm	ppm	ppm	ppm	ppm	ppm	ppm	ppm	ppm	ppm	ppm	%	%
0.0	0.25	20.66	36.86	0.06	0.39	0.0	0.05	0.0	131.79	0.0	0.01	0.0	0.01	0.16	0.08	0.0	1.2	0.06	2.69	0.0	0.0	0.01

46	47	48	49	50	51	52	53	54	55	56	57	58	59	60	61	62	63	64	65	66
Fe2O3 (Fe)	MnO (Mn)	MgO (Mg)	CaO (Ca)	Na2O(Na)	K2O(K)	TiO2(Ti)	P2O5(P)	B	Li	H2Otot (H)	Stot (S)	CO2 tot (C)	O,rock	O,water	Cl nat AMS	Ca ICP	Z (position sur le scarp)	Thickness sample	[36Cl] AMS	uncertainty
%	%	%	%	%	%	%	%	ppm	ppm	%	%	%			ppm	ppm	cm	cm	at/g.rock	
																moy site moy replicat				
0.0	0.0	0.45	54.94	0.0	0.0	0.0	0.03	1.0	0.88	0.4	0.01	44.08	0.0	0.0	7.79	391559	5	3	377556	8981
0.0	0.0	0.45	54.94	0.0	0.0	0.0	0.03	1.0	0.88	0.4	0.01	44.08	0.0	0.0	7.55	395144	15	2.5	370170	512
0.0	0.0	0.45	54.94	0.0	0.0	0.0	0.03	1.0	0.88	0.4	0.01	44.08	0.0	0.0	7.14	391267	25	2.5	359016	6589
0.0	0.0	0.45	54.94	0.0	0.0	0.0	0.03	1.0	0.88	0.4	0.01	44.08	0.0	0.0	6.49	395144	35	3	363426	6419
0.0	0.0	0.45	54.94	0.0	0.0	0.0	0.03	1.0	0.88	0.4	0.01	44.08	0.0	0.0	4.59	401105	45	2	380303	6286
0.0	0.0	0.45	54.94	0.0	0.0	0.0	0.03	1.0	0.88	0.4	0.01	44.08	0.0	0.0	6.12	395144	55	2	384483	8773
0.0	0.0	0.45	54.94	0.0	0.0	0.0	0.03	1.0	0.88	0.4	0.01	44.08	0.0	0.0	4.88	382551	65	2	397151	7485
0.0	0.0	0.45	54.94	0.0	0.0	0.0	0.03	1.0	0.88	0.4	0.01	44.08	0.0	0.0	3.76	395144	75	1.5	385888	11305
0.0	0.0	0.45	54.94	0.0	0.0	0.0	0.03	1.0	0.88	0.4	0.01	44.08	0.0	0.0	2.78	393423	85	2	390038	6917
0.0	0.0	0.45	54.94	0.0	0.0	0.0	0.03	1.0	0.88	0.4	0.01	44.08	0.0	0.0	3.61	395144	95	3	401879	7101
0.0	0.0	0.45	54.94	0.0	0.0	0.0	0.03	1.0	0.88	0.4	0.01	44.08	0.0	0.0	3.31	397547	105	1.5	417004	9694
0.0	0.0	0.45	54.94	0.0	0.0	0.0	0.03	1.0	0.88	0.4	0.01	44.08	0.0	0.0	3.96	395144	115	2	396288	8296
0.0	0.0	0.45	54.94	0.0	0.0	0.0	0.03	1.0	0.88	0.4	0.01	44.08	0.0	0.0	3.41	408927	125	1.5	407615	13206
0.0	0.0	0.45	54.94	0.0	0.0	0.0	0.03	1.0	0.88	0.4	0.01	44.08	0.0	0.0	3.75	386201	145	2	422901	7757
0.0	0.0	0.45	54.94	0.0	0.0	0.0	0.03	1.0	0.88	0.4	0.01	44.08	0.0	0.0	4.74	395144	155	2.5	427983	9074
0.0	0.0	0.45	54.94	0.0	0.0	0.0	0.03	1.0	0.88	0.4	0.01	44.08	0.0	0.0	4.07	394891	164	2	424316	7783
0.0	0.0	0.45	54.94	0.0	0.0	0.0	0.03	1.0	0.88	0.4	0.01	44.08	0.0	0.0	5.53	395144	174	1	438786	8041
0.0	0.0	0.45	54.94	0.0	0.0	0.0	0.03	1.0	0.88	0.4	0.01	44.08	0.0	0.0	6.04	397985	184	1.5	472253	8895
0.0	0.0	0.45	54.94	0.0	0.0	0.0	0.03	1.0	0.88	0.4	0.01	44.08	0.0	0.0	11.86	395144	192	3	512394	18027
0.0	0.0	0.45	54.94	0.0	0.0	0.0	0.03	1.0	0.88	0.4	0.01	44.08	0.0	0.0	12.18	392703	199	3	536860	9643
0.0	0.0	0.45	54.94	0.0	0.0	0.0	0.03	1.0	0.88	0.4	0.01	44.08	0.0	0.0	12.88	398477	209	3.5	529542	11952
0.0	0.0	0.45	54.94	0.0	0.0	0.0	0.03	1.0	0.88	0.4	0.01	44.08	0.0	0.0	8.71	391866	220	3	541076	12872
0.0	0.0	0.45	54.94	0.0	0.0	0.0	0.03	1.0	0.88	0.4	0.01	44.08	0.0	0.0	6.38	393435	241	3	535670	12707
0.0	0.0	0.45	54.94	0.0	0.0	0.0	0.03	1.0	0.88	0.4	0.01	44.08	0.0	0.0	4.68	395144	250	2	532039	9750
0.0	0.0	0.45	54.94	0.0	0.0	0.0	0.03	1.0	0.88	0.4	0.01	44.08	0.0	0.0	4.48	395901	260	2	536074	14736
0.0	0.0	0.45	54.94	0.0	0.0	0.0	0.03	1.0	0.88	0.4	0.01	44.08	0.0	0.0	5.87	401379	270	2	558724	9996
0.0	0.0	0.45	54.94	0.0	0.0	0.0	0.03	1.0	0.88	0.4	0.01	44.08	0.0	0.0	5.73	396594	295	3	604588	14867
0.0	0.0	0.45	54.94	0.0	0.0	0.0	0.03	1.0	0.88	0.4	0.01	44.08	0.0	0.0	5.35	395182	305	2.5	608367	6339
0.0	0.0	0.45	54.94	0.0	0.0	0.0	0.03	1.0	0.88	0.4	0.01	44.08	0.0	0.0	6.39	395144	315	2	617007	11053
0.0	0.0	0.45	54.94	0.0	0.0	0.0	0.03	1.0	0.88	0.4	0.01	44.08	0.0	0.0	5.74	403542	334	3	640950	19535
0.0	0.0	0.45	54.94	0.0	0.0	0.0	0.03	1.0	0.88	0.4	0.01	44.08	0.0	0.0	6.39	395144	345	2	655642	12008
0.0	0.0	0.45	54.94	0.0	0.0	0.0	0.03	1.0	0.88	0.4	0.01	44.08	0.0	0.0	7.76	395298	355	2.5	663495	18542
0.0	0.0	0.45	54.94	0.0	0.0	0.0	0.03	1.0	0.88	0.4	0.01	44.08	0.0	0.0	8.18	402284	364	3	677348	13888
0.0	0.0	0.45	54.94	0.0	0.0	0.0	0.03	1.0	0.88	0.4	0.01	44.08	0.0	0.0	6.18	393873	375	2	656380	16174
0.0	0.0	0.45	54.94	0.0	0.0	0.0	0.03	1.0	0.88	0.4	0.01	44.08	0.0	0.0	5.46	395144	385	2	706197	18673
0.0	0.0	0.45	54.94	0.0	0.0	0.0	0.03	1.0	0.88	0.4	0.01	44.08	0.0	0.0	4.99	397585	395	2	715888	17635
0.0	0.0	0.45	54.94	0.0	0.0	0.0	0.03	1.0	0.88	0.4	0.01	44.08	0.0	0.0	6.91	397243	405	2	722763	13060
0.0	0.0	0.45	54.94	0.0	0.0	0.0	0.03	1.0	0.88	0.4	0.01	44.08	0.0	0.0	6.56	400169	415	2.5	704679	30847
0.0	0.0	0.45	54.94	0.0	0.0	0.0	0.03	1.0	0.88	0.4	0.01	44.08	0.0	0.0	6.75	395144	425	2.5	750103	15060
0.0	0.0	0.45	54.94	0.0	0.0	0.0	0.03	1.0	0.88	0.4	0.01	44.08	0.0	0.0	7.81	393595	434	2	761491	18747
0.0	0.0	0.45	54.94	0.0	0.0	0.0	0.03	1.0	0.88	0.4	0.01	44.08	0.0	0.0	12.52	397193	487	2.5	818085	21137
0.0	0.0	0.45	54.94	0.0	0.0	0.0	0.03	1.0	0.88	0.4	0.01	44.08	0.0	0.0	13.35	397636	496	1.5	835546	20526
0.0	0.0	0.45	54.94	0.0	0.0	0.0	0.03	1.0	0.88	0.4	0.01	44.08	0.0	0.0	10.87	395144	506	1.5	847910	15669
0.0	0.0	0.45	54.94	0.0	0.0	0.0	0.03	1.0	0.88	0.4	0.01	44.08	0.0	0.0	6.92	386504	516	2	799197	19674
0.0	0.0	0.45	54.94	0.0	0.0	0.0	0.03	1.0	0.88	0.4	0.01	44.08	0.0	0.0	8.51	395144	526	2	869821	15509
0.0	0.0	0.45	54.94	0.0	0.0	0.0	0.03	1.0	0.88	0.4	0.01	44.08	0.0	0.0	8.66	393976	536	3	831017	13686
0.0	0.0	0.45	54.94	0.0	0.0	0.0	0.03	1.0	0.88	0.4	0.01	44.08	0.0	0.0	8.75	395144	546	2.5	871769	15527
0.0	0.0	0.45	54.94	0.0	0.0	0.0	0.03	1.0	0.88	0.4	0.01	44.08	0.0	0.0	11.64	399993	556	2.5	891727	14788
0.0	0.0	0.45	54.94	0.0	0.0	0.0	0.03	1.0	0.88	0.4	0.01	44.08	0.0	0.0	10.69	395144	566	1.5	904663	16158
0.0	0.0	0.45	54.94	0.0	0.0	0.0	0.03	1.0	0.88	0.4	0.01	44.08	0.0	0.0	8.01	390977	576	2.5	895470	26214
0.0	0.0	0.45	54.94	0.0	0.0	0.0	0.03	1.0	0.88	0.4	0.01	44.08	0.0	0.0	8.7	393916	586	3	927772	5101
0.0	0.0	0.45	54.94	0.0	0.0	0.0	0.03	1.0	0.88	0.4	0.01	44.08	0.0	0.0	8.93	392005	596	3	932388	6306
0.0	0.0	0.45	54.94	0.0	0.0	0.0	0.03	1.0	0.88	0.4	0.01	44.08	0.0	0.0	8.47	395144	607	3	931947	16617
0.0	0.0	0.45	54.94	0.0	0.0	0.0	0.03	1.0	0.88	0.4	0.01	44.08	0.0	0.0	8.25	397971	617	3	953068	15201
0.0	0.0	0.45	54.94	0.0	0.0	0.0	0.03	1.0	0.88	0.4	0.01	44.08	0.0	0.0	10.07	395144	627	3	970769	29468
0.0	0.0	0.45	54.94	0.0	0.0	0.0	0.03	1.0	0.88	0.4	0.01	44.08	0.0	0.0	10	396990	637	2.5	996097	12524
0.0	0.0	0.45	54.94	0.0	0.0	0.0	0.03	1.0	0.88	0.4	0.01	44.08	0.0	0.0	9.12	395144	647	1.5	979695	17741
0.0	0.0	0.45	54.94	0.0	0.0	0.0	0.03	1.0	0.88	0.4	0.01	44.08	0.0	0.0	8.16	391629	670	3	1006405	14351
0.0	0.0	0.45	54.94	0.0	0.0	0.0	0.03	1.0	0.88	0.4	0.01	44.08	0.0	0.0	8.56	395144	677	2.5	993532	14522
0.0	0.0	0.45	54.94	0.0	0.0	0.0	0.03	1.0	0.88	0.4	0.01	44.08	0.0	0.0	6.79	393071	687	2	1025517	14587
0.0	0.0	0.45	54.94	0.0	0.0	0.0	0.03	1.0	0.88	0.4	0.01	44.08	0.0	0.0	5.3	395144	697	2	991354	20063

	1	2	3	4	5	6	7	8	9	10	11	12	13	14	15	16	17	18	19	20	21	22
SITE TR	As	Ba	Be	Bi	Cd	Ce	Co	Cr	Cs	Cu	Dy	Er	Eu	Ga	Gd	Ge	Hf	Ho	In	La	Lu	Mo
om échantillo	ppm	ppm	ppm	ppm	ppm	ppm	ppm	ppm	ppm	ppm	ppm	ppm	ppm	ppm	ppm	ppm	ppm	ppm	ppm	ppm	ppm	ppm
TR-45	0.0	4.27	0.0	0.0	0.14	0.25	1.33	0.0	0.0	1.97	0.02	0.01	0.0	0.0	0.0	0.0	0.0	0.0	0.0	0.16	0.0	0.0
TR-44	0.0	4.27	0.0	0.0	0.14	0.25	1.33	0.0	0.0	1.97	0.02	0.01	0.0	0.0	0.0	0.0	0.0	0.0	0.0	0.16	0.0	0.0
TR-43	0.0	4.27	0.0	0.0	0.14	0.25	1.33	0.0	0.0	1.97	0.02	0.01	0.0	0.0	0.0	0.0	0.0	0.0	0.0	0.16	0.0	0.0
TR-42	0.0	4.27	0.0	0.0	0.14	0.25	1.33	0.0	0.0	1.97	0.02	0.01	0.0	0.0	0.0	0.0	0.0	0.0	0.0	0.16	0.0	0.0
TR-41	0.0	4.27	0.0	0.0	0.14	0.25	1.33	0.0	0.0	1.97	0.02	0.01	0.0	0.0	0.0	0.0	0.0	0.0	0.0	0.16	0.0	0.0
TR-40	0.0	4.27	0.0	0.0	0.14	0.25	1.33	0.0	0.0	1.97	0.02	0.01	0.0	0.0	0.0	0.0	0.0	0.0	0.0	0.16	0.0	0.0
TR-39	0.0	4.27	0.0	0.0	0.14	0.25	1.33	0.0	0.0	1.97	0.02	0.01	0.0	0.0	0.0	0.0	0.0	0.0	0.0	0.16	0.0	0.0
TR-38	0.0	4.27	0.0	0.0	0.14	0.25	1.33	0.0	0.0	1.97	0.02	0.01	0.0	0.0	0.0	0.0	0.0	0.0	0.0	0.16	0.0	0.0
TR-37	0.0	4.27	0.0	0.0	0.14	0.25	1.33	0.0	0.0	1.97	0.02	0.01	0.0	0.0	0.0	0.0	0.0	0.0	0.0	0.16	0.0	0.0
TR-36	0.0	4.27	0.0	0.0	0.14	0.25	1.33	0.0	0.0	1.97	0.02	0.01	0.0	0.0	0.0	0.0	0.0	0.0	0.0	0.16	0.0	0.0
TR-35	0.0	4.27	0.0	0.0	0.14	0.25	1.33	0.0	0.0	1.97	0.02	0.01	0.0	0.0	0.0	0.0	0.0	0.0	0.0	0.16	0.0	0.0
TR-34	0.0	4.27	0.0	0.0	0.14	0.25	1.33	0.0	0.0	1.97	0.02	0.01	0.0	0.0	0.0	0.0	0.0	0.0	0.0	0.16	0.0	0.0
TR-33	0.0	4.27	0.0	0.0	0.14	0.25	1.33	0.0	0.0	1.97	0.02	0.01	0.0	0.0	0.0	0.0	0.0	0.0	0.0	0.16	0.0	0.0
TR-32	0.0	4.27	0.0	0.0	0.14	0.25	1.33	0.0	0.0	1.97	0.02	0.01	0.0	0.0	0.0	0.0	0.0	0.0	0.0	0.16	0.0	0.0
TR-31	0.0	4.27	0.0	0.0	0.14	0.25	1.33	0.0	0.0	1.97	0.02	0.01	0.0	0.0	0.0	0.0	0.0	0.0	0.0	0.16	0.0	0.0
TR-30	0.0	4.27	0.0	0.0	0.14	0.25	1.33	0.0	0.0	1.97	0.02	0.01	0.0	0.0	0.0	0.0	0.0	0.0	0.0	0.16	0.0	0.0
TR-29	0.0	4.27	0.0	0.0	0.14	0.25	1.33	0.0	0.0	1.97	0.02	0.01	0.0	0.0	0.0	0.0	0.0	0.0	0.0	0.16	0.0	0.0
TR-28	0.0	4.27	0.0	0.0	0.14	0.25	1.33	0.0	0.0	1.97	0.02	0.01	0.0	0.0	0.0	0.0	0.0	0.0	0.0	0.16	0.0	0.0
TR-27	0.0	4.27	0.0	0.0	0.14	0.25	1.33	0.0	0.0	1.97	0.02	0.01	0.0	0.0	0.0	0.0	0.0	0.0	0.0	0.16	0.0	0.0
TR-26	0.0	4.27	0.0	0.0	0.14	0.25	1.33	0.0	0.0	1.97	0.02	0.01	0.0	0.0	0.0	0.0	0.0	0.0	0.0	0.16	0.0	0.0
TR-25	0.0	4.27	0.0	0.0	0.14	0.25	1.33	0.0	0.0	1.97	0.02	0.01	0.0	0.0	0.0	0.0	0.0	0.0	0.0	0.16	0.0	0.0
TR-24	0.0	4.27	0.0	0.0	0.14	0.25	1.33	0.0	0.0	1.97	0.02	0.01	0.0	0.0	0.0	0.0	0.0	0.0	0.0	0.16	0.0	0.0
TR-23	0.0	4.27	0.0	0.0	0.14	0.25	1.33	0.0	0.0	1.97	0.02	0.01	0.0	0.0	0.0	0.0	0.0	0.0	0.0	0.16	0.0	0.0
TR-22	0.0	4.27	0.0	0.0	0.14	0.25	1.33	0.0	0.0	1.97	0.02	0.01	0.0	0.0	0.0	0.0	0.0	0.0	0.0	0.16	0.0	0.0
TR-21	0.0	4.27	0.0	0.0	0.14	0.25	1.33	0.0	0.0	1.97	0.02	0.01	0.0	0.0	0.0	0.0	0.0	0.0	0.0	0.16	0.0	0.0
TR-20	0.0	4.27	0.0	0.0	0.14	0.25	1.33	0.0	0.0	1.97	0.02	0.01	0.0	0.0	0.0	0.0	0.0	0.0	0.0	0.16	0.0	0.0
TR-19	0.0	4.27	0.0	0.0	0.14	0.25	1.33	0.0	0.0	1.97	0.02	0.01	0.0	0.0	0.0	0.0	0.0	0.0	0.0	0.16	0.0	0.0
TR-18	0.0	4.27	0.0	0.0	0.14	0.25	1.33	0.0	0.0	1.97	0.02	0.01	0.0	0.0	0.0	0.0	0.0	0.0	0.0	0.16	0.0	0.0
TR-17	0.0	4.27	0.0	0.0	0.14	0.25	1.33	0.0	0.0	1.97	0.02	0.01	0.0	0.0	0.0	0.0	0.0	0.0	0.0	0.16	0.0	0.0
TR-16	0.0	4.27	0.0	0.0	0.14	0.25	1.33	0.0	0.0	1.97	0.02	0.01	0.0	0.0	0.0	0.0	0.0	0.0	0.0	0.16	0.0	0.0
TR-15	0.0	4.27	0.0	0.0	0.14	0.25	1.33	0.0	0.0	1.97	0.02	0.01	0.0	0.0	0.0	0.0	0.0	0.0	0.0	0.16	0.0	0.0
TR-14	0.0	4.27	0.0	0.0	0.14	0.25	1.33	0.0	0.0	1.97	0.02	0.01	0.0	0.0	0.0	0.0	0.0	0.0	0.0	0.16	0.0	0.0
TR-13	0.0	4.27	0.0	0.0	0.14	0.25	1.33	0.0	0.0	1.97	0.02	0.01	0.0	0.0	0.0	0.0	0.0	0.0	0.0	0.16	0.0	0.0
TR-12	0.0	4.27	0.0	0.0	0.14	0.25	1.33	0.0	0.0	1.97	0.02	0.01	0.0	0.0	0.0	0.0	0.0	0.0	0.0	0.16	0.0	0.0
TR-11	0.0	4.27	0.0	0.0	0.14	0.25	1.33	0.0	0.0	1.97	0.02	0.01	0.0	0.0	0.0	0.0	0.0	0.0	0.0	0.16	0.0	0.0
TR-10	0.0	4.27	0.0	0.0	0.14	0.25	1.33	0.0	0.0	1.97	0.02	0.01	0.0	0.0	0.0	0.0	0.0	0.0	0.0	0.16	0.0	0.0
TR-9	0.0	4.27	0.0	0.0	0.14	0.25	1.33	0.0	0.0	1.97	0.02	0.01	0.0	0.0	0.0	0.0	0.0	0.0	0.0	0.16	0.0	0.0
TR-8	0.0	4.27	0.0	0.0	0.14	0.25	1.33	0.0	0.0	1.97	0.02	0.01	0.0	0.0	0.0	0.0	0.0	0.0	0.0	0.16	0.0	0.0
TR-7	0.0	4.27	0.0	0.0	0.14	0.25	1.33	0.0	0.0	1.97	0.02	0.01	0.0	0.0	0.0	0.0	0.0	0.0	0.0	0.16	0.0	0.0
TR-6 (S high)	0.0	4.27	0.0	0.0	0.14	0.25	1.33	0.0	0.0	1.97	0.02	0.01	0.0	0.0	0.0	0.0	0.0	0.0	0.0	0.16	0.0	0.0
TR-5	0.0	4.27	0.0	0.0	0.14	0.25	1.33	0.0	0.0	1.97	0.02	0.01	0.0	0.0	0.0	0.0	0.0	0.0	0.0	0.16	0.0	0.0
TR-4	0.0	4.27	0.0	0.0	0.14	0.25	1.33	0.0	0.0	1.97	0.02	0.01	0.0	0.0	0.0	0.0	0.0	0.0	0.0	0.16	0.0	0.0
TR-3	0.0	4.27	0.0	0.0	0.14	0.25	1.33	0.0	0.0	1.97	0.02	0.01	0.0	0.0	0.0	0.0	0.0	0.0	0.0	0.16	0.0	0.0
TR-2	0.0	4.27	0.0	0.0	0.14	0.25	1.33	0.0	0.0	1.97	0.02	0.01	0.0	0.0	0.0	0.0	0.0	0.0	0.0	0.16	0.0	0.0
TR-1	0.0	4.27	0.0	0.0	0.14	0.25	1.33	0.0	0.0	1.97	0.02	0.01	0.0	0.0	0.0	0.0	0.0	0.0	0.0	0.16	0.0	0.0
TR-TOP	0.0	2.74	0.0	0.0	0.38	0.11	1.14	0.0	0.0	0.0	0.02	0.01	0.0	0.0	0.0	0.0	0.0	0.0	0.0	0.12	0.0	0.0

23	24	25	26	27	28	29	30	31	32	33	34	35	36	37	38	39	40	41	42	43	44	45
Nb	Nd	Ni	Pb	Pr	Rb	Sb	Sm	Sn	Sr	Ta	Tb	Th	Tm	U	V	W	Y	Yb	Zn	Zr	SiO2 (Si)	Al2O3 (Al)
ppm	ppm	ppm	ppm	ppm	ppm	ppm	ppm	ppm	ppm	ppm	ppm	ppm	ppm	ppm	ppm	ppm	ppm	ppm	ppm	ppm	%	%
0.0	0.11	11.38	0.21	0.03	0.73	0.0	0.02	0.0	86.84	0.0		0 0.03	0.0	0.21	0.0	0.0	0.0	0.01	6.87	0.0	0.0	0.03

46	47	48	49	50	51	52	53	54	55	56	57	58	59	60	61	62	63	64	65	66
Fe2O3 (Fe)	MnO (Mn)	MgO (Mg)	CaO (Ca)	Na2O(Na)	K2O(K)	TiO2(Ti)	P2O5(P)	B	Li	H2Otot (H)	Stot (S)	CO2 tot (C)	O,rock	O,water	Cl nat AMS	Ca ICP	Z (position sur le scarp)	Thickness sample	[36Cl] AMS	uncertainty
%	%	%	%	%	%	%	%	ppm	ppm	%	%	%			ppm	ppm	cm	cm	at/g.rock	
																moyenne repliquas				
0.0	0.0	0.32	54.9	0.0	0.0	0.0	0.02	2	0.95	0.28	0.01	44.04	0.0	0.0	7.34	366827	5	3.7	358904	9421
0.0	0.0	0.32	54.9	0.0	0.0	0.0	0.02	2	0.95	0.28	0.01	44.04	0.0	0.0	6.69	368709	15	4	359660	6486
0.0	0.0	0.32	54.9	0.0	0.0	0.0	0.02	2	0.95	0.28	0.01	44.04	0.0	0.0	6.38	368804	25	4	384624	6826
0.0	0.0	0.32	54.9	0.0	0.0	0.0	0.02	2	0.95	0.28	0.01	44.04	0.0	0.0	7.3	369164	35	4	395363	6983
0.0	0.0	0.32	54.9	0.0	0.0	0.0	0.02	2	0.95	0.28	0.01	44.04	0.0	0.0	8.35	355697	45	3.7	383815	6830
0.0	0.0	0.32	54.9	0.0	0.0	0.0	0.02	2	0.95	0.28	0.01	44.04	0.0	0.0	8.97	378671	55	3.8	404423	6918
0.0	0.0	0.32	54.9	0.0	0.0	0.0	0.02	2	0.95	0.28	0.01	44.04	0.0	0.0	12.34	370947	65	3.5	425856	10564
0.0	0.0	0.32	54.9	0.0	0.0	0.0	0.02	2	0.95	0.28	0.01	44.04	0.0	0.0	8.62	374437	75	3.8	415273	7916
0.0	0.0	0.32	54.9	0.0	0.0	0.0	0.02	2	0.95	0.28	0.01	44.04	0.0	0.0	13.1	376177	85	3.7	425446	7627
0.0	0.0	0.32	54.9	0.0	0.0	0.0	0.02	2	0.95	0.28	0.01	44.04	0.0	0.0	18.34	377229	95	3.5	445904	7876
0.0	0.0	0.32	54.9	0.0	0.0	0.0	0.02	2	0.95	0.28	0.01	44.04	0.0	0.0	12.61	372731	105	3.5	454223	8059
0.0	0.0	0.32	54.9	0.0	0.0	0.0	0.02	2	0.95	0.28	0.01	44.04	0.0	0.0	8.85	365761	115	3	454195	8680
0.0	0.0	0.32	54.9	0.0	0.0	0.0	0.02	2	0.95	0.28	0.01	44.04	0.0	0.0	9.33	366696	125	3.7	458355	8142
0.0	0.0	0.32	54.9	0.0	0.0	0.0	0.02	2	0.95	0.28	0.01	44.04	0.0	0.0	11.64	363044	135	3.6	478934	8520
0.0	0.0	0.32	54.9	0.0	0.0	0.0	0.02	2	0.95	0.28	0.01	44.04	0.0	0.0	11.85	367403	145	3	498988	8857
0.0	0.0	0.32	54.9	0.0	0.0	0.0	0.02	2	0.95	0.28	0.01	44.04	0.0	0.0	8.28	375245	155	3.8	487742	8700
0.0	0.0	0.32	54.9	0.0	0.0	0.0	0.02	2	0.95	0.28	0.01	44.04	0.0	0.0	6.93	389294	165	3.5	520171	9232
0.0	0.0	0.32	54.9	0.0	0.0	0.0	0.02	2	0.95	0.28	0.01	44.04	0.0	0.0	5.21	394957	175	3.7	526211	9520
0.0	0.0	0.32	54.9	0.0	0.0	0.0	0.02	2	0.95	0.28	0.01	44.04	0.0	0.0	4.62	378671	185	3.5	559072	10658
0.0	0.0	0.32	54.9	0.0	0.0	0.0	0.02	2	0.95	0.28	0.01	44.04	0.0	0.0	5.95	393980	195	3.5	573395	11578
0.0	0.0	0.32	54.9	0.0	0.0	0.0	0.02	2	0.95	0.28	0.01	44.04	0.0	0.0	8.13	396361	205	3.5	588921	11289
0.0	0.0	0.32	54.9	0.0	0.0	0.0	0.02	2	0.95	0.28	0.01	44.04	0.0	0.0	10.81	378671	215	3.7	609964	9975
0.0	0.0	0.32	54.9	0.0	0.0	0.0	0.02	2	0.95	0.28	0.01	44.04	0.0	0.0	11.65	393322	225	3.8	646315	12130
0.0	0.0	0.32	54.9	0.0	0.0	0.0	0.02	2	0.95	0.28	0.01	44.04	0.0	0.0	13.04	380938	235	3.5	648250	11616
0.0	0.0	0.32	54.9	0.0	0.0	0.0	0.02	2	0.95	0.28	0.01	44.04	0.0	0.0	12.26	387511	245	3.5	651526	12246
0.0	0.0	0.32	54.9	0.0	0.0	0.0	0.02	2	0.95	0.28	0.01	44.04	0.0	0.0	11.66	373097	255	3.5	666056	12292
0.0	0.0	0.32	54.9	0.0	0.0	0.0	0.02	2	0.95	0.28	0.01	44.04	0.0	0.0	14.32	371884	265	3.7	739234	13861
0.0	0.0	0.32	54.9	0.0	0.0	0.0	0.02	2	0.95	0.28	0.01	44.04	0.0	0.0	10.84	375630	275	3.5	748831	14432
0.0	0.0	0.32	54.9	0.0	0.0	0.0	0.02	2	0.95	0.28	0.01	44.04	0.0	0.0	10.54	380933	285	3.8	752217	21241
0.0	0.0	0.32	54.9	0.0	0.0	0.0	0.02	2	0.95	0.28	0.01	44.04	0.0	0.0	7.46	400878	295	3.8	757882	16895
0.0	0.0	0.32	54.9	0.0	0.0	0.0	0.02	2	0.95	0.28	0.01	44.04	0.0	0.0	8.7	379651	305	3.7	801066	15204
0.0	0.0	0.32	54.9	0.0	0.0	0.0	0.02	2	0.95	0.28	0.01	44.04	0.0	0.0	11.76	391492	315	3.8	762438	16859
0.0	0.0	0.32	54.9	0.0	0.0	0.0	0.02	2	0.95	0.28	0.01	44.04	0.0	0.0	10.83	392962	325	3.8	810591	14877
0.0	0.0	0.32	54.9	0.0	0.0	0.0	0.02	2	0.95	0.28	0.01	44.04	0.0	0.0	9.99	395543	335	3.7	807493	13207
0.0	0.0	0.32	54.9	0.0	0.0	0.0	0.02	2	0.95	0.28	0.01	44.04	0.0	0.0	10.25	383233	345	4	861818	15285
0.0	0.0	0.32	54.9	0.0	0.0	0.0	0.02	2	0.95	0.28	0.01	44.04	0.0	0.0	10.09	391954	355	3.5	890517	15736
0.0	0.0	0.32	54.9	0.0	0.0	0.0	0.02	2	0.95	0.28	0.01	44.04	0.0	0.0	10.72	388740	365	3.5	957382	17005
0.0	0.0	0.32	54.9	0.0	0.0	0.0	0.02	2	0.95	0.28	0.01	44.04	0.0	0.0	10.78	380121	375	3.9	984762	40877
0.0	0.0	0.32	54.9	0.0	0.0	0.0	0.02	2	0.95	0.28	0.01	44.04	0.0	0.0	11.14	381939	385	3.7	1027721	15872
0.0	0.0	0.32	54.9	0.0	0.0	0.0	0.02	2	0.95	0.28	0.01	44.04	0.0	0.0	11.54	389859	395	4	1051175	18583
0.0	0.0	0.32	54.9	0.0	0.0	0.0	0.02	2	0.95	0.28	0.01	44.04	0.0	0.0	11.35	383150	405	3.9	1089735	16699
0.0	0.0	0.32	54.9	0.0	0.0	0.0	0.02	2	0.95	0.28	0.01	44.04	0.0	0.0	12.69	385880	415	3.8	1154112	20354
0.0	0.0	0.32	54.9	0.0	0.0	0.0	0.02	2	0.95	0.28	0.01	44.04	0.0	0.0	11.32	378671	425	3.7	1187118	18263
0.0	0.0	0.32	54.9	0.0	0.0	0.0	0.02	2	0.95	0.28	0.01	44.04	0.0	0.0	12.5	378671	435	3.5	1301444	23047
0.0	0.0	0.32	54.9	0.0	0.0	0.0	0.02	2	0.95	0.28	0.01	44.04	0.0	0.0	12.69	381358	445	3.5	1341185	20463
0.0	0.0	0.46	55.87	0.0	0.0	0.0	0.0	2	1	0.22	0.01	44.62	0.0	0.0	9.74	347161	1300	2.5	1890698	33373

	1	2	3	4	5	6	7	8	9	10	11	12	13	14	15	16	17	18	19	20	21	22	23	24	25	26	27	28	29	30	31
SITE_RP2	**As**	**Ba**	**Be**	**Bi**	**Cd**	**Ce**	**Co**	**Cr**	**Cs**	**Cu**	**Dy**	**Er**	**Eu**	**Ga**	**Gd**	**Ge**	**Hf**	**Ho**	**In**	**La**	**Lu**	**Mo**	**Nb**	**Nd**	**Ni**	**Pb**	**Pr**	**Rb**	**Sb**	**Sm**	**Sn**
nom échantillon	**ppm**	**ppm**	**ppm**	**ppm**	**ppm**	**ppm**	**ppm**	**ppm**	**ppm**	**ppm**	**ppm**	**ppm**	**ppm**	**ppm**	**ppm**	**ppm**	**ppm**	**ppm**	**ppm**	**ppm**	**ppm**	**ppm**	**ppm**	**ppm**	**ppm**	**ppm**	**ppm**	**ppm**	**ppm**	**ppm**	**ppm**
	0.183	**3.887**	**0**	**0**	**0.203**	**0.516**	**1.132**	**0**	**0**	**2.089**	**0.129**	**0.088**	**0.027**	**0**	**0.12**	**0**	**0.002**	**0.03**	**0**	**1.257**	**0.013**	**0**	**0.01**	**0.616**	**8.094**	**0.618**	**0.15**	**0.426**	**0**	**0.111**	**0**
A1R-75	0.183	3.887	0	0	0.203	0.516	1.132	0	0	2.089	0.129	0.088	0.027	0	0.12	0	0.002	0.03	0	1.257	0.013	0	0.01	0.616	8.094	0.618	0.15	0.426	0	0.111	0
A1R-74	0.183	3.887	0	0	0.203	0.516	1.132	0	0	2.089	0.129	0.088	0.027	0	0.12	0	0.002	0.03	0	1.257	0.013	0	0.01	0.616	8.094	0.618	0.15	0.426	0	0.111	0
A1R-73	0.183	3.887	0	0	0.203	0.516	1.132	0	0	2.089	0.129	0.088	0.027	0	0.12	0	0.002	0.03	0	1.257	0.013	0	0.01	0.616	8.094	0.618	0.15	0.426	0	0.111	0
A1R-72	0.183	3.887	0	0	0.203	0.516	1.132	0	0	2.089	0.129	0.088	0.027	0	0.12	0	0.002	0.03	0	1.257	0.013	0	0.01	0.616	8.094	0.618	0.15	0.426	0	0.111	0
A1R-71n°2 =71	0.183	3.887	0	0	0.203	0.516	1.132	0	0	2.089	0.129	0.088	0.027	0	0.12	0	0.002	0.03	0	1.257	0.013	0	0.01	0.616	8.094	0.618	0.15	0.426	0	0.111	0
A1R-70	0.183	3.887	0	0	0.203	0.516	1.132	0	0	2.089	0.129	0.088	0.027	0	0.12	0	0.002	0.03	0	1.257	0.013	0	0.01	0.616	8.094	0.618	0.15	0.426	0	0.111	0
A1R-69	0.183	3.887	0	0	0.203	0.516	1.132	0	0	2.089	0.129	0.088	0.027	0	0.12	0	0.002	0.03	0	1.257	0.013	0	0.01	0.616	8.094	0.618	0.15	0.426	0	0.111	0
A1R-68	0.183	3.887	0	0	0.203	0.516	1.132	0	0	2.089	0.129	0.088	0.027	0	0.12	0	0.002	0.03	0	1.257	0.013	0	0.01	0.616	8.094	0.618	0.15	0.426	0	0.111	0
A1R-67	0.183	3.887	0	0	0.203	0.516	1.132	0	0	2.089	0.129	0.088	0.027	0	0.12	0	0.002	0.03	0	1.257	0.013	0	0.01	0.616	8.094	0.618	0.15	0.426	0	0.111	0
A1R-66	0.183	3.887	0	0	0.203	0.516	1.132	0	0	2.089	0.129	0.088	0.027	0	0.12	0	0.002	0.03	0	1.257	0.013	0	0.01	0.616	8.094	0.618	0.15	0.426	0	0.111	0
A1R-65	0.183	3.887	0	0	0.203	0.516	1.132	0	0	2.089	0.129	0.088	0.027	0	0.12	0	0.002	0.03	0	1.257	0.013	0	0.01	0.616	8.094	0.618	0.15	0.426	0	0.111	0
A1R-64	0.183	3.887	0	0	0.203	0.516	1.132	0	0	2.089	0.129	0.088	0.027	0	0.12	0	0.002	0.03	0	1.257	0.013	0	0.01	0.616	8.094	0.618	0.15	0.426	0	0.111	0
A1R-63	0.183	3.887	0	0	0.203	0.516	1.132	0	0	2.089	0.129	0.088	0.027	0	0.12	0	0.002	0.03	0	1.257	0.013	0	0.01	0.616	8.094	0.618	0.15	0.426	0	0.111	0
A1R-62	0.183	3.887	0	0	0.203	0.516	1.132	0	0	2.089	0.129	0.088	0.027	0	0.12	0	0.002	0.03	0	1.257	0.013	0	0.01	0.616	8.094	0.618	0.15	0.426	0	0.111	0
A1R-61	0.183	3.887	0	0	0.203	0.516	1.132	0	0	2.089	0.129	0.088	0.027	0	0.12	0	0.002	0.03	0	1.257	0.013	0	0.01	0.616	8.094	0.618	0.15	0.426	0	0.111	0
A1R-60	0.183	3.887	0	0	0.203	0.516	1.132	0	0	2.089	0.129	0.088	0.027	0	0.12	0	0.002	0.03	0	1.257	0.013	0	0.01	0.616	8.094	0.618	0.15	0.426	0	0.111	0
A1R-59	0.183	3.887	0	0	0.203	0.516	1.132	0	0	2.089	0.129	0.088	0.027	0	0.12	0	0.002	0.03	0	1.257	0.013	0	0.01	0.616	8.094	0.618	0.15	0.426	0	0.111	0
A1R-58	0.183	3.887	0	0	0.203	0.516	1.132	0	0	2.089	0.129	0.088	0.027	0	0.12	0	0.002	0.03	0	1.257	0.013	0	0.01	0.616	8.094	0.618	0.15	0.426	0	0.111	0
A1R-57	0.183	3.887	0	0	0.203	0.516	1.132	0	0	2.089	0.129	0.088	0.027	0	0.12	0	0.002	0.03	0	1.257	0.013	0	0.01	0.616	8.094	0.618	0.15	0.426	0	0.111	0
A1R-56	0.183	3.887	0	0	0.203	0.516	1.132	0	0	2.089	0.129	0.088	0.027	0	0.12	0	0.002	0.03	0	1.257	0.013	0	0.01	0.616	8.094	0.618	0.15	0.426	0	0.111	0
A1R-55	0.183	3.887	0	0	0.203	0.516	1.132	0	0	2.089	0.129	0.088	0.027	0	0.12	0	0.002	0.03	0	1.257	0.013	0	0.01	0.616	8.094	0.618	0.15	0.426	0	0.111	0
A1R-53	0.183	3.887	0	0	0.203	0.516	1.132	0	0	2.089	0.129	0.088	0.027	0	0.12	0	0.002	0.03	0	1.257	0.013	0	0.01	0.616	8.094	0.618	0.15	0.426	0	0.111	0
A1R-52	0.183	3.887	0	0	0.203	0.516	1.132	0	0	2.089	0.129	0.088	0.027	0	0.12	0	0.002	0.03	0	1.257	0.013	0	0.01	0.616	8.094	0.618	0.15	0.426	0	0.111	0
A1R-51	0.183	3.887	0	0	0.203	0.516	1.132	0	0	2.089	0.129	0.088	0.027	0	0.12	0	0.002	0.03	0	1.257	0.013	0	0.01	0.616	8.094	0.618	0.15	0.426	0	0.111	0
A1R-50	0.183	3.887	0	0	0.203	0.516	1.132	0	0	2.089	0.129	0.088	0.027	0	0.12	0	0.002	0.03	0	1.257	0.013	0	0.01	0.616	8.094	0.618	0.15	0.426	0	0.111	0
A1R-49	0.183	3.887	0	0	0.203	0.516	1.132	0	0	2.089	0.129	0.088	0.027	0	0.12	0	0.002	0.03	0	1.257	0.013	0	0.01	0.616	8.094	0.618	0.15	0.426	0	0.111	0
A1R-48	0.183	3.887	0	0	0.203	0.516	1.132	0	0	2.089	0.129	0.088	0.027	0	0.12	0	0.002	0.03	0	1.257	0.013	0	0.01	0.616	8.094	0.618	0.15	0.426	0	0.111	0
A1R-47mean	0.183	3.887	0	0	0.203	0.516	1.132	0	0	2.089	0.129	0.088	0.027	0	0.12	0	0.002	0.03	0	1.257	0.013	0	0.01	0.616	8.094	0.618	0.15	0.426	0	0.111	0
A1R-46	0.183	3.887	0	0	0.203	0.516	1.132	0	0	2.089	0.129	0.088	0.027	0	0.12	0	0.002	0.03	0	1.257	0.013	0	0.01	0.616	8.094	0.618	0.15	0.426	0	0.111	0
A1R-45	0.183	3.887	0	0	0.203	0.516	1.132	0	0	2.089	0.129	0.088	0.027	0	0.12	0	0.002	0.03	0	1.257	0.013	0	0.01	0.616	8.094	0.618	0.15	0.426	0	0.111	0
A1R-44	0.183	3.887	0	0	0.203	0.516	1.132	0	0	2.089	0.129	0.088	0.027	0	0.12	0	0.002	0.03	0	1.257	0.013	0	0.01	0.616	8.094	0.618	0.15	0.426	0	0.111	0
A1R-43	0.183	3.887	0	0	0.203	0.516	1.132	0	0	2.089	0.129	0.088	0.027	0	0.12	0	0.002	0.03	0	1.257	0.013	0	0.01	0.616	8.094	0.618	0.15	0.426	0	0.111	0
A1R-42	0.183	3.887	0	0	0.203	0.516	1.132	0	0	2.089	0.129	0.088	0.027	0	0.12	0	0.002	0.03	0	1.257	0.013	0	0.01	0.616	8.094	0.618	0.15	0.426	0	0.111	0
A1R-41	0.183	3.887	0	0	0.203	0.516	1.132	0	0	2.089	0.129	0.088	0.027	0	0.12	0	0.002	0.03	0	1.257	0.013	0	0.01	0.616	8.094	0.618	0.15	0.426	0	0.111	0
A1R-40	0.183	3.887	0	0	0.203	0.516	1.132	0	0	2.089	0.129	0.088	0.027	0	0.12	0	0.002	0.03	0	1.257	0.013	0	0.01	0.616	8.094	0.618	0.15	0.426	0	0.111	0
A1R-39	0.183	3.887	0	0	0.203	0.516	1.132	0	0	2.089	0.129	0.088	0.027	0	0.12	0	0.002	0.03	0	1.257	0.013	0	0.01	0.616	8.094	0.618	0.15	0.426	0	0.111	0
A1R-38	0.183	3.887	0	0	0.203	0.516	1.132	0	0	2.089	0.129	0.088	0.027	0	0.12	0	0.002	0.03	0	1.257	0.013	0	0.01	0.616	8.094	0.618	0.15	0.426	0	0.111	0
A1R-37	0.183	3.887	0	0	0.203	0.516	1.132	0	0	2.089	0.129	0.088	0.027	0	0.12	0	0.002	0.03	0	1.257	0.013	0	0.01	0.616	8.094	0.618	0.15	0.426	0	0.111	0
A1R-36	0.183	3.887	0	0	0.203	0.516	1.132	0	0	2.089	0.129	0.088	0.027	0	0.12	0	0.002	0.03	0	1.257	0.013	0	0.01	0.616	8.094	0.618	0.15	0.426	0	0.111	0
A1R-35	0.183	3.887	0	0	0.203	0.516	1.132	0	0	2.089	0.129	0.088	0.027	0	0.12	0	0.002	0.03	0	1.257	0.013	0	0.01	0.616	8.094	0.618	0.15	0.426	0	0.111	0
A1R-34	0.183	3.887	0	0	0.203	0.516	1.132	0	0	2.089	0.129	0.088	0.027	0	0.12	0	0.002	0.03	0	1.257	0.013	0	0.01	0.616	8.094	0.618	0.15	0.426	0	0.111	0
A1R-33	0.183	3.887	0	0	0.203	0.516	1.132	0	0	2.089	0.129	0.088	0.027	0	0.12	0	0.002	0.03	0	1.257	0.013	0	0.01	0.616	8.094	0.618	0.15	0.426	0	0.111	0
A1R-32	0.183	3.887	0	0	0.203	0.516	1.132	0	0	2.089	0.129	0.088	0.027	0	0.12	0	0.002	0.03	0	1.257	0.013	0	0.01	0.616	8.094	0.618	0.15	0.426	0	0.111	0
A1R-31	0.183	3.887	0	0	0.203	0.516	1.132	0	0	2.089	0.129	0.088	0.027	0	0.12	0	0.002	0.03	0	1.257	0.013	0	0.01	0.616	8.094	0.618	0.15	0.426	0	0.111	0
A1R-30	0.183	3.887	0	0	0.203	0.516	1.132	0	0	2.089	0.129	0.088	0.027	0	0.12	0	0.002	0.03	0	1.257	0.013	0	0.01	0.616	8.094	0.618	0.15	0.426	0	0.111	0
A1R-29	0.183	3.887	0	0	0.203	0.516	1.132	0	0	2.089	0.129	0.088	0.027	0	0.12	0	0.002	0.03	0	1.257	0.013	0	0.01	0.616	8.094	0.618	0.15	0.426	0	0.111	0
A1R-28	0.183	3.887	0	0	0.203	0.516	1.132	0	0	2.089	0.129	0.088	0.027	0	0.12	0	0.002	0.03	0	1.257	0.013	0	0.01	0.616	8.094	0.618	0.15	0.426	0	0.111	0
A1R-27	0.183	3.887	0	0	0.203	0.516	1.132	0	0	2.089	0.129	0.088	0.027	0	0.12	0	0.002	0.03	0	1.257	0.013	0	0.01	0.616	8.094	0.618	0.15	0.426	0	0.111	0
A1R-26	0.183	3.887	0	0	0.203	0.516	1.132	0	0	2.089	0.129	0.088	0.027	0	0.12	0	0.002	0.03	0	1.257	0.013	0	0.01	0.616	8.094	0.618	0.15	0.426	0	0.111	0
A1R-25	0.183	3.887	0	0	0.203	0.516	1.132	0	0	2.089	0.129	0.088	0.027	0	0.12	0	0.002	0.03	0	1.257	0.013	0	0.01	0.616	8.094	0.618	0.15	0.426	0	0.111	0
A1R-24	0.183	3.887	0	0	0.203	0.516	1.132	0	0	2.089	0.129	0.088	0.027	0	0.12	0	0.002	0.03	0	1.257	0.013	0	0.01	0.616	8.094	0.618	0.15	0.426	0	0.111	0
A1R-23	0.183	3.887	0	0	0.203	0.516	1.132	0	0	2.089	0.129	0.088	0.027	0	0.12	0	0.002	0.03	0	1.257	0.013	0	0.01	0.616	8.094	0.618	0.15	0.426	0	0.111	0
A1R-22	0.183	3.887	0	0	0.203	0.516	1.132	0	0	2.089	0.129	0.088	0.027	0	0.12	0	0.002	0.03	0	1.257	0.013	0	0.01	0.616	8.094	0.618	0.15	0.426	0	0.111	0
A1R-21	0.183	3.887	0	0	0.203	0.516	1.132	0	0	2.089	0.129	0.088	0.027	0	0.12	0	0.002	0.03	0	1.257	0.013	0	0.01	0.616	8.094	0.618	0.15	0.426	0	0.111	0
A1R-20	0.183	3.887	0	0	0.203	0.516	1.132	0	0	2.089	0.129	0.088	0.027	0	0.12	0	0.002	0.03	0	1.257	0.013	0	0.01	0.616	8.094	0.618	0.15	0.426	0	0.111	0
A1R-19	0.183	3.887	0	0	0.203	0.516	1.132	0	0	2.089	0.129	0.088	0.027	0	0.12	0	0.002	0.03	0	1.257	0.013	0	0.01	0.616	8.094	0.618	0.15	0.426	0	0.111	0
A1R-18	0.183	3.887	0	0	0.203	0.516	1.132	0	0	2.089	0.129	0.088	0.027	0	0.12	0	0.002	0.03	0	1.257	0.013	0	0.01	0.616	8.094	0.618	0.15	0.426	0	0.111	0
A1R-17	0.183	3.887	0	0	0.203	0.516	1.132	0	0	2.089	0.129	0.088	0.027	0	0.12	0	0.002	0.03	0	1.257	0.013	0	0.01	0.616	8.094	0.618	0.15	0.426	0	0.111	0
A1R-16	0.183	3.887	0	0	0.203	0.516	1.132	0	0	2.089	0.129	0.088	0.027	0	0.12	0	0.002	0.03	0	1.257	0.013	0	0.01	0.616	8.094	0.618	0.15	0.426	0	0.111	0
A1R-15	0.183	3.887	0	0	0.203	0.516	1.132	0	0	2.089	0.129	0.088	0.027	0	0.12	0	0.002	0.03	0	1.257	0.013	0	0.01	0.616	8.094	0.618	0.15	0.426	0	0.111	0
A1R-14	0.183	3.887	0	0	0.203	0.516	1.132	0	0	2.089	0.129	0.088	0.027	0	0.12	0	0.002	0.03	0	1.257	0.013	0	0.01	0.616	8.094	0.618	0.15	0.426	0	0.111	0
A1R-13	0.183	3.887	0	0	0.203	0.516	1.132	0	0	2.089	0.129	0.088	0.027	0	0.12	0	0.002	0.03	0	1.257	0.013	0	0.01	0.616	8.094	0.618	0.15	0.426	0	0.111	0
A1R-12	0.183	3.887	0	0	0.203	0.516	1.132	0	0	2.089	0.129	0.088	0.027	0	0.12	0	0.002	0.03	0	1.257	0.013	0	0.01	0.616	8.094	0.618	0.15	0.426	0	0.111	0
A1R-11	0.183	3.887	0	0	0.203	0.516	1.132	0	0	2.089	0.129	0.088	0.027	0	0.12	0	0.002	0.03	0	1.257	0.013	0	0.01	0.616	8.094	0.618	0.15	0.426	0	0.111	0
A1R-10	0.183	3.887	0	0	0.203	0.516	1.132	0	0	2.089	0.129	0.088	0.027	0	0.12	0	0.002	0.03	0	1.257	0.013	0	0.01	0.616	8.094	0.618	0.15	0.426	0	0.111	0
A1R-09	0.183	3.887	0	0	0.203	0.516	1.132	0	0	2.089	0.129	0.088	0.027	0	0.12	0	0.002	0.03	0	1.257	0.013	0	0.01	0.616	8.094	0.618	0.15	0.426	0	0.111	0
A1R-08	0.183	3.887	0	0	0.203	0.516	1.132	0	0	2.089	0.129	0.088	0.027	0	0.12	0	0.002	0.03	0	1.257	0.013	0	0.01	0.616	8.094	0.618	0.15	0.426	0	0.111	0
A1R-07	0.183	3.887	0	0	0.203	0.516	1.132	0	0	2.089	0.129	0.088	0.027	0	0.12	0	0.002	0.03	0	1.257	0.013	0	0.01	0.616	8.094	0.618	0.15	0.426	0	0.111	0
A1R-06	0.183	3.887	0	0	0.203	0.516	1.132	0	0	2.089	0.129	0.088	0.027	0	0.12	0	0.002	0.03	0	1.257	0.013	0	0.01	0.616	8.094	0.618	0.15	0.426	0	0.111	0
A1R-05	0.183	3.887	0	0	0.203	0.516	1.132	0	0	2.089	0.129	0.088	0.027	0	0.12	0	0.002	0.03	0	1.257	0.013	0	0.01	0.616	8.094	0.618	0.15	0.426	0	0.111	0
A1R-04	0.183	3.887	0	0	0.203	0.516	1.132	0	0	2.089	0.129	0.088	0.027	0	0.12	0	0.002	0.03	0	1.257	0.013	0	0.01	0.616	8.094	0.618	0.15	0.426	0	0.111	0
A1R-03	0.183	3.887	0	0	0.203	0.516	1.132	0	0	2.089	0.129	0.088	0.027	0	0.12	0	0.002	0.03	0	1.257	0.013	0	0.01	0.616	8.094	0.618	0.15	0.426	0	0.111	0
A1R-02	0.183	3.887	0	0	0.203	0.516	1.132	0	0	2.089	0.129	0.088	0.027	0	0.12	0	0.002	0.03	0	1.257	0.013	0	0.01	0.616	8.094	0.618	0.15	0.426	0	0.111	0
A1R-01k	0.183	3.887	0	0	0.203	0.516	1.132	0	0	2.089	0.129	0.088	0.027	0	0.12	0	0.002	0.03	0	1.257	0.013	0	0.01	0.616	8.094	0.618	0.15	0.426	0	0.111	0
A1R-99mean	0.183	3.887	0	0	0.203	0.516	1.132	0	0	2.089	0.129	0.088	0.027	0	0.12	0	0.002	0.03	0	1.257	0.013	0	0.01	0.616	8.094	0.618	0.15	0.426	0	0.111	0
A1R-98	0.183	3.887	0	0	0.203	0.516	1.132	0	0	2.089	0.129	0.088	0.027	0	0.12	0	0.002	0.03	0	1.257	0.013	0	0.01	0.616	8.094	0.618	0.15	0.426	0	0.111	0
A1R-97	0.183	3.887	0	0	0.203	0.516	1.132	0	0	2.089	0.129	0.088	0.027	0	0.12	0	0.002	0.03	0	1.257	0.013	0	0.01	0.616	8.094	0.618	0.15	0.426	0	0.111	0
A1R-96	0.183	3.887	0	0	0.203	0.516	1.132	0	0	2.089	0.129	0.088	0.027	0	0.12	0	0.002	0.03	0	1.257	0.013	0	0.01	0.616	8.094	0.618	0.15	0.426	0	0.111	0
A1R-95	0.183	3.887	0	0	0.203	0.516	1.132	0	0	2.089	0.129	0.088	0.027	0	0.12	0	0.002	0.03	0	1.257	0.013	0	0.01	0.616	8.094	0.618	0.15	0.426	0	0.111	0
A1R-94	0.183	3.887	0	0	0.203	0.516	1.132	0	0	2.089	0.129	0.088	0.027	0	0.12	0	0.002	0.03	0	1.257	0.013	0	0.01	0.616	8.094	0.618	0.15	0.426	0	0.111	0
A1R-93	0.183	3.887	0	0	0.203	0.516	1.132	0	0	2.089	0.129	0.088	0.027	0	0.12	0	0.002	0.03	0	1.257	0.013	0	0.01	0.616	8.094	0.618	0.15	0.426	0	0.111	0
A1R-92	0.183	3.887	0	0	0.203	0.516	1.132	0	0	2.089	0.129	0.088	0.027	0	0.12	0	0.002	0.03	0	1.257	0.013	0	0.01	0.616	8.094	0.618	0.15	0.426	0	0.111	0
A1R-91	0.183	3.887	0	0	0.203	0.516	1.132	0	0	2.089	0.129	0.088	0.027	0	0.12	0	0.002	0.03	0	1.257	0.013	0	0.01	0.616	8.094	0.618	0.15	0.426	0	0.111	0
A1R-90	0.183	3.887	0	0	0.203	0.516	1.132	0	0	2.089	0.129	0.088	0.027	0	0.12	0	0.002	0.03	0	1.257	0.013	0	0.01	0.616	8.094	0.618	0.15	0.426	0	0.111	0
A1R-89	0.183	3.887	0	0	0.203	0.516	1.132	0	0	2.089	0.129	0.088	0.027	0	0.12	0	0.002	0.03	0	1.257	0.013	0	0.01	0.616	8.094	0.618	0.15	0.426	0	0.111	0
A1R-88	0.183	3.887	0	0	0.203	0.516	1.132	0	0	2.089	0.129	0.088	0.027	0	0.12	0	0.002	0.03	0	1.257	0.013	0	0.01	0.616	8.094	0.618	0.15	0.426	0	0.111	0
A1R-87	0.183	3.887	0	0	0.203	0.516	1.132	0	0	2.089	0.129	0.088	0.027	0	0.12	0	0.002	0.03	0	1.257	0.013	0	0.01	0.616	8.094	0.618	0.15	0.426	0	0.111	0
A1R-86	0.183	3.887	0	0	0.203	0.516	1.132	0	0	2.089	0.129	0.088	0.027	0	0.12	0	0.002	0.03	0	1.257	0.013	0	0.01	0.616	8.094	0.618	0.15	0.426	0	0.111	0
A1R-85	0.183	3.887	0	0	0.203	0.516	1.132	0	0	2.089	0.129	0.088	0.027	0	0.12	0	0.002	0.03	0	1.257	0.013	0	0.01	0.616	8.094	0.618	0.15	0.426	0	0.111	0
A1R-84	0.183	3.887	0	0	0.203	0.516	1.132	0	0	2.089	0.129	0.088	0.027	0	0.12	0	0.002	0.03	0	1.257	0.013	0	0.01	0.616	8.094	0.618	0.15	0.426	0	0.111	0
A1R-83	0.183	3.887	0	0	0.203	0.516	1.132	0	0	2.089	0.129	0.088	0.027	0	0.12	0	0.002	0.03	0	1.257	0.013	0	0.01	0.616	8.094	0.618	0.15	0.426	0	0.111	0
A1R-82	0.183	3.887	0	0	0.203	0.516	1.132	0	0	2.089	0.129	0.088	0.027	0	0.12	0	0.002	0.03	0	1.257	0.013	0	0.01	0.616	8.094	0.618	0.15	0.426	0	0.111	0
A1R-81	0.183	3.887	0	0	0.203	0.516	1.132	0	0	2.089	0.129	0.088	0.027	0	0.12	0	0.002	0.03	0	1.257	0.013	0	0.01	0.616	8.094	0.618	0.15	0.426	0	0.111	0
A1R-80	0.183	3.887	0	0	0.203	0.516	1.132	0	0	2.089	0.129	0.088	0.027	0	0.12	0	0.002	0.03	0	1.257	0.013	0	0.01	0.616	8.094	0.618	0.15	0.426	0	0.111	0
A1R-79	0.183	3.887	0	0	0.203	0.516	1.132	0	0	2.089	0.129	0.088	0.027	0	0.12	0	0.002	0.03	0	1.257	0.013	0	0.01	0.616	8.094	0.618	0.15	0.426	0	0.111	0
A1R-78	0.183	3.887	0	0	0.203	0.516	1.132	0	0	2.089	0.129	0.088	0.027	0	0.12	0	0.002	0.03	0	1.257	0.013	0	0.01	0.616	8.094	0.618	0.15	0.426	0	0.111	0
A1R-77	0.183	3.887	0	0	0.203	0.516	1.132	0	0	2.089	0.129	0.088	0.027	0	0.12	0	0.002	0.03	0	1.257	0.013	0	0.01	0.616	8.094	0.618	0.15	0.426	0	0.111	0
A1R-76	0.183	3.887	0	0	0.203	0.516	1.132	0	0	2.089	0.129	0.088	0.027	0	0.12	0	0.002	0.03	0	1.257	0.013	0	0.01	0.616	8.094	0.618	0.15	0.426	0	0.111	0

32	33	34	35	36	37	38	39	40	41	42	43	44	45	46	47	48	49	50	51	52	53	54	55	56	57	58	59	60	61	62	63	64	
Sr	Ta	Tb	Th	Tm	U	V	W	Y	Yb	Zn	Zr	SiO2 (Si)	Al2O3 (Al)	Fe2O3 (Fe)	MnO (Mn)	MgO (Mg)	CaO (Ca)	Na2O(Na)	K2O(K)	TiO2(Ti)	P2O5(P)	B	Li	H2Otot (H)	Stot (S)	CO2 tot (C)	O.rock	O.water	Cl nat AMS	Ca ICP	Z (position sur le scarp)	Thickness sample	
ppm	ppm	ppm	ppm	ppm	ppm	ppm	ppm	ppm	ppm	ppm	ppm	%	%	%	%	%	%	%	%	%	%	ppm	ppm	%	%	%			ppm	ppm	cm	cm	
282.947	**0**	**0.018**	**0.038**	**0.012**	**0.482**	**2.361**	**0**	**1.569**	**0.08**	**7.584**	**0**	**0**	**0.036**	**0.01**	**0.002**	**0.384**	**55.453**	**0**	**0**	**0**	**0.029**	**2.133**	**1.027**	**0.305**	**0.021**	**43.949**	**0**	**0**	**29**	**379078 (moyenne)**			
282.947	0	0.018	0.038	0.012	0.482	2.361	0	1.569	0.08	7.584	0	0	0.036	0.01	0.002	0.384	55.453	0	0	0	0.029	2.133	1.027	0.305	0.021	43.949	0	0	30.13	364050	3	3.2	
282.947	0	0.018	0.038	0.012	0.482	2.361	0	1.569	0.08	7.584	0	0	0.036	0.01	0.002	0.384	55.453	0	0	0	0.029	2.133	1.027	0.305	0.021	43.949	0	0	29.69	379078	10	3.8	
282.947	0	0.018	0.038	0.012	0.482	2.361	0	1.569	0.08	7.584	0	0	0.036	0.01	0.002	0.384	55.453	0	0	0	0.029	2.133	1.027	0.305	0.021	43.949	0	0	37.77	379078	20	3.5	
282.947	0	0.018	0.038	0.012	0.482	2.361	0	1.569	0.08	7.584	0	0	0.036	0.01	0.002	0.384	55.453	0	0	0	0.029	2.133	1.027	0.305	0.021	43.949	0	0	37.51	370000	30	3.3	
282.947	0	0.018	0.038	0.012	0.482	2.361	0	1.569	0.08	7.584	0	0	0.036	0.01	0.002	0.384	55.453	0	0	0	0.029	2.133	1.027	0.305	0.021	43.949	0	0	34.67	367668	40		3
282.947	0	0.018	0.038	0.012	0.482	2.361	0	1.569	0.08	7.584	0	0	0.036	0.01	0.002	0.384	55.453	0	0	0	0.029	2.133	1.027	0.305	0.021	43.949	0	0	30.69	369245	50	3.5	
282.947	0	0.018	0.038	0.012	0.482	2.361	0	1.569	0.08	7.584	0	0	0.036	0.01	0.002	0.384	55.453	0	0	0	0.029	2.133	1.027	0.305	0.021	43.949	0	0	27.92	379858	61	3.5	
282.947	0	0.018	0.038	0.012	0.482	2.361	0	1.569	0.08	7.584	0	0	0.036	0.01	0.002	0.384	55.453	0	0	0	0.029	2.133	1.027	0.305	0.021	43.949	0	0	22.55	364250	71	3.5	
282.947	0	0.018	0.038	0.012	0.482	2.361	0	1.569	0.08	7.584	0	0	0.036	0.01	0.002	0.384	55.453	0	0	0	0.029	2.133	1.027	0.305	0.021	43.949	0	0	20.93	370657	81		3
282.947	0	0.018	0.038	0.012	0.482	2.361	0	1.569	0.08	7.584	0	0	0.036	0.01	0.002	0.384	55.453	0	0	0	0.029	2.133	1.027	0.305	0.021	43.949	0	0	27.41	371455	91	3.2	
282.947	0	0.018	0.038	0.012	0.482	2.361	0	1.569	0.08	7.584	0	0	0.036	0.01	0.002	0.384	55.453	0	0	0	0.029	2.133	1.027	0.305	0.021	43.949	0	0	31.13	365805	101	3.3	
282.947	0	0.018	0.038	0.012	0.482	2.361	0	1.569	0.08	7.584	0	0	0.036	0.01	0.002	0.384	55.453	0	0	0	0.029	2.133	1.027	0.305	0.021	43.949	0	0	31.38	377505	111		3
282.947	0	0.018	0.038	0.012	0.482	2.361	0	1.569	0.08	7.584	0	0	0.036	0.01	0.002	0.384	55.453	0	0	0	0.029	2.133	1.027	0.305	0.021	43.949	0	0	31.72	367497	121	2.5	
282.947	0	0.018	0.038	0.012	0.482	2.361	0	1.569	0.08	7.584	0	0	0.036	0.01	0.002	0.384	55.453	0	0	0	0.029	2.133	1.027	0.305	0.021	43.949	0	0	30.78	361650	131	2.7	
282.947	0	0.018	0.038	0.012	0.482	2.361	0	1.569	0.08	7.584	0	0	0.036	0.01	0.002	0.384	55.453	0	0	0	0.029	2.133	1.027	0.305	0.021	43.949	0	0	27.71	371005	143	2.8	
282.947	0	0.018	0.038	0.012	0.482	2.361	0	1.569	0.08	7.584	0	0	0.036	0.01	0.002	0.384	55.453	0	0	0	0.029	2.133	1.027	0.305	0.021	43.949	0	0	28.82	368498	153	2.5	
282.947	0	0.018	0.038	0.012	0.482	2.361	0	1.569	0.08	7.584	0	0	0.036	0.01	0.002	0.384	55.453	0	0	0	0.029	2.133	1.027	0.305	0.021	43.949	0	0	29.06	367549	162		3
282.947	0	0.018	0.038	0.012	0.482	2.361	0	1.569	0.08	7.584	0	0	0.036	0.01	0.002	0.384	55.453	0	0	0	0.029	2.133	1.027	0.305	0.021	43.949	0	0	28.98	369914	172	3.5	
282.947	0	0.018	0.038	0.012	0.482	2.361	0	1.569	0.08	7.584	0	0	0.036	0.01	0.002	0.384	55.453	0	0	0	0.029	2.133	1.027	0.305	0.021	43.949	0	0	30.81	368035	182	3.3	
282.947	0	0.018	0.038	0.012	0.482	2.361	0	1.569	0.08	7.584	0	0	0.036	0.01	0.002	0.384	55.453	0	0	0	0.029	2.133	1.027	0.305	0.021	43.949	0	0	32.25	369967	193	3.5	
282.947	0	0.018	0.038	0.012	0.482	2.361	0	1.569	0.08	7.584	0	0	0.036	0.01	0.002	0.384	55.453	0	0	0	0.029	2.133	1.027	0.305	0.021	43.949	0	0	30.84	379078	203	2.5	
282.947	0	0.018	0.038	0.012	0.482	2.361	0	1.569	0.08	7.584	0	0	0.036	0.01	0.002	0.384	55.453	0	0	0	0.029	2.133	1.027	0.305	0.021	43.949	0	0	29.33	383806	222	2.5	
282.947	0	0.018	0.038	0.012	0.482	2.361	0	1.569	0.08	7.584	0	0	0.036	0.01	0.002	0.384	55.453	0	0	0	0.029	2.133	1.027	0.305	0.021	43.949	0	0	30.33	383432	233		3
282.947	0	0.018	0.038	0.012	0.482	2.361	0	1.569	0.08	7.584	0	0	0.036	0.01	0.002	0.384	55.453	0	0	0	0.029	2.133	1.027	0.305	0.021	43.949	0	0	32.19	376991	243		3
282.947	0	0.018	0.038	0.012	0.482	2.361	0	1.569	0.08	7.584	0	0	0.036	0.01	0.002	0.384	55.453	0	0	0	0.029	2.133	1.027	0.305	0.021	43.949	0	0	32.71	377976	253		3
282.947	0	0.018	0.038	0.012	0.482	2.361	0	1.569	0.08	7.584	0	0	0.036	0.01	0.002	0.384	55.453	0	0	0	0.029	2.133	1.027	0.305	0.021	43.949	0	0	29.08	377383	262	2.1	
282.947	0	0.018	0.038	0.012	0.482	2.361	0	1.569	0.08	7.584	0	0	0.036	0.01	0.002	0.384	55.453	0	0	0	0.029	2.133	1.027	0.305	0.021	43.949	0	0	37.28	379742	272	2.5	
282.947	0	0.018	0.038	0.012	0.482	2.361	0	1.569	0.08	7.584	0	0	0.036	0.01	0.002	0.384	55.453	0	0	0	0.029	2.133	1.027	0.305	0.021	43.949	0	0	35.32	379596	282		3
282.947	0	0.018	0.038	0.012	0.482	2.361	0	1.569	0.08	7.584	0	0	0.036	0.01	0.002	0.384	55.453	0	0	0	0.029	2.133	1.027	0.305	0.021	43.949	0	0	31.8	390732	292	2.9	
282.947	0	0.018	0.038	0.012	0.482	2.361	0	1.569	0.08	7.584	0	0	0.036	0.01	0.002	0.384	55.453	0	0	0	0.029	2.133	1.027	0.305	0.021	43.949	0	0	26.37	377580	302	2.8	
282.947	0	0.018	0.038	0.012	0.482	2.361	0	1.569	0.08	7.584	0	0	0.036	0.01	0.002	0.384	55.453	0	0	0	0.029	2.133	1.027	0.305	0.021	43.949	0	0	28.54	392813	312	2.5	
282.947	0	0.018	0.038	0.012	0.482	2.361	0	1.569	0.08	7.584	0	0	0.036	0.01	0.002	0.384	55.453	0	0	0	0.029	2.133	1.027	0.305	0.021	43.949	0	0	33.71	377376	322	2.5	
282.947	0	0.018	0.038	0.012	0.482	2.361	0	1.569	0.08	7.584	0	0	0.036	0.01	0.002	0.384	55.453	0	0	0	0.029	2.133	1.027	0.305	0.021	43.949	0	0	33.14	392206	333	2.8	
282.947	0	0.018	0.038	0.012	0.482	2.361	0	1.569	0.08	7.584	0	0	0.036	0.01	0.002	0.384	55.453	0	0	0	0.029	2.133	1.027	0.305	0.021	43.949	0	0	30.07	382797	343	2.7	
282.947	0	0.018	0.038	0.012	0.482	2.361	0	1.569	0.08	7.584	0	0	0.036	0.01	0.002	0.384	55.453	0	0	0	0.029	2.133	1.027	0.305	0.021	43.949	0	0	30.92	385909	353		2
282.947	0	0.018	0.038	0.012	0.482	2.361	0	1.569	0.08	7.584	0	0	0.036	0.01	0.002	0.384	55.453	0	0	0	0.029	2.133	1.027	0.305	0.021	43.949	0	0	37.82	384152	363	2.5	
282.947	0	0.018	0.038	0.012	0.482	2.361	0	1.569	0.08	7.584	0	0	0.036	0.01	0.002	0.384	55.453	0	0	0	0.029	2.133	1.027	0.305	0.021	43.949	0	0	36.45	375397	373		3
282.947	0	0.018	0.038	0.012	0.482	2.361	0	1.569	0.08	7.584	0	0	0.036	0.01	0.002	0.384	55.453	0	0	0	0.029	2.133	1.027	0.305	0.021	43.949	0	0	34.68	386750	382		3
282.947	0	0.018	0.038	0.012	0.482	2.361	0	1.569	0.08	7.584	0	0	0.036	0.01	0.002	0.384	55.453	0	0	0	0.029	2.133	1.027	0.305	0.021	43.949	0	0	31.61	388266	392		3
282.947	0	0.018	0.038	0.012	0.482	2.361	0	1.569	0.08	7.584	0	0	0.036	0.01	0.002	0.384	55.453	0	0	0	0.029	2.133	1.027	0.305	0.021	43.949	0	0	29.13	378714	402	2.9	
282.947	0	0.018	0.038	0.012	0.482	2.361	0	1.569	0.08	7.584	0	0	0.036	0.01	0.002	0.384	55.453	0	0	0	0.029	2.133	1.027	0.305	0.021	43.949	0	0	30.87	383776	412	2.7	
282.947	0	0.018	0.038	0.012	0.482	2.361	0	1.569	0.08	7.584	0	0	0.036	0.01	0.002	0.384	55.453	0	0	0	0.029	2.133	1.027	0.305	0.021	43.949	0	0	28.93	388572	422		3
282.947	0	0.018	0.038	0.012	0.482	2.361	0	1.569	0.08	7.584	0	0	0.036	0.01	0.002	0.384	55.453	0	0	0	0.029	2.133	1.027	0.305	0.021	43.949	0	0	25.19	381798	433		3
282.947	0	0.018	0.038	0.012	0.482	2.361	0	1.569	0.08	7.584	0	0	0.036	0.01	0.002	0.384	55.453	0	0	0	0.029	2.133	1.027	0.305	0.021	43.949	0	0	25.38	393497	443		3
282.947	0	0.018	0.038	0.012	0.482	2.361	0	1.569	0.08	7.584	0	0	0.036	0.01	0.002	0.384	55.453	0	0	0	0.029	2.133	1.027	0.305	0.021	43.949	0	0	25.1	365857	453		3
282.947	0	0.018	0.038	0.012	0.482	2.361	0	1.569	0.08	7.584	0	0	0.036	0.01	0.002	0.384	55.453	0	0	0	0.029	2.133	1.027	0.305	0.021	43.949	0	0	25.39	391846	463		3
282.947	0	0.018	0.038	0.012	0.482	2.361	0	1.569	0.08	7.584	0	0	0.036	0.01	0.002	0.384	55.453	0	0	0	0.029	2.133	1.027	0.305	0.021	43.949	0	0	25.95	393012	473		3
282.947	0	0.018	0.038	0.012	0.482	2.361	0	1.569	0.08	7.584	0	0	0.036	0.01	0.002	0.384	55.453	0	0	0	0.029	2.133	1.027	0.305	0.021	43.949	0	0	25.41	389891	484	3.2	
282.947	0	0.018	0.038	0.012	0.482	2.361	0	1.569	0.08	7.584	0	0	0.036	0.01	0.002	0.384	55.453	0	0	0	0.029	2.133	1.027	0.305	0.021	43.949	0	0	23.23	386107	495	3.5	
282.947	0	0.018	0.038	0.012	0.482	2.361	0	1.569	0.08	7.584	0	0	0.036	0.01	0.002	0.384	55.453	0	0	0	0.029	2.133	1.027	0.305	0.021	43.949	0	0	24.65	378574	504		3
282.947	0	0.018	0.038	0.012	0.482	2.361	0	1.569	0.08	7.584	0	0	0.036	0.01	0.002	0.384	55.453	0	0	0	0.029	2.133	1.027	0.305	0.021	43.949	0	0	25.37	387350	514	3.2	
282.947	0	0.018	0.038	0.012	0.482	2.361	0	1.569	0.08	7.584	0	0	0.036	0.01	0.002	0.384	55.453	0	0	0	0.029	2.133	1.027	0.305	0.021	43.949	0	0	22.93	387987	523		3
282.947	0	0.018	0.038	0.012	0.482	2.361	0	1.569	0.08	7.584	0	0	0.036	0.01	0.002	0.384	55.453	0	0	0	0.029	2.133	1.027	0.305	0.021	43.949	0	0	23.32	380644	534		3
282.947	0	0.018	0.038	0.012	0.482	2.361	0	1.569	0.08	7.584	0	0	0.036	0.01	0.002	0.384	55.453	0	0	0	0.029	2.133	1.027	0.305	0.021	43.949	0	0	22.91	395294	544		3
282.947	0	0.018	0.038	0.012	0.482	2.361	0	1.569	0.08	7.584	0	0	0.036	0.01	0.002	0.384	55.453	0	0	0	0.029	2.133	1.027	0.305	0.021	43.949	0	0	21.18	382829	554	3.5	
282.947	0	0.018	0.038	0.012	0.482	2.361	0	1.569	0.08	7.584	0	0	0.036	0.01	0.002	0.384	55.453	0	0	0	0.029	2.133	1.027	0.305	0.021	43.949	0	0	20.94	392401	563		3
282.947	0	0.018	0.038	0.012	0.482	2.361	0	1.569	0.08	7.584	0	0	0.036	0.01	0.002	0.384	55.453	0	0	0	0.029	2.133	1.027	0.305	0.021	43.949	0	0	26.05	383895	573		3
282.947	0	0.018	0.038	0.012	0.482	2.361	0	1.569	0.08	7.584	0	0	0.036	0.01	0.002	0.384	55.453	0	0	0	0.029	2.133	1.027	0.305	0.021	43.949	0	0	31.8	383414	583		3
282.947	0	0.018	0.038	0.012	0.482	2.361	0	1.569	0.08	7.584	0	0	0.036	0.01	0.002	0.384	55.453	0	0	0	0.029	2.133	1.027	0.305	0.021	43.949	0	0	27.76	380869	593		3
282.947	0	0.018	0.038	0.012	0.482	2.361	0	1.569	0.08	7.584	0	0	0.036	0.01	0.002	0.384	55.453	0	0	0	0.029	2.133	1.027	0.305	0.021	43.949	0	0	32.55	372809	603		3
282.947	0	0.018	0.038	0.012	0.482	2.361	0	1.569	0.08	7.584	0	0	0.036	0.01	0.002	0.384	55.453	0	0	0	0.029	2.133	1.027	0.305	0.021	43.949	0	0	34.66	380881	614		3
282.947	0	0.018	0.038	0.012	0.482	2.361	0	1.569	0.08	7.584	0	0	0.036	0.01	0.002	0.384	55.453	0	0	0	0.029	2.133	1.027	0.305	0.021	43.949	0	0	33.16	381076	624	2.6	
282.947	0	0.018	0.038	0.012	0.482	2.361	0	1.569	0.08	7.584	0	0	0.036	0.01	0.002	0.384	55.453	0	0	0	0.029	2.133	1.027	0.305	0.021	43.949	0	0	30.67	384030	634		3
282.947	0	0.018	0.038	0.012	0.482	2.361	0	1.569	0.08	7.584	0	0	0.036	0.01	0.002	0.384	55.453	0	0	0	0.029	2.133	1.027	0.305	0.021	43.949	0	0	26.81	361838	644	2.8	
282.947	0	0.018	0.038	0.012	0.482	2.361	0	1.569	0.08	7.584	0	0	0.036	0.01	0.002	0.384	55.453	0	0	0	0.029	2.133	1.027	0.305	0.021	43.949	0	0	24.8	379078	654		3
282.947	0	0.018	0.038	0.012	0.482	2.361	0	1.569	0.08	7.584	0	0	0.036	0.01	0.002	0.384	55.453	0	0	0	0.029	2.133	1.027	0.305	0.021	43.949	0	0	24.96	369279	664		3
282.947	0	0.018	0.038	0.012	0.482	2.361	0	1.569	0.08	7.584	0	0	0.036	0.01	0.002	0.384	55.453	0	0	0	0.029	2.133	1.027	0.305	0.021	43.949	0	0	27.3	389997	674	2.7	
282.947	0	0.018	0.038	0.012	0.482	2.361	0	1.569	0.08	7.584	0	0	0.036	0.01	0.002	0.384	55.453	0	0	0	0.029	2.133	1.027	0.305	0.021	43.949	0	0	26.22	370851	683	2.5	
282.947	0	0.018	0.038	0.012	0.482	2.361	0	1.569	0.08	7.584	0	0	0.036	0.01	0.002	0.384	55.453	0	0	0	0.029	2.133	1.027	0.305	0.021	43.949	0	0	31.19	391710	693	2.5	
282.947	0	0.018	0.038	0.012	0.482	2.361	0	1.569	0.08	7.584	0	0	0.036	0.01	0.002	0.384	55.453	0	0	0	0.029	2.133	1.027	0.305	0.021	43.949	0	0	31.12	364998	703	2.7	
282.947	0	0.018	0.038	0.012	0.482	2.361	0	1.569	0.08	7.584	0	0	0.036	0.01	0.002	0.384	55.453	0	0	0	0.029	2.133	1.027	0.305	0.021	43.949	0	0	28.52	377404	714	2.7	
282.947	0	0.018	0.038	0.012	0.482	2.361	0	1.569	0.08	7.584	0	0	0.036	0.01	0.002	0.384	55.453	0	0	0	0.029	2.133	1.027	0.305	0.021	43.949	0	0	30.33	377237	725	2.8	
282.947	0	0.018	0.038	0.012	0.482	2.361	0	1.569	0.08	7.584	0	0	0.036	0.01	0.002	0.384	55.453	0	0	0	0.029	2.133	1.027	0.305	0.021	43.949	0	0	31.42	383456	735	2.5	
282.947	0	0.018	0.038	0.012	0.482	2.361	0	1.569	0.08	7.584	0	0	0.036	0.01	0.002	0.384	55.453	0	0	0	0.029	2.133	1.027	0.305	0.021	43.949	0	0	29.59	380000	745		2
282.947	0	0.018	0.038	0.012	0.482	2.361	0	1.569	0.08	7.584	0	0	0.036	0.01	0.002	0.384	55.453	0	0	0	0.029	2.133	1.027	0.305	0.021	43.949	0	0	28.56	386990	765	3.5	
282.947	0	0.018	0.038	0.012	0.482	2.361	0	1.569	0.08	7.584	0	0	0.036	0.01	0.002	0.384	55.453	0	0	0	0.029	2.133	1.027	0.305	0.021	43.949	0	0	22.3	376226	775		3
282.947	0	0.018	0.038	0.012	0.482	2.361	0	1.569	0.08	7.584	0	0	0.036	0.01	0.002	0.384	55.453	0	0	0	0.029	2.133	1.027	0.305	0.021	43.949	0	0	19.45	382145	785		3
282.947	0	0.018	0.038	0.012	0.482	2.361	0	1.569	0.08	7.584	0	0	0.036	0.01	0.002	0.384	55.453	0	0	0	0.029	2.133	1.027	0.305	0.021	43.949	0	0	19.74	385654	795	3.5	
282.947	0	0.018	0.038	0.012	0.482	2.361	0	1.569	0.08	7.584	0	0	0.036	0.01	0.002	0.384	55.453	0	0	0	0.029	2.133	1.027	0.305	0.021	43.949	0	0	23.66	376332	805	3.5	
282.947	0	0.018	0.038	0.012	0.482	2.361	0	1.569	0.08	7.584	0	0	0.036	0.01	0.002	0.384	55.453	0	0	0	0.029	2.133	1.027	0.305	0.021	43.949	0	0	26.39	381844	815	3.2	
282.947	0	0.018	0.038	0.012	0.482	2.361	0	1.569	0.08	7.584	0	0	0.036	0.01	0.002	0.384	55.453	0	0	0	0.029	2.133	1.027	0.305	0.021	43.949	0	0	26.75	393471	826		3
282.947	0	0.018	0.038	0.012	0.482	2.361	0	1.569	0.08	7.584	0	0	0.036	0.01	0.002	0.384	55.453	0	0	0	0.029	2.133	1.027	0.305	0.021	43.949	0	0	24.76	361770	846	2.5	
282.947	0	0.018	0.038	0.012	0.482	2.361	0	1.569	0.08	7.584	0	0	0.036	0.01	0.002	0.384	55.453	0	0	0	0.029	2.133	1.027	0.305	0.021	43.949	0	0	26.29	378414	856		3
282.947	0	0.018	0.038	0.012	0.482	2.361	0	1.569	0.08	7.584	0	0	0.036	0.01	0.002	0.384	55.453	0	0	0	0.029	2.133	1.027	0.305	0.021	43.949	0	0	29.44	385874	866		3
282.947	0	0.018	0.038	0.012	0.482	2.361	0	1.569	0.08	7.584	0	0	0.036	0.01	0.002	0.384	55.453	0	0	0	0.029	2.133	1.027	0.305	0.021	43.949	0	0	26.86	385349	875		3
282.947	0	0.018	0.038	0.012	0.482	2.361	0	1.569	0.08	7.584	0	0	0.036	0.01	0.002	0.384	55.453	0	0	0	0.029	2.133	1.027	0.305	0.021	43.949	0	0	35.46	383870	885		3
282.947	0	0.018	0.038	0.012	0.482	2.361	0	1.569	0.08	7.584	0	0	0.036	0.01	0.002	0.384	55.453	0	0	0	0.029	2.133	1.027	0.305	0.021	43.949	0	0	36.34	380265	901	3.5	
282.947	0	0.018	0.038	0.012	0.482	2.361	0	1.569	0.08	7.584	0	0	0.036	0.01	0.002	0.384	55.453	0	0	0	0.029	2.133	1.027	0.305	0.021	43.949	0	0	26.12	379078	919		3
282.947	0	0.018	0.038	0.012	0.482	2.361	0	1.569	0.08	7.584	0	0	0.036	0.01	0.002	0.384	55.453	0	0	0	0.029	2.133	1.027	0.305	0.021	43.949	0	0	20.46	380620	930	3.3	
282.947	0	0.018	0.038	0.012	0.482	2.361	0	1.569	0.08	7.584	0	0	0.036	0.01	0.002	0.384	55.453	0	0	0	0.029	2.133	1.027	0.305	0.021	43.949	0	0	26.18	380019	939	3.2	
282.947	0	0.018	0.038	0.012	0.482	2.361	0	1.569	0.08	7.584	0	0	0.036	0.01	0.002	0.384	55.453	0	0	0	0.029	2.133	1.027	0.305	0.021	43.949	0	0	26.19	386921	949	3.3	
282.947	0	0.018	0.038	0.012	0.482	2.361	0	1.569	0.08	7.584	0	0	0.036	0.01	0.002	0.384	55.453	0	0	0	0.029	2.133	1.027	0.305	0.021	43.949	0	0	32.52	377596	958		3
282.947	0	0.018	0.038	0.012	0.482	2.361	0	1.569	0.08	7.584	0	0	0.036	0.01	0.002	0.384	55.453	0	0	0	0.029	2.133	1.027	0.305	0.021	43.949	0	0	37.39	391435	967	3.2	
282.947	0	0.018	0.038	0.012	0.482	2.361	0	1.569	0.08	7.584	0	0	0.036	0.01	0.002	0.384	55.453	0	0	0	0.029	2.133	1.027	0.305	0.021	43.949	0	0	42.32	389432	977	3.5	
282.947	0	0.018	0.038	0.012	0.482	2.361	0	1.569	0.08	7.584	0	0	0.036	0.01	0.002	0.384	55.453	0	0	0	0.029	2.133	1.027	0.305	0.021	43.949	0	0	34.96	362664	988	3.2	
282.947	0	0.018	0.038	0.012	0.482	2.361	0	1.569	0.08	7.584	0	0	0.036	0.01	0.002	0.384	55.453	0	0	0	0.029	2.133	1.027	0.305	0.021	43.949	0	0	28.31	367604	998	3.5	
282.947	0	0.018	0.038	0.012	0.482	2.361	0	1.569	0.08	7.584	0	0	0.036	0.01	0.002	0.384	55.453	0	0	0	0.029	2.133	1.027	0.305	0.021	43.949	0	0	32.2	360779	1007	3.5	
282.947	0	0.018	0.038	0.012	0.482	2.361	0	1.569	0.08	7.584	0	0	0.036	0.01	0.002	0.384	55.453	0	0	0	0.029	2.133	1.027	0.305	0.021	43.949	0	0	36.4	369662	1017	3.7	

65	66
[36Cl] AMS at/g rock	uncertainty
125255	3568
124946	3883
125560	5769
126952	3865
137745	3995
124277	3251
129608	3111
131301	5924
126192	3307
134123	3228
137995	3358
142893	3284
138044	3403
143070	3439
148728	4020
145095	3836
142171	4636
149582	4105
151238	4705
161130	5895
150199	4138
157613	6137
161284	7081
155949	4677
160694	3873
166643	4776
177153	10779
169885	5560
177531	4512
168269	4205
180180	4458
187674	3625
183519	3910
182528	3715
184610	2980
198201	6612
189081	7330
200102	5118
212322	6013
205156	5076
204374	7654
211315	8421
209257	4231
214662	4381
213663	4601
198727	5457
208767	5607
226434	5498
216208	5344
223333	5508
229786	5787
229484	5879
231888	7680
245353	6115
239887	6399
224996	8294
239105	12710
267742	8530
246644	6294
260629	6667
262157	7091
268412	8296
278964	7743
269312	6958
270975	7548
288888	6967
291305	7405
284546	7235
300620	9535
325029	8260
308040	9220
315570	10651
340842	8849
333579	6648
326801	8726
321558	11780
333294	5850
329472	5711
343769	5971
374491	16856
358540	13322
379145	6630
403964	7101
404528	8000
391266	8613
419677	8324
429877	8799
409570	8286
369815	7594
420452	7924
426366	8090
443369	7947
481742	12442
522709	10824
522839	10085
536348	20980
543588	17885
598378	16906

"modèles$_{pref}$"

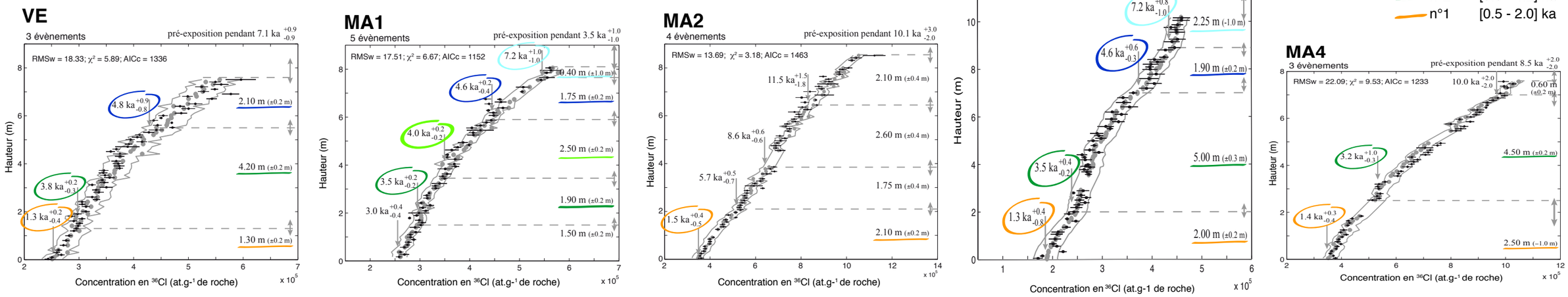

- n°5 [6.2 - 8.2] ka
- n°4 [4.0 - 5.0] ka
- n°3 ~4.0 ka
- n°2 [3.0 - 4.2] ka
- n°1 [0.5 - 2.0] ka

"modèles$_{opt}$"

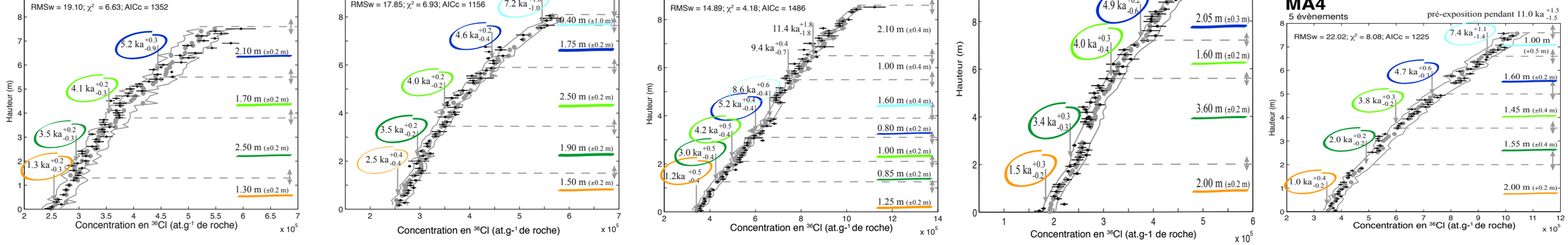

- n°5 7.6 (± 1.6) ka
- n°4 4.9 (± 0.7) ka
- n°3 4.0 (± 0.7) ka
- n°2 3.3 (± 0.7) ka
- n°1 1.2 (± 0.5) ka

"modèles$_{max}$"

Mauvais ajustement des données avec le modèle pré-exposition 'simique'

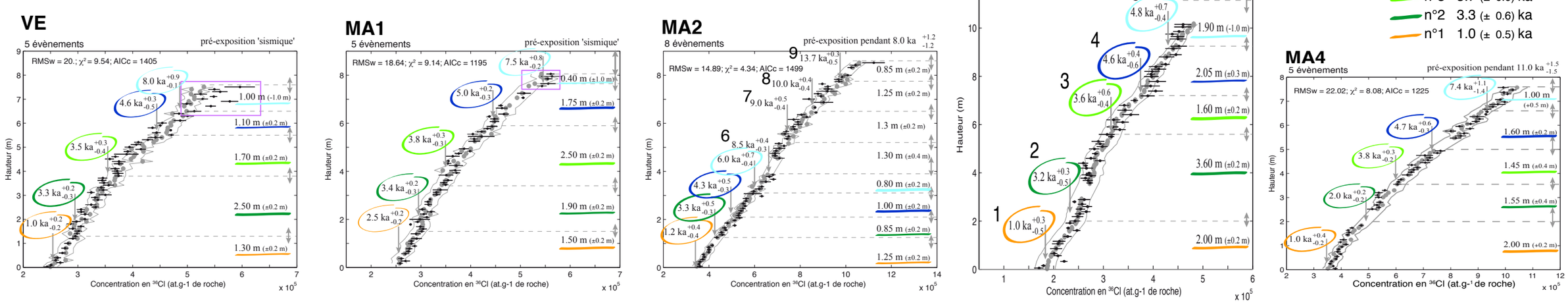

- n°5 7.2 (± 1.7) ka
- n°4 4.6 (± 0.7) ka
- n°3 3.7 (± 0.6) ka
- n°2 3.3 (± 0.6) ka
- n°1 1.0 (± 0.5) ka

Annexe IV
(du chapitre 6)

Earth and Planetary Science Letters 273 (2008) 299–311

Contents lists available at ScienceDirect

Earth and Planetary Science Letters

journal homepage: www.elsevier.com/locate/epsl

Incremental growth of normal faults: Insights from a laser-equipped analog experiment

Aloé Schlagenhauf [a,b,*], Isabelle Manighetti [a], Jacques Malavieille [b], Stéphane Dominguez [b]

[a] Laboratoire de Géophysique Interne et Tectonophysique (LGIT), CNRS, Observatoire de Grenoble (OSUG), Université J. Fourier, Maison des Géosciences, BP 53, 38041 Grenoble cédex 9, France
[b] Géosciences Montpellier, UMR 5243, CNRS, Université Montpellier 2, Place E. Bataillon, 34095 Montpellier cédex 05, France

ARTICLE INFO

Article history:
Received 19 February 2007
Received in revised form 19 June 2008
Accepted 25 June 2008
Available online 6 July 2008

Editor: R.D. van der Hilst

Keywords:
fault growth
analog modeling
normal faults
slip profiles
slip increments

ABSTRACT

We conducted a laser-equipped analog experiment aimed at quasi-continuously monitoring the growth of a dense population of normal faults in homogeneous conditions. To further understand the way geological faults progressively gain in slip and length as they accumulate more strain, we measured with great precision the incremental slip and length changes that the analog faults sustain as they grow. These measurements show that the analog faults share common features with the natural ones. In particular, during their growth, the faults develop and maintain cumulative slip profiles that are generally triangular and asymmetric. The growth takes place through two distinct phases: an initial, short period of rapid lateral lengthening, followed by a longer phase of slip accumulation with little or no lengthening. The incremental slip is found to be highly variable in both space (along the faults) and time, resulting in variable slip rates. In particular, 'short- and long-term' slip rates are markedly different. We also find that slip measurements at local points on fault traces do not contain clear information on the slip increment repeat mode. Finally, while the fault growth process is highly heterogeneous when considered at the scale of a few slip events, it appears homogeneous and self-similar at longer time scales which integrate many slip increments. This is likely to be the result of a feedback between stress heterogeneities and slip development. The long-term scale homogeneity also implies that the long-term faulting process is primarily insensitive to the short-term heterogeneities that are rapidly smoothed or redistributed. We propose a new conceptual scenario of fault growth that integrates the above observations and we suggest that faults grow in a bimodal way as a result of a self-driven and self-sustaining process.

1. Introduction

Faults generally grow, that is, accumulate slip and lengthen, through the repetition of earthquakes. Yet, how such a growth occurs is still unclear as we lack data documenting how earthquake slip events repeat on faults. Consequently, fundamental questions such as 'Do repeating earthquake slip events have similar amplitudes and lengths? Does any major slip event on a fault contribute to its further lengthening? How do repeating earthquake slips relate to cumulative displacements on long-term faults?' are still unanswered. We have only sparse information, arising partly from rare observations, and partly from models.

Paleoseismological data show that, in some cases, the paleo-slip events have followed at regular time intervals with similar amplitudes and lengths (e.g., Rockwell et al., 2001; Klinger et al., 2003; Haibing et al., 2005). This suggests that faults may grow by accumulating constant slip without lengthening. Yet, in other cases, the paleo-earthquakes are found to have occurred at irregular time intervals and to have been dissimilar in size and location (e.g., Weldon et al., 2004; Palumbo et al., 2004; Daeron et al., 2007). This behavior is a sign of greater complexities in the fault growth process. On the other hand, the analyses of long-term faults whose cumulative displacements are the sum of hundreds to thousands of earthquakes (e.g., Taylor et al., 2004) generally provide little information on those past earthquakes. They thus fail to establish a link between repeat of earthquake slip events and fault growth.

Contrasting with the scarcity of data is our capacity of producing models and qualitative scenarios depicting how faults may grow. These are rooted in *a priori* hypotheses, such as faults behaving as simple, narrow, elastic cracks with no cohesion, linear elastic behavior of the crust, and elastic rebound theory (e.g., Scholz, 2002 for a review). The community interested in earthquakes provides numerical models that describe how earthquake slip events repeat on faults depending on the level of stress/strain being accumulated and relaxed (e.g. Shimazaki and Nakata, 1980), and on some other parameters such

* Corresponding author. LGIT, Maison des Géosciences, BP 53, 38041 Grenoble cédex 9, France. Tel.: +33 476 63 51 70; fax: +33 476 63 52 52.
E-mail addresses: aloe.schlagenhauf@obs.ujf-grenoble.fr (A. Schlagenhauf), isabelle.manighetti@obs.ujf-grenoble.fr (I. Manighetti), jacques.malavieille@gm.univ-montp2.fr (J. Malavieille), stephane.dominguez@gm.univ-montp2.fr (S. Dominguez).

0012-821X/$ – see front matter © 2008 Elsevier B.V. All rights reserved.
doi:10.1016/j.epsl.2008.06.042

as friction on the fault plane (e.g. Tse and Rice, 1986; Rice and Ben-Zion, 1996). These models are useful as they can be directly compared with real earthquake slip data. By contrast, they are never compared with long-term slip measurements, so they do not provide any link between repeat of earthquake slip events and fault growth. On the other hand, the community more interested in overall fault behavior provides qualitative scenarios and more rarely numerical models that describe how faults may grow over long time spans (10^4–10^7 yr; Segall and Pollard, 1980; Walsh and Watterson, 1987, 1988; Peacock and Sanderson, 1991; Marrett and Allmendinger, 1991; Cowie and Scholz, 1992a,b; Bürgmann et al., 1994; Cartwright et al., 1995; Willemse et al., 1996; Cowie, 1998; Cowie and Roberts, 2001; Walsh et al., 2002; Kim and Sanderson, 2005). These scenarios are useful for comparison with real long-term slip measurements, but they are rarely confronted with earthquake slip data or with earthquake mechanics. They do therefore also fail to provide a link between repeat of earthquake slip events and fault growth.

Our objective is to explore an alternative field between observation of natural faults and developments of *ad hoc* models. We aim at examine and better understand how slip increments follow in space and time on a fault to make it grow. We address that topic through an analog experiment that allows for a large number of normal faults to form and grow under homogeneous conditions, while their surface lengths and slips are measured quasi- continuously with an interferometric laser system. Although this approach does not reproduce the earthquake process, it sheds light upon the way faults progressively gain in slip and length as they accommodate more strain. Note that, while many analog models have already been produced to simulate fault development (with a particular focus on normal faults; e.g. Horsfield, 1977; Faugeres and Brun, 1984; Ackermann et al., 2001), with a few of them being monitored (Mansfield and Cartwright, 2001; Bellahsen et al., 2003; Marchal et al., 2003; Bellahsen and Daniel, 2005), this is the first time that the incremental fault growth is measured quasi-continuously, and at such a high resolution. This is also the first time the analysis is carried out with a sufficiently dense population of incremental slip events to identify common properties.

2. Experimental protocol

2.1. Experimental design and scaling

We study normal faults because their displacements can be easily measured at the model surface. Since we seek identifying general, intrinsic properties of the fault growth process, we need make the faults developing in the absence of any local complexity. Heterogeneous stress boundary conditions, variations of material properties, influence of preexisting discontinuities, etc… are as many factors – not systematic in nature – that may indeed modify the fault growth process (e.g. Bürgmann et al., 1994; Buiter and Schreurs, 2006). To avoid such possible effects, we have developed a new analog protocol that allows normal faults to be formed and grown in a homogeneous material and a homogeneous stress field. It is important to note that most available analog models do not fulfill the later condition (details in supporting online material A). We adopt, with some modifications, the approach developed by Schreurs et al. (2002). The model is constructed on top of a thick foam bar that has been previously shortened by compression. The foam bar is then let to progressively 'decompress', which transfers a continuous, homogeneous extension over the width of the overlying model. For reasons explained in many

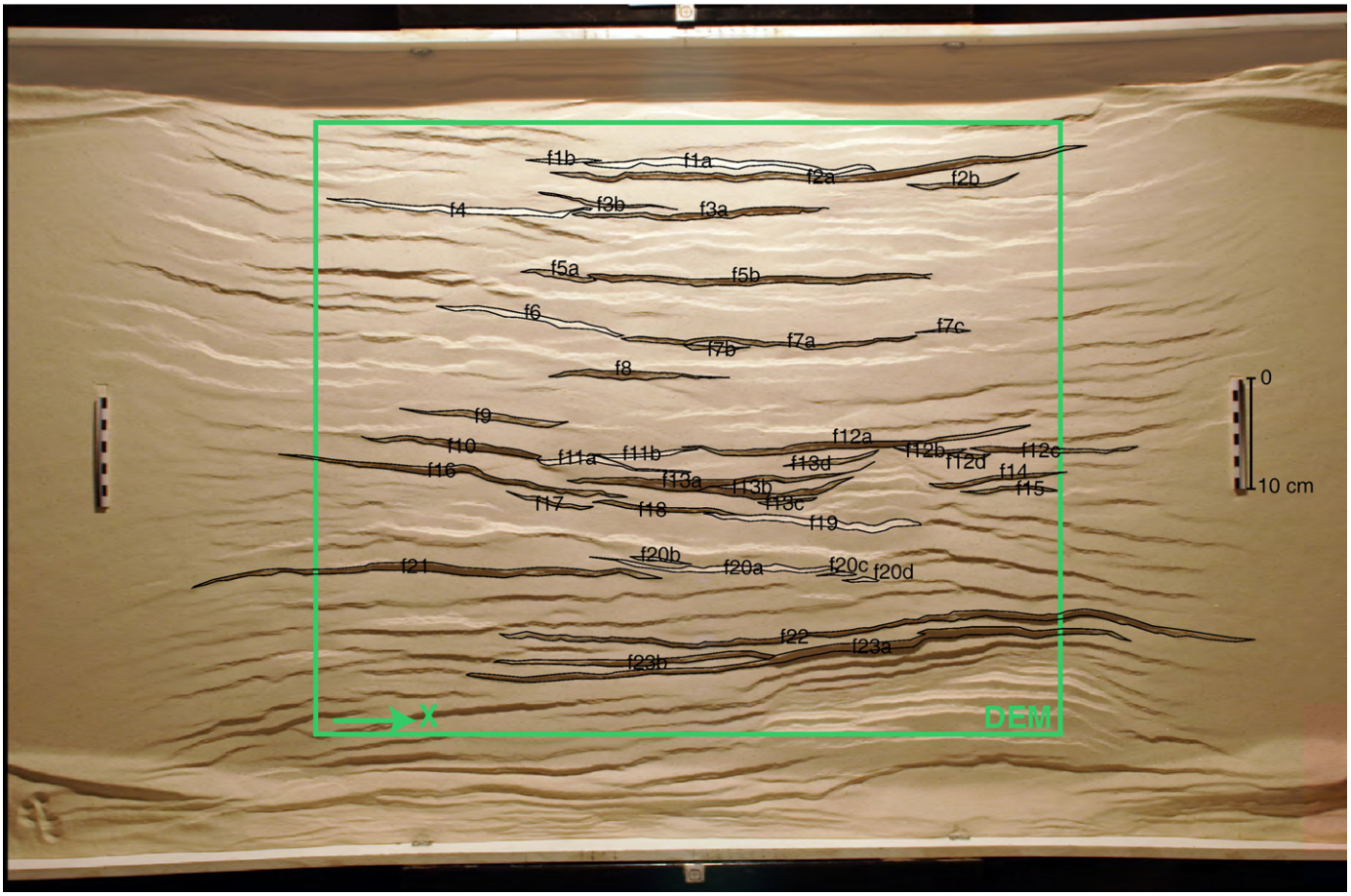

Fig. 1. Map view of the analog model at the end of the experiment. The frame is the zone under study. Analyzed faults are circled in black, with their names indicated. Synthetic and antithetic faults appear in different tones due to shading.

papers (e.g., Hubbert, 1937; Davy and Cobbold, 1991; Lallemand and Malavieille, 1992; Lohrman et al., 2003; Buiter and Schreurs, 2006), dry quartz sand is used to approximate the brittle crust. The one we use is 98.5% made of SiO_2, has a mean density of 2.1, and a mean grain size of 112 μm. The scaling factor that results is $1–2.10^{-5}$ (1 cm in the model represents 1–2 km in the field). Since we want to produce a large number of growing faults, the model does not include any basal material such as silicone putty that would make strain localizing onto a few large faults only (e.g. Davy et al., 1995; Bellahsen et al., 2003).

The apparatus is presented in supporting online material B. In a first step, the foam bar is compressed by 25% between two metallic jaws. Then an 8 cm-thick layer of sand is deposited on top of the compressed foam. The model is sprinkled with a thin powder (25% silica, 74% sand, and 1% black rubber dust; not a rheological interface) aimed at increasing its surface cohesion while allowing 'ground reference points' to be defined. Then the foam bar is progressively decompressed from operating back the two jaws; the decompression transfers extension to the overlaying sand layer. The plastic-made sidewalls of the apparatus avoid longitudinal compression to develop in the sand cake, so that the strain field imposed at the base of the model is homogeneous in its central part (i.e., between the jaws), and decreases to zero on either side. Our study only focuses on the model central part (frame, Fig. 1).

Note that we have repeatedly performed the above experiment to ensure the strength of the results that we describe below. We have in particular varied the thickness of the sand cake; that of 8 cm revealed to be a good compromise between the number of faults being produced and the height of their surface escarpments.

2.2. Measurements

Measurements were performed at each 1 mm-decompression step, hence quasi-continuously. Yet, for clarity and brevity reasons, we only describe results at each 1 cm-step. In total, we decompressed the bar by 12 such steps, making the foam still slightly compressed by the end of the experiment. The total experiment corresponds to having stretched the sand model by 20%, by successive steps of 1.7%.

First, numerical high-resolution pictures were taken with a camera at each 1 mm-extension step. The combination of these pictures allows the space-time evolution of the faults to be visualized quasi-continuously (supporting movie, online material C). Second, the model was equipped with an interferometric laser system allowing accurate (pixel size 0.3 mm) digital elevation models (DEM) of the sand surface to be constructed at each step. The laser system operates as standard Radar Interferometry (e.g., Bürgmann et al., 2000) and is described in Graveleau and Dominguez, 2008. Twelve DEMs were constructed to monitor the evolution of the model topography at every 1 cm step of extension. From each DEM, we extracted elevation profiles following the top and base of the fault scarps. Where a fault trace had several closely spaced strands at the same along-strike

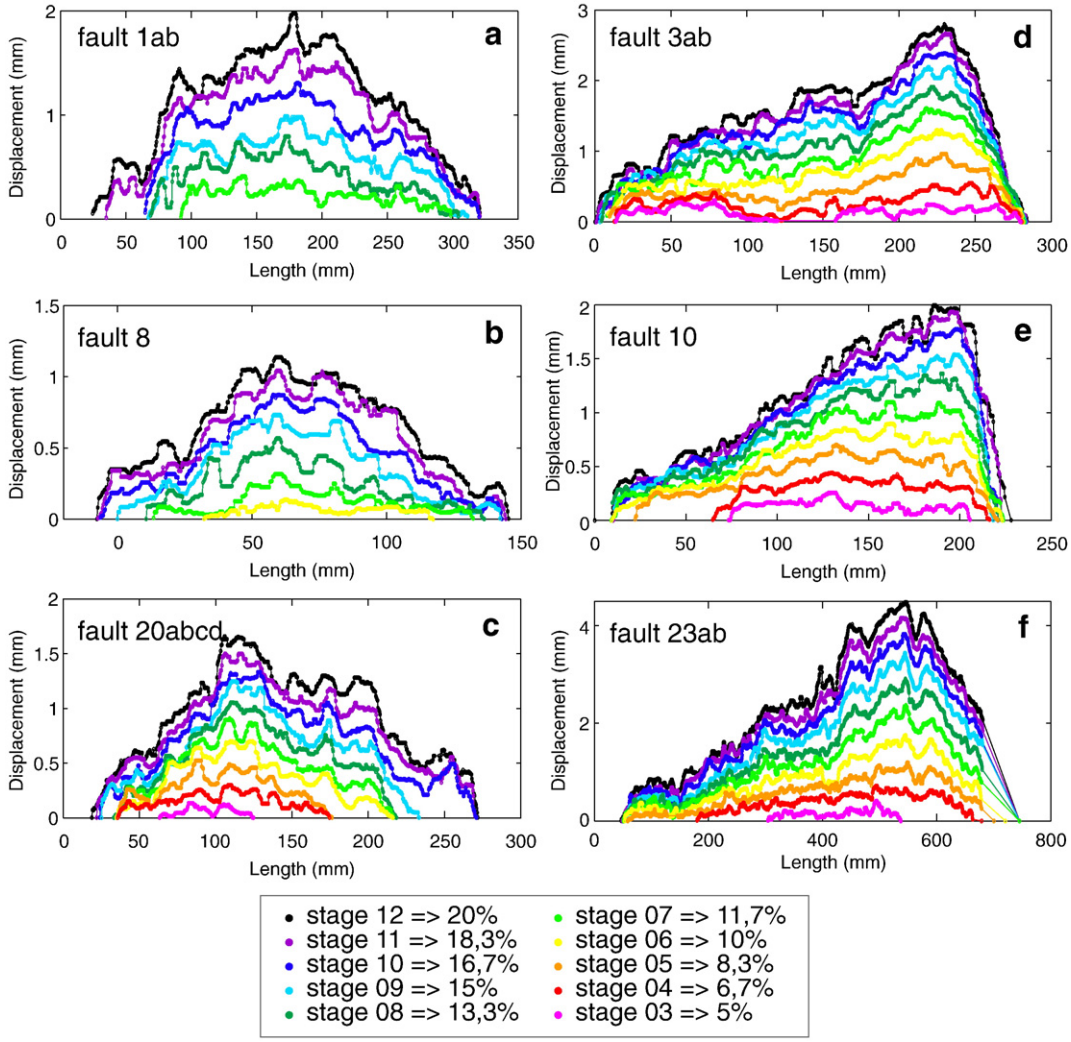

Fig. 2. Slip-length profiles on six example faults (location in Fig. 1). Naming a fault 'ab' for instance means that the fault, that contains two segments a and b, is considered as a whole. The color scale indicates the successive time steps, in percentage of extension. Stages 1 and 2 do not appear because no surface escarpment was formed at these stages.

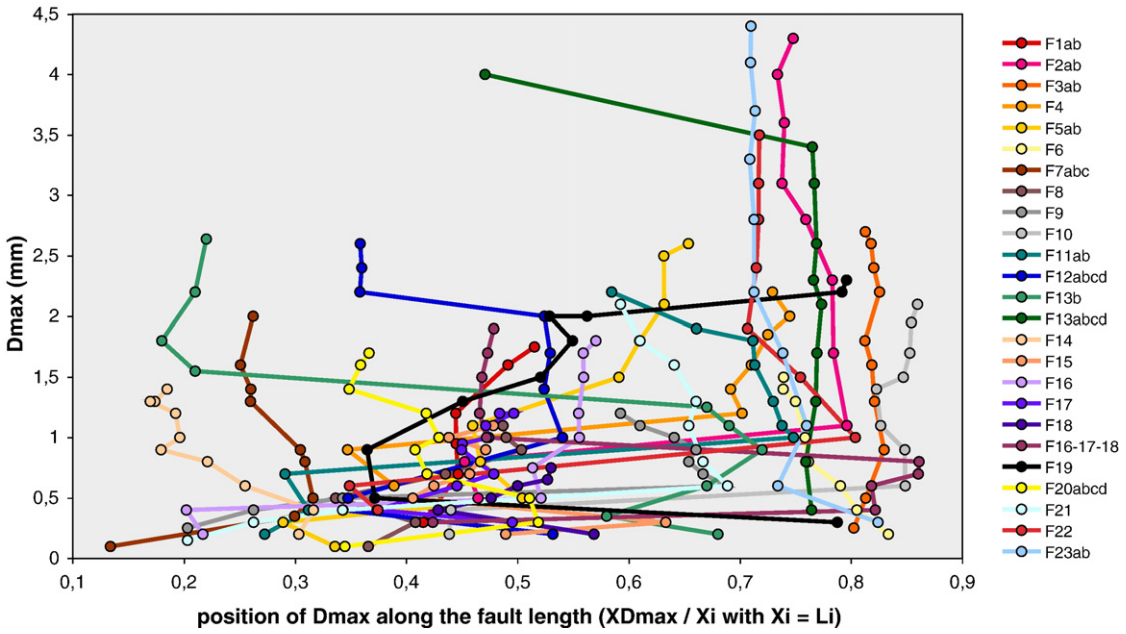

Fig. 3. Variation over time of the along-strike position of the maximum displacement D_{max}. Each point represents the position of D_{max} at each stage of the fault growth, hence is (XD_{max}/X_i), with X_i the length of the fault at stage i, and $X=0$ taken at the left tips of the faults. For clarity reasons, only the largest faults are represented.

position, the extracted profiles were made to include them. From the top and base profiles, we calculated the variation of vertical displacement along strike. The faults have steep scarps (≥60°) so that those vertical displacements approximate the actual fault slips. Results were then plotted as strike-parallel vertical projections for analysis (Fig. 2). Overall, about 100 faults formed and evolved in the interior of the central frame (Fig. 1). We restricted our analysis to the largest ones. A few faults initiated in the central frame and propagated outside of it. We considered only those that ended hardly beyond the frame. In total, we thus analyzed a population of 30 faults, synthetic and antithetic, representing a total of 250 incremental slip profiles.

2.3. Errors

Most faults have lengths that rapidly (at most, over the first third of the experiment) became greater than twice the thickness of the sand layer, which they thus cut through. We are thus confident that the 2D measurements of lengths and displacements performed at the model surface are representative of the 3D fault evolution at depth, at least over the last two thirds of the experiment.

Errors on the measurements have multiple sources. The largest likely arises from the hand- extraction of the elevation profiles, particularly during the first stages of growth when fault traces are

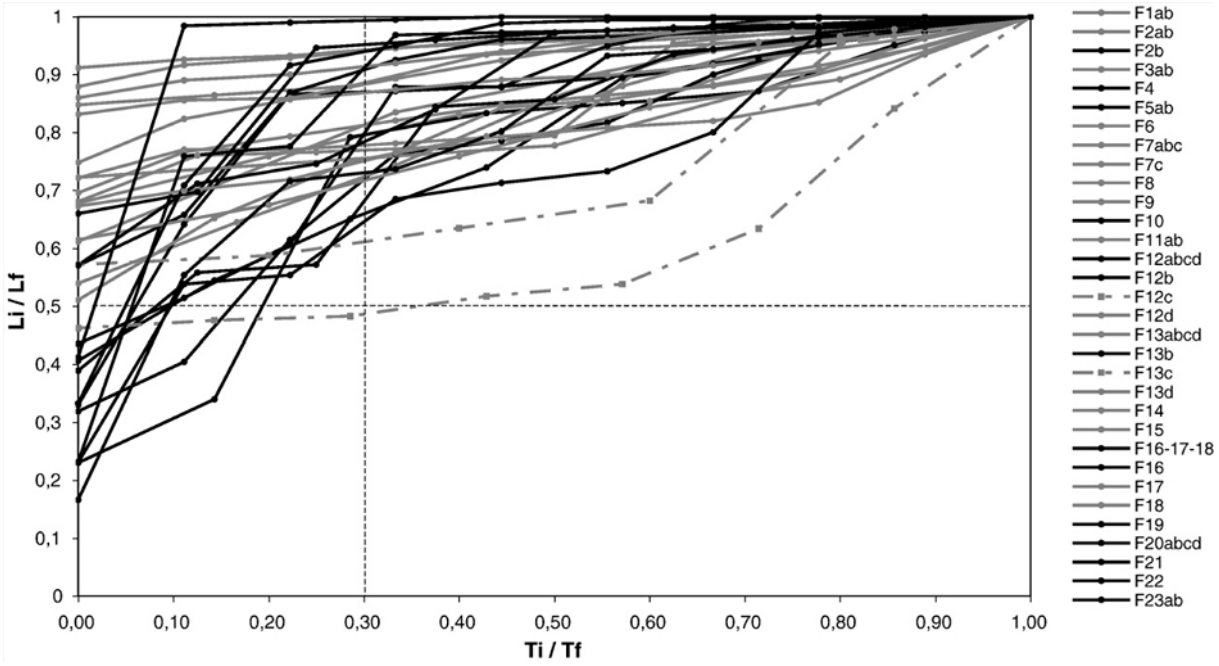

Fig. 4. Fault length increase as a function of time. On the X axis, time (T_i) is normalized by the total duration of the fault growth (T_f). On the Y axis, the length (L_i) is normalized by the final total length of the faults (L_f). See discussion in text.

tenuous. The smallest slips that we could distinctly measure in the first stages of the experiment are 0.1–0.15 mm, and happened to be on faults a few cm-long. Also, the granular nature of the sand introduces a roughness of ≈0.1 mm. The calibration of the laser introduces a periodic noise in the DEMs, having an amplitude and a wavelength of 0.25 and 10 mm, respectively. We removed that noise by slightly filtering the slip profiles (supporting online material D). From the combination of the errors above, we estimate that fault length and slip are determined with a maximum error of a few mm and of 0.1–0.15 mm, respectively, over most of the experiment but the very first stages. In those first stages (at most, stages 1–4), fault length may be underestimated by a few cm.

3. Data analysis

The experiment is presented as a movie in supporting online material C. Most faults start forming surface traces soon after extension has begun. Faults initiate evenly over the central section of the model, which confirms that the extensional stress field is homogeneous. Fault traces evolve from tenuous zones of dilatance in

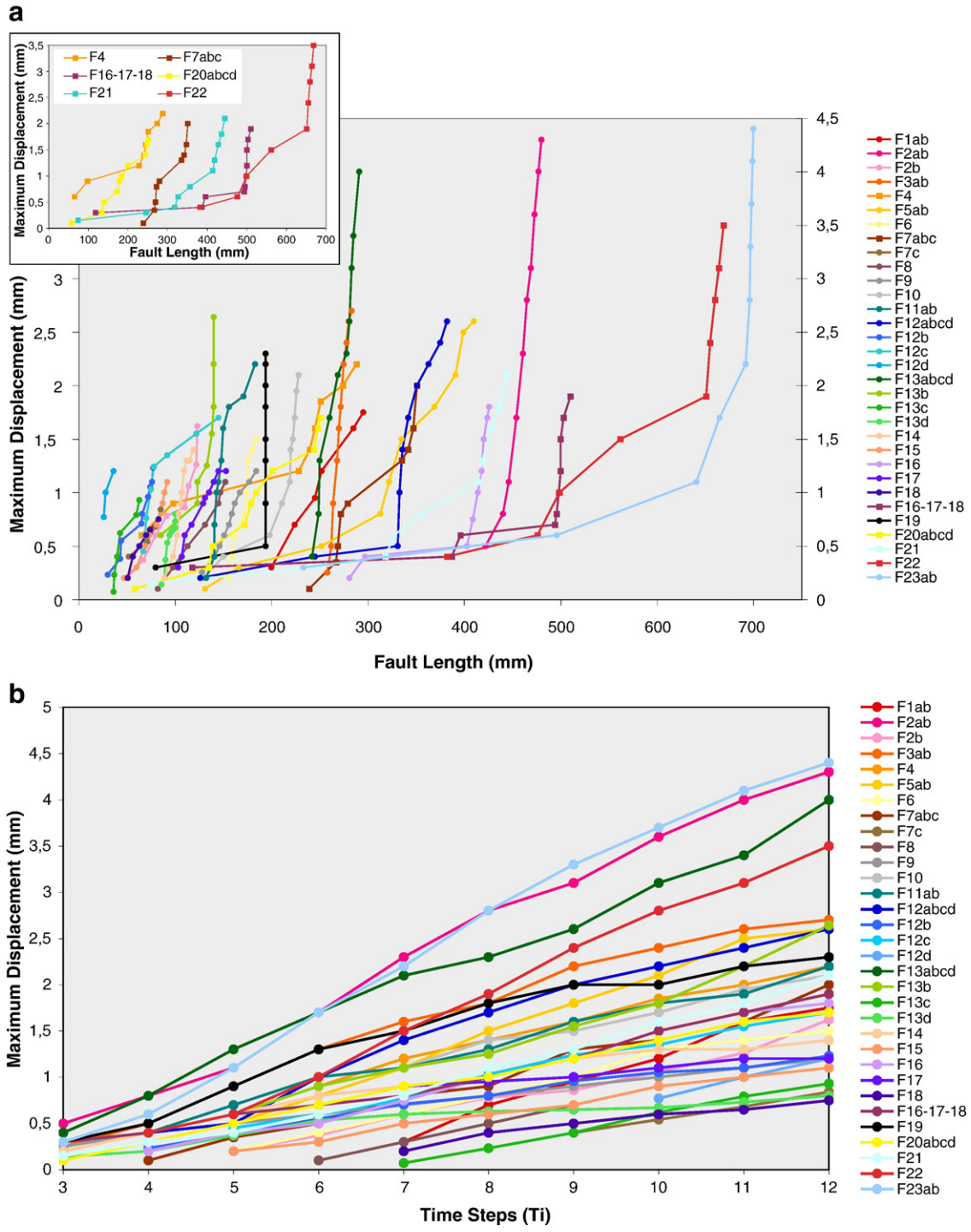

Fig. 5. a) Evolution of maximum displacement with fault lengthening. Faults possibly sustaining alternating phases of dominant lengthening and of dominant slip accumulation are highlighted in inset. b) Evolution of maximum displacement with time. See discussion in text.

the first stages, to topographic escarpments that grow higher and longer as extension increases. In the following, we define 'fault initiation' as the stage when vertical displacements become resolvable at the surface (stages 3 or 4, at most 5% extension). 'Slip' and 'displacement' are used similarly. Maximum displacement is noted D_{max}. A 'slip increment' (or 'slip event') is the slip-length change recorded by a fault at the model surface as the model sustains an additional 1 cm-step of extension. 'Slip rate' is used to describe the displacement accumulated over a specific time span.

3.1. Overall shape of the slip profiles

As they grow, faults develop slip profiles that generally have a well-defined envelope shape (Fig. 2). Two types of shapes are most commonly observed, that of a symmetric triangle (Fig. 2a-b-c) and that of a strongly asymmetric triangle (Fig. 2d-e-f). A few more complex shapes are found; yet they generally arise from the evolution of triangular shapes (supporting online material E). These more complex shapes have in common to exhibit high slip gradients at both tips. In some cases, faults maintain the same overall shape as they grow (ex: Fig. 2a-b-d-f); in other cases, the shape of the slip profile changes as the fault grows: although still triangular overall, it shifts from symmetric to asymmetric (ex: Fig. 2c-e) or vice-versa. This shows that the position of the maximum displacement may vary in time along a fault (Fig. 3). While the slip profiles show any degree of asymmetry in the very first stages of growth (Fig. 3 and supporting online material F-a), they pertain to only two categories, symmetric or asymmetric, in the last stages (supporting online material F-b). Commonly, asymmetry and high slip gradient develop where a growing fault meets another, generally oblique or antithetic fault (supporting online material C).

3.2. Fault lengthening versus slip increase — overall behavior

Fig. 4 and supporting online material G show the evolution of fault lengths as a function of time. About 45% of the faults (black, Fig. 4) initiate with a 'short' length generally less than half their final length, then rapidly lengthen laterally in the following few stages so that, at 30% of the experiment, they have reached a length almost as long as their final one. About 50% of the faults (grey, Fig. 4) conversely initiate with a length more than half their final length, then hardly lengthen further laterally over the whole experiment. Note that, because fault lengths may be underestimated in the very first stages of the experiment, the 50% value is a minimum. Finally, two faults (dotted grey, Fig. 4) initiate with a length averaging their half final length, then hardly lengthen during most of the experiment but at the very last stages when they resume lengthening. Together these show that at least 80% of the faults achieved 70% or more of their final length in the first third of the faulting history. This demonstrates that faults grow in two distinct, successive phases. They sustain an initial phase when they essentially gain in length and this occurs rapidly; then they sustain a subsequent period when they go on growing without much lengthening.

Whether they are lengthening or not, faults accumulate vertical slip (Fig. 5a). The variation of maximum displacement versus time plots roughly as a straight line for each fault (Fig. 5b), suggesting a roughly regular vertical growth. The fan-looking distribution of the D_{max}-Time curves further suggests that the vertical growth is more or less rapid depending on which fault is concerned; the shortest faults seem to be those most slowly increasing in slip (Fig. 5a). When variations of D_{max} are scaled to fault size (Fig. 6), they appear roughly similar for all faults but the smallest ones. Hence, although it occurs at different rates, and although the locus of maximum slip may move over time along the faults, the vertical growth, here taken as the progressive increase in D_{max}, is homogeneous and regular overall.

Fig. 7 depicts how the ratio of maximum displacement over length (D_{max}/L) varies as the faults lengthen. When faults are in a stage of rapid lengthening (Fig. 7a), their D_{max}/L ratio keeps roughly constant, on the order of $1–2.10^{-3}$. By contrast, when faults are in a stage of slip accumulation with little or no lengthening (Fig. 7b), their D_{max}/L ratio increases as the faults accumulate more slip (up to one order of magnitude). It results that the D_{max}/L ratios spread a broad range of values when the whole fault population is considered over the whole time of the experiment (supporting online material H). Faults with triangular profiles (red and orange) seem to have lower D_{max}/L ratios than faults whose profiles end with high slip gradients (blue).

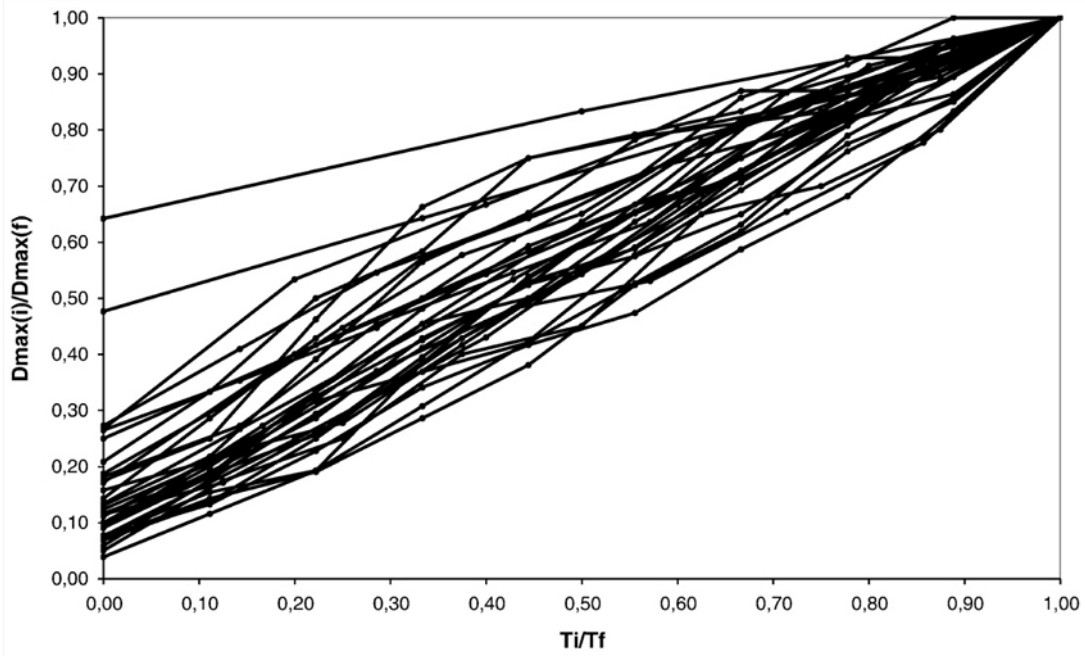

Fig. 6. Increase in vertical slip as a function of time. On the *X* axis, time (T_i) is normalized by the total duration of the fault growth (T_f). On the *Y* axis, the maximum slip ($D_{max}i$) is normalized by the final total maximum displacement on the faults ($D_{max}f$).

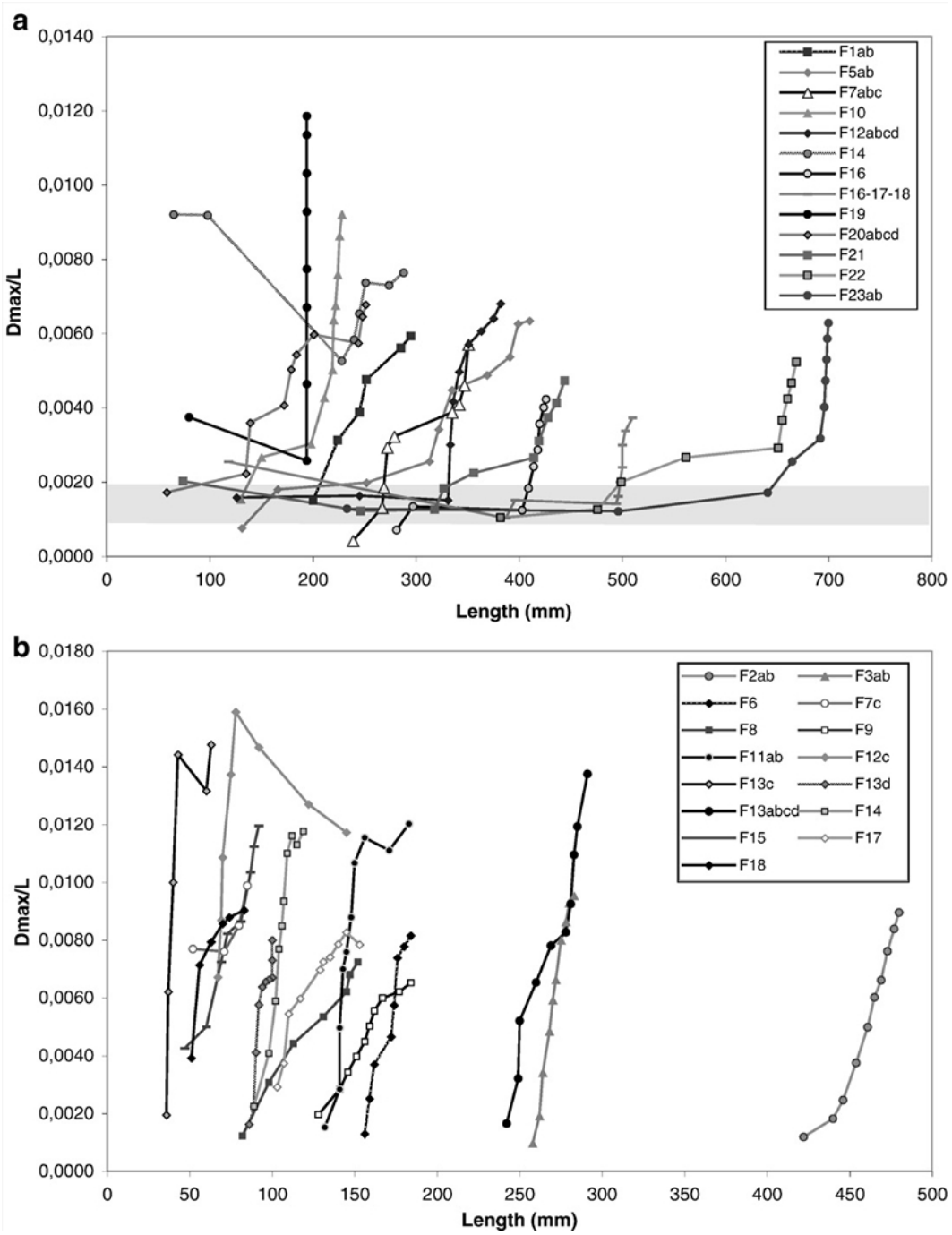

Fig. 7. Variation of the D_{max}/L ratio with fault lengthening. a) Faults whose growth starts by an observable, rapid lengthening phase. That occurs at roughly constant D_{max}/L ratio (grey horizontal bar). b) Faults whose initial lengthening phase is too rapid to be observed (it occurred at less than 5% of extension); those faults thus appear as mainly growing by increasing their slip. See discussion in text.

3.3. Fault lengthening versus slip increase — small-scale features

Additional observations can be made when fault growth is analyzed in greater details. While most faults show an initial phase of rapid lengthening, they do not extend similarly (supporting online material I). In most cases, the fault looks as lengthening continuously (at the resolution of the experiment), through the lateral propagation of one or both of its tips. In other few cases, the fault lengthens abruptly by connecting to another, initially distinct, fault segment. Generally, that segment initiates just ahead of the expending tip of the main fault, hardly before the connection is made. In more rare cases, the segment initiates at some distance from the expending fault, much before the connection occurs.

Fig. 8 shows the details of the incremental growth of two example faults. The faults look like made of small patches that slip differently in both space and time. At any one time-step, the faults slip along their entire length but the slip distribution is highly heterogeneous. At any stage of growth, several patches along the fault slip by large amounts while other zones hardly or do not slip at all (top plots). Moreover, at any stage of growth, there are several, distinct areas along the fault that slip by similar large amounts (middle plots). These large slip zones are not necessarily where the final displacement is the largest,

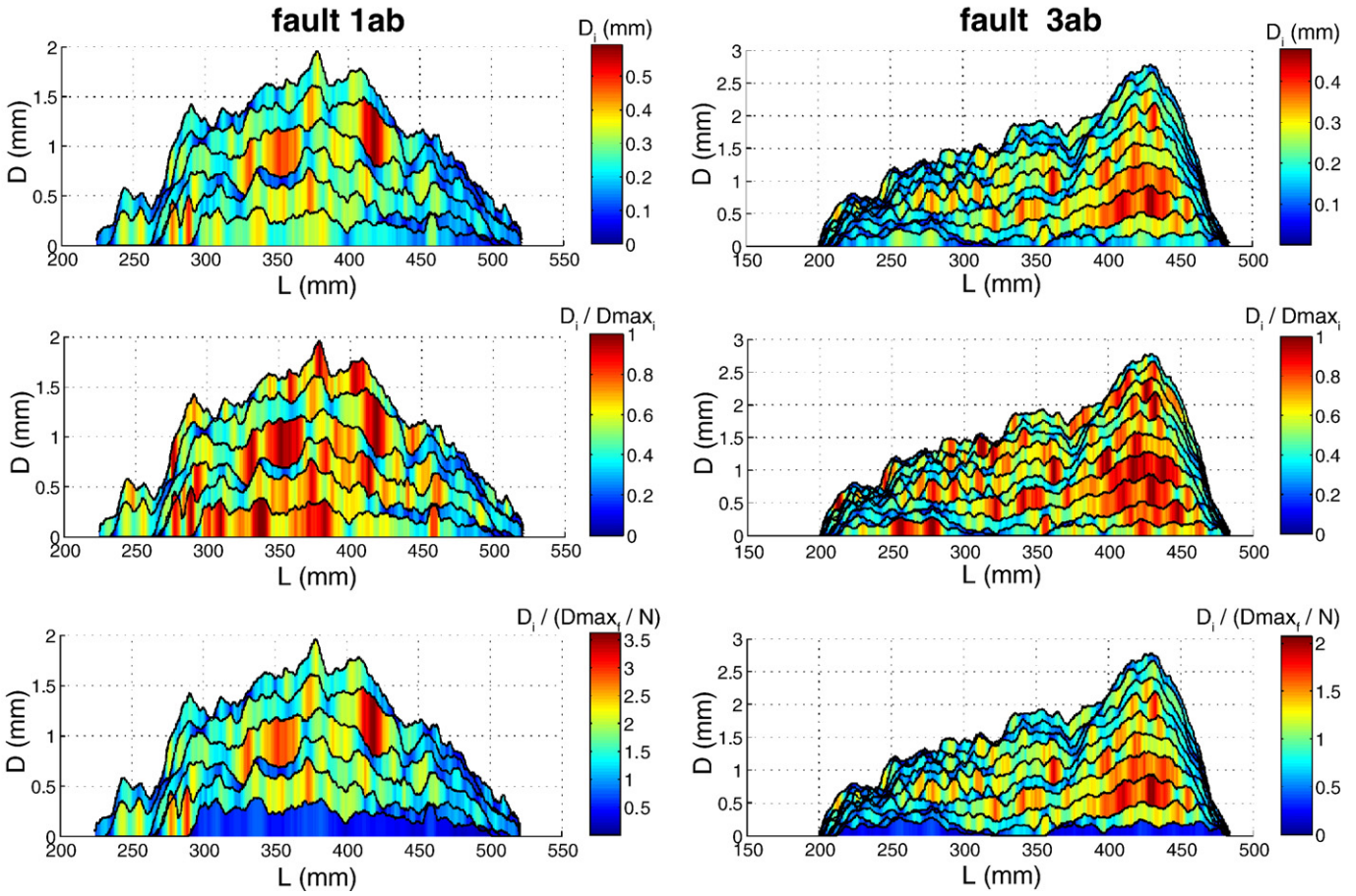

Fig. 8. Space-time slip variability during fault growth. For both fault examples, top plots present the successive slip increments in absolute amplitude (mm); middle plots present the slip increments each normalized by its maximum slip value ($D_{max}i$); bottom plots present the slip increments each normalized by the average value of the maximum slip ($D_{max}f/N$, with $D_{max}f$ the maximum slip value at the end of the experiment and N the number of slip increments).

though the zone of final D_{max} is among those slipping most. It is important to note that most of the slip patches do not coincide with any clear segment along the fault trace. Slip increase also varies in time. At any point along a fault, slip increases by variable amounts, commonly alternating from being large to being small (top and middle plots). This results in any slip gap being eventually 'filled' over the entire fault history. The time over which the gap is filled is variable; it is longer in zones where distinct segments have eventually connected. One can note that the incremental slip is generally either much larger (yellow to red, bottom plots) or much lower (pale to dark blue, bottom plots) than the average value that one would infer from scaling the total final slip by the number of slip increments. Finally, the figures also suggest that faults generally grow a bit slower (in term of slip increase) at both the beginning and end of their history (bottom plots).

4. Discussion

Having analyzed before hundreds of natural fault slip profiles, both long-term (Manighetti et al., 2001) and co-seismic (Manighetti et al., 2005), we cannot avoid noting that the analog profiles share many common features with the natural ones. This suggests that the experimental observations are meaningful, and that those common features are inherent properties shared by natural and analogue faults.

4.1. Common features to natural and analog slip profiles

A first feature common to natural and analog slip profiles is their triangular, and commonly asymmetric, envelope shape. Indeed, while it has long been thought that geological faults had elliptical or bell-shaped slip profiles in accordance with the predictions of the elastic crack theory (e.g. Pollard and Segall, 1987; Cowie and Scholz, 1992a,b; Scholz, 2002), a number of recent observations show that faults more commonly exhibit triangular slip distributions (Peacock and Sanderson, 1996; Nicol et al., 1996; Cowie and Shipton, 1998; Cartwright and Mansfield, 1998; de Joussineau et al., 2001; Manighetti et al., 2001 for normal faults; Ellis and Dunlap, 1988; Shaw et al., 2002; Davis et al., 2005 for reverse faults; Pachell and Evans, 2002 for strike-slip faults). Besides, although most available fault models assume that maximum displacement is at the fault center (e.g. Pollard and Segall, 1987; Cowie and Scholz, 1992a; Willemse et al., 1996; Cowie and Shipton, 1998; Kim and Sanderson, 2005), natural faults more commonly show asymmetric slip profiles (e.g. Peacock and Sanderson, 1991; Cartwright and Mansfield, 1998; Maerten et al., 1999; Manighetti et al., 2001; Shaw et al., 2002; Pachell and Evans, 2002; Davis et al., 2005). We make similar observations here; most analog faults grow by developing asymmetric, triangular slip profiles, basically made of a long linear section gently tapering to zero at one fault tip while ending through a high slip gradient at the other fault tip. As for natural faults, the long linear sections slant in the direction of fault lengthening (ex: faults e-f, Fig. 2). Also as for natural faults, the high slip gradients develop where the fault meets an 'obstacle' (or 'barrier') to its further lengthening (as an example, see the right tip of fault 3ab in figures 1 and 2d). That is commonly a parallel antithetic fault. Thus, as for natural faults, a slip profile remains symmetric as long as the fault has not met any barrier, and starts distorting once one fault tip at least has met an obstacle to its further lengthening. In that case, the zone of

maximum slip progressively translates toward the 'arrested' tip, where it may subsequently remain stable for a long time. Yet if the other fault tip also meets a barrier, the zone of D_{max} may shift again laterally. Thus the position of D_{max} may change over the fault lifetime. Furthermore, the zone where slip ends to be largest does not necessarily coincide with the locus of fault initiation, as it has been suggested (e.g. Ellis and Dunlap, 1988). It is important to note that the development of long linear sections in the slip profiles is not in keeping with the elastic crack theory (see Manighetti et al., 2001 for an extended discussion). One way to reconcile these profiles with that theory is to admit that the excess stresses that they produce on the fault plane are diffused off that plane, possibly in the form of distributed damage (Manighetti et al., 2004). We do not have the resolution to verify whether or not such diffuse deformation occurs nearby the linear slants.

A second feature common to natural and analog faults is their bimodal mode of growth; faults are found to grow in two successive phases, an initial period of dominant, rapid lengthening, and a subsequent phase of dominant slip increase with no or little lengthening. Both phases have been observed in natural cases, but the scarcity of available data in respect to the long fault lifetimes (10^5–10^7 yr) has not allowed describing them in detail (Armijo et al., 1996; Morewood and Roberts, 1999; Contreras et al., 2000; Poulimenos, 2000; Goldsworthy and Jackson, 2001; Meyer et al., 2002; Walsh et al., 2002; Gawthorpe et al., 2003; Childs et al., 2003; Taylor et al., 2004; Bennett et al., 2005; Nicol et al., 2005). The numerical modeling and analog experiment of Cowie and Shipton (1998) and Mansfield and Cartwright (2001) respectively, also suggest the existence of such two phases, but the data are too few to describe them in detail. The initial lengthening phase is brief, hardly more than the third of the fault lifetime (considering the experiment duration as the 'lifetime'), while the lengthening is rapid with most faults reaching more than their half-final length by the end of that initial phase. The lengthening generally occurs through the lateral propagation of the fault tip(s) (see Marchal et al., 1998, for similar observations). We do not have the resolution to determine whether or not the fault tip propagation is a continuous process. Nor do we have the resolution to depict how some faults initiate with a length almost as long as their final one. In any case, such initial long lengths do not result from pre-existing structures being reactivated as suggested or observed in some natural cases (Meyer et al., 2002; Walsh et al., 2002; Nicol et al., 2005; Kim and Sanderson, 2005), nor from the linkage of simultaneously formed major segments, as commonly proposed (e.g., Cowie and Roberts, 2001). While they are lengthening, the faults accumulate some slip. The process is homogeneous overall, such that the D_{max}/L ratio remains constant on each fault and similar for all faults (2 ± 1.10^{-3}). This suggests that faults behave as elastic cracks with constant stress drop during their initial lengthening phase. Following the initial period of rapid lengthening, the faults enter a subsequent phase during which they mainly accumulate vertical slip while hardly or no longer lengthening. Note that while many faults stop lengthening when at least one of their tips has met a barrier, that condition is not required. The phase of dominant slip accumulation is homogeneous as far as it is considered overall. The maximum displacement increases quite regularly on each fault, and in same proportions for all faults. Such a homogeneous vertical growth results in the cumulative slip profiles keeping the same overall shape, – only distorted vertically – as the faults accumulate more slip. Overall, the phase of dominant slip accumulation lasts longer than that of lengthening, generally about two thirds of the fault life. It makes the faults increasing their D_{max} by 300% on average (and up to 700%; in respect to the value of D_{max} at the beginning of the slip accumulation phase). The D_{max}/L ratios increase accordingly during that phase, making the faults not behaving as elastic cracks and not having similar stress drops. By the end of the experiment, most faults still are in a phase of slip accumulation at constant length. We thus have no data to document how the faults go on growing as they accumulate even more strain. In natural cases, it has been found that faults do not accumulate slip over a maximum threshold D_{max}/L ratio averaging 10^{-1} (e.g., Manighetti et al., 2001). This implies that faults must lengthen laterally once they have reached that maximum slip accumulation ratio. This would suggest that faults may resume lengthening by the end of a phase of dominant slip accumulation. The inset of Fig. 5a indeed shows a few fault cases that resume lengthening by the end of a slip accumulation phase. It is noteworthy that those few faults have in common to have their tips not being arrested by any clear barrier (see example faults, f6, f11ab or f19 in Fig. 1), contrary to the rest of the faults. This suggests that faults pinned at both ends may accumulate more slip without lengthening than unrestricted faults. The same conclusion has been reached for natural cases (Manighetti et al., 2001). Note that, when resuming after a slip accumulation phase, the lengthening occurs through the connection of the main fault with a smaller segment ahead of its tips(s), hence differently than over the initial lengthening period.

A third feature common to analog and natural faults is their capacity of being together homogeneous and heterogeneous; while the fault growth process is clearly homogeneous overall, it is highly irregular in detail. This duality has been suggested for a few geological faults (e.g. Manighetti et al., 2001; Bull et al., 2006), as in a few analog and numerical experiments (Cowie and Shipton, 1998; Mansfield and Cartwright, 2001). The balance between regularity and irregularity roots in the time scale. When the fault growth is considered over a long time span that includes many slip increments, it appears homogeneous; the slip profile maintains the same envelop shape; the slip and length increases are regular overall. In contrast, when the fault growth is considered over time scales that are short in relation to the entire fault history, it appears highly heterogeneous; the slip profile shape exhibits saw-tooth patterns; the slip and length increases are markedly variable in space and time.

4.2. Implications on D_{max}/L 'scaling'

The bimodal growth of the faults causes their maximum displacement and length to change by various proportions over time. As recognized by Mansfield and Cartwright (2001) and Walsh et al. (2002), those changes produce irregular growth paths in D_{max}-L space, that diverge from the roughly linear relationship that has been derived from available natural D_{max}-L data ($D_{max} = k \cdot L$ with $k \approx 10^{-2}$; e.g., Schlische et al., 1996; Manighetti et al., 2001; Davis et al., 2005). The question then arises of whether or not a scaling of the form $D_{max} = k \cdot L$ may be used to prescribe the way natural faults are growing (e.g. Cartwright et al., 1995; Mansfield and Cartwright, 2001). Our experiment suggests that the answer roots in the time scale over which the fault growth process is analyzed. When that process is considered over time scales that are short in relation to the entire fault history, the scaling does not apply and data exhibit a broad range of scatter (Fig. 5a). This has been shown to be true in natural cases: on the shortest time scale which is that of individual earthquakes, displacement and length of ruptures are clearly not related by a unique function (Manighetti et al., 2007). By contrast, when the fault growth is considered over a long time span including a large number of slip increments, the linear scaling likely applies, as revealed by the natural data. Thus, for natural faults whose growth history is unknown, the D_{max}-L measurements may be difficult to interpret. Manighetti et al. (2001) have shown that the D_{max}/L ratio of a fault depends on the overall shape of its slip profile: profiles unrestricted at both tips (symmetric triangles) have the lowest ratios reaching at most 2.10^{-2}; those restricted at one tip (asymmetric triangles) have higher ratios with a threshold value of $3–4.10^{-2}$; those pinned at both tips have the highest values up to 10^{-1}. This suggests that the combined knowledge of a fault slip profile shape and of its corresponding D_{max}/L ratio may indicate the current 'growth mode' of the fault: dominant slip accumulation if the measured ratio is far

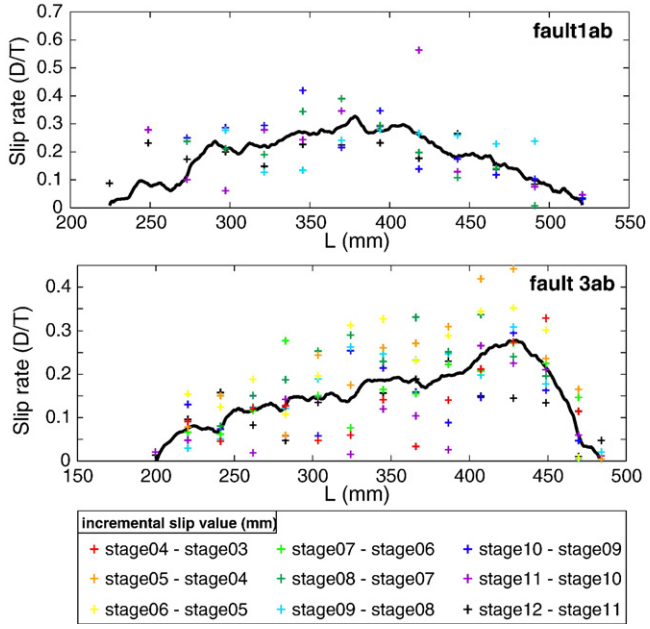

Fig. 9. Comparison of 'long-term' and 'short-term' slip rates. For both fault examples, the black curve is the long-term slip rate profile that one would infer from dividing the final cumulative slip profile by the total number of growth time steps. Conversely, the color crosses represent the short-term slip rates that one would infer from dividing each incremental slip value by one single time lapse. Colors indicate, as before, the succession in time.

below the threshold value corresponding to its profile shape; dominant lengthening if that ratio is close to the threshold value. Though more variable, our analog data are in keeping with that inference (supporting online material H).

4.3. Implications on space-time slip and slip rate variability

Determining the rates at which faults slip is a critical issue for these rates indicate the degree of activity of the faults (e.g. Nicol et al., 1997). Numerous studies have thus been conducted in the last 30 yr to determine the past and present motion rates on the major active faults worldwide. Most, however, have restricted their analysis to a single slip rate determination at one spot of the fault length (e.g. Wright et al., 2004; Frankel et al., 2007). The underlying assumption is that the slip rate does not vary much along fault strike. Our experiment suggests that this may be incorrect. At any instant of the fault evolution, the displacement varies markedly along the fault length; so thus would the slip rate. Studies providing several slip rate estimates along a fault actually reach the same conclusion (e.g. Tapponnier et al., 2001; Taylor et al., 2004; Bull et al., 2006). Most studies that report slip rates also implicitly admit that fault rate does not vary much either in time (e.g. Wright et al., 2004). Our experiment shows that this may be incorrect. Fig. 8 shows that slip varies widely in time at one given spot of the fault length. Fig. 9 is even clearer. In each plot, the black curve is the mean slip rate that one would infer from measuring and dating the total cumulative slip profile. It is thus equivalent to the long-term slip rate profile. The colors dots are the slip rates that one would infer from measuring the slip produced at each step of the growth, with the step duration being known. The black curve clearly results from highly variable slip rates being averaged. This shows that, at any spot of the fault length, the slip rate averaged over a long time span is far different, by an order of magnitude, from the slip rate averaged over a short time span. The incremental rate is particularly low both in the very first and very last stages of the fault growth. The experiment thus demonstrates that the slips and slip rates on faults are markedly variable in both space and time. A similar conclusion has been reached in the rare studies that analyzed the natural fault slip behavior at different space and times scales (e.g. Weldon et al., 2004; Chevalier et al., 2005; Bull et al., 2006). One consequence is that the common assertion that earthquake ruptures showing a similar slip amplitude at one local spot of a fault are characteristic (e.g. Nishenko and Bulland, 1987; Rockwell et al., 2001; Klinger et al., 2003; Haibing et al., 2005) is likely erroneous.

4.4. Proposed scenario of overall fault growth

Fig. 10 presents a scenario of overall fault growth that includes the major observations described above. That scenario is only qualitative for modeling the physics of faulting and earthquakes is not the scope of the paper. Also, it only describes the general features of the growth process for a fault that would ideally remain isolated throughout its evolution. Integrating the small-scale complexities of the fault evolution is a further step of work.

In a first phase (Fig. 10a), the fault rapidly propagates laterally while accumulating slip in proportion so that, overall, the fault behaves as an elastic crack. At this stage, the lengthening likely occurs continuously.

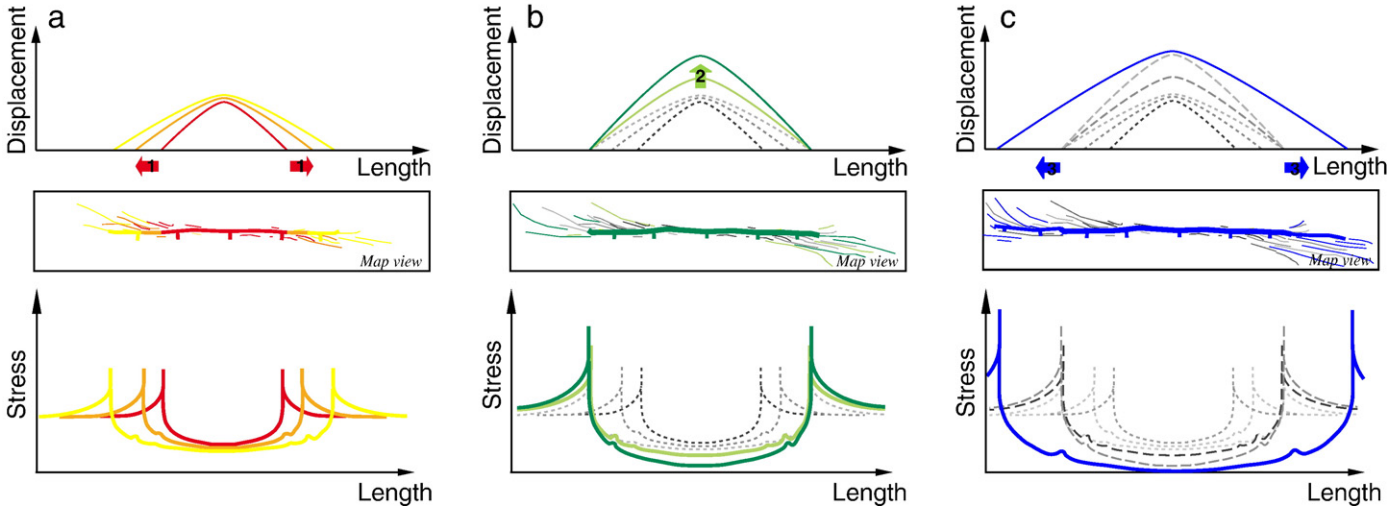

Fig. 10. A qualitative scenario of fault growth compatible with the observations. The scenario is drawn for an ideal, isolated fault, thus having a triangular, symmetric slip profile. Top plots present the slip distribution on the growing fault. Middle plots present the fault in map view. Bottom plots presents the stress distribution resulting in the 'faulted volume' (fault plane + damage zone). The dotted grey lines remind the previous stages. See the text for more details.

While lengthening, the fault develops a roughly triangular slip profile. As that profile develops, the medium holding the linear slants sustains extended damage, possibly in the form of multiplied micro-cracking (Marder and Fineberg, 1996; Manighetti et al., 2004). Large triangular zones of damage having their apex centered on the point of fault initiation are requested to maintain a triangular profile (Manighetti et al., 2004). The damage zone accommodates the excess stresses that result from the triangular shape of the slip profile, so that stress on the fault plane remains about constant, compatible with the elastic crack behavior and the self-similarity.

The fault then stops propagating, generally as it starts interacting with nearby faults. Once arrested, the fault continues growing by accumulating more slip (Fig. 10b). As it does so, the overall shape of its slip profile is vertically distorted while the stress concentration at its tips increases. The increased amount of stress accommodated within the damage zone likely makes some of the damage cracks growing larger. Some of these cracks may eventually form well-expressed segments ahead of the main fault tips. Since excess stresses are accommodated within the damage zone, the stress on the fault plane still remains about constant.

Once slip, hence stress, accumulation is such that the strength of the damage zone ahead of the fault tips is overcome, we hypothesize that the fault resumes lengthening, likely by connecting to one of the largest damage cracks (Fig. 10c). Note that the D_{max}/L ratios of the connecting fault and segment are unlikely to be similar, as commonly assessed (e.g., Cowie and Roberts, 2001). As the fault lengthens, its D_{max}/L ratio drops, while its slip profile remains triangular overall. Since the fault length increases, the damage zone widens. New damage structures are thus created, while previous structures either continue accommodating stress and strain, or become inactive and possibly offset by the lengthening fault.

We suggest that faults basically grow through alternating phases of dominant lengthening and dominant slip accumulation. The initial phase of rapid lengthening that occupies the first third of the fault lifetime is likely different however than any subsequent phase of further lengthening; that initial phase occurs through fault tip propagation, while subsequent lengthening rather occurs through segment connection. Interestingly, the bimodal growth that we describe in Fig. 10 is 'self-driven' and 'self-sustaining': as a fault accumulates some slip, it damages the adjacent medium, particularly at its tips. That damage in turn helps the fault accumulating more slip (without lengthening), for it diffuses the high stresses that would otherwise result on the fault plane, particularly at its tips. As the fault accumulates more slip, stresses increase within the damage zone, so that a few individual fault segments may eventually form ahead of the growing fault. At some level of slip accumulation, the strength of the damage zone is overcome and the fault lengthens by connecting to the segment(s) previously produced ahead of its tips. The process then repeats. It is thus self-driven since the fault itself produces the features that contribute to both its steady growth at constant length (the damage zone) and its further lengthening (the segments ahead). It is also self-sustaining since, as the fault grows longer, the stresses to be diffused in the damage zone grow higher, making the process unable to stop (in the absence of any local complexity, such as 'external' barriers). One implication is that the segments that eventually connect to form a larger fault, do not initiate randomly nor simultaneously, as commonly assumed (Cowie and Roberts, 2001; Davis et al., 2005; Walsh et al., 2003; Kim and Sanderson, 2005; Nicol et al., 2005). Besides their length is somehow dictated by the 'strength' of the medium (actually, its apparent stiffness) where the fault is growing.

Note that growth in isolation conditions as described above must be seldom. Yet, the encounter of a fault with a barrier does not change the general process. The barrier only increases the strength of the zone ahead of the fault tips, and this may increase the duration of the slip accumulation phase (hence more slip is accumulated), while distorting the slip profile from symmetric to asymmetric.

5. Conclusions

Our laser-equipped analog experiment led to the formation and growth of a dense network of normal faults for which we could measure the slip and length changes at successive short time lapses. This provides a unique opportunity to visualize and quantify the fault growth process and to examine how slip increments follow on a fault to make it grow. The analog faults are found to exhibit a number of features similar to those observed on geological faults. This suggests that these features may be intrinsic properties of faults, which thus should be reproduced by fault models. This furthermore suggests that the experiment is meaningful, with its results likely to apply to faults of any slip mode. The quasi-continuous observation of the fault growth that we perform allows us to examine these properties with far more detail than what is possible on natural faults. The major properties that we have identified are the following:

- Slip distributions have linear sections almost as long as the entire faults, and those sections generally persist during the fault evolution. This observation is not in keeping with the elastic crack theory. It suggests that extended damage of the medium is likely to result from the growth of a fault.
- Faults start growing in two successive phases: an initial, short (first third of the fault lifetime) period dominated by rapid lengthening, followed by a subsequent, longer (last two thirds of the fault lifetime) phase of mainly slip increase at roughly constant length.
- Faults are likely to go on growing through the alternation of phases of dominant lengthening and phases of dominant slip accumulation. Additional data are however necessary to confirm this hypothesis. Such bimodal growth is likely to be 'self-driven' and 'self-sustaining'.
- Faults grow overall homogeneously even though the individual slip events are characterized by large slip and stress heterogeneities. This suggests that there is a feedback between stress heterogeneities and slip development. The consequence of this is that the long-term faulting process is primarily insensitive to the short-term heterogeneities that are rapidly smoothed or redistributed.

One implication of this duality between heterogeneous and homogeneous behavior is that the short- and long-term slips and slip rates on natural faults are likely to be markedly different. Successive slip events are likely to also significantly differ in both slip amplitude and distribution. Together these results call for great caution when interpreting the available slip data on faults and ruptures, particularly when doing so in terms of 'characteristic earthquakes', as commonly done.

Acknowledgments

This work has been funded by the INSU-CNRS Dyeti program, and by the French ANR (project QUAKonSCARPS, n° ANR-06-CATT-008-01 and ANR-06-CATT-008-03). We thank M. Campillo, F. Cotton, Y. Delaby, and Y. Gaudemer for fruitful discussions. We are also grateful to two anonymous reviewers whose thorough and constructive comments helped improve the manuscript.

Appendix A. Supplementary data

Supplementary data associated with this article can be found, in the online version, at doi:10.1016/j.epsl.2008.06.042.

References

Ackermann, R.V., Schlische, R.W., Withjack, M.O., 2001. The geometric and statistical evolution of normal fault systems: an experimental study of the effects of mechanical layer thickness on scaling laws. J. Struct. Geol. 23, 1803–1819.

Armijo, R., Meyer, B., King, G., Rigo, A., Papanastassiou, D., 1996. Quaternary evolution of the Corinth rift and its implications for the late Cenozoic evolution of the Aegean. Geophys. J. Int. 126 (1), 11–53.

Bellahsen, N., Daniel, J.M., 2005. Fault reactivation control on normal fault growth: an experimental study. J. Struct. Geol. 27, 769–780.
Bellahsen, N., Daniel, J.M., Bollinger, L., Burov, E., 2003. Influence of viscous layers on the growth of normal faults: insights from experimental and numerical models. J. Struct. Geol. 25, 1471–1485.
Bennett, E., Youngson, J.H., Jackson, J., Norris, R., Raisbeck, G., Yiou, F., Fielding, E., 2005. Growth of South Rough ridge, Central Otago, New Zealand: using in situ cosmogenic isotopes and geomorphology to study an active, blind reverse fault. J. Geophys. Res. 110 (B02404). doi:10.1029/2004JB003184.
Buiter, S., Schreurs, G. (Eds.), 2006. Analogue and Numerical Modelling of Crustal-Scale Processes. Special Publications. Geological Society, London, p. 253.
Bull, J., Barnes, P., Lamarche, G., Sanderson, D., Cowie, P., Taylor, S., Dix, J., 2006. High-resolution record of displacement accumulation on an active normal fault system: implications for models of slip accumulation during repeated earthquakes. J. Struct. Geol. 28 (7), 1146–1166.
Bürgmann, R., Pollard, D., Martel, S., 1994. Slip distributions on faults: effects of stress gradients, inelastic deformation, heterogeneous host-rock stiffness, and fault interaction. J. Struct. Geol. 16 (12), 1675–1690.
Bürgmann, R., Rosen, P., Fielding, E., 2000. Synthetic aperture radar interferometry to measure Earth's surface topography and its deformation. Annu. Rev. Earth Planet. Sci. 28, 169–209.
Cartwright, J., Mansfield, C., 1998. Lateral displacement variations and lateral tip geometry of normal faults in the Canyonlands National park, Utah. J. Struct. Geol. 20 (1), 3–19.
Cartwright, J., Trudgill, B., Mansfield, C., 1995. Fault growth by segment linkage: an explanation for scatter in maximum displacement and trace length data from the Canyonlands gradens of SE Utah. J. Struct. Geol. 17 (9), 1319–1326.
Chevalier, M.L., Ryerson, F.J., Tapponnier, P., Finkel, R.C., Van der Woerd, J., Haibing, L., Qing, L., 2005. Slip-rate measurements on the Karakorum fault may imply secular variations in fault motion. Science 307, 411–414.
Childs, C., Nicol, A., Walsh, J., Watterson, J., 2003. The growth and propagation of synsedimentary faults. J. Struct. Geol. 25, 633–648.
Contreras, J., Anders, M., Scholz, C., 2000. Growth of a normal fault system: observations from the lake Malawi basin of the East African rift. J. Struct. Geol. 22, 159–168.
Cowie, P., 1998. A healing-reloading feedback control on the growth rate of seimogenic faults. J. Struct. Geol. 20 (8), 1075–1087.
Cowie, P., Scholz, C., 1992a. Physical explanation for the displacement-length relationship of faults using a post-yield fracture mechanics model. J. Struct. Geol. 14 (10), 1133–1148.
Cowie, P., Scholz, C., 1992b. Displacement-length scaling relationship for faults: data synthesis and discussion. J. Struct. Geol. 14 (10), 1149–1156.
Cowie, P., Shipton, Z., 1998. Fault tip displacement gradients and process zone dimensions. J. Struct. Geol. 20 (8), 983–997.
Cowie, P., Roberts, G., 2001. Constraining slip rates and spacing for active normal faults. J. Struct. Geol. 23, 1901–1915.
Daeron, M., Klinger, Y., Tapponnier, P., Elias, A., Jacques, E., Sursock, A., 2007. 12,000-year-long record of 10 to 13 paleoearthquakes on the Yammoûneh fault, Levant fault system, Lebanon, Bull. Seism. Soc. Am. 97 (3), 749–771.
Davis, K., Burbank, D., Fisher, D., Wallace, S., Nobes, D., 2005. Thrust-fault growth and segment linkage in the active Ostler fault zone, New Zealand. J. Struct. Geol. 27, 1528–1546.
Davy, P., Cobbold, P., 1991. Experiments on shortening of a 4-layer model of the continental lithosphere. Tectonophysics 188 (1-2), 1–25.
Davy, P., Hansen, A., Bonnet, E., Zhang, S.Z., 1995. Localization and fault growth in layered brittle-ductile systems: implications for deformations of the continental lithosphere. J. Geophys. Res. 100 (B4), 6281–6294.
de Joussineau, G., Bouissou, S., Petit, J.P., Barquins, M., 2001. Experimental analysis of slip distribution along a fault segment under stick-slip and stable sliding conditions. Tectonophysics 337, 85–98.
Ellis, M., Dunlap, W., 1988. Displacement variation along thrust faults: implications for the development of large faults. J. Struct. Geol. 10 (2), 183–192.
Faugeres, E., Brun, J.P., 1984. Modélisation expérimentale de la distension continentale. C. R. Acad. Sci. Paris 299, 365–370.
Frankel, K.L., Brantley, K.S., Dolan, J.F., Finkel, R.C., Klinger, R.E., Knott, J.R., Machette, M.N., Owen, L.A., Phillips, F.M., Slate, J.L., Wernicke, B.P., 2007. Cosmogenic 10Be and 36Cl geochronology of offset alluvial fans along the northern Death Valley fault zone: implications for transient strain in the Eastern California Shear Zone. J. Geophys. Res. 112 (B06407). doi:10.1029/2006JB004350.
Gawthorpe, R., Jackson, C.L., Young, M., Sharp, I., Moustafa, A., Leppard, C., 2003. Normal fault growth, displacement localisation and the evolution of normal fault populations: the Hammam Faraun fault block, Suez rift, Egypt. J. Struct. Geol. 25, 883–895.
Goldsworthy, M., Jackson, J., 2001. Migration of activity within normal fault systems: examples from the quaternary of mainland Greece. J. Struct. Geol. 23 (2-3), 489–506.
Graveleau, F., Dominguez, S., 2008. Analogue modelling of the interaction between tectonics, erosion and sedimentation in foreland thrust belts. C. R. Geosci. 340, 324–333.
Haibing, L., Van der Woerd, J., Tapponnier, P., Klinger, Y., Xuexiang, Q., Jingsui, Y., Yintang, Z., 2005. Slip rate on the Kunlun fault at Hongshui Gou, and recurrence time of great events comparable to the 14/11/2001, Mw 7.9 Kokoxili earthquake. Earth Planet. Sci. Lett. 237, 285–299.
Horsfield, W.T., 1977. An experimental approach to basement-controlled faulting. Geol. Mijnb. 56 (4), 363–370.
Hubbert, M.K., 1937. Theory of scale models as applied to the study of geologic structures. Geol. Soc. Am. Bull. 48 (10), 1459–1519.
Kim, Y., Sanderson, D., 2005. The relationship between displacement and length of faults. Earth-Sci. Rev. 68, 317–334.
Klinger, Y., Sieh, K., Altunel, E., Akoglu, A., Barka, A., Dawson, T., Gonzalez, T., Meltzner, A., Rockwell, T., 2003. Paleoseismic evidence of characteristic slip on the western segment of the North Anatolian fault, Turkey. Bull. Seismol. Soc. Am. 93 (6), 2317–2332.
Lallemand, S., Malavieille, J., 1992. Coulomb theory applied to accretionary and non-accretionary wedges. Eos, Trans. - Am. Geophys. Union 73 (14), 7–23.
Lohrman, J., Kukowski, N., Adam, J., Oncken, O., 2003. The impact of analogue material properties on the geometry, kinematics and dynamics of convergent sand wedges. J. Struct. Geol. 25, 1691–1711.
Maerten, L., Willemse, E., Pollard, D., Rawnsley, K., 1999. Slip distributions on intersecting normal faults. J. Struct. Geol. 21, 259–271.
Manighetti, I., King, G., Gaudemer, Y., Scholz, C., Doubre, C., 2001. Slip accumulation and lateral propagation of active normal faults in Afar. J. Geophys. Res. 106 (B7), 13667–13696.
Manighetti, I., King, G., Sammis, C., 2004. The role of off-fault damage in the evolution of normal faults. Earth Planet. Sci. Lett. 217, 399–408.
Manighetti, I., Campillo, M., Sammis, C., Mai, P., King, G., 2005. Evidence for self-similar, triangular slip distributions on earthquakes: implications for earthquake and fault mechanics. J. Geophys. Res. 110 (B05302). doi:10.1029/2004JB003174.
Manighetti, I., Campillo, M., Bouley, S., Cotton, F., 2007. Earthquake scaling, fault segmentation and structural maturity. Earth Planet. Sci. Lett. 253, 429–438.
Mansfield, C., Cartwright, J., 2001. Fault growth by linkage: observations and implications from analogue models. J. Struct. Geol. 23, 745–763.
Marchal, D., Guiraud, M., Rives, T., Van der Driessche, J., 1998. Space and time propagation processes of normal faults. In: Jones, G., Fisher, Q.P., Knipe, R.J. (Eds.), Faulting, Fault Sealing and Fluid Flow in Hydrocarbon Reservoirs. Special Publications, vol. 147. Geol. Soc., London, pp. 51–70.
Marchal, D., Guiraud, M., Rives, T., 2003. Geometric and morphologic evolution of normal fault planes and traces from 2D to 4D data. J. Struct. Geol. 25, 135–158.
Marder, M., Fineberg, J., 1996. How things break. Phys. Today 49, 24.
Marrett, R., Allmendinger, R.W., 1991. Estimates of strain due to brittle faulting: sampling of fault populations. J. Struct. Geol. 13 (6), 735–738.
Meyer, V., Nicol, A., Childs, C., Walsh, J., Watterson, J., 2002. Progressive localisation of strain during the evolution of a normal fault population. J. Struct. Geol. 24, 1215–1231.
Morewood, N., Roberts, G., 1999. Lateral propagation of the surface trace of the south Alkyonides normal fault segment, central Greece: its impact on models of fault growth and displacement-length relationships. J. Struct. Geol. 21, 635–652.
Nicol, A., Watterson, J., Walsh, J., Childs, C., 1996. The shapes, major axis orientations and displacement patterns of fault surfaces. J. Struct. Geol. 18 (2-3), 235–248.
Nicol, A., Walsh, J.J., Watterson, J., Underhill, J.R., 1997. Displacement rates of normal faults. Nature 390, 157–159.
Nicol, A., Walsh, J., Berryman, K., Nodder, S., 2005. Growth of a normal fault by accumulation of slip over millions of years. J. Struct. Geol. 27, 327–342.
Nishenko, S.P., Bulland, R., 1987. A generic recurrence interval distribution for earthquake forecasting. Bull. Seismol. Soc. Am. 77, 1382–1399.
Pachell, M.A., Evans, J., 2002. Growth, linkage, and termination processes of a 10-km-long strike-slip fault in jointed granite: the Gemini fault zone, Sierra Nevada, California. J. Struct. Geol. 24, 1903–1924.
Palumbo, L., Benedetti, L., Bourles, D., Cinque, A., Finkel, R., 2004. Slip history of the Magnola fault (Apennines, Central Italy) from 36Cl surface exposure dating: evidence for strong earthquakes over the Holocene. Earth Planet. Sci. Lett. 225, 163–176.
Peacock, D., Sanderson, D., 1991. Displacements, segment linkage and relay ramps in normal fault zones. J. Struct. Geol. 13 (6), 721–733.
Peacock, D., Sanderson, D., 1996. Effects of propagation rate on displacement variations along faults. J. Struct. Geol. 18 (2-3), 311–320.
Pollard, D.D., Segall, P., 1987. Theoretical displacements and stresses near fractures in rock: with applications to faults, joints, veins, dikes, and solution surfaces. In: Atkinson, B.K. (Ed.), Fracture Mechanics of Rocks. Acad. Press Geology Series, London.
Poulimenos, G., 2000. Scaling properties of normal fault populations in the Western Corinth graben, Greece: implications for fault growth in large strain settings. J. Struct. Geol. 22, 307–322.
Rice, J.R., Ben-Zion, Y., 1996. Slip complexity in earthquake fault models. Proc. Nat. Acad. Sci. U. S. A. 93, 3811–3818.
Rockwell, T., Barka, A., Dawson, T., Akyuz, S., Thorup, K., 2001. Paleoseismology of the Gazikoy-Saros segment of the North Anatolia fault, northwestern Turkey: comparison of the historical and paleoseismic records, implications of regional seismic hazard, and models of earthquake recurrence. J. Seismol. 5 (3), 433–448.
Schlische, R., Young, S., Ackermann, R., Gupta, A., 1996. Geometry and scaling relations of a population of very small rift-related normal faults. Geology. 24 (8), 683–686.
Scholz, C., 2002. The Mechanics of Earthquakes and Faulting. Cambridge University Press.
Schreurs, G., Hänni, R., Vock, P., 2002. The influence of brittle-viscous multilayers on faulting during rifting: an analogue modelling approach. In: Schellart, W.P., Passchier, C. (Eds.), Analogue modelling of large-scale tectonic processes. J. Virt. Expl., vol. 6, pp. 89–97.
Segall, P., Pollard, D., 1980. Mechanics of discontinuous faults. J. Geophys. Res. 85 (B8), 4337–4350.
Shaw, J.H., Plesch, A., Dolan, J.F., Pratt, T.L., Fiore, P., 2002. Puente Hills blind-thrust system, Los Angeles, California. Bull. Seismol. Soc. Am. 92, 2946–2960.
Shimazaki, K., Nakata, T., 1980. Time predictable recurrence model for large earthquakes. Geophys. Res. Lett. 7, 279–282.

Tapponnier, P., Ryerson, F.J., Van der Woerd, J., Mériaux, A.S., Lasserre, C., 2001. Long-term slip rates and characteristic slip: keys to active fault behaviour and earthquake hazard. C. R. Acad. Sci. Paris. 333, 483–494.
Taylor, S., Bull, J., Lamarche, G., Barnes, P., 2004. Normal fault growth and linkage in the Whakatane graben, New Zealand, during the last 1.3 myr. J. Geophys. Res. 109. doi:10.1029/2003JB002412.
Tse, S.T., Rice, J.R., 1986. Crustal earthquake instability in relation to the depth variation of frictional slip properties. J. Geophys. Res. 91, 9452–9472.
Walsh, J., Watterson, J., 1987. Distributions of cumulative displacement and seismic slip on a normal fault surface. J. Struct. Geol. 9 (8), 1039–1046.
Walsh, J., Watterson, J., 1988. Analysis of the relationship between displacements and dimensions of faults. J. Struct. Geol. 10 (3), 239–247.
Walsh, J., Nicol, A., Childs, C., 2002. An alternative model for the growth of faults. J. Struct. Geol. 24, 1669–1675.
Walsh, J.J., Bailey, W.R., Childs, C., Nicol, A., Bonson, C.G., 2003. Formation of segmented normal faults: a 3D perspective. J. Struct. Geol. 25, 1251–1262.
Weldon, R., Scharer, K., Fumal, T., Biasi, G., 2004. Wrightwood and the earthquake cycle: What a long recurrence record tells us about how faults work. GSA Today 14 (9), 4–10.
Willemse, E., Pollard, D., Aydin, A., 1996. Three-dimensional analyses of slip distributions on normal fault arrays with consequences for fault scaling. J. Struct. Geol. 18 (2/3), 295–309.
Wright, T.J., Parsons, B., England, P.C., Fielding, E.J., 2004. InSAR observations of low slip rates on the major faults of Western Tibet. Science 305, 236–239.

Supporting online material A – Schlagenhauf et al, EPSL, 2008.

Brief description of the extensional analog models produced.

In the majority of the analogue models published so far, the extension is generated by gravity: a basal plate is tilted, so that the ductile overlying material sustains a tangential component of the gravity force that transmits extension to the sand above (e.g. Vendeville and Cobbold, 1987; Childs et al., 1993; Marchal et al., 1998, 2003; Mansfield and Cartwright, 2001; Medwedeff and Kranz, 2002; Acocella et al., 2005). In that case, the fault initiation is diachronic, while most faults are synthetic. Other experiments produce extension by imposing a sliding discontinuity within the model: one side of the model is fixed while the other side rests on a basal plate that is progressively pulled apart. In that case, fault initiation is also diachronic; at any stage, new faults initiate above the sliding discontinuity while faults previously formed stop slipping (e.g. Basile et al., 1992; Brun and Tron, 1993; Brun and Nalpas, 1996; Acocella et al., 1999). Finally, some other models produce extension by stretching a basal rubber sheet; that stretching transmits a quite homogeneous extension to the overlying materials (e.g. McClay and Ellis, 1987; Higgins and Harris, 1997; Clifton et al., 2000; Le Calvez and Vendeville, 2002; McClay et al., 2002; Bellahsen et al., 2003, 2005; Hus et al., 2005). Yet, as the rubber sheet stretches, compressional stresses are induced perpendicular to the stretched zone. That compression interacts with the extension, producing a heterogeneous stress field when large amounts of deformation are imposed.

References :

Acocella, V., Faccena, C., Funiciello, R., Rossetti, F., 1999. Sand-box modelling of basement-controlled transfer zones in extensional domains. Terra Nova. 11, 149–156.

Acocella V., Morvillo, P., Funiciello, R., 2005. What controls relay ramps and transfer faults within rift zones? Insights from analogue models. J. Struct. Geol. 27, 397–408.

Basile C., Brun, J.P., Mascle, J., 1992. Structure et formation de la marge transformante de Côte d'Ivoire-Ghana: apports de la sismique réflexion et de la modélisation analogique. Bull. Soc. Géol. France. 163(3), 207-216.

Bellahsen N., Daniel, J.M., Bollinger, L., Burov, E., 2003. Influence of viscous layers on the growth of normal faults: insights from experimental and numerical models. J. Struct. Geol. 25, 1471–1485.

Bellahsen N., Daniel, J.M., 2005. Fault reactivation control on normal fault growth: an experimental study. J. Struct. Geol. 27, 769–780.

Brun J.P., Tron, V., 1993. Development of the North Viking Graben: inferences from laboratory modelling. Sedimentary Geology. 86, 31-51.

Brun J.P., Nalpas, T., 1996. Graben inversion in nature and experiments. Tectonics. 15, 677–687.

Childs C., Easton, S., Vendeville, B., Jackson, M., Lin, S., Walsh, J., Watterson, J., 1993. Kinematic analysis of faults in a physical model of growth faulting above a viscous salt analogue. Tectonophysics. 228, 313–329.

Clifton A., Schlische, R., Withjack, M., Ackermann, R., 2000. Influence of rift obliquity on fault-population systematics: results of experimental clay model. J. Struct. Geol. 22, 1491–1509.

Higgins R., Harris, L., 1997. The effect of cover composition on extensional faulting above re-activated basement faults: results from analogue modelling. J. Struct. Geol. 19(1), 89–98.

Hus R., Acocella, V., Funiciello, R., Batist, M.D., 2005. Sandbox models of relay ramp structure and evolution. J. Struct. Geol. 27, 459–473.

Le Calvez J.H., Vendeville, B.C., 2002. Experimental designs to model along-strike fault interaction, In : Schellart W.P. and Passchier C., Analogue modelling of large-scale tectonic processes, J. Virtual Explorer. 7, 7-23.

Mansfield C., Cartwright, J., 2001. Fault growth by linkage: observations and implications from analogue models. J. Struct. Geol. 23, 745–763.

Marchal D., Guiraud, M., Rives, T., Van der Driessche, J., 1998. Space and time propagation processes of normal faults. In: Jones, G., Fisher, Q.P. & Knipe, R.J. (eds) Faulting, Fault Sealing and Fluid Flow in Hydrocarbon Reservoirs, Geol. Soc., London, Spec. Publ. 147, 51–70.

Marchal D., Guiraud, M., Rives, T., 2003. Geometric and morphologic evolution of normal fault planes and traces from 2D to 4D data. J. Struct. Geol. 25, 135–158.

McClay K., Ellis, P., 1987. Geometries of extensional fault systems developed in model experiments. Geology. 15, 341–344.

McClay K., Dooley, T., Whitehouse, P., Mills, M., 2002. 4-D evolution of rift systems: insights from scaled physical models. AAPG Bulletin. 86(6), 935–959.

Medwedeff D.A., Krantz, R.W., 2002. Kinematic and analog modelling of 3-D extensional ramps: observations and a new 3-D deformation model. J. Struct. Geol. 24(4), 763-772.

Vendeveille B., Cobbold, P.R., 1987. Glissements gravitaires synsédimentaires et failles normales listriques: modèles expérimentaux. C.R. Acad. Sci. Paris. 305(II), 1313

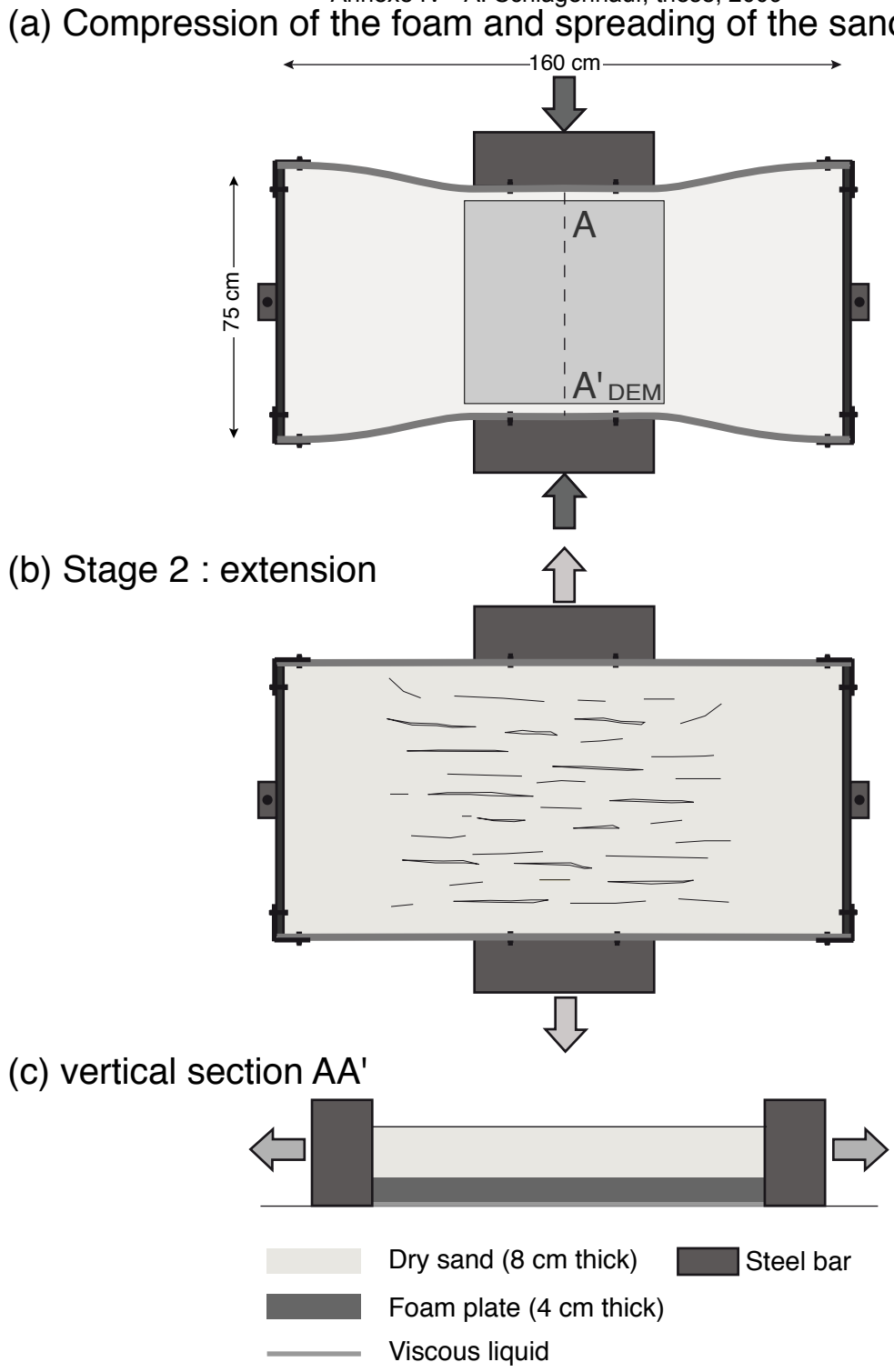

Supporting online material B - Schlagenhauf et al., EPSL, 2008

View of the experiment. The apparatus is 160 x 75 cm2. The 4 cm-thick foam plate is tightly enclosed within a frame having its two shortest sides rigid and its two longest sides flexible (Komacel plastic). The foam and frame are sealed together with silicone. The foam rests on a basal rigid plate. A thin layer of viscous liquid between the foam and the basal plate allows the foam to slide homogeneously with no buckling. Further details are given in text.

Supporting online material C - Schlagenhauf et al., EPSL, 2008

Movie, in map view, of the model from its initial stage with no extension to its final stage with 20 % of extension. Faults initiate evenly throughout the model from the very first stages of the experiment. They then go on growing over the entire duration of the experiment.

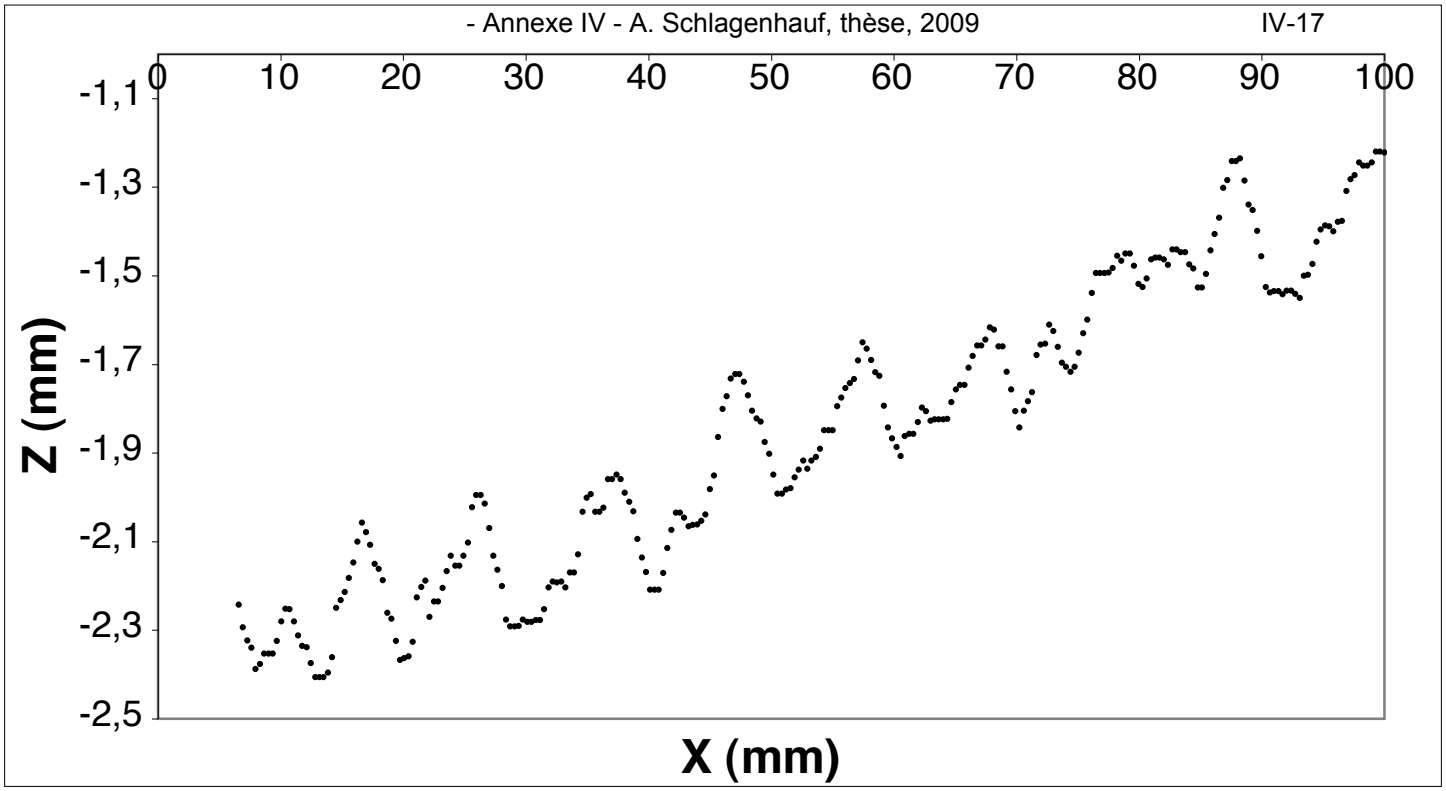

Supporting online material D - Schlagenhauf et al., EPSL, 2008

Example of the laser-induced noise. The noise is periodic, with a mean amplitude of 0.25 mm, and a wavelength of 10 mm that includes about 19 points of measurement. We have thus filtered the elevation profiles by averaging the data by sets of 19 points.

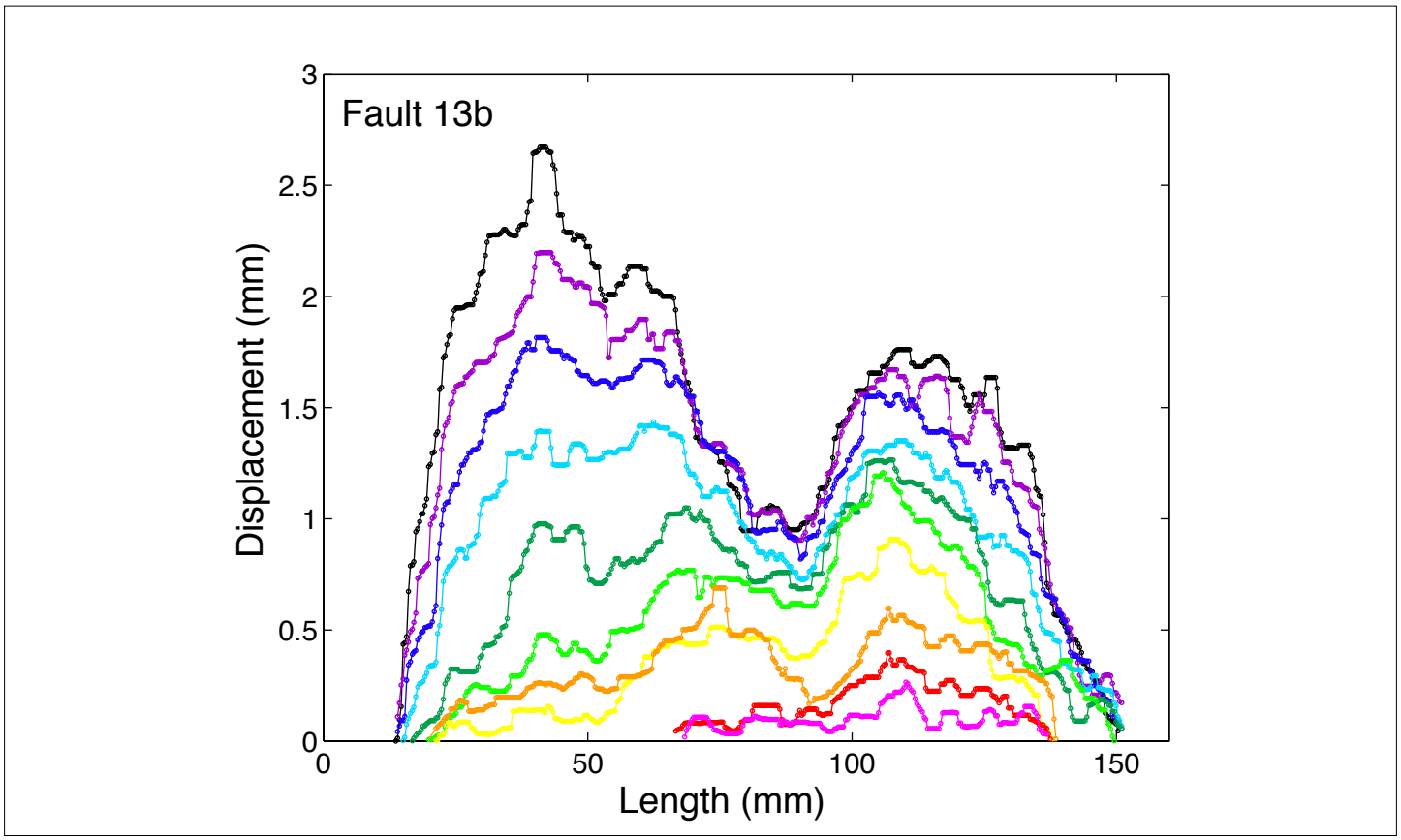

Supporting online material E - Schlagenhauf et al., EPSL, 2008

Example of a fault having a 'complex' slip profile shape. That shape however arises from the evolution of a more simple triangular shape. The final profile exhibits high slip gradients at both tips.

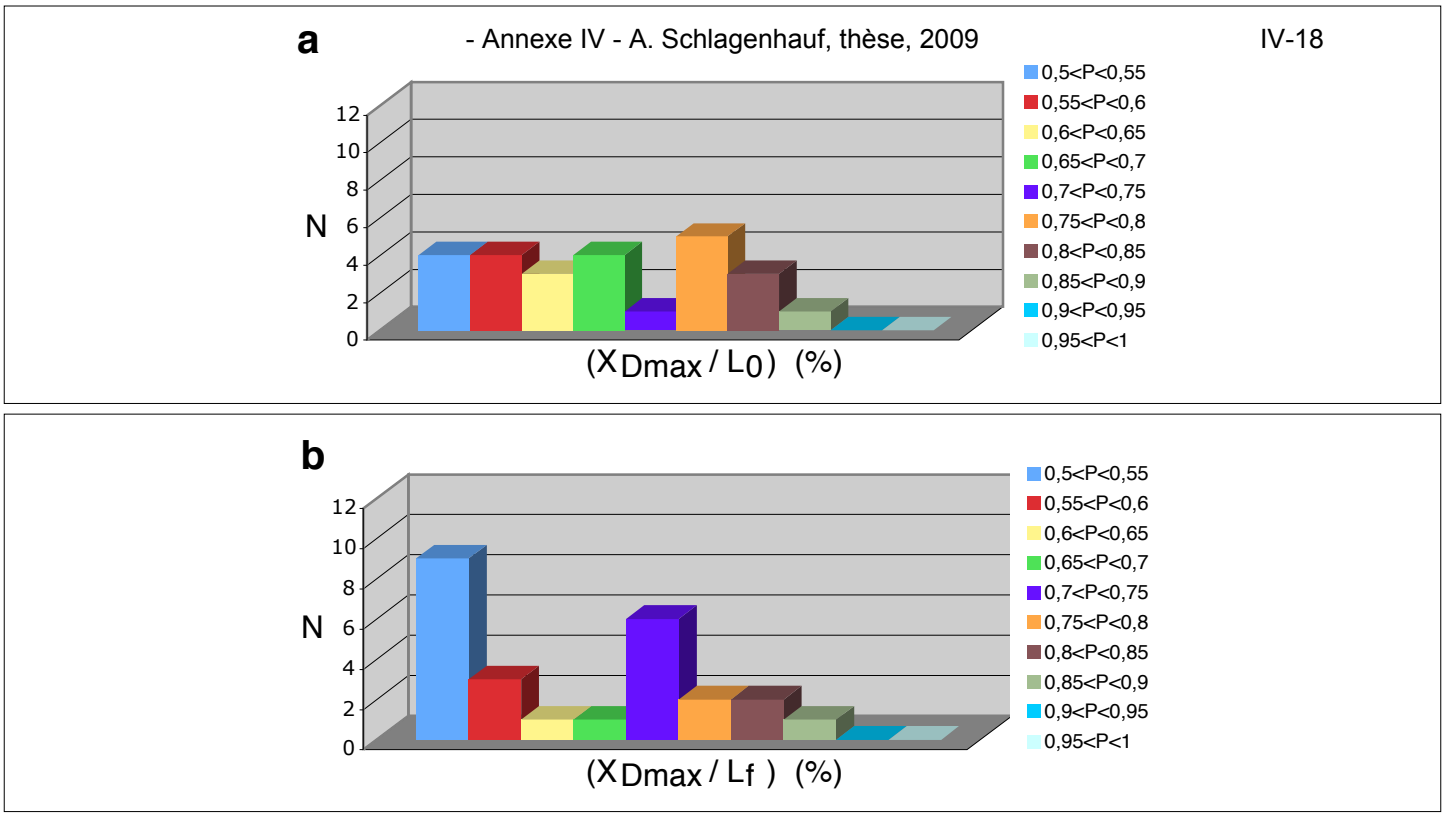

Supporting online material F - Schlagenhauf et al., EPSL, 2008

a) Position of the maximum displacement along the faults at their initial stage of growth (which generally coincides with stage 3 or 4). The X axis plots the position of Dmax at the first stage of growth (XDmax) divided by the initial fault length (L0). b) Position of the maximum displacement along the faults at their final stage of growth (stage 12 for all faults). The X axis plots the position of Dmax at the final stage of growth (XDmax) divided by the final fault length (Lf). In both figures, the position is referred to the fault half-length.

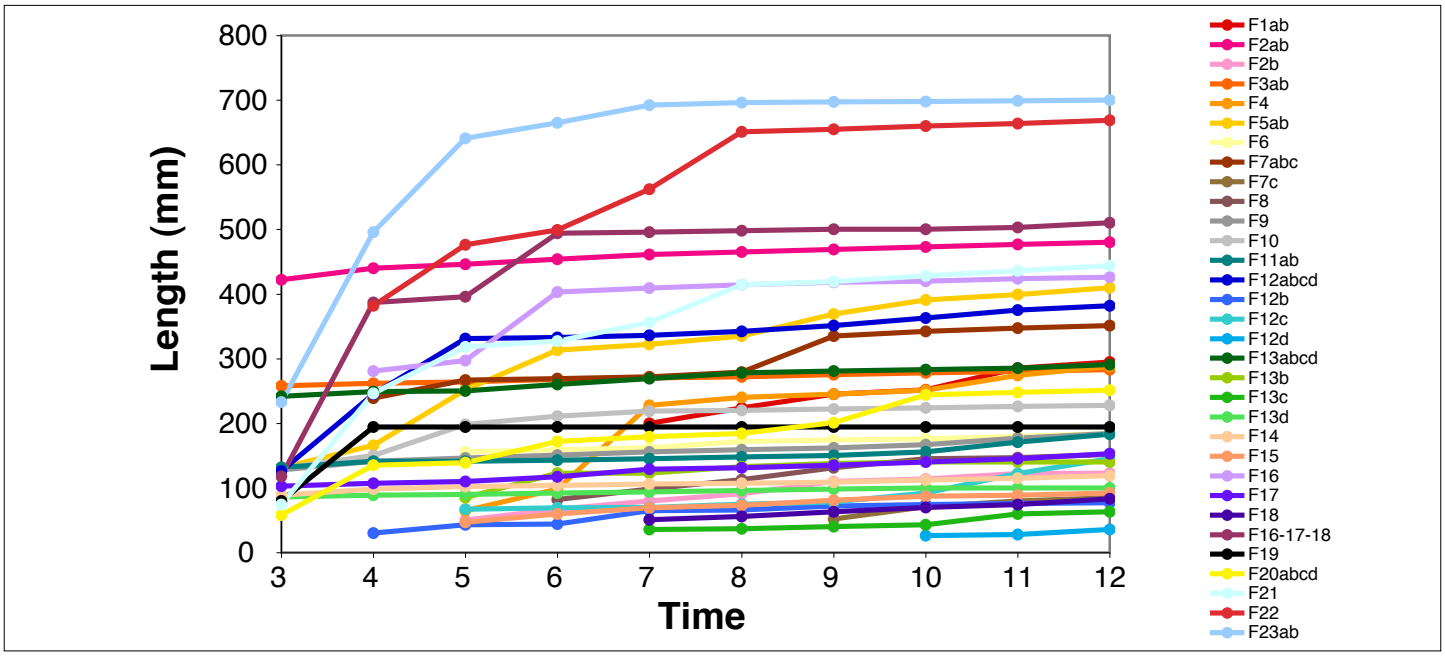

Supporting online material G - Schlagenhauf et al., EPSL, 2008

Evolution of fault length as a function of time. More than half of the faults reach their final length in the very first stages of the experiment (under less than 5% of extension), before any vertical slip is visible at the model surface.

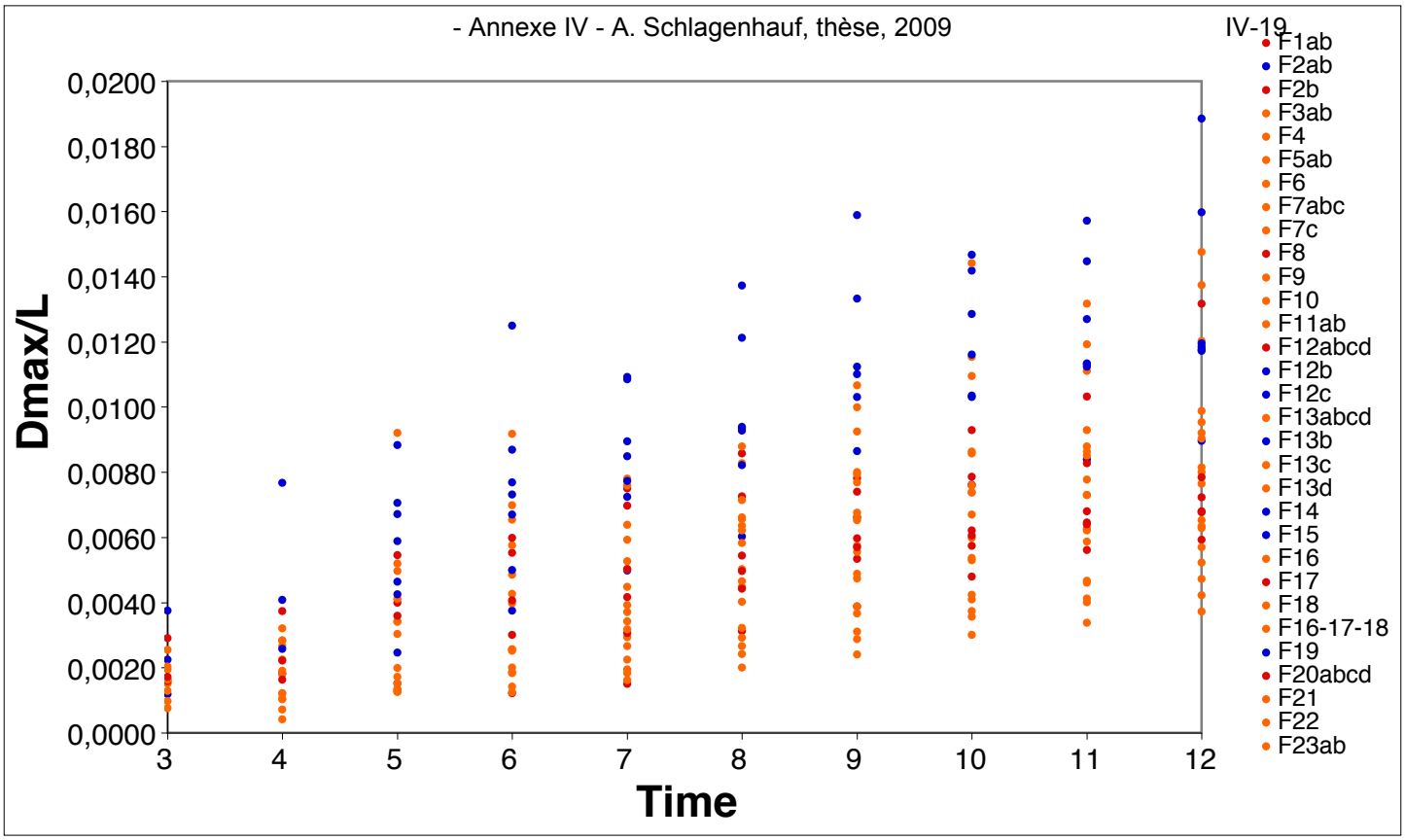

Supporting online material H - Schlagenhauf et al., EPSL, 2008

Evolution of the Dmax/L ratio as a function of time. The envelop shape of the slip profiles is indicated by colors, red for triangular and symmetric profiles, orange for triangular and asymmetric profiles, and blue for profiles with more complex shapes having high slip gradients at both tips. The later generally accumulate more slip that the former.

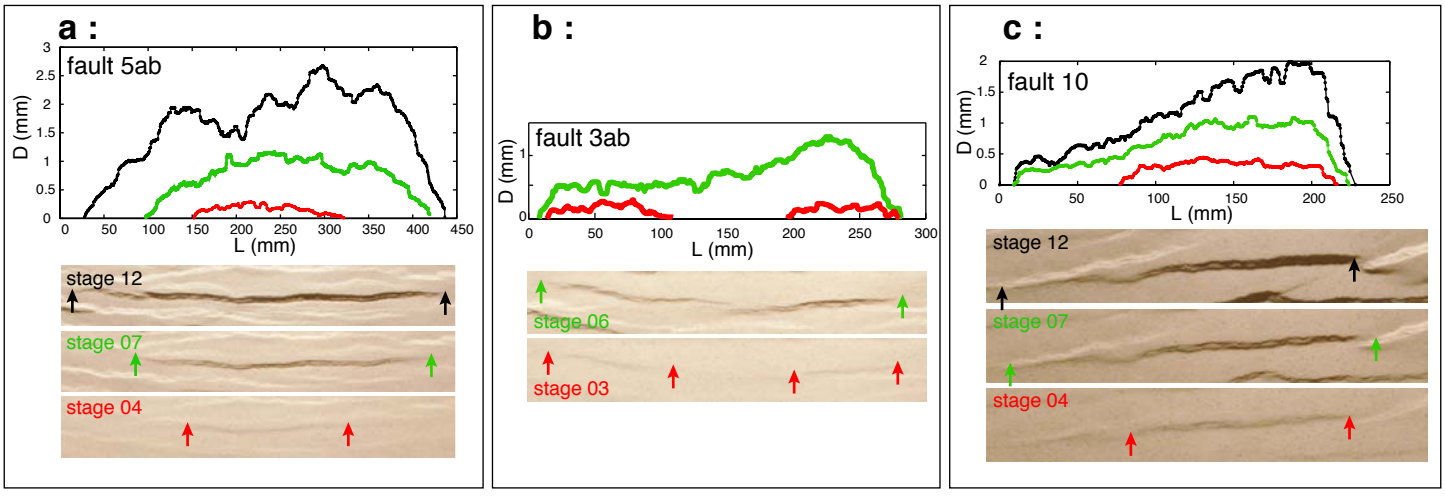

Supporting online material I - Schlagenhauf et al., EPSL, 2008

Illustrating the different modes of fault lengthening. In all figures, top plots are the growing slip profiles, while bottom plots show the growing faults in map view. Colors refer to the various stages of growth. a) Both tips of the fault propagate laterally, as if continuously; the slip profile keeps roughly symmetric. b) Two initially distinct fault segments propagate toward each other and eventually meet and connect to form a larger-scale fault. c) The larger fault further lengthens by connecting to a segment formed due ahead of one of its tips. Note that the fault is rapidly arrested at both tips as it meets two antithetic faults. High slip gradients develop at the arrested tips.

Earth and Planetary Science Letters 271 (2008) 145–158

Contents lists available at ScienceDirect

Earth and Planetary Science Letters

journal homepage: www.elsevier.com/locate/epsl

Identifying past earthquakes on an active normal fault (Magnola, Italy) from the chemical analysis of its exhumed carbonate fault plane

Julien Carcaillet [a,b], Isabelle Manighetti [a,*], Catherine Chauvel [b], Aloé Schlagenhauf [a], Jean-Marc Nicole [a]

[a] Laboratoire de Géophysique Interne et Tectonophysique (LGIT), CNRS, Observatoire de Grenoble (OSUG), Université J. Fourier, Maison des Géosciences, BP 53, 38041 Grenoble Cédex 9, France
[b] Laboratoire de Géodynamique des Chaînes Alpines (LGCA), CNRS, Observatoire de Grenoble (OSUG), Université J. Fourier, Maison des Géosciences, BP 53, 38041 Grenoble Cédex 9, France

ARTICLE INFO

Article history:
Received 7 November 2007
Received in revised form 26 March 2008
Accepted 27 March 2008
Available online 11 April 2008

Editor: R.D. van der Hilst

Keywords:
past earthquake history
paleoseismology
normal fault
fault scarp rocks
carbonate weathering
major and trace elements
Apennines

ABSTRACT

A normal fault scarp exhumed by repeated strong earthquakes is made of a series of rupture zones that were exposed, thus weathered, over significantly different time spans. We show that such differential weathering can be detected in the chemical content of the fault scarp rocks, and its signature used as a base to decipher the past earthquake history of the fault. We focus on the Magnola normal fault, Central Italy, whose Holocene seismic slip history has already been determined by Palumbo et al. (ESPL, 225, 163–176, 2004) from *in situ* ^{36}Cl cosmic ray exposure dating of the fault limestone scarp surface. Five major earthquakes were found to have occurred over the last 12 ka, with slips of 1.5–3 m and recurrence times of 0.7–3.1 ka. We analyze the major and trace element concentrations of 15 carbonate samples collected from base to top of the 10 m-high Magnola Holocene scarp, next to the previous sampling done by Palumbo et al. [Palumbo, L., Benedetti, L., Bourlès, D., Cinque, A., Finkel, R., 2004. Slip history of the Magnola fault (Apennines, Central Italy) from ^{36}Cl surface exposure dating: evidence for strong earthquake over Holocene. Earth Planet. Sci. Lett. 225, 163–176.]. We find that most element concentrations decrease upscarp at a rate averaging 5%/m. This decrease is attributed to leaching and re-precipitation of purer calcite that increase with exposure time. Superimposed to the overall leaching, concentration peaks are found at the transition zones separating the earthquake ruptures. These concentration peaks likely result from enrichment of the scarp sections that remained stuck in the 30–50 cm-thick impurity-rich upper soil during the quiescence periods that separated the earthquakes. Because the rare earth elements (REE) are among those most significantly enriched at the earthquake transition zones, they are the best chemical markers of past large seismic events. We finally propose a first-order model that reproduces adequately the observations. Our preliminary work thus suggests that geochemical analyses of preserved, seismically exhumed limestone fault scarp rocks may help deciphering the seismic slip history of a fault.

1. Introduction

If a complete catalog of the major earthquakes (M>6) that have occurred on active faults over the last few tens of thousands years was available, we would know how such earthquakes have repeated in the past, so that anticipating how similar strong earthquakes may occur in the future would become possible. Unfortunately such catalog does not exist and never will. As a result, our only chance to learn how major earthquakes have repeated in the past is to analyze their surface geological record, if any. Yet methods to analyze that record are currently scarce and costly. The most common approach, paleoseismology, consists in digging few m-deep trenches across active faults (e.g., Daëron et al., 2005; Haibing et al., 2005; Kumar et al., 2006), which often reveals logistically difficult. Besides, while paleoseismology allows identification and dating of the few last major earthquakes on the faults, it more rarely allows determining the displacements produced by those earthquakes. Another, more recent approach focuses on faults having an escarpment at surface, and consists in determining the exposure time of that escarpment through the measurement of its content in *in situ* cosmogenic ^{36}Cl (e.g., Zreda and Noller, 1998; Mitchell et al., 2001; Benedetti et al., 2002, 2003; Palumbo et al., 2004). The method is powerful, yet extremely costly.

Our aim is to explore a new method that may help recovering past earthquake histories in a simpler and less expensive way than presently possible. We focus on normal faults, for those are the only ones to provide a complete geological record of their past major ruptures. Indeed, the action of a large earthquake on a normal fault is to uplift its footwall, so that a portion of the fault plane becomes

* Corresponding author. LGIT, Maison des Géosciences, BP 53, 38041 Grenoble, Cedex 9, France. Tel.: +33 476 82.80.26; fax: +33 476.82.81.01.
E-mail addresses: julien.carcaillet@ujf-grenoble.fr (J. Carcaillet), isabelle.manighetti@obs.ujf-grenoble.fr (I. Manighetti), catherine.chauvel@ujf-grenoble.fr (C. Chauvel), aloe.schlagenhauf@obs.ujf-grenoble.fr (A. Schlagenhauf), jean-marc.nicole@ujf-grenoble.fr (J.-M. Nicole).

0012-821X/$ – see front matter © 2008 Elsevier B.V. All rights reserved.
doi:10.1016/j.epsl.2008.03.059

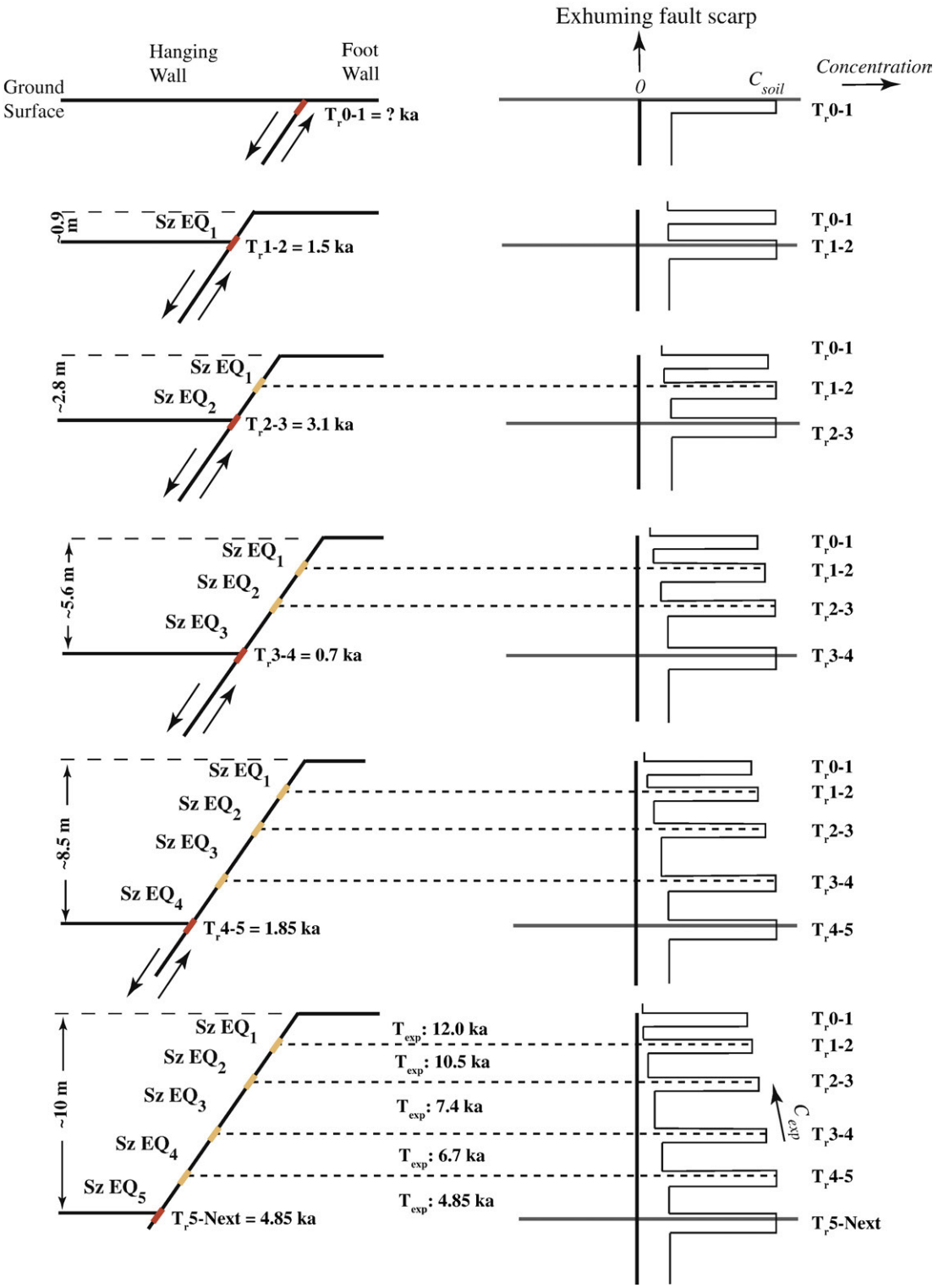

Fig. 1. Formation of an exhumed normal fault scarp through the repetition of major earthquakes (left panel), and upscarp evolution of chemical element concentrations observed in present study (right panel). Sz EQ$_n$ for slip zone exhumed by earthquake n. The five major earthquake-exhumed slip zones identified by Palumbo et al. (2004) on the Holocene Magnola fault scarp are reported, with the corresponding ages of exhumation (T_{exp}). The transition zones between earthquakes n and n' are indicated (color patches and horizontal dashed lines) with the corresponding time of residence (T_r $n-n'$) of the scarp rocks in the upper soil. See text and Fig. 9 for explanation of the right panel (For interpretation of the references to colour in this figure legend, the reader is referred to the web version of this article.)

exposed to the atmosphere (Fig. 1, left panel). Hence, as large earthquakes repeat on a normal fault, the fault plane is progressively exhumed. The earthquake succession eventually leads to the formation of a high topographic escarpment, all the higher as the earthquake history is longer (Fig. 2b). When the offset rocks are limestones, the youngest parts of such escarpments are commonly preserved in the form of ≈10 m high scarps running at their base (Fig. 2b–c). Those scarps basically represent the section of the fault plane that has been exhumed by the few last major earthquakes on the fault.

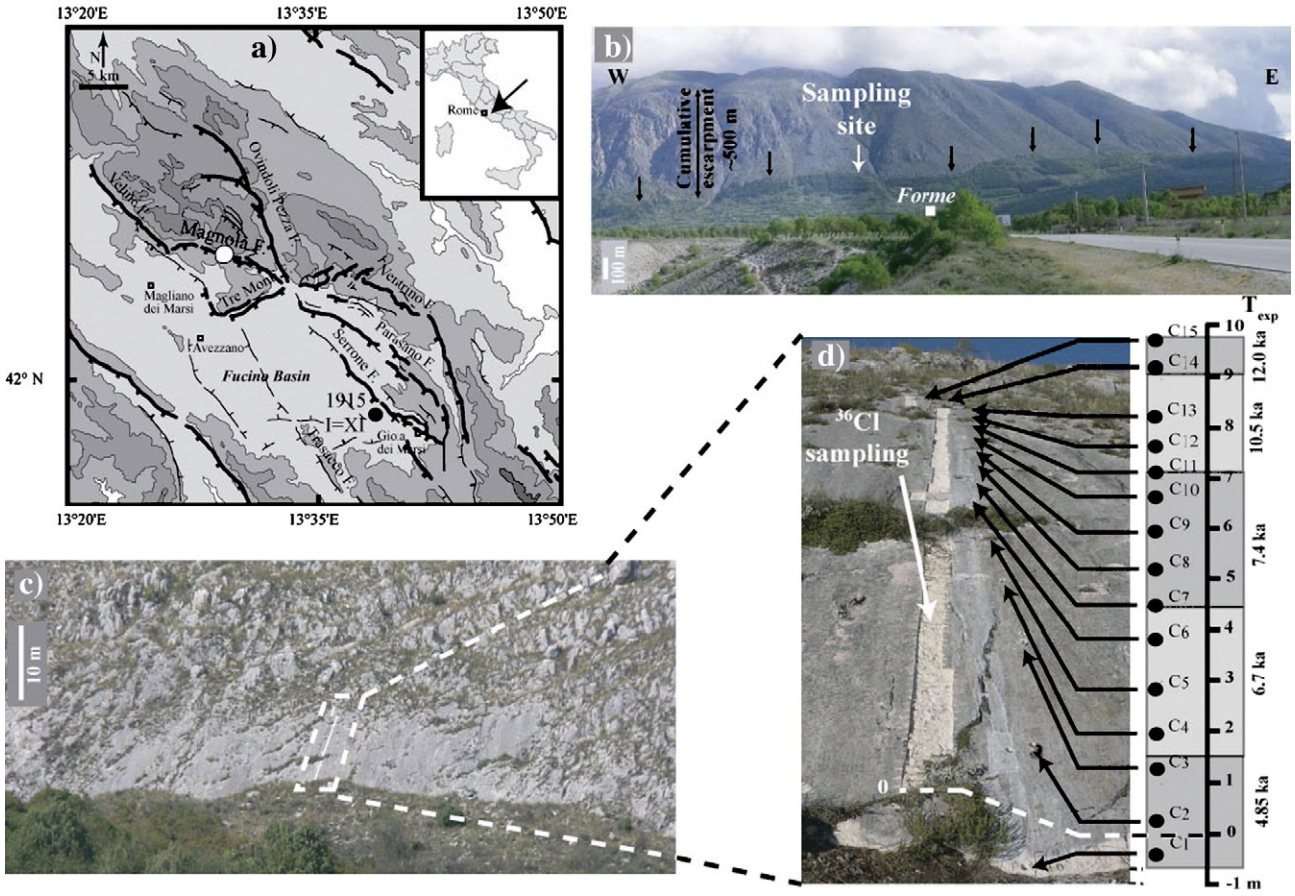

Fig. 2. Sampling site on the Magnola fault. a) General tectonic setting (redrawn from Palumbo et al., 2004). Only major active faults are reported, all normal. Grey colors are for topography. The 1915 Fucino earthquake is indicated. The dot on the Magnola fault locates the sampling site. b) Northward view of the Magnola cumulative escarpment. The Holocene limestone scarp is indicated with black arrows. The Forme village is indicated. c) Closer view of the Holocene limestone scarp at the site of sampling. The white line is the vertical groove sampled by Palumbo et al. (2004) for ^{36}Cl exposure dating. d) Closer view of the ^{36}Cl-sampled site, together with the position of the cores (shown by the black arrows) sampled and analyzed in the present study. The upscarp positions of the cores are reported relative to the bottommost sample of Palumbo et al. (2004), taken as the zero. The grey zones indicate the major exhumed slip zones identified by Palumbo et al. (2004), with their exposure ages (T_{exp}). Note that the scarp surface shows noticeable differences from base to top. The very base of the scarp appears as a white, 20 cm high strip that contrasts with the grey color of the rest of the scarp. On its bottom first 4–5 m, the scarp surface is smoothed with little evidence of disruption and weathering. Further above, it becomes rougher and locally dissected by karstic fissures, vertical flutes, and pits whose density increases with height. Above a height of ≈10 m the surface of the scarp is dismantled into chaotic blocks.

We focus on one of these limestone scarps, that of the Magnola fault in Central Apennines, Italy. Magnola is one of the main faults of the Fucino system, part of which ruptured in a devastating, $M \approx 7$ earthquake in 1915 (Fig. 2a; Odonne 1915, Michetti et al., 1996, Galadini and Galli 1999). The Holocene activity of the Magnola fault is expressed by a continuous limestone scarp that runs at the base of its 500 m-high cumulative escarpment (Fig. 2b–c). The Magnola fault is an ideal target to explore a new method for past earthquake recovering, since its Holocene seismic slip history is already known. This slip history was derived from top to base-continuous *in situ* ^{36}Cl cosmic ray exposure dating of the scarp surface, at one spot of the fault length (Palumbo et al., 2004, Fig. 2c–d). The ^{36}Cl concentration distribution was best explained by five successive major earthquake exhumations over the last ≈12 ka, with slips between 1.5 and 3 m, separated by 1–3.1 ka-long periods of quiescence (Fig. 2d). Though powerful to recover seismic slip histories, cosmic-ray exposure dating is extremely costly, thus cannot be used as a routine.

We here explore a new approach that may help overcoming these limitations. As a normal fault breaks in a large earthquake, a section of its plane is suddenly exhumed and exposed to supergene weathering; rain, wind, snow, vegetation, bacterial activity, etc… The longer the surface is exposed, the more intense may be the weathering. A normal fault scarp is thus made of a series of rupture zones having been exposed, thus weathered, over significantly different time spans. We suspect that such differential weathering may be detected in the chemical content of the fault scarp rocks, and its 'signature' used as a base to identify the various rupture zones on the scarps.

We thus investigate the chemical content of 15 carbonate rock samples collected from the base to the top of the Magnola Holocene scarp, where Palumbo et al. (2004) earlier determined the seismic slip history of the fault (Fig. 2d). We analyze major and trace element concentrations in the samples, and examine the concentration changes as a function of scarp height, hence of exposure time. We find that the chemical composition of the host-rock primarily varies as a function of scarp height, with significant step-changes correlating with the major seismic slip events recognized by Palumbo et al. (2004). This preliminary work thus suggests that simple geochemical analyses of seismically exhumed fault rocks may help recovering the seismic slip history of the fault.

2. Seismotectonic Holocene history of the Magnola fault

The NW-striking, 15 km-long Magnola is one of the largest active normal faults of the Fucino system, which dissects the central part of the Apennine chain (Piccardi et al., 1999). Its 500 m-high cumulative escarpment is underlined by a continuous, ≈10 m-high, 50°-steep

Table 1
Major and trace element concentrations measured in host rocks

	Average concentration (ppm)	Minimum uncertainty (%)	Average Uncertainty (%)	Maximum Uncertainty (%)	C1	C2	C2*	C3	C3′	C4	C4*	C5	C6
				Elevation(m)	-0.35	0.3	0.3	1.25	1.25	1.95	1.95	2.85	3.85
Trace elements (ppm)													
Li	0.356	0	5	11	0.413	0.303	0.311	0.374	0.349	0.384	0.371	0.400	0.380
Sr	144	0	2	3	156	163	161	147	152	137	140	138	135
Y	1.614	1	2	6	2.12	1.41	1.39	1.98	2.00	2.26	2.24	1.25	1.96
Zr	0.485	0	3	6	0.858	0.519	0.527	0.594	0.559	0.522	0.521	0.429	0.562
Nb	0.036	2	6	8	(0.150)	0.039	0.038	0.041	0.044	0.026	0.029	0.021	0.037
Cs	0.024	0	5	10	(0.059)	0.020	0.021	0.032	0.029	0.025	0.025	0.015	0.026
Ba	4.68	1	3	4	2.88	3.78	3.87	3.03	3.16	(16.4)	(16.6)	2.70	3.33
La	0.575	0	3	6	0.885	0.558	0.551	0.785	0.813	0.887	0.891	0.400	0.718
Ce	0.362	1	3	6	0.686	0.382	0.385	0.481	0.489	0.431	0.460	0.257	0.399
Pr	0.091	0	3	11	0.159	0.084	0.085	0.130	0.136	0.139	0.140	0.060	0.113
Nd	0.401	0	2	6	0.670	0.364	0.365	0.546	0.567	0.597	0.605	0.271	0.526
Sm	0.080	1	7	14	0.137	0.066	0.067	0.118	0.120	0.114	0.128	0.044	0.105
Eu	0.019	0	9	14	0.028	0.018	0.018	0.029	0.025	0.030	0.028	0.014	0.024
Gd	0.109	1	4	12	0.175	0.101	0.100	0.135	0.153	0.165	0.164	0.074	0.136
Tb	0.017	2	6	11	0.028	0.015	0.016	0.023	0.022	0.025	0.027	0.011	0.021
Dy	0.117	0	5	14	0.170	0.098	0.105	0.158	0.151	0.180	0.154	0.090	0.143
Ho	0.028	1	5	12	0.040	0.026	0.026	0.037	0.037	0.041	0.043	0.023	0.034
Er	0.088	1	5	11	0.127	0.079	0.078	0.116	0.112	0.127	0.132	0.072	0.106
Yb	0.077	4	8	12	0.108	0.073	0.066	0.092	0.099	0.121	0.106	0.064	0.091
Lu	0.013	2	7	16	0.017	0.012	0.011	0.016	0.016	0.016	0.015	0.010	0.016
Pb	0.282	0	3	6	0.264	0.236	0.246	0.228	0.227	0.300	0.293	0.255	0.262
Th	0.026	4	10	19	0.050	0.026	0.021	0.043	0.046	0.028	0.033	0.014	0.031
U	0.324	0	3	7	0.299	0.281	0.281	0.307	0.294	0.261	0.266	0.346	0.327
Major element (%)													
Al_2O_3	0.005	–	–	22	(0.024)	0.002		0.007	0.006	–		–	0.003
CaO	56.349	–	–	4.5	55.57	57.45		56.23	56.59	55.41		56.66	55.23
MgO	0.422	–	–	4	0.425	0.401		0.440	0.437	0.449		0.425	0.436
Na_2O	0.013	–	–	9	0.013	0.010		0.013	0.012	0.015		0.013	0.013
K_2O	0.004	–	–	5	0.006	0.003		0.005	0.004	0.004		0.003	0.004
Fe_2O_3	0.010	–	–	3	0.015	0.011		0.011	0.010	0.011		0.010	0.011
MnO	0.005	–	–	7	0.004	0.005		0.005	0.005	0.003		0.005	0.004
TiO_2	0.001	–	–	10	0.003	0.001		0.002	0.002	0.002		0.001	0.002
P_2O_5	0.032	–	–	7	0.035	0.024		0.036	0.039	0.039		0.022	0.043

For trace elements, measurements and associated uncertainties are expressed in ppm, while they are in % for major elements. Measurements considered as outliers (see text) are in brackets. Measured concentrations close to 3–4 times the blank values are in italic. Hyphens indicate concentrations too low to be measured. Concentrations measured on standards BIR, BR24, UBN and BHVO-2 are indicated for information. Note that no data are reported for Rb, Ta and Hf because concentrations in all samples were always below the detection limit.

scarp, that has been shown to be the youngest, Holocene section of the seismically exhumed fault plane (Palumbo et al., 2004). Since the fault offsets Meso-Cenozoic carbonates, its slip surface, i.e., the fault plane, is made of carbonates as well. More specifically, the Holocene section of the fault plane appears as a 1–15 cm-thick layer of tough, recristallized calcite locally embedding small limestone clasts, whose outer, exposed surface has been smoothed into a flat plane by the repeated fault slips (Fig. A-a in the Appendix; see description of similar faults in Agosta et al., 2007; Agosta and Aydin, 2006). The smooth fault plane overlies a thicker zone (a few m) of densely fissured, brecciated carbonates. The overall fault structure is thus similar to that of most active faults.

Palumbo et al. (2004) have determined the Holocene seismic slip history of the Magnola fault, at one central spot of its length (Fig. 2a). The slip history was traced using the distribution of in situ ^{36}Cl concentration versus height of the Holocene scarp, distribution best explained by five successive major earthquake exhumations having occurred 12,000, 10,500, 7400, 6700, and 4850 years ago (Fig. 1 and 2d).

Thus, at the site sampled by Palumbo et al. (2004), the Holocene scarp surface consists of a uniform and smooth layer of calcite which, from top to base, includes at least five distinct sections, each 1.5 to 3 m high, that have been exposed to supergene weathering over 12, 10.5, 7.4, 6.7 and 4.85 ka. We analyze the chemical composition of rock samples taken from each of the five sections, and examine whether or not the composition varies as a function of exposure time.

3. Sampling and chemical processing

Using a portable driller, we collected fifteen cores (C1-15; Fig. A-b in the Appendix) along a vertical profile less than a meter away from the sampling groove of Palumbo et al. (2004) (Fig. 2c–d). The difficulty of the sampling (made by roping down the scarp) and the toughness of the carbonates forced us to limit the number of collected samples. The cores were sampled every 0.5–1 m from base to top of the scarp. Their upscarp position is defined with respect to the lowest sample collected by Palumbo et al. (2004).

The cores are overlain with a ~100 μm-thick dark coating that markedly contrasts with the white color of the host rock (Fig. A-b in the Appendix). We captured high-resolution images of the coating by Scanning Electron Microscopy (SEM) and made qualitative chemical analyses of that coating using a coupled Electron Dispersive Spectroscopy (EDS) Microprobe. Because the coating is too thin to be isolated from the underlying rock sample, we could not perform any detailed and accurate mineralogical analyses (such as X-ray diffraction). However, we report semi-quantitative major element analyses performed using a non-destructive μX-Ray Fluorescence spectrometry

C7	C7′	C8	C9	C10	C11	C11*	C12	C13	C13*	C14	C15	BIR	BR24	UBN	BHVO-2
4.45	4.45	5.25	5.95	6.65	7.15	7.15	7.65	8.2	8.2	9.2	9.7				
0.324	0.325	0.259	0.149	0.358	0.383	0.365	0.438	0.337	0.378	0.449	0.388	3.49	6.68	28.80	4.84
150	147	151	139	130	130	133	159	135	135	137	146	116	6.84	588	413
1.56	1.53	1.57	1.12	1.72	1.55	1.65	1.03	0.79	0.78	1.51	2.35	18.0	2.57	31.1	29.3
0.464	0.448	0.376	0.411	0.433	0.490	0.499	0.382	*0.348*	0.347	0.400	0.501	16.0	3.34	311	186
0.033	0.031	0.019	0.022	0.025	0.034	0.031	0.028	*0.009*	0.015	0.025	0.026	0.593	0.045	41.8	19.8
0.018	0.018	0.027	0.030	0.026	0.024	0.022	0.014	*0.005*	*0.005*	0.014	0.028	0.007	11.3	0.461	0.101
3.02	2.89	2.59	4.35	2.34	1.95	1.90	1.98	1.79	1.82	3.00	(16.9)	6.58	26.00	385	131
0.545	0.547	0.498	0.317	0.577	0.456	0.474	0.324	0.223	0.209	0.522	0.907	0.610	0.331	33.3	15.1
0.351	0.330	0.328	0.233	0.344	0.311	0.314	0.275	0.156	0.148	0.344	0.440	1.94	0.812	72.6	37.8
0.084	0.086	0.070	0.051	0.091	0.075	0.075	0.048	0.033	0.030	0.083	0.141	0.374	0.119	9.36	5.32
0.367	0.374	0.322	0.214	0.409	0.331	0.332	0.198	0.143	0.135	0.375	0.674	2.41	0.603	39.3	24.4
0.082	0.073	0.066	0.044	0.081	0.076	0.075	0.039	0.031	0.027	0.074	0.125	1.10	0.217	8.20	6.07
0.020	0.018	0.015	0.010	0.021	0.017	0.020	*0.008*	*0.006*	*0.005*	0.021	0.032	0.514	0.078	2.45	2.01
0.102	0.103	0.085	0.072	0.108	0.095	0.102	0.063	0.041	0.042	0.112	0.164	1.842	0.311	7.18	5.98
0.014	0.015	0.015	0.011	0.017	0.015	0.013	0.007	*0.006*	0.007	0.015	0.027	0.370	0.060	1.08	0.952
0.110	0.111	0.111	0.075	0.120	0.110	0.114	0.062	0.047	0.046	0.113	0.180	2.53	0.400	5.55	5.18
0.026	0.027	0.025	0.020	0.029	0.025	0.029	0.015	0.011	0.012	0.027	0.043	0.580	0.094	1.04	0.987
0.088	0.078	0.079	0.059	0.094	0.083	0.093	0.055	0.044	0.043	0.074	0.122	1.73	0.289	2.65	2.55
0.070	0.075	0.074	0.047	0.077	0.076	0.069	0.046	0.035	0.037	0.077	0.109	1.65	0.293	2.05	1.99
0.013	0.013	0.015	0.008	0.013	0.013	0.013	0.008	0.006	0.007	0.013	0.017	0.254	0.046	0.293	0.284
0.200	0.206	0.227	(0.755)	0.240	0.280	0.282	0.222	0.202	0.214	0.261	0.290	2.86	12.73	3.47	1.55
0.024	0.021	0.017	0.019	0.026	0.029	0.028	0.015	0.012	0.011	0.022	0.032	0.030	0.064	4.73	1.25
0.316	0.300	0.288	0.349	0.392	0.427	0.432	0.268	0.218	0.235	0.525	0.262	0.012	0.063	1.21	0.408
–	–	–	–	0.002	0.004		–	–		0.001	0.001				
56.87	55.89	56.91	55.87	55.55	57.08		57.31	56.89		55.45	57.07				
0.422	0.430	0.358	0.372	0.389	0.443		0.464	0.418		0.425	0.463				
0.014	0.013	0.010	0.008	0.013	0.015		0.018	0.014		0.016	0.017				
0.004	0.004	0.003	0.003	0.003	0.004		0.003	0.002		0.004	0.004				
0.009	0.009	0.011	0.010	0.011	0.013		0.007	0.007		0.011	0.011				
0.006	0.006	0.005	0.006	0.006	0.006		0.005	0.006		0.010	0.004				
0.001	0.001	0.001	0.001	0.001	0.001		0.001	0.001		0.001	0.002				
0.029	0.031	0.022	0.047	0.036	0.033		0.025	0.017		0.032	0.040				

(μXRF, Eagle® III EDAX; energy of 20 keV). These analyses were obtained on the coatings (spot diameter of 300 μm) and on the underlying rock samples (spot diameter of 30 μm) at increasing distances from the surface (first analysis at 0.1 cm depth, then every 0.5 cm from surface to bottom; Fig. A-b in the Appendix). Results are given in Table A (Appendix). Because measurements were homogeneous in the deepest parts of the cores (i.e., below 0.1 cm), only few cores were completely analyzed.

Accurate major and trace element contents were measured in the host rock of all cores (Table 1). The first 2 mm of each core was removed to eliminate the surface coating. Measurements were done on sub-samples collected in the first 1.5 cm of the coating-free cores (Fig. A-b in the Appendix). Trace elements were measured by ICP-MS (VG® PQ turbo +) using the procedure described by Marini et al. (2005) but slightly modified to eliminate the carbonates before whole rock dissolution. Measurements were corrected for machine drift using a multispike (Be, As, In, Tl and Bi) and calibration of the signal was done using repeated analyses of the reference material BHVO-2. The precision on measurements can be evaluated from the analysis of the international rock standards UBN and BIR-1 and the in-house standard BR24. Because UBN and BIR-1 have very low trace element contents, the precision is not very good but usually better than 10% (Table 1). Analytical uncertainties are estimated by comparing results obtained on multiple data acquisition for the same sample and complete duplicate analyses of selected samples (Table 1). Those uncertainties are ≈5% for most elements, lower than 15% for some elements and reach higher values (≈20%) for the few elements whose concentration is hardly higher than 4 times the blank values (Th, Lu). In the following, we propagate the maximum uncertainty obtained for each trace element to the whole series of measurements of that element. Major element concentrations were determined from aliquots of the solution used for trace element analyses (Table 1, concentrations expressed as oxides). Analyses were carried out using a ICP-AES (Perkin Elmer® Optima 3300 DV). Calibration was done using Fluka® standard solutions for atomic spectrometry. The analytical uncertainties are estimated from three repeated measurements of each sample. The maximum uncertainties range between 3 and 10% for all elements except Al_2O_3 whose concentrations are very low. Here again, we propagate the maximum uncertainty obtained for each element to the entire set of measurements of that element.

In Table 1, all measured concentrations, even when they approach the detection limit, are listed. In brackets are the concentrations that are more than double the average concentration of the entire sample collection; we consider these values as outliers, and as such, we ignore them in all calculations presented below.

4. Data analysis

The Magnola scarp rock consists of a very homogeneous, low magnesium carbonate (56±0.6 % CaO and 0.40±0.05% MgO; Table 1).

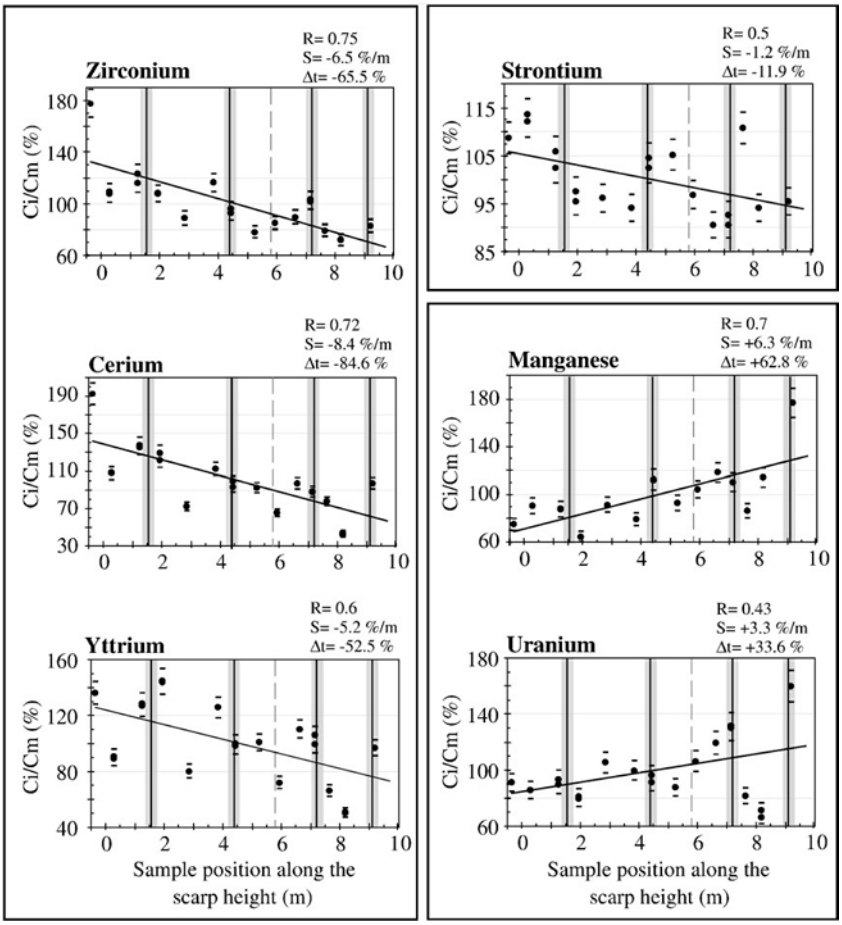

Fig. 3. Concentrations of Zr, Ce, Y, Sr, Mn, and U, as a function of scarp height. In all plots, *X* is the on-fault position of the samples increasing upward and *Y* is the concentration of sample *i* (Ci) normalized by the mean concentration (Cm) averaged over the whole sample collection, in percent. Solid vertical lines represent the transitions between the major earthquake slip zones identified by Palumbo et al. (2004), with their position uncertainties in grey (uncertainties on the on-scarp position of the transitions are ±25 cm on average according to the Fig. 5c of Palumbo et al., 2004). The thin dotted vertical line locates a possible additional earthquake suggested by Palumbo et al. (2004). The slanted straight lines are the regression curves calculated from all measurements (but those in C15 sample). When several measurements were done for the same sample, only the average was used for the regression calculation, but all measurements are plotted in the figure. Concentrations are given in Table 1 and regression parameters shown on the plots are given in Table C-b (Appendix).

The trace element compositions define patterns parallel to that of Reference Shales (Sholkovitz, 1988; Fig. B-a in the Appendix), but with much lower and relatively constant contents related to the high carbonate content (Plank and Langmuir, 1998). The seawater origin of the Magnola carbonates is well preserved in the samples, as demonstrated by the systematic negative Ce anomalies (Fig. B-b in the Appendix).

4.1. Evolution of host rock chemical content as a function of scarp height

To examine how the major and trace element concentrations measured in the host rock vary as a function of scarp height, hence as a function of exposure time, we built a series of figures that we will first describe before analyzing them.

First, because of the large number of measured elements, we calculate regression coefficients between element pairs to highlight possible common behaviors. The regression coefficients are reported in Table B-a (Appendix). Expected affinities appear clearly, such as those linking the REE together and to Yttrium, and those linking the insoluble elements together. Thus, in the following, we may discuss the behavior of the REE-Y and insoluble elements by restricting our analysis to only one well-constrained element representative of each group.

Second, we built a series of plots (Fig. 3 and Fig. C-a in the Appendix) documenting the behavior of each element as a function of scarp height. In all these plots, the element concentration in each sample (Ci) is normalized to the average concentration of that element in the whole sample collection (Cm), and plotted as a function of scarp height. Error bars on normalized concentrations are calculated using the maximum uncertainties given in Table 1. The transitions separating the major earthquake slip zones identified by Palumbo et al. (2004) are reported as vertical lines, with their on-scarp position uncertainties (grey bands). Then, for each element, a linear regression is calculated as a function of scarp height (straight line). The regression parameters are reported in Table C-a in the Appendix. Finally, Fig. 4 shows the total base-to-top concentration change values (Δt) obtained for all elements (empty dots). Maximum uncertainties on concentration measurements being ±25% in the worse case, any number falling within the ±25% stippled band indicates no significant concentration variation with scarp height. Figs. 3, 4 and Fig. C-a in the Appendix show that most element concentrations vary as a function of scarp height. The total concentration changes from base to top are significant with values up to 65% (Fig. 4, empty dots; Al_2O_3 not well constrained). Though irregular in detail, the overall base to top evolutions are generally satisfactorily averaged by linear trends with regression coefficients up to 0.6 (Table C-a in the Appendix). When the topmost and oldest C15 sample is excluded from the calculations, those coefficients significantly increase (up to 0.75) (Table C-b and Fig. C-b in the Appendix). We suspect that C15 is not representative of the original scarp composition because of the significant mechanical disruptions that alter the crest of the scarp where C15 was sampled. We thus

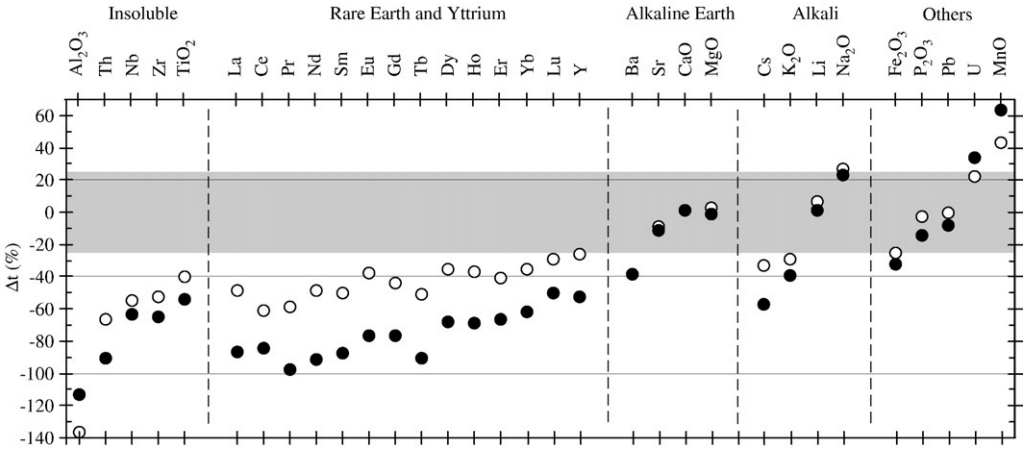

Fig. 4. Overall concentration changes from base to top of the scarp. Elements are listed by chemical affinities. The *Y*-axis is the total concentration change (Δt, in %) inferred from the regression calculations (Table C in the Appendix). Empty and solid dots are Δt values from Tables C-a and C-b in the Appendix, respectively. Changes smaller than ±25% (grey horizontal field) are considered insignificant.

exclude C15 from the analysis. The recalculated parameters are shown in Figs. 3, 4 (solid dots) and Table C-b in the Appendix.

Three distinct overall behaviors are distinguished. About 22% of the elements (Pb, Sr, Ca, Mg, P, Na, Li) do not show any significant variation along the scarp height; their concentrations change by less than 25% from base to top. Note that among these 'stable' elements are those most abundant in the carbonate host rock. The vast majority of elements (72%) display a significant concentration decrease, between 30 and 100%, as one goes from the base to the top of the scarp. These 'decreasing' elements include the REE, both light and heavy (LREE and HREE, respectively), together with Yttrium, the insoluble elements, some of the alkaline (K, Cs) and alkaline Earth elements (Ba), iron (Fe), and aluminum (Al; though not well-constrained). The decrease of the LREE is larger than that of the HREE. Finally, the remaining 6% of the elements, namely Mn and U, show an opposite behavior, with concentrations increasing by 30–60% from base to top of the scarp.

A closer inspection of the concentration versus height plots (Fig. 3 and Fig. C-b in the Appendix) shows that, though the element concentrations follow a roughly linear trend when considered overall, they also display peaks that significantly depart from the average trend. A way to quantify those peaks is to measure them with respect to the average concentration of the considered element in the whole scarp (Cm); the peak amplitude thus is the difference Δi between Ci (concentration in sample *i*) and Cm. Since we want to compare the peak amplitudes for a large number of elements, we need to normalize them so that they eventually fall in a similar range of values. We choose here to normalize each peak amplitude Δi by the mean absolute value calculated from all Δi (for a given element,

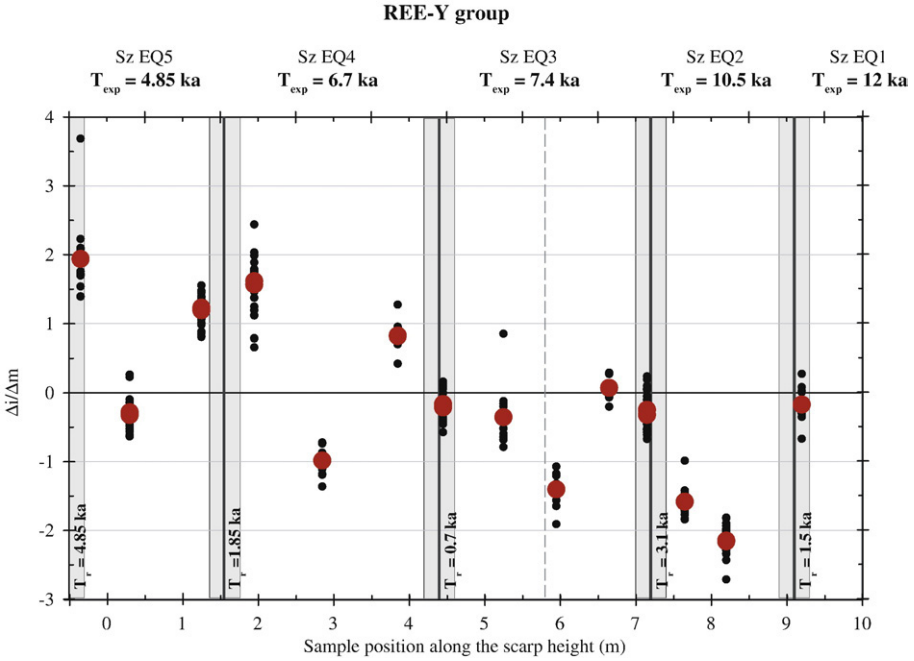

Fig. 5. Concentration variability of the REE-Y group as a function of sample position along the fault scarp. Transitions between slip zones are shown as in Fig. 3. The *Y*-axis measures the difference Δi between a given concentration in core *i* (Ci) and the mean concentration over the whole core collection (Cm), normalized to the mean absolute value of those differences ($\Delta m = \sum|\Delta i|/N$ with *N* the number of measurements); *Y* thus plots $\Delta i/\Delta m$ (that is $(Ci - Cm)/\Delta m$). The black dots are individual element measurements while the red dots correspond to the average behavior of all the REE-Y. Sz EQi for slip zone exhumed by earthquake *i*. T_{exp} is exposure time while T_r is residence time in upper soil (For interpretation of the references to colour in this figure legend, the reader is referred to the web version of this article.)

$\Delta m = \sum|\Delta i|/N$ with N the number of measurements). Fig. 5 shows the result for the REE-Y group. It first confirms that the REE and Y (black dots) behave in a similar manner. Their peak amplitudes can thus be averaged (red dots). Plotted as a function of scarp height, the red dots define sort of a 'wavy' curve, with maxima 'crest-to-trough' amplitudes up to 100% of the mean concentration Cm (see Fig. 3 and Fig. C-b in the Appendix for values in %). The crest values decrease overall as one goes upscarp, to reach negative values at its top. All concentration maxima are found at or close to the transition zones that separate the successive earthquake slip surfaces, while all concentration minima are roughly in the middle of the slip surfaces. Fig. 6 shows that the vast majority of analyzed elements have the same 'wavy behavior' as the REE-Y group. Fig. 6a examines whether the various elements show a similar variation pattern within a given slip zone. It is thus designed to highlight the shape of the 'waves'. Note however that data are not dense enough to constrain the precise shape of the so-called 'waves', so that the term 'wave' is only used in a general sense. Fig. 6b shows the amplitude of the concentration changes, hence of the 'waves', depicted in Fig. 6a. The way these two figures are built is described in the caption. Fig. 6a shows that most element concentrations vary similarly both within each slip zone and from one slip zone to the other.

In any slip zone, the concentrations draw a concave-up 'wave' centered at about the half-slip zone height, with maxima at or close to both edges of the slip zone. Most elements show that pattern repeated in all slip zones (REE-Y group, Zr, Th, K, Ti, Nb), or in most of them (Cs, U, Mg, Na, P, Pb, Fe, Mn, Li). Fig. 6b shows that in any slip zone the crest-to-trough amplitudes of the waves are large for most elements, reaching up to 100% of Cm. The elements with the largest variations (>40% Cm) in all or most slip zones include the REE-Y group, Th, Cs, and P.

4.2. Evolution of the coating composition with scarp height

The SEM images of the core surfaces (Fig. 7) suggest that the roughness of the exposed fault plane increases as one goes upscarp; while striated small spots are preserved in the bottommost sample (Fig. 7j), none is found further upward where the sample surfaces rather show an increasing density of microscopic pits (Fig. 7a–c–e–g). At a smaller scale, the pitted samples appear coated with a large number of spherical and/or flattened features ~5 μm in size, most entrapped in pits (Fig. 7f), and with >10 μm-long filaments (Fig. 7d–h). The shape and size of the former features suggest that they may be algae (Smith et al., 2000), while the filaments may be rhizines of

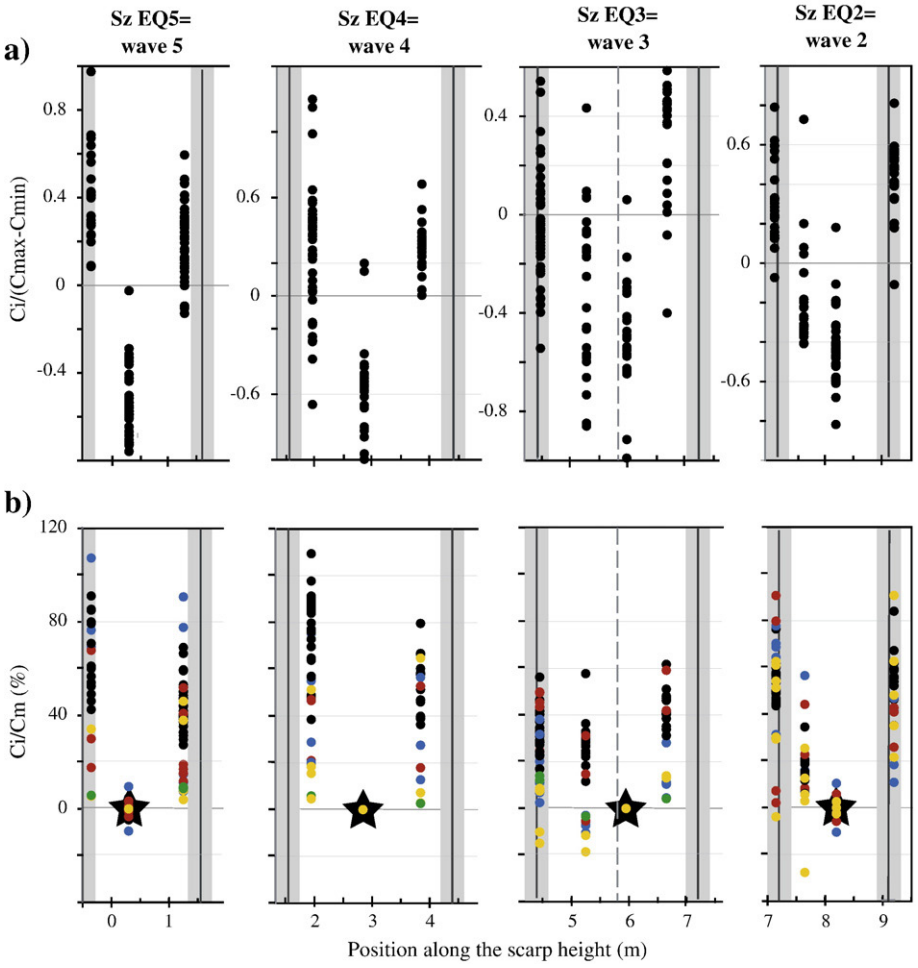

Fig. 6. Concentration oscillations within seismic slip zones. In both a and b, each slip zone is treated independently so that each plot includes only the data pertaining to this slip zone. a) Common pattern of the concentration oscillations. Elements are in black. The X-axis and transition zones are as in Fig. 3. Sz EQi for slip zone exhumed by earthquake i. The Y-axis plots the concentrations Ci normalized by the crest-to-trough amplitude of the wave ($C_{max} - C_{min}$), with respect to the regression curve calculated from all measurements (but C15). The concentrations vary with the same pattern in each slip zone. The detailed list of elements plotted is given in Table E (Appendix). b) Amplitudes of the concentration oscillations. Colors distinguish the elements using their chemical affinities: blue, insoluble; black, REE-Y; green, alkaline earth; red, alkali; yellow, others. The X-axis and transition zones are as in Fig. 3. The Y-axis plots the concentrations Ci normalized by the mean concentration Cm, with the value considered as the trough of the wave being forced to zero for all elements (star; note that it is not necessarily C_{min}). The amplitudes of the concentration oscillations are large for most elements. Their values are reported in Table E (Appendix) (For interpretation of the references to colour in this figure legend, the reader is referred to the web version of this article.)

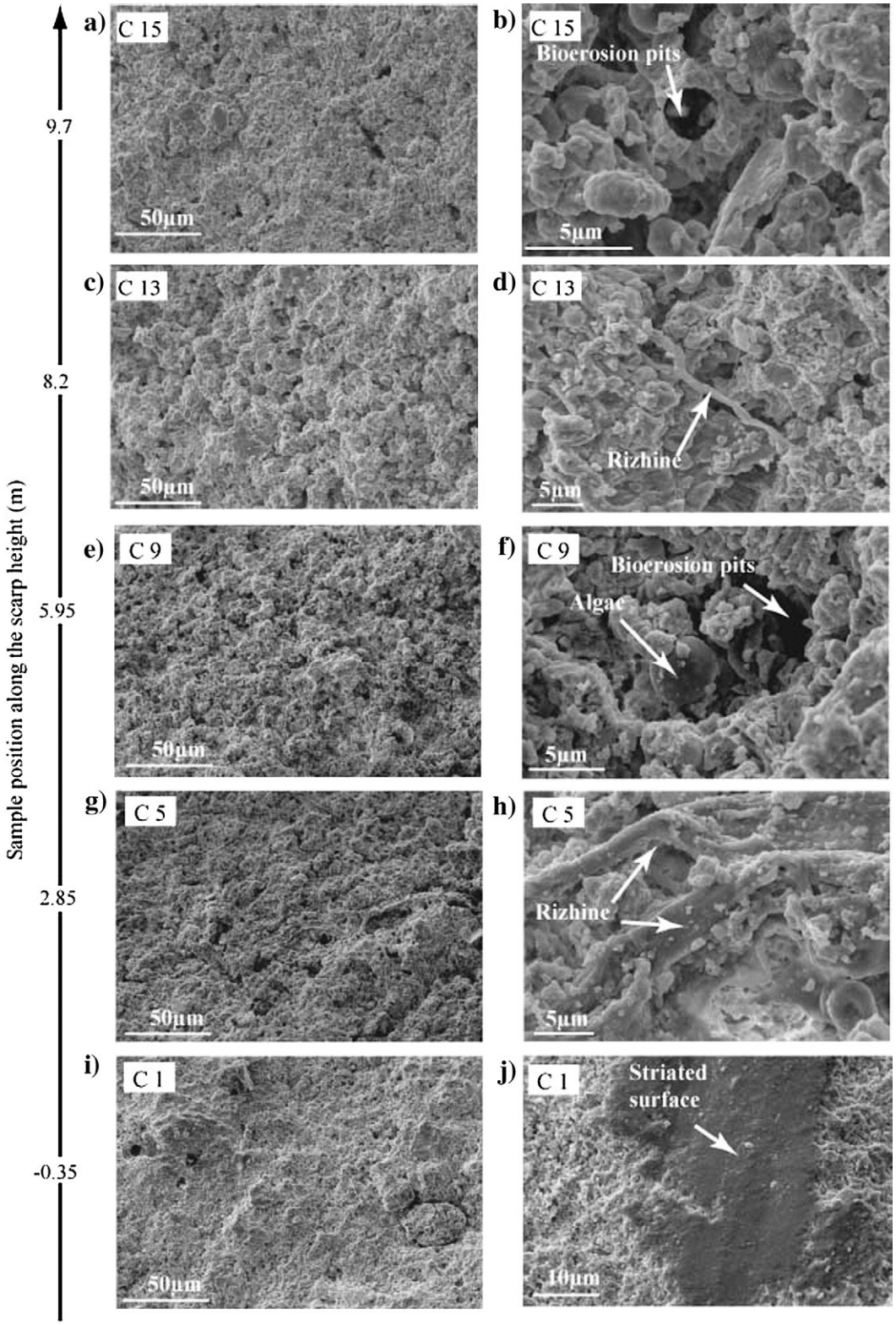

Fig. 7. SEM images of the core surfaces. Panels a, c, e, g, and i show general views of the surfaces, while panels b, d, f, h and j show close-up.

lichens. The close proximity of the rounded algae and the pits (Fig. 7f), the peculiar shape of the pits — as rounded as the algae (Fig. 7b–f), and the apparent penetration of the rhizines into the rock (Fig. 7d–h), combine to demonstrate the presence of organic compounds on (epilithic) and within (endolithic) the rocks. The EDS analyses of the surface coating reveal the presence of non-carbonated particles, such as scarce micrometer-scale iron sulphides (Fig. D-a in the Appendix) and decamicrometer-scale aluminum-rich silicates (Fig. D-b in the Appendix). These particles contrast with the carbonate composition of the host rock suggesting that part of the coating material is not derived from the host rock; external agents thus likely contribute to the coating formation. The semi-quantitative major element analyses

performed by μXRF on the coatings are given in Table A (Appendix) and are markedly different from the values obtained for the same elements in the host rocks. Even though the coatings consist mainly of CaO, they also contain a significantly higher proportion of SiO_2 and Al_2O_3. In Table D (Appendix), we provide correlation coefficients between the various elements measured in the coating, and the coefficients highlight significant relationships between SiO_2, Al_2O_3, TiO_2, and Fe_2O_3, but also between K_2O and SO_3. Together with the microscopic observations and the EDS analyses, these correlations confirm that the coating is partially made of aluminum-rich silicates and iron-sulphides. These could be a combination of various minerals including clays and jarosite. When plotted as a function of scarp height, the major element contents of the coatings do not show any specific pattern or trend, and most of them remain constant despite local variability.

5. Discussion

5.1. Overview of carbonates chemical weathering processes

The carbonate weathering processes have been studied in considerable detail, particularly because of the ubiquity of calcite in the sub-surface environments (e.g., Sweeting, 1966; Trudgill, 1985; Smith et al., 2000; Plan, 2005). The most critical property of calcite is its highly reactive nature; the calcite bulk equilibrium is weak and many factors may disrupt it, leading to calcite dissolution or degradation.

Calcite dissolution occurs under the action of agents such as rain, moisture, acidic fluid circulations, and/or biogenic features (e.g., Trudgill, 1985; Budd et al., 1995; White and Blum, 1995). Any fluid containing carbon dioxide has the ability, once in contact with calcite, to dissolve it, even at the microscale. Significant fluid circulations occur at shallow depth (<1–2 km), where the carbonates are buried before they are possibly exhumed and those fluids are harmful to limestone, particularly in the sub-surface where they reside and flow through an acidic soil. Indeed, the shallow soil, and particularly its 30–50 first cm, is a zone of intense acidification due to the high density of microorganisms, humus material and plant roots. Such materials produce large amounts of CO_2 through processes such as root respiration, oxidation of organic material and microbial respiration (e.g., Reardon et al., 1979; Paul and Clark, 1989; Fierer et al., 2003), which lead to relatively low, thus acidic soil–water pH. Additional bacterial acidification also commonly occurs (Le Métayer-Levrel et al., 1999). Altogether these processes contribute to dissolve the carbonates. Once exposed to free air, the carbonates experience additional chemical weathering under supergene agents such as rain (pH≈5.7), moisture or biogenic features (such as lichens, bacteria, etc…; Danin et al., 1983; Chen et al., 2000; White, 2000; Burford et al., 2003). This weathering leads to further dissolution of the calcite. Because biotic weathering and internal fracturing may also occur and contribute to open paths into the rock, the calcite dissolution front may go deep into the host rock, at least several cm (e.g., Le Métayer-Levrel et al., 1999).

Once calcite dissolution has occurred, dissolution products may either re-precipitate or be leached away. In the former case, while re-precipitating, the calcite may incorporate impurity elements in its new lattice. Elements most favorably incorporated into a re-precipitating calcite lattice are those with an ionic radius similar to, and a valence compatible with, that of Ca^{2+}, because they can substitute to Ca and produce minimum spatial disorder in the calcite lattice. Those elements include Sr, Pb, Mg and P (e.g., Mucci and Morse, 1983; Pingitore and Eastman, 1986; de Leeuw, 2002), and possibly Co, Cd, Ba, Zn (e.g., Reeder et al., 2001; de Leeuw, 2002). Under reducing conditions, U and Mn can also be incorporated into a calcite lattice. Indeed, Mn^{2+} can occupy an on-center position within the calcite lattice, with spatial disorder not significantly different from the host Ca^{2+} (Cheng et al., 2001; Sturchio et al. 1998). The uptake of uranium by calcite is more complex and depends on the uranium valence. In oxidized surface environments, uranium exists as U^{6+} and U^{4+}, U^{6+} being usually much more soluble and mobile than U^{4+} (Langmuir, 1997; Elzinga et al., 2004). U^{6+} behaves roughly as Mn and is easily incorporated in the calcite structure (Sturchio et al., 1998; Reeder et al., 2001; Kelly et al., 2003). U^{4+} forms in reducing conditions, which prevail in the presence of organic matter and/or of specific bacteria (Lovley et al., 1991; Anderson and Lovley, 2002; Ohnuki et al., 2005). In that case, the U^{4+} ion occupies the Ca position with minimal distortion and has thus a stable location in calcite (Lovley et al., 1991; Sturchio et al., 1998; Reeder et al., 2001). U^{4+} can therefore be integrated within the calcite structure for very long times. Usually, the incorporation of U into calcite is coupled with that of Na (Kelly et al., 2003; Sturchio et al., 1998), though in smaller proportions. Any disruption of the calcite equilibrium leading to calcite dissolution and re-precipitation in the presence of the elements listed above likely results in some element-calcite solid solution formation, so that these elements are incorporated into the re-precipitated calcite lattice and remain in the final material. On the other hand, this is not the case of other elements such as Al, REE and high-field strength elements (Nb, Th, Zr, Ti), which are not easily accommodated in the calcite structure and are most probably trapped at grain boundaries. These elements are released during calcite dissolution, but are not accepted in the re-precipitating structure. The net result is a loss of these elements in the final calcite. Note that, in such carbonate environment, the process that governs the trace element behavior differs from that most commonly found in alteration profiles such as lateritic profiles where the elements least affected by mobility are the insoluble high field strength elements (Braun et al., 1993). In addition, some elements (such as Fe and REE) are preferentially complexed by organic matter (e.g., Zhaoliang et al., 2006; Pourret, 2006), and/or are taken up by specific bacteria (e.g., Takahashi et al., 2005). The dissolved REE can easily be assimilated onto certain bacteria cell walls by adsorption on carboxylate and phosphate sites (e.g., Takahashi et al., 2005). As a result of interaction between host rock and organic matter or bacteria, trace elements incompatible with the calcite structure may thus be progressively removed from the host rock to form organic complexes. Taken together, the combined processes of calcite dissolution–(re)precipitation and leaching eventually result in the crystallization of a purer calcite within the host rock, and in the removal of a range of impurity elements that become free to circulate in the medium around.

5.2. Implications on the Magnola scarp rock chemical contents

The weathering processes described above account well for the upscarp concentration changes that we document.

First, it has to be noted that the scarp rocks that we analyze have formed at depth, likely in the first kilometer below the ground surface (the total slip accommodated by the fault is less than 1 km). The exposed slip surface that we study is actually a 1–15 cm-thick layer of tough cemented rocks. Such architecture is common to most active normal faults offsetting carbonates (e.g., Agosta and Aydin, 2006). The cemented slip zone is generally thought to have formed as a result of mixed processes such as comminution of the original rock due to intense shearing during repeated earthquake slip events, dissolution/precipitation of the host rock minerals, various chemical reactions between rock minerals and external agents, etc… (e.g., Sibson, 1977; Chester and Logan, 1986). The high content in calcite crystals and the low Mg concentration of the Magnola fault carbonates suggest that the scarp rocks have initially formed at depth through repeated events of dissolution–precipitation (e.g., Busemberg and Plummer, 1989). We thus expect the carbonate scarp rocks to have had a homogeneous composition before they were exposed to the free air. In any case the trace elements pattern of the initial host limestone is preserved and uniform in the cemented slip zone at the scale of the scarp (Fig. B in the Appendix). More than 70% of the analyzed elements have their

concentration decreasing upward along the scarp height and therefore as a function of exposure time. The rate of decrease is high, averaging 5% per meter, and leads to concentration reductions up to 100% in the topmost samples that have been exposed for the longest time. This shows that the limestone scarp is increasingly degraded as exposure time increases, with that degradation consisting in the progressive leaching of most chemical elements. It is likely that such leaching occurs concomitant with a steady-state dissolution–(re) precipitation of the calcite. Such steady-state dissolution–(re)precipitation process is consistent with the observed upscarp stability of the elements that easily substitute to Ca in the calcite lattice (Pb, Sr, Mg and P). The REE-Y elements are particularly affected by the upscarp leaching. This may be because these trace elements occupy weak positions (such as grain boundaries) within the carbonate assemblages, and as such, can be easily mobilized, even in the absence of any lattice destruction. The LREE are leached more efficiently (−8.6%/m) than the HREE (−6.9%/m), possibly because endolithic bacteria that are known to live in carbonate host rocks retain LREE less efficiently than HREE (Takahashi et al., 2005).

In contrast to most trace elements, Mn, U and possibly Na concentrations increase as a function of exposure time. It could be related to the capacity of Mn, U and Na to enter the calcite structure. Yet, as we highlighted the presence of organic matter on the core surfaces, it is more likely that the upscarp increase in uranium concentration results from interaction between the rock and organic material present on or next to the surface.

Superimposed to the overall concentration changes discussed above, an additional signal – concentration peaks at the transition zones separating the major slip events – is identified in most concentration-scarp height profiles (Fig. 5 and 6). The concentrations of most elements increase by up to 100% (compared to the average value Cm) within a 0.5–1 m thick zone that brackets the earthquake transitions. As shown in Fig. 1, the transitions separating the different exhumed fault sections are specific because they remain at the interface between soil and atmosphere for the long periods of time (commonly several thousands of years) that separate the major earthquakes. As seen before, the soil–atmosphere interface, and more specifically the first 30–50 cm of the soil, is a zone of intense acidification, extremely harmful to limestone. Not only the large amounts of acidic fluids that reside through the soil enhance calcite dissolution, but also the high enrichment of those fluids in numerous chemical impurities contributes to contaminate the re-precipitating calcite by introducing various trace elements in its structure and/or at its grain boundaries. We thus suggest that the concentration peaks observed at the transition zones between earthquakes result from the scarp rock calcite having re-precipitated in an impurity-rich upper soil. The impurities that accumulated in the soil and in the fluids, colloids and particles, likely have their origin in the weathering of the footwall section of the scarp already exhumed above the soil. The REE-Y being the elements most affected by leaching of the exposed scarp, they are expected to be highly concentrated in the upper soil and residing fluids (e.g., Duddy, 1980; Dia et al., 2000; Tauton et al., 2000; Tyler, 2004; Zhaoliang et al., 2006; Pourret et al., 2007). This is consistent with those elements having the largest concentration peaks at the transition zones. Because a colluvial layer (that can be locally several 10 cm thick; e.g., Palumbo et al., 2004) progressively builds up at the base of the scarp as the scarp degrades, the thickness of the acidic layer can locally increase and extend the zone of concentration peaks slightly 'above' the actual transition zone (Fig. 1, right panel).

The scenario that we suggest implies that the concentration peaks measured at the transition zones built up during the quiescence periods that separated the major earthquakes. According to Palumbo et al. (2004), those periods, which we call 'residence times in the upper soil', range from 0.7 to 4.85 ka (Fig. 5). Fig. 8 shows the concentration peaks (in %) at the transition zones, as a function of residence time in the upper soil (data in Table E in the Appendix). The black dots correspond to individual elements while the red symbols show their average behavior. The concentration peaks differ depending on the considered element. Yet the average values are roughly constant, about 46% (dotted-line), regardless of the residence time. This constancy suggests that the concentration peaks build up rapidly in the soil (concentrations reach the average peak value in less than 0.7 ka), where they are subsequently preserved (concentration peaks remain constant regardless of residence time). The elements with concentration peaks higher than the average value are primarily the REE and *Y* (Table E in the Appendix). We could not really evaluate whether the coatings follow a similar pattern because the layer is too thin to be analyzed by the same technique as the host rocks. However, our qualitative major element study shows that the coatings have chemical compositions different from that of the host rock and partly derive from external contributions. We suggest that the chemical composition of the coating essentially reflects the local, intense chemical exchanges that occur between the rock surface and the biologic compounds that reside on that surface. Micro-scale disruptions of the rock surface may also favor trapping of exogenous materials such as the observed Al, Si, Fe, and S-bearing particles (Potter and Rossman, 1977; Dorn, 1998, 2007). The coating chemical content is thus constantly remobilized and modified by external agents, so that it probably does not retain the signal observed in the 'preserved' host rock.

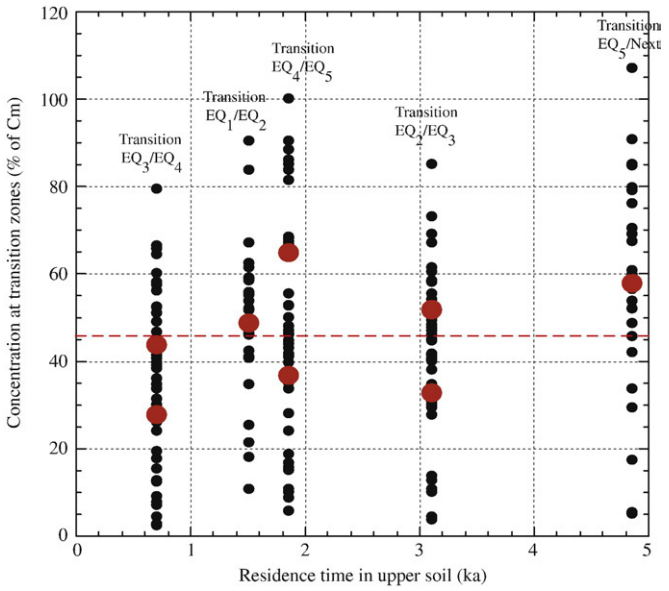

Fig. 8. Concentration peaks in transition zones as a function of residence time in upper soil. Concentrations (in % of Cm) are measured relative to the trough of the wave identified in each seismic zone (see Fig. 6b). Data from Table E (Appendix). Individual elements are shown with black dots while red symbols correspond to the average concentrations of all elements. Transition zones between earthquakes are indicated. Note that concentration peaks are shown by one or two values for they are defined by one or two values bracketing the transition zones (see Figs. 5 and 6). The horizontal dotted-line indicates the average, steady-state concentration at the transition zones.

5.3. Inferring earthquake slip history from the chemical content of fault scarp rocks

Our study shows that:

- The concentrations of most major and trace elements decrease as a function of exposure time of the fault scarp surface, at a rate averaging 5%/m and 4.5%/ka. The REE and *Y* have the highest decrease rate (≈8%/m and 7.2%/ka; Table C-b in the Appendix).
- Concentration peaks are found at the transition zones between seismically exhumed scarp sections. They most likely result from enrichment processes occurring while the rocks are long standing in the upper soil.

- Those enrichments in the soil occur at a fast rate since steady-state concentration peaks are reached in less than 700 years.

We suggest that these observations can be generalized to unravel the recent (<10–15 ka) earthquake slip history of a normal fault having a well-preserved limestone scarp at the ground surface. The approach would consist in:

- Sampling the rocks from the base to the top of the preserved fault scarp; a sampling performed every 30–50 cm should be sufficient to capture the major earthquake ruptures; samples need not be thicker than 2 cm;
- Measure the host rock *Y* and REE contents, which are the best markers, and report them as a function of scarp height;
- Concentration peaks should be found that locate the transition zones between the past major earthquake ruptures; the concentration-height plots may thus allow identifying the major earthquake rupture zones on the scarp, while measuring the amplitude of the slip produced at surface by those earthquakes (at the site of study);
- The age of the identified earthquakes might then be obtained by exposure dating of a few samples only taken from each identified rupture zone.

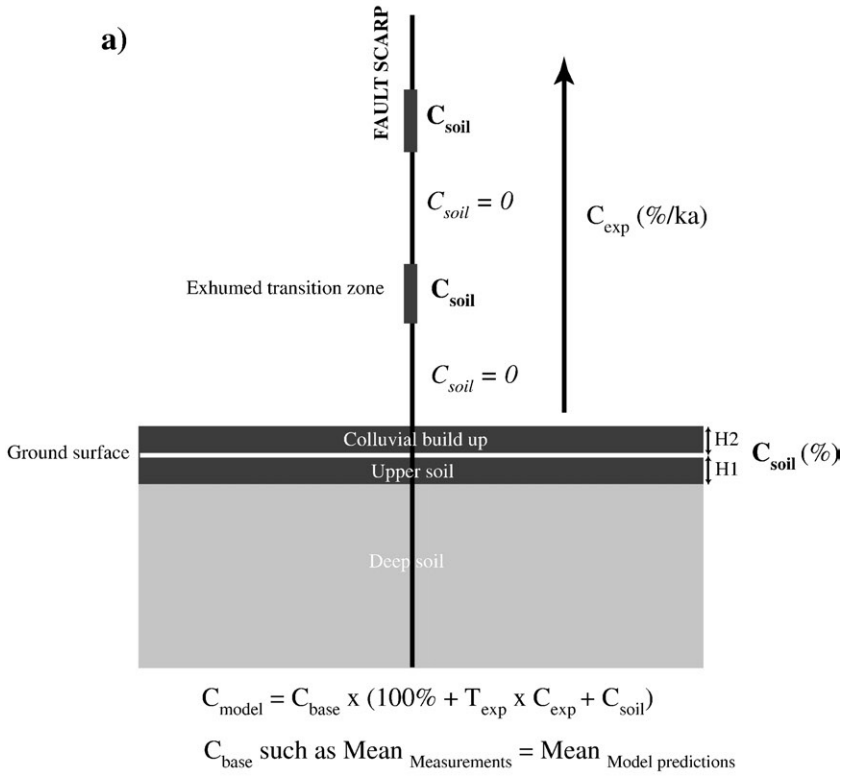

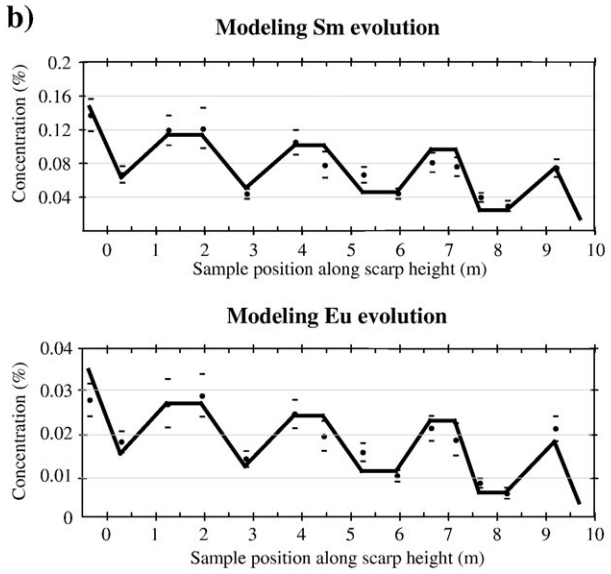

Fig. 9. First-order model proposed to reproduce the observations. a) Basic parameters of the model. The fault scarp is sketched in cross-section. The evolution of concentrations as earthquake slip events repeat is sketched in Fig. 1 (right panel). In the absence of data to document it, the transition from C_{soil} to C in deeper soil is assumed to be sharp. b) Model predictions (broken line) compared to measurements (dots) for Sm and Eu. The fit coefficients *R* are reported in Table F (Appendix).

It is noteworthy that faults with a fresh scarp that exposes the preserved fault plane, generally are active normal faults that offset limestone rocks in a temperate environment; other rock types and/or conditions do not allow fault planes to be preserved very long at the surface. This suggests that the approach that we have developed may be applicable to any fault exhibiting a preserved scarp surface.

5.4. A possible model to recover the seismic slip histories

To strengthen and generalize our approach, we built a first-order numerical model presented in Fig. 9. The model input parameters are (Fig. 9a): 1) the existence of a 0.5–1 m thick zone of enrichment at the soil–atmosphere interface (half extending in the upper soil [H1], half in colluvial buildup at the scarp base [H2]). Note that we consider a rather large transition zone to allow realistic uncertainties on the transition positions; 2) a constant concentration peak C_{soil} (%) in the transition zones; 3) a constant concentration decrease rate C_{exp} (%/ka) in the exposed scarp surface. Note that we ignore how the concentrations evolve from the upper to the deeper soil; in the absence of data, we thus simply hypothesize a sharp transition between C_{soil} and C in the deeper soil (Fig. 1, right panel). The model calculates the concentration C_{model} of an element as a function of scarp height, with the formula $C_{model} = C_{base} \times (100\% + T_{exp} \times C_{exp} + C_{soil})$, with C_{base} a reference chosen such that the average measurement concentration equals that of the model values, while T_{exp} is the exposure time of the sample. The earthquake slip history is that inferred by Palumbo et al. (2004), as discussed before. Fig. 9b shows the calculated values for two elements, Sm and Eu, while Table F (Appendix) reports the fit coefficient R between measurements and model predictions for all REE-Y elements. We used a value of C_{soil} of 53%, which corresponds to the average concentration peak for the REE-Y group (Table E in the Appendix), while C_{exp} is −7.2%/ka, the average decrease rate for the REE-Y group (Table C-b in the Appendix). The model shown by the thick line in Fig. 9b fits well the measured concentrations shown by the dots and their error bars, with R coefficients averaging 91%, thus much better than a simple linear regression (Table F in the Appendix, right column). This suggests that our simple model reproduces quite well the observations. Provided that the sampling is dense enough along the scarp to precisely locate the transition zones and that a few exposure ages are available, the model might be inverted to recover part of an ignored earthquake slip history.

6. Conclusions

So far, identification of past major earthquakes on faults has been a difficult and costly task, reachable through only two techniques, paleoseismology and cosmogenic exposure dating. Though powerful, those methods are costly. In the present study, we have developed a new method that may help deciphering the recent (last 10–15 ka) earthquake history of a normal fault having a well-preserved limestone scarp at the ground surface, in a simpler and less expensive way (an order of magnitude cheaper) than presently possible.

We showed that the chemical content of young limestone fault scarp rocks contains quantitative information on the scarp exhumation history. The element concentrations vary as the result of two parameters: (1) the time during which rocks are exposed to the air, and (2) the time during which rocks are in contact with the upper soil (30–50 first cm). The former correlates with the age of the earthquakes, while the later correlates with their recurrence time. The exposure time governs the duration, hence the intensity, of the various weathering processes that affect the exposed carbonate surface. In our case, steady-state microscopic calcite dissolution–precipitation seems to be the dominant process, resulting in progressive leaching of most elements, at a roughly constant rate of 5%/m or 4.5%/ka. On the other hand, the residence time of the scarp rocks at the soil–atmosphere interface governs the duration, hence the intensity, of the weathering processes that occur in the upper soil. Calcite dissolution–precipitation seems again the dominant process. Yet only the narrow scarp section in contact with the impurity-doped upper soil is affected by that process, while other parts of the escarpment are not. Narrow concentration peaks thus result that precisely locate the paleo-positions of the upper soil, hence of the transition zones between the successive major earthquakes.

We conclude that simple geochemical analyses may help recovering the seismic slip history of a fault having a preserved escarpment. The only requirement is that sampling is dense enough from base to top of the scarp for concentration-scarp height curves to be determined with sufficient detail. REE and *Y* seem to be the best tracers. Local concentration peaks along the scarp height should correspond to the location of transition zones between major earthquake ruptures. Knowing the position of the transition zones should help determining the amplitude of the slips produced by the successive earthquakes. We propose a first-order model that reproduces well the observations. Provided that a fault scarp is sampled densely enough for the concentration-scarp height curves to be precisely determined, the model might be inverted to recover, through iterative adjustments, the best-fitting earthquake slip exhumation history on the fault. This would significantly limit the number of required dating of the fault scarp.

Acknowledgments

This work has been done in the framework of a post-doctoral research funded by the French CNRS to the first author, while the analyses have been funded in the framework of a scientific project (QUAKonSCARPS) funded by the French ANR (N° ANR-06-CATT-008-01). We thank Yves Delaby for his precious help in processing the data. We also thank L. Benedetti, E. Carrio, L. centerlet and Y. Gaudemer for fruitful discussions, S. Campillo and D. Tisserand for their help in the chemistry lab, and an anonymous reviewer for his thorough comments that helped improving the manuscript.

Appendix A. Supplementary data

Supplementary data associated with this article can be found, in the online version, at doi:10.1016/j.epsl.2008.03.059.

References

Agosta, F., Aydin, A., 2006. Architecture and deformation mechanism of a basin-bounding normal fault in Mesozoic platform carbonates, central Italy. J. Struct. Geol. 28, 1445–1467.
Agosta, F., Parasad, M., Aydin, A., 2007. Physical properties of carbonate fault rocks, Fucino basin, central Italy: implications for fault seal in platform carbonates. Geofluids 7, 19–32.
Anderson, R.T., Lovley, D.R., 2002. Microbial redox interaction with uranium: an environmental perspective. In: Keith-Roach, M.J., Livens, F.R. (Eds.), Interactions of microorganisms with radionuclides. Elsevier, Amsterdam, pp. 205–223.
Benedetti, L., Finkel, R., Papanastassiou, D., King, G., Armijo, R., Ryerson, F., Farber, D., Flerit, F., 2002. Post-glacial slip history of the Sparta fault (Greece) determined by ^{36}Cl cosmogenic dating: evidence for non-periodic earthquakes. Geophys. Res. Lett. 29. doi:10.1029/2001GL014510.
Benedetti, L., Finkel, R., King, G., Armijo, R., Papanastassiou, D., Ryerson, F.J., Flerit, F., Farber, D., Stavrakakis, G., 2003. Motion on the Kaparelli fault (Greece) prior to the 1981 earthquake sequence determined from 36 Cl cosmogenic dating. Terra Nova 15, 118–124.
Braun, J.J., Pagel, M., Herbillon, A., Rosin, C., 1993. Mobilization and redistribution of REEs and Thorium in a syenitic laterite profile: a mass balance study. Geochim. Cosmochim. Acta 57, 4419–4434.
Budd, D.A., Saller, A.H., Harris, P.M., 1995. Unconformities and porosity in carbonate strata. AAPG Mem. 63 313 pages.
Burford, E.P., Fomina, M., Gadd, G.M., 2003. Fungal involvement in bioweathering and biotransformation of rocks and minerals. Mineral. Mag. 67, 1127–1155.
Busemberg, E., Plummer, L.N., 1989. Thermodynamics of magnesian calcite solid-solutions at 25 °C and 1 atm total pressure. Geochim. Cosmochim. Acta 53, 1189–1208.
Chen, J., Blume, H.P., Beyer, L., 2000. Weathering of rocks induced by lichen colonization — a review. Catena, 39, 121–146.

Cheng, L., Sturchio, N.C., Bedzyk, M.J., 2001. Impurity structure in a molecular ionic crystal: Atomic-scale X-ray study of $CaCO_3$: Mn^{2+}. Phys. Rev. B 63, 144104.1–144104.6.
Chester, F.M., Logan, J.M., 1986. Composite planar fabric of gouge from the Punchbwol fault, California. J. Struct. Geol. 9, 621–634.
Daëron, M., Klinger, Y., Tapponnier, P., Elias, A., Jacques, E., Sursock, A., 2005. Sources of the large A.D. 1202 and 1759 Near East earthquakes. Geology 33, 529–532.
Danin, A., Gerson, R., Garty, J., 1983. Weathering patterns on hard limestone and dolomite by endolithic lichens and cyanobacteria: supporting evidence for eolian contribution to Terra Rossa soil. Soil Sci. 136, 213–217.
de Leeuw, N.H., 2002. Molecular dynamics simulations of the growth inhibiting effect of Fe^{2+}, Mg^{2+}, Cd^{2+}, and Sr^{2+} on calcite crystal growth. J. Phys. Chem. B 106, 5241–5249.
Dia, A., Gruau, G., Olivié-Lauquet, G., Riou, C., Molénat, J., Curmi, P., 2000. The distribution of rare earth elements in ground-water: assessing the role of source-rock composition, redox changes and colloidal particles. Geochim. Cosmochim. Acta 64, 4131–4151.
Dorn, R.I., 1998. In: Shroder, J.F. (Ed.), Rock coatings, vol. 6. Elsevier, Amsterdam. 428 pp.
Dorn, R.I., 2007. Rock varnish. In: Nash, D.J., McLaren, S.J. (Eds.), Geochemical sediments and landscapes. Blackwell, London, pp. 246–297.
Duddy, L.R., 1980. Redistribution and fractionation of rare-earth and other elements in a weathering profile. Chem. Geol. 30, 363–381.
Elzinga, E.J., Tait, C.D., Reeder, R.J., Rector, K.D., Donohoe, R.J., Morris, D.E., 2004. Spectroscopic investigation of U(VI) sorption at the calcite–water interface. Geochim. Cosmochim. Acta 68, 2437–2448.
Fierer, N., Allen, A.S., Schimel, J.P., Holden, P.A., 2003. Controls on microbial CO_2 production: a comparison of surface and subsurface soil horizons. Glob. Chang. Biol. 9, 1322–1332.
Galadini, F., Galli, P., 1999. The Holocene paleoearthquakes on the 1915 Avezzano earthquakes faults (central Italy). Tectonophysics 308, 143–170.
Haibing, L., van der Woerd, J., Klinger, Y., Tapponnier, P., Xuexiang, Q., Jingsui, Y., Yintang, Z., 2005. Slip rate on the Kunlun Fault and recurrence time of great earthquake comparable to the 14/11/2001, Mw~7.8 Kokoxili earthquake at Hongshui Gou. Earth Planet. Sci. Lett. 237, 285–299.
Kelly, S.D., Newville, M.G., Cheng, L., Kemner, K.M., Sutton, S.R., Fenter, P., Sturchio, N.C., Spötl, C., 2003. Uranyl incorporation in natural calcite. Environ. Sci. Technol. 37, 1284–1287.
Kumar, S., Wesnousky, S.G., Rockwell, T.K., Briggs, R.W., Thakur, V.C., Jayangondaperumal, R., 2006. Paleoseismic evidence of great surface rupture earthquakes along the Indian Himalaya. J. Geophys. Res. 111. doi:10.1029/2004JB003309.
Langmuir, D., 1997. Aqueous Environmental Geochemistry: Upper Saddle River. Prentice-Hall, New Jersey. 600 pp.
Le Métayer-Levrel, G., Castanier, S., Orial, G., Loubière, J.F., Perhuisot, J.P., 1999. Application of bacterial carbogenesis to the protection and regeneration of limestones in buildings and historic patrimony. Sediment. Geol. 126, 25–34.
Lovley, D.R., Phillips, E.J.P., Gorby, Y.A., Landa, E.R., 1991. Microbial reduction of uranium. Nature 350, 413–416.
Marini, J.C., Chauvel, C., Maury, R.C., 2005. Hf isotope compositions of northern Luzon arc lavas suggest involvement of pelagic sediments in their source. Contrib. Mineral. Petrol. 149, 216–232.
Michetti, A.M., Brunamonte, F., Serva, L., Vittori, E., 1996. Trench investigations of the 1915 Fucino earthquake fault scarp (Abruzzo, central Italy): geological evidence of large historical events. J. Geophys. Res. 101, 5921–5936.
Mitchell, S.G., Matmon, A., Bierman, P.R., Enzel, Y., Caffee, M., Rizzo, D., 2001. Displacement history of a limestone normal fault scarp, northern Israel, from cosmogenic ^{36}Cl. J. Geophys. Res. 106, 4247–4264.
Mucci, A., Morse, J.W., 1983. The incorporation of Mg^{2+} and Sr^{2+} into calcite overgrowths: influences of growth rate and solution composition. Geochim. Cosmochim. Acta 47, 217–233.
Odonne, E., 1915. Gli elementi fisici del grande terremonto marsicano-fucence del 13 gennaio 1915. Boll. Soc. Sismol. It. 19, 71–215.
Ohnuki, T., Yoshida, T., Ozaki, T., Samadfam, M., Kozai, N., Yubuta, K., Mitsugashira, T., Kasama, T., Francis, A.J., 2005. Interactions of uranium with bacteria and kaolinite clay. Chem. Geol. 220, 237–243.
Palumbo, L., Benedetti, L., Bourlès, D., Cinque, A., Finkel, R., 2004. Slip history of the Magnola fault (Apennines, Central Italy) from ^{36}Cl surface exposure dating: evidence for strong earthquake over Holocene. Earth Planet. Sci. Lett. 225, 163–176.
Paul, E.A., Clark, F.E., 1989. Soil microbiology and biochemistry. Academic Press, San Diego. 275 pp.
Piccardi, L., Gaudemer, Y., Tapponier, P., Boccaletti, M., 1999. Active oblique extension in the central Apennines (Italy): evidence from the Fucino region. Geophys. J. Int. 139, 499–530.
Pingitore, N.E., Eastman, M.P., 1986. The coprecipitation of Sr^{2+} with calcite at 25 °C and 1 atm. Geochim. Cosmochim. Acta 50, 2195–2203.
Plan, L., 2005. Factors controlling carbonate dissolution rates quantified in a field test in the Austrian Alps. Geomorphology 68, 201–212.
Plank, T., Langmuir, C.H., 1998. The Chemical composition of subducting sediment and its consequences for the crust and mantle. Chem. Geol. 145, 325–394.
Potter, R.S., Rossman, G.R., 1977. Desert varnish: the importance of clay minerals. Science 196, 1446–1448.
Pourret, O., 2006. Impact de la matière organique sur le comportement des terres rares en solution: étude expérimentale et modélisation, PhD thesis, Univ. Rennes, 172 p.
Pourret, O., Davranche, M., Gruau, G., Dia, A., 2007. Organic complexation of rare earth elements in natural waters: evaluating model calculations from ultrafiltration data. Geochim. Cosmochim. Acta 71, 2718–2735.
Reardon, E.J., Allison, G.B., Fritz, P., 1979. Seasonal chemical and isotopic variations of soil CO_2 at Trout Creek, Ontario. J. Hydrology 43, 355–371.
Reeder, R.J., Nugent, M., Drew Tait, C., Morris, D.E., Heald, S.M., Beck, K.M., Hess, W.P., Lanzirotti, A., 2001. Coprecipitation of uranium (VI) with calcite: XAFS, micro-XAS, and luminescence centeracterization. Geochim. Cosmochim. Acta 65, 3491–3503.
Sholkovitz, E.R., 1988. Rare earth elements in the sediments of the North Atlantic Ocean, Amazon delta and East China Sea: reinterpretation of terrigenous input patterns to the oceans. Am. J. Sci. 288, 236–281.
Sibson, R.H., 1977. Fault rocks and fault mechanisms. J. Geol. Soc. London 133, 191–213.
Smith, B.J., Warke, P.A., Mose, C.A., 2000. Limestone weathering in contemporary arid environments: a case study from southern Tunisia. Earth surf. Processes Landf. 25, 1343–1354.
Sturchio, N.C., Antonio, M.R., Soderholm, L., Sutton, S.R., Brannon, J.C., 1998. Tetravalent uranium in calcite. Science 281, 971–973.
Sweeting, M.M., 1966. The weathering of limestone. In: Dury, G.H. (Ed.), Essays in geomorphology. Heinemann, London, pp. 177–210.
Takahashi, Y., Châtellier, X., Hattori, K.H., Kato, K., Fortin, D., 2005. Adsorption of rare earth elements onto bacterial cell walls and its implication for REE sorption onto natural microbial mats. Chem. Geol. 219, 53–67.
Tauton, A.E., Welch, S.A., Banfield, J.F., 2000. Microbial controls on phosphate and lanthanide distributions during granite weathering and soil formation. Chem. Geol. 169, 371–382.
Trudgill, S., 1985. Limestone geomorphology. In: Clayton, K. (Ed.), Geomorphology. Longman, London, pp. 53–70.
Tyler, G., 2004. Rare earth elements in soils and plant systems — A review. Plant Soil 267, 191–206.
White, A.F., Blum, A.E., 1995. Effect of climate on chemical weathering in watersheds. Geochim. Cosmochim. Acta 59, 1729–1747.
White, W.B., 2000. Dissolution of limestone from field observations. In: Klimchouk, A., Ford, D.C., Palmer, A.N., Dreybrodt, W. (Eds.), Speleogenesis-evolution of karst aquifers. National Speleogical Society, Huntsville, pp. 149–155.
Zreda, M., Noller, J.S., 1998. Ages of prehistoric earthquake revealed by cosmogenic chlorine-36 in a bedrock fault scarp at Hebgen Lake. Science 282, 1097–1099.
Zhaoliang, S., Congqiang, L., Guilin, H., Zhongliang, W., Zhaozhou, Z., Cheng, Y., 2006. Enrichment and release of Rare Earth Elements during weathering of sedimentary rocks in Wujiang catchments, Southwest China. J. Rare Earths 24, 491–496.

a)

b)

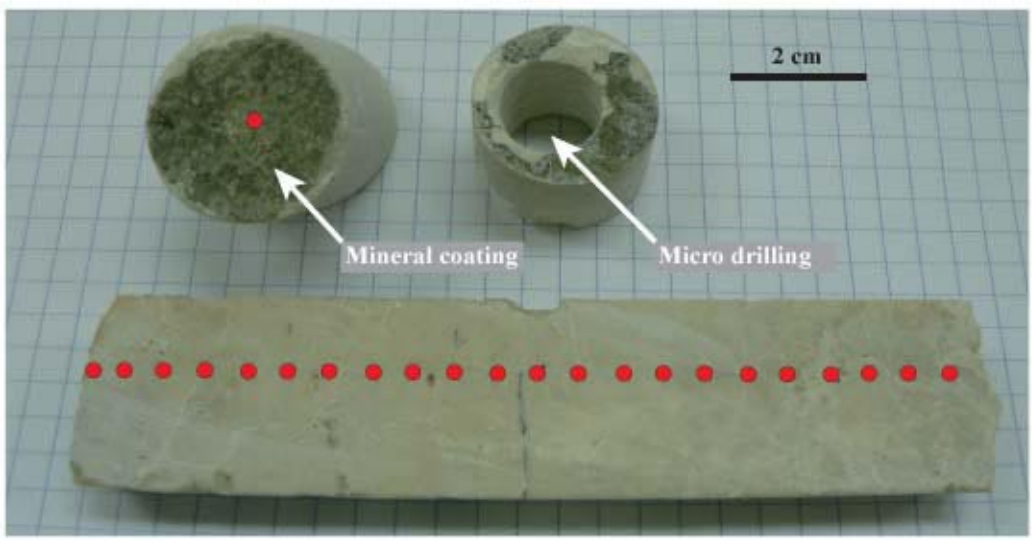

a) Westward view in cross-section of the Magnola fault scarp, showing the 1-15 cm-thick carbonate-made slip zone, overlaying carbonate breaches.
b) View of one sampled core. The top left piece shows the surface coating with a dark color while the half-core at the bottom shows the light color of the inner rock (host rock). The red dots locate the semi-quantitative measurements done with μXRF. Major and trace element concentrations were measured in micro-samples drilled within the host rock, as shown in the top-right figure.

Carcaillet et al., Electronic Figure A

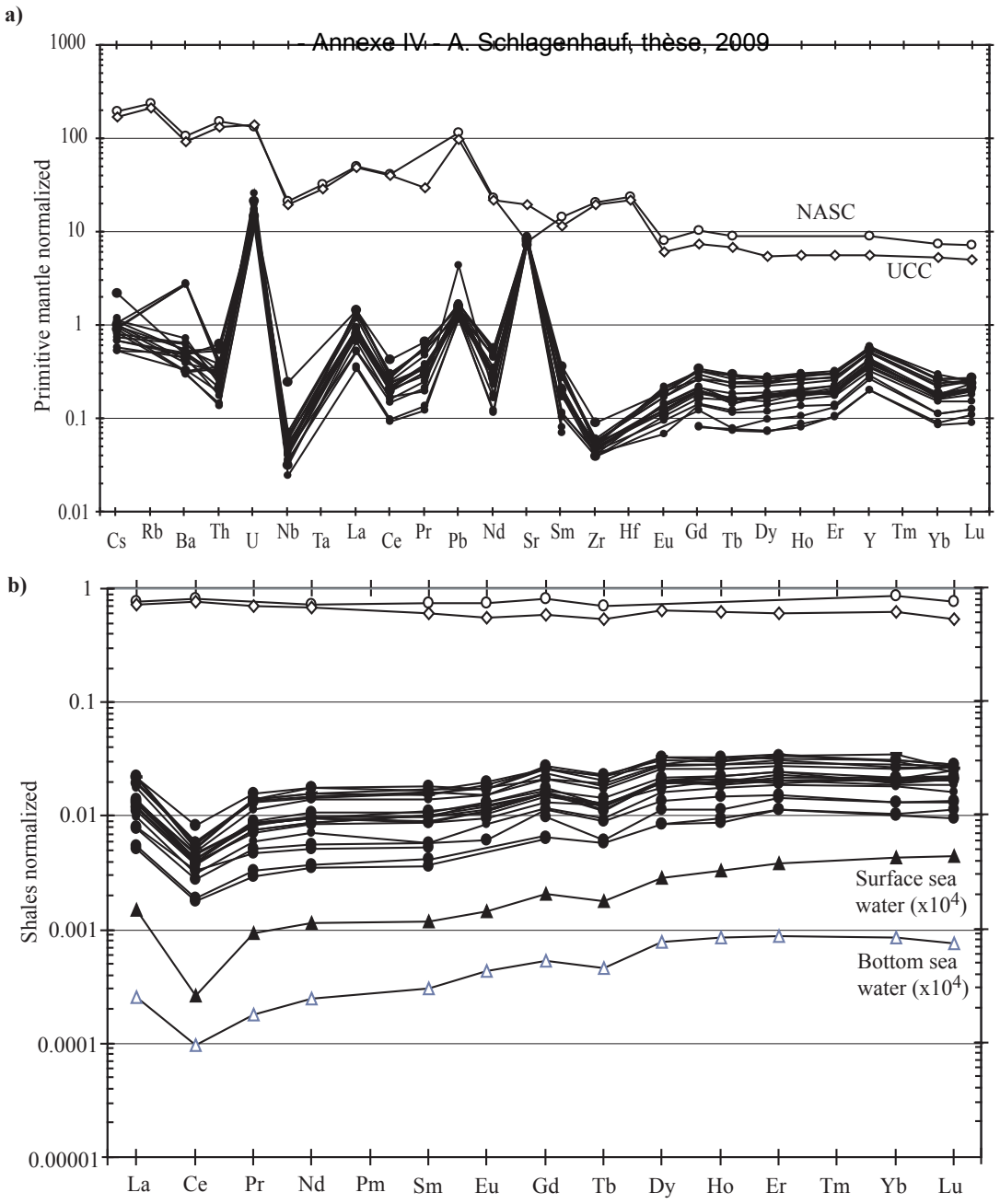

Trace element and Rare Earth patterns for the Magnola samples.
a) The concentrations are normalized to primitive mantle (Hofmann, 1988). The black dots show data from this study while the empty dots show the pattern of the North American Shale Composite (Gromet et al., 1984; Condie, 1993) and the empty diamonds, the pattern of average Upper Continental Crust (Mc Lennan, 2001). The Magnola host rocks exhibit the same general pattern as the two references, but the absolute concentrations are lower by two orders of magnitude. This suggests that the Magnola carbonates have a chemical signature close to that of other sediments, but with an overall depletion that can be related to the high carbonate content (e. g., Plank and Langmuir, 1998). Significant positive anomalies in Ba, U, Sr, and Y, and a negative anomaly in Ce are also highlighted.
b) The REE concentrations are normalized to Reference Shales (Sholkovitz, 1988). Symbols as in a, with solid and empty triangles for surface and bottom seawater, respectively (x 104; Alibo and Nozaki, 1999). The Magnola REE patterns closely resemble that of seawater, though concentrations are five to six orders of magnitude higher. This shows that the seawater origin of the Magnola carbonates is preserved in the analyzed samples.

Carcaillet et al., Figure B - Electronic Supplement

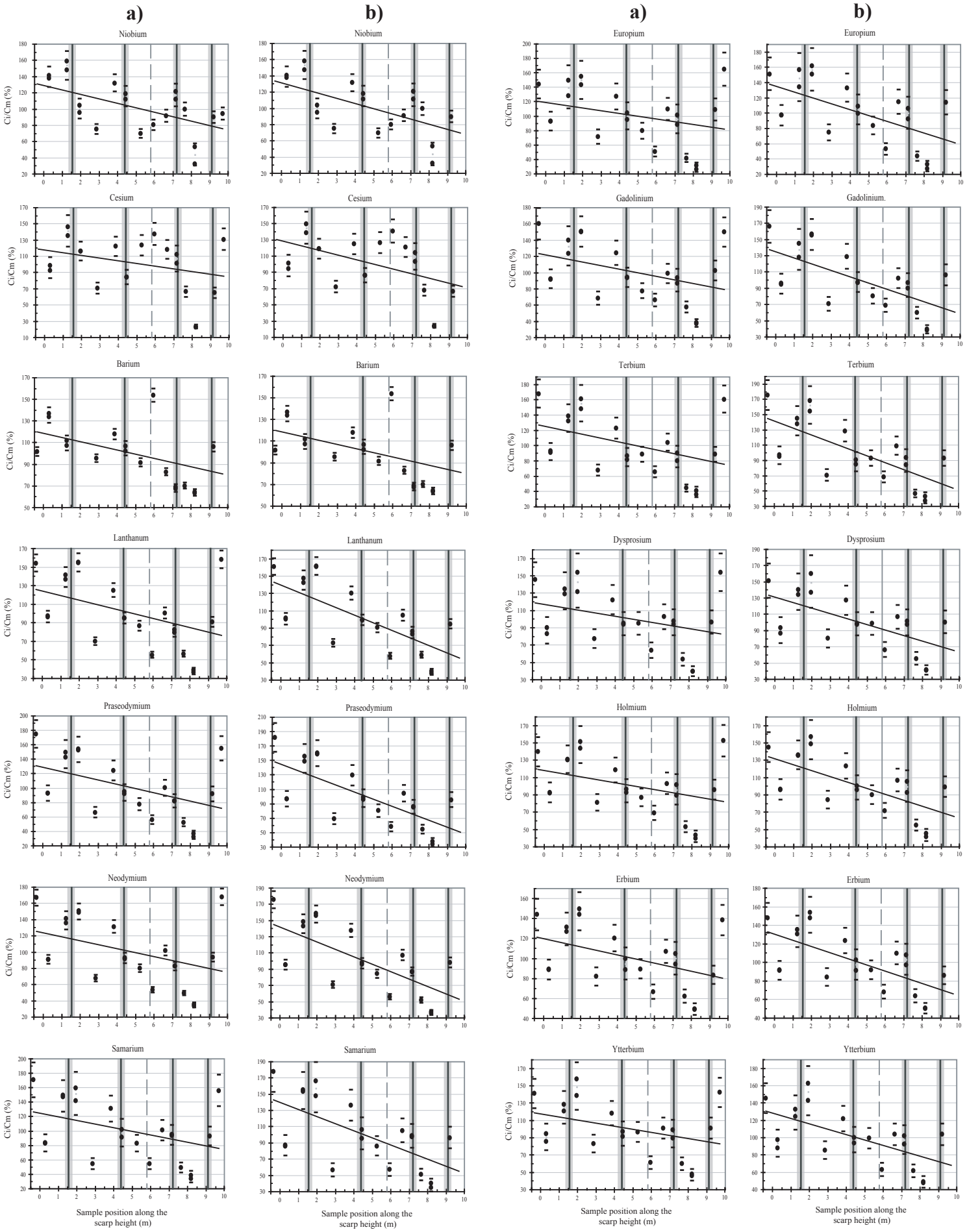

Carcaillet et al., Figure C - Electronic Supplement (caption in following)

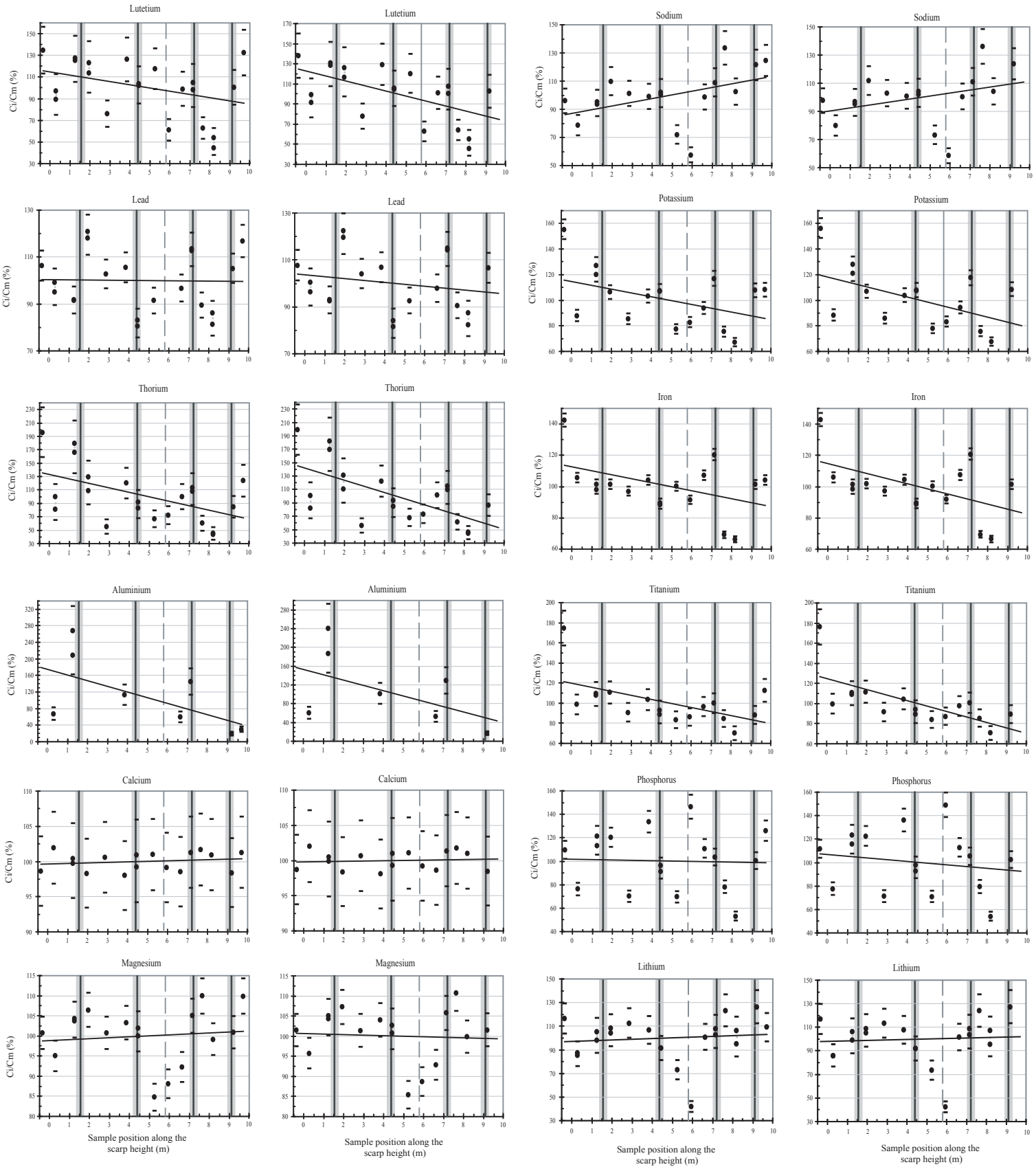

Element concentrations vs. sampling height for all elements not presented in Figure 3. In all plots, X is the on-fault position of the samples, in meters, increasing upward; Y is the concentration of sample i (Ci) normalized by the mean concentration (Cm) averaged over the whole sample collection, in percentage. Solid vertical lines represent the transitions between the major earthquake slip zones identified by Palumbo et al. (2004), with their position uncertainties in grey. The thin dotted vertical line locates a possible additional earthquake suggested by Palumbo et al. (2004). The slanted straight lines are the regression curves calculated from all measurements. When several measurements were done for the same sample, only the average was used for the regression calculation, but all measurements are plotted in the figure.

a) Regressions are calculated using all measurements listed in Table 1. Regression parameters are reported in Table C-a.

b) Regressions are calculated as in a) but without sample C15. Regression parameters are reported in Table C-b.

Carcaillet et al., Figure C (following) - Electronic Supplement

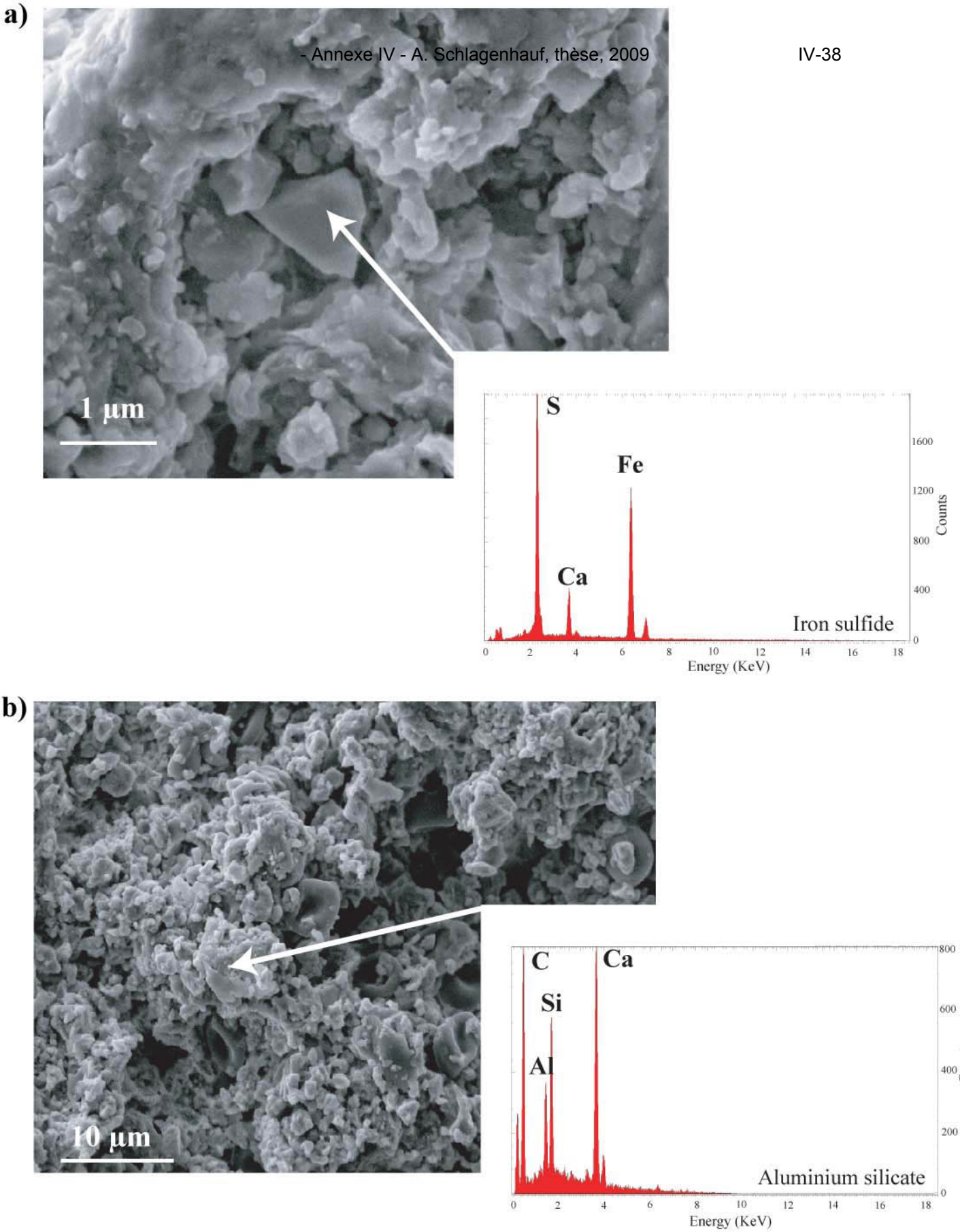

SEM images and EDS analyzes of minerals embedded in the coating. Photographs on the left are SEM images of the coating in core C9, while plots show EDS analyses of the two minerals shown by the arrows.

Carcaillet et al., Figure D - Electronic Supplement

Samples	Elevation (m)	Detph in core (cm)	Na_2O (%)	MgO (%)	Al_2O_3 (%)	SiO_2 (%)	P_2O_5 (%)	SO_3 (%)	K_2O (%)	CaO (%)	TiO_2 (%)	MnO (%)	Fe_2O_3 (%)
C1	-0.35	*Coating*	*1.79*	*0.52*	*0.78*	*2.65*	*1.9*	*0.49*	*0.49*	*91.47*	*0.1*	*0.03*	*0.3*
		0.1	2.39	0.82	0.18	0.44	2.06	0.3	0.24	93.42	0.01	0.01	0.14
		0.5	2.37	0.72	0.03	0.08	2.02	0.25	0.24	94.1	0.03	0.02	0.14
		1	2.81	0.85	0.25	0.27	2.21	0.38	0.26	92.8	0.05	0.01	0.11
		1.5	3.1	0.9	0.2	0.18	2.15	0.36	0.25	92.69	0.05	0.02	0.09
		2	2.43	0.67	0	0.07	2.01	0.25	0.27	94.15	0.02	0.01	0.12
		2.5	2.46	1.02	0.27	0.28	2.21	0.4	0.25	92.74	0.24	0.01	0.11
		3	2.67	0.83	0.36	0.3	2.17	0.36	0.28	92.84	0.04	0.03	0.12
		3.5	2.39	0.82	0.18	0.44	2.06	0.3	0.24	93.42	0.01	0.01	0.14
		4	2.59	0.7	0.18	0.26	2.28	0.38	0.29	93.13	0.07	0.01	0.11
		4.5	2.83	0.72	0.15	0.27	2.14	0.44	0.33	92.96	0.06	0.01	0.1
		5	0.59	0.84	0.19	0.26	2.22	0.38	0.28	94.82	0.21	0.01	0.2
		5.5	2.93	0.95	0.25	0.24	2.19	0.38	0.28	92.61	0.04	0.01	0.11
		6	2.34	0.95	0.19	0.29	2.07	0.29	0.28	93.4	0.01	0.02	0.17
		6.5	2.34	0.95	0.19	0.29	2.07	0.29	0.28	93.4	0.01	0.02	0.17
		7	2.6	0.87	0.3	0.3	2.19	0.41	0.26	92.86	0.03	0.02	0.15
		7.5	2.5	0.8	0.16	0.22	2.16	0.37	0.27	93.35	0.03	0.02	0.12
		8	2.37	0.63	0	0.07	2	0.25	0.25	94.21	0.03	0.01	0.18
		8.5	2.69	0.86	0.25	0.31	2.16	0.42	0.28	92.87	0.07	0.01	0.09
		9	2	0.63	0.1	0.23	2.09	0.28	0.27	94.22	0.03	0.01	0.13
C2	0.30	*Coating*	*1.75*	*0.49*	*1.18*	*2.77*	*1.83*	*0.46*	*0.52*	*90.38*	*0.12*	*0.02*	*0.47*
		0.1	1.86	0.52	0.11	0.25	1.95	0.42	0.32	94.32	0.06	0.02	0.17
		0.5	2.81	0.74	0.16	0.1	1.9	0.29	0.3	93.49	0.05	0.03	0.13
		1	2.49	0.73	0.2	0.22	1.97	0.36	0.3	93.37	0.1	0.03	0.23
		1.5	2.22	0.75	0.2	0.22	1.96	0.4	0.39	93.56	0.1	0.07	0.15
		2	0	0.47	0.1	0.22	1.96	0.34	0.21	96.54	0.04	0.01	0.09
		2.5	2.89	0.63	0.17	0.26	1.94	0.37	0.28	93.2	0.06	0.03	0.17
		3	1.65	0.55	0.05	0.07	1.9	0.32	0.3	94.94	0.03	0.03	0.15
		3.5	1.32	0.66	0.18	0.19	1.97	0.37	0.28	94.73	0.03	0.02	0.25
		4	2.06	0.62	0.16	0.2	1.96	0.35	0.29	94.1	0.07	0.03	0.15
		4.5	1.74	0.64	0.16	0.31	2.3	0.38	0.31	93.86	0.06	0.04	0.2
C3	1.25	*Coating*	*1.7*	*0.49*	*1.48*	*4.2*	*1.81*	*0.45*	*0.52*	*88.35*	*0.2*	*0.03*	*0.8*
C4	1.95	*Coating*	*1.04*	*0.28*	*2.39*	*7.2*	*1.9*	*0.6*	*0.64*	*84.79*	*0.25*	*0.04*	*0.88*
		0.1	2.24	0.73	0.15	0.09	1.91	0.44	0.3	93.9	0.06	0.03	0.16
		0.5	2.2	0.81	0.21	0.09	1.9	0.33	0.29	93.92	0.1	0.02	0.15
		1	1.97	0.57	0.05	0.08	1.92	0.34	0.27	94.56	0.07	0.03	0.13
		1.5	1.85	0.59	0.17	0.24	1.98	0.41	0.31	94.13	0.12	0.02	0.15
		2	1.71	0.69	0.17	0.18	1.97	0.36	0.34	94.28	0.07	0.02	0.21
		2.5	2.14	0.48	0.06	0.08	1.93	0.3	0.27	94.43	0.08	0.07	0.17
		3	2.24	0.69	0.07	0.09	1.91	0.35	0.3	94.08	0.07	0.04	0.16
		3.5	1.9	0.6	0.15	0.24	2.01	0.36	0.35	94.13	0.06	0.04	0.16
		4	1.98	0.62	0.12	0.2	1.96	0.35	0.37	94.14	0.09	0.03	0.14
		4.5	1.53	0.61	0.13	0.24	1.95	0.39	0.3	94.64	0.02	0.18	0.08
		5	1.99	0.66	0.13	0.31	1.83	0.33	0.28	94.14	0.06	0.04	0.23
C5	2.85	*Coating*	*1.09*	*0.04*	*1.56*	*3.94*	*1.85*	*0.55*	*0.63*	*89.62*	*0.14*	*0.04*	*0.56*
C6	3.85	*Coating*	*0.94*	*0.5*	*3.75*	*7.53*	*2.05*	*0.88*	*0.71*	*82.74*	*0.17*	*0.03*	*0.7*
C7	4.45	*Coating*	*1.45*	*0.34*	*1.45*	*4.39*	*1.79*	*0.43*	*0.49*	*88.91*	*0.13*	*0.03*	*0.6*
C8	5.25	*Coating*	*1.02*	*0.08*	*1.86*	*4.44*	*1.86*	*0.52*	*0.53*	*88.81*	*0.16*	*0.04*	*0.66*
		0.1	1.81	0.44	0	0.03	1.86	0.27	0.28	95.07	0.05	0.04	0.16
		0.5	1.45	0.78	0.08	0.29	1.93	0.27	0.34	94.52	0.1	0.02	0.21
		1	1.77	0.56	0.09	0.08	1.98	0.34	0.28	94.68	0.06	0.06	0.1
		1.5	1.74	0.42	0.13	0.21	2.03	0.38	0.3	94.54	0.09	0.03	0.13
		2	1.92	0.53	0.14	0.19	2.02	0.38	0.36	94.07	0.18	0.03	0.2
		2.5	1.96	0.58	0.06	0.08	1.97	0.37	0.26	94.51	0.02	0.02	0.18
		3	1.38	0.58	0.11	0.27	1.91	0.28	0.22	94.97	0.02	0.03	0.23
		3.5	2.03	0.61	0.2	0.5	1.89	0.28	0.32	93.86	0.07	0.03	0.2
		4	1.75	0.5	0.16	0.23	2	0.41	0.34	94.33	0.11	0.03	0.14
		4.5	2.18	0.72	0.25	0.24	1.98	0.28	0.27	93.77	0.06	0.04	0.21
		5	2.28	0.73	0.22	0.26	2.02	0.37	0.31	93.49	0.09	0.03	0.19
		5.5	2.21	0.64	0.25	0.3	2	0.27	0.28	93.76	0.08	0.02	0.18
		6	2.07	0.56	0	0.05	1.92	0.28	0.26	94.62	0.07	0.02	0.16
		6.5	1.94	0.65	0.18	0.26	2.04	0.4	0.29	93.97	0.1	0.02	0.16
		7	1.97	0.79	0.16	0.07	1.87	0.3	0.25	94.3	0.08	0.04	0.18
		7.5	2.09	0.71	0.14	0.19	2.01	0.37	0.27	93.97	0.06	0.03	0.15
		8	1.98	0.75	0.17	0.19	2.05	0.4	0.3	93.89	0.07	0.04	0.18
C9	5.95	*Coating*	*1.7*	*0.34*	*0.96*	*2.28*	*1.94*	*0.48*	*0.42*	*91.38*	*0.11*	*0.03*	*0.34*
C10	6.65	*Coating*	*1.95*	*0.38*	*0.67*	*1.81*	*1.93*	*0.4*	*0.41*	*91.82*	*0.11*	*0.03*	*0.51*
C11	7.15	*Coating*	*1.75*	*0.26*	*1.03*	*2.83*	*1.86*	*0.51*	*0.47*	*90.71*	*0.1*	*0.03*	*0.46*
C12	7.65	*Coating*	*1.95*	*0.43*	*0.26*	*0.49*	*1.85*	*0.37*	*0.34*	*93.99*	*0.06*	*0.03*	*0.24*
C13	8.20	*Coating*	*2.09*	*0.59*	*1.26*	*3.29*	*1.86*	*0.62*	*0.63*	*88.97*	*0.14*	*0.04*	*0.52*
		0.1	3.31	0.94	0.26	0.24	2.17	0.42	0.34	92.15	0.04	0.02	0.12
		0.5	2.88	0.72	0.15	0.23	2.17	0.43	0.32	92.91	0.05	0.02	0.13
		1	3.26	0.92	0.23	0.2	2.13	0.39	0.32	92.39	0.04	0.01	0.12
		1.5	3.07	0.68	0.25	0.28	2.21	0.42	0.38	92.51	0.1	0.02	0.1
		2	3.14	0.87	0.2	0.24	2.15	0.43	0.31	92.48	0.06	0.02	0.11
		2.5	2.92	0.73	0.22	0.27	2.17	0.4	0.31	92.81	0.04	0.02	0.11
		3	2.75	0.63	0.2	0.22	2.16	0.41	0.32	93	0.03	0.01	0.26
		3.5	2.89	0.67	0.21	0.26	2.15	0.42	0.34	92.87	0.05	0.02	0.11
		4	2.7	0.6	0.15	0.25	2.15	0.41	0.33	93.24	0.05	0.01	0.12
		4.5	3.53	0.99	0.25	0.28	2.14	0.42	0.34	91.88	0.06	0.01	0.11
		5	3.47	0.91	0.28	0.29	2.08	0.32	0.32	92.14	0.03	0.03	0.13
		5.5	3.27	0.96	0.3	0.32	2.13	0.46	0.32	92.07	0.05	0.02	0.1
		6	3.07	0.88	0.17	0.23	2.14	0.4	0.32	92.6	0.05	0.01	0.12
		6.5	2.51	0.55	0.13	0.21	2.16	0.41	0.35	93.5	0.07	0.01	0.11
		7	3.28	0.95	0.25	0.24	2.16	0.4	0.32	92.23	0.04	0.01	0.12
		7.5	3.36	0.88	0.16	0.2	2.15	0.41	0.33	92.34	0.05	0.02	0.11
C14	9.20	*Coating*	*1.22*	*0.27*	*1.58*	*4.58*	*1.89*	*0.51*	*0.57*	*88.46*	*0.19*	*0.04*	*0.69*
		0.1	1.74	0.71	0.12	0.33	2.11	0.32	0.34	94.08	0.06	0.03	0.17
		0.5	2.1	0.8	0.17	0.05	1.76	0.27	0.32	94.24	0.08	0.02	0.19
		1	2.16	0.74	0.16	0.23	1.89	0.36	0.32	93.94	0.05	0.03	0.13
		1.5	1.82	0.7	0.15	0.22	1.89	0.33	0.35	94.27	0.07	0.03	0.19
		2	2.26	0.76	0.19	0.21	1.88	0.37	0.35	93.74	0.09	0.02	0.14
		2.5	2.21	0.79	0.03	0.07	1.74	0.27	0.31	94.32	0.09	0.02	0.15
		3	2.01	0.69	0.01	0.03	1.74	0.23	0.3	94.73	0.07	0.02	0.15
		3.5	2.15	0.69	0.16	0.26	1.93	0.36	0.35	93.84	0.08	0.03	0.15
		4	1.98	0.77	0	0.05	1.71	0.26	0.35	94.61	0.07	0.03	0.19
		4.5	1.8	0.85	0.19	0.46	1.76	0.27	0.38	94.02	0.08	0.02	0.17
		5	2.65	0.85	0.02	0.04	1.73	0.26	0.31	93.93	0.05	0.02	0.15
		5.5	2.09	0.71	0.19	0.25	1.9	0.38	0.32	93.9	0.08	0.02	0.15
		6	2.09	0.91	0.19	0.25	1.86	0.36	0.34	93.59	0.23	0.02	0.15
		6.5	1.79	0.6	0.14	0.23	1.96	0.36	0.33	94.33	0.07	0.03	0.17
		7	2.62	1.04	0.17	0.48	1.78	0.31	0.37	92.94	0.07	0.03	0.2
		7.5	1.95	0.68	0	0.06	1.74	0.23	0.3	94.8	0.05	0.03	0.17
		8	1.95	0.64	0.13	0.18	1.93	0.41	0.3	94.15	0.1	0.02	0.2
		8.5	1.97	0.68	0.11	0.17	1.87	0.36	0.32	94.26	0.08	0.02	0.16
		9	1.88	0.71	0.13	0.25	1.89	0.36	0.32	94.19	0.07	0.02	0.17
C15	9.70	*Coating*	*1.74*	*0.34*	*0.92*	*2.5*	*1.9*	*0.49*	*0.51*	*90.94*	*0.13*	*0.03*	*0.5*

Semi-quantitative analyses of major element in the mineral coating and in the host-rock as inferred from µXRF measurements based on Ka-lines area and using Vision 32© (EDAX). Note that these semi-quantitative measurements do not take into account the CO_2 contents. Measurements in coatings are shown in italics.

Carcaillet et al., Electronic Table A

a)

	Sr	Y	Zr	Nb	Cs	Ba	La	Ce	Pr	Nd	Sm	Eu	Gd	Tb	Dy	Ho	Er	Yb	Lu	Pb	Th	U	Al_2O_3	CaO	MgO	Na_2O	K_2O	Fe_2O_3	MnO	TiO_2	P_2O_3
Sr		0.0	9.6	11.6	0.0	4.7	2.6	14.7	2.8	1.6	1.1	0.1	1.2	1.2	0.4	0.2	0.3	0.4	1.9	8.6	3.5	23.1	1.2	21.1	0.2	0.5	1.1	0.1	13.8	9.0	7.1
Y	0.0		41.9	23.6	47.3	3.7	95.2	67.4	91.3	94.8	93.9	95.9	93.3	94.3	98.7	97.5	96.3	97.0	88.1	44.6	64.5	0.1	2.4	17.1	11.2	3.1	53.2	45.2	19.8	47.9	35.3
Zr	9.6	41.9		73.2	36.2	5.0	52.5	83.7	64.1	56.9	60.2	43.3	59.1	58.0	48.5	47.1	54.9	47.1	43.8	14.2	81.0	1.3	49.7	12.1	5.9	0.2	76.0	63.4	20.4	93.8	14.5
Nb	11.6	23.6	73.2		22.9	12.9	29.5	53.8	33.4	27.8	33.1	29.3	31.2	22.9	25.0	26.0	28.1	22.4	30.3	1.6	57.9	0.5	61.0	0.2	10.5	0.1	48.5	23.4	5.7	49.4	14.0
Cs	0.0	47.3	36.2	22.9		27.3	39.7	43.3	40.6	39.4	43.1	36.6	40.1	47.3	45.8	44.7	45.6	37.1	43.6	17.8	47.3	0.0	32.8	8.7	2.7	15.3	24.4	40.5	19.1	47.5	56.1
Ba	4.7	3.7	5.0	12.9	27.3		6.7	4.7	6.1	5.9	3.7	5.7	8.0	7.7	5.2	8.3	2.8	3.6	2.5	1.9	3.4	0.4	0.5	9.9	15.7	43.6	1.4	4.1	0.9	2.3	32.4
La	2.6	95.2	52.5	29.5	39.7	6.7		78.4	98.0	98.7	96.3	95.0	97.1	97.3	96.9	96.9	95.8	96.7	83.7	36.2	71.2	1.8	3.7	15.8	13.6	3.0	56.6	41.6	23.7	56.9	28.7
Ce	14.7	67.4	83.7	53.8	43.3	4.7	78.4		86.2	80.1	82.3	68.9	81.8	80.1	73.9	70.7	75.2	73.6	70.7	18.2	85.9	0.6	22.9	13.9	6.5	0.5	76.9	61.2	17.0	87.4	16.7
Pr	2.8	91.3	64.1	33.4	40.6	6.1	98.0	86.2		98.5	98.0	92.4	98.3	97.5	94.8	94.5	95.0	93.9	80.8	33.4	81.4	1.1	8.4	19.1	13.6	2.5	68.0	48.3	21.3	68.4	30.1
Nd	1.6	94.8	56.9	27.8	39.4	5.9	98.7	80.1	98.5		97.4	95.4	98.0	98.0	97.2	96.5	95.0	95.5	83.7	38.1	74.6	0.9	1.7	17.7	14.2	3.5	61.8	46.3	21.0	62.0	31.4
Sm	1.1	93.9	60.2	33.1	43.1	3.7	96.3	82.3	98.0	97.4		93.2	97.3	96.2	95.9	94.0	95.3	93.7	85.8	33.0	82.7	0.4	12.9	19.6	13.4	2.8	69.8	48.6	18.2	63.6	33.4
Eu	0.1	95.9	43.3	29.3	36.6	5.7	95.0	68.9	92.4	95.4	93.2		94.8	92.3	97.1	97.5	92.3	95.9	85.3	42.8	66.3	0.3	0.8	17.8	13.7	4.8	59.2	46.0	10.9	47.7	32.2
Gd	1.2	93.3	59.1	31.2	40.1	8.0	97.1	81.8	98.3	98.0	97.3	94.8		96.9	95.9	96.1	94.3	95.4	80.7	42.1	76.8	0.0	2.3	22.6	14.6	3.5	67.4	49.7	16.7	64.3	36.8
Tb	1.2	94.3	58.0	22.9	47.3	7.7	97.3	80.1	97.5	98.0	96.2	92.3	96.9		96.7	96.4	95.8	95.2	81.6	40.4	74.8	1.1	2.4	19.9	8.5	0.9	60.0	51.1	23.1	64.1	33.4
Dy	0.4	98.7	48.5	25.0	45.8	5.2	96.9	73.9	94.8	97.2	95.9	97.1	95.9	96.7		98.7	96.4	98.2	89.2	42.8	70.0	0.0	3.4	17.3	10.9	2.5	60.0	49.6	18.3	54.4	33.0
Ho	0.2	97.5	47.1	26.0	44.7	8.3	96.9	70.7	94.5	96.5	94.0	97.5	96.1	96.4	98.7		96.5	97.5	82.9	46.2	67.8	0.1	3.0	17.5	12.0	2.3	57.8	47.5	19.1	52.5	35.6
Er	0.3	96.3	54.9	28.1	45.6	2.8	95.8	75.2	95.0	95.0	95.3	92.3	94.3	95.8	96.4	96.5		96.1	82.5	42.1	73.6	0.9	13.3	18.3	12.6	2.2	60.5	49.8	26.6	59.4	31.5
Yb	0.4	97.0	47.1	22.4	37.1	3.6	96.7	73.6	93.9	95.5	93.7	95.9	95.4	95.2	98.2	97.5	96.1		86.9	47.1	65.1	0.1	1.9	18.8	12.0	3.7	57.3	47.9	17.7	53.4	26.6
Lu	1.9	88.1	43.8	30.3	43.6	2.5	83.7	70.7	80.8	83.7	85.8	85.3	80.7	81.6	89.2	82.9	82.5	86.9		26.2	63.4	0.1	11.2	11.2	4.1	0.7	55.7	52.0	12.0	45.6	19.6
Pb	8.6	44.6	14.2	1.6	17.8	1.9	36.2	18.2	33.4	38.1	33.0	42.8	42.1	40.4	42.8	46.2	42.1	47.1	26.2		16.5	6.1	19.8	13.0	16.8	8.0	18.9	33.8	7.1	20.4	41.2
Th	3.5	64.5	81.0	57.9	47.3	3.4	71.2	85.9	81.4	74.6	82.7	66.3	76.8	74.8	70.0	67.8	73.6	65.1	63.4	16.5		0.0	71.0	17.0	9.8	0.2	86.0	57.1	13.7	77.7	29.3
U	23.1	0.1	1.3	0.5	0.0	0.4	1.8	0.6	1.1	0.9	0.4	0.3	0.0	1.1	0.0	0.1	0.9	0.1	0.1	6.1	0.0		6.5	13.9	1.4	0.9	4.4	9.9	58.8	0.7	5.1
Al_2O_3	1.2	2.4	49.7	61.0	32.8	0.5	3.7	22.9	8.4	1.7	12.9	0.8	2.3	2.4	3.4	3.0	13.3	1.9	11.2	19.8	71.0	6.5		0.1	5.2	14.2	48.7	0.8	11.3	20.2	1.9
CaO	21.1	17.1	12.1	0.2	8.7	9.9	15.8	13.9	19.1	17.7	19.6	17.8	22.6	19.9	17.3	17.5	18.3	18.8	11.2	13.0	17.0	13.9	0.1		0.6	0.7	16.1	13.2	1.7	12.7	37.7
MgO	0.2	11.2	5.9	10.5	2.7	15.7	13.6	6.5	13.6	14.2	13.4	13.7	14.6	8.5	10.9	12.0	12.6	12.0	4.1	16.8	9.8	1.4	5.2	0.6		72.1	12.2	0.1	7.3	6.4	1.4
Na_2O	0.5	3.1	0.2	0.1	15.3	43.6	3.0	0.5	2.5	3.5	2.8	4.8	3.5	0.9	2.5	2.3	2.2	3.7	0.7	8.0	0.2	0.9	14.2	0.7	72.1		2.3	2.4	0.6	0.7	1.1
K_2O	1.1	53.2	76.0	48.5	24.4	1.4	56.6	76.9	68.0	61.8	69.8	59.2	67.4	60.0	60.0	57.8	60.5	57.3	55.7	18.9	86.0	4.4	48.7	16.1	12.2	2.3		65.3	2.4	76.1	22.2
Fe_2O_3	0.1	45.2	63.4	23.4	40.5	4.1	41.6	61.2	48.3	46.3	48.6	46.0	49.7	51.1	49.6	47.5	49.8	47.9	52.0	33.8	57.1	9.9	0.8	13.2	0.1	2.4	65.3		2.8	66.1	16.6
MnO	13.8	19.8	20.4	5.7	19.1	0.9	23.7	17.0	21.3	21.0	18.2	10.9	16.7	23.1	18.3	19.1	26.6	17.7	12.0	7.1	13.7	58.8	11.3	1.7	7.3	0.6	2.4	2.8		19.4	3.7
TiO_2	9.0	47.9	93.8	49.4	47.5	2.3	56.9	87.4	68.4	62.0	63.6	47.7	64.3	64.1	54.4	52.5	59.4	53.4	45.6	20.4	77.7	0.7	20.2	12.7	6.4	0.2	76.7	66.7	19.0		15.4
P_2O_3	7.1	35.3	14.5	14.0	56.1	32.4	28.7	16.7	30.1	31.4	33.4	32.2	36.8	33.4	33.0	35.6	31.5	26.6	19.6	41.2	29.3	5.1	1.9	37.7	1.4	1.1	22.2	16.6	3.7	15.4	

b)

	Sr	Y	Zr	Nb	Cs	Ba	La	Ce	Pr	Nd	Sm	Eu	Gd	Tb	Dy	Ho	Er	Yb	Lu	Pb	Th	U	Al_2O_3	CaO	MgO	Na_2O	K_2O	Fe_2O_3	MnO	TiO_2	P_2O_3
Sr		0.0	9.5	12.2	0.0	4.7	2.2	14.4	2.5	1.2	0.8	0.0	0.9	0.8	0.1	0.0	0.1	0.2	1.6	11.9	3.3	23.0	3.5	21.1	0.0	1.0	1.0	0.1	13.7	8.1	8.6
Y	0.0		49.7	35.0	44.4	3.7	94.3	71.2	90.6	93.5	93.6	94.9	92.6	93.1	98.4	96.9	96.9	97.0	87.8	35.3	68.9	0.6	46.7	36.5	4.2	0.1	59.2	52.2	13.2	50.3	30.2
Zr	9.5	49.7		77.5	34.3	5.0	60.9	85.3	71.4	68.1	67.0	51.1	66.5	67.4	57.3	55.8	60.5	53.0	47.4	16.2	82.1	1.2	58.1	13.6	6.2	0.3	76.2	63.4	21.4	94.3	14.8
Nb	12.2	35.0	77.5		26.2	12.9	42.7	63.5	46.3	43.6	45.2	42.4	43.7	34.9	37.4	38.5	37.1	31.0	38.4	3.1	64.5	0.3	55.6	0.1	13.9	0.3	52.4	24.8	7.5	64.1	16.6
Cs	0.0	44.4	34.3	26.2		27.3	35.6	39.5	36.4	35.8	39.1	32.2	35.9	44.6	42.8	41.4	41.7	32.5	39.5	11.6	44.3	0.6	62.8	14.5	8.5	27.9	21.9	39.4	14.8	43.1	53.2
Ba	4.7	3.7	5.0	12.9	27.3		6.7	4.7	6.1	5.9	3.7	5.7	8.0	7.7	5.2	8.3	2.8	3.6	2.5	1.9	3.4	0.4	0.5	9.9	15.7	43.6	1.4	4.1	0.9	2.3	32.4
La	2.2	94.3	60.9	42.7	35.6	6.7		82.5	98.0	98.5	96.1	94.0	96.8	96.7	96.3	96.3	95.7	96.2	82.1	27.0	75.3	0.2	44.7	32.3	6.5	0.1	61.7	46.6	17.4	59.1	23.4
Ce	14.4	71.2	85.3	63.5	39.5	4.7	82.5		88.9	85.9	84.6	72.6	84.6	84.4	78.3	74.7	76.4	75.7	71.0	16.0	85.6	0.2	51.8	19.0	4.4	0.0	77.0	61.7	14.7	87.1	14.5
Pr	2.5	90.6	71.4	46.3	36.4	6.1	98.0	88.9		99.2	97.7	91.8	98.0	97.5	94.6	94.3	94.4	93.0	78.5	25.7	84.4	0.1	52.7	34.0	7.3	0.2	72.2	52.3	15.7	70.2	25.3
Nd	1.2	93.5	68.1	43.6	35.8	5.9	98.5	85.9	99.2		97.9	94.3	98.3	97.7	96.6	95.6	95.3	95.2	82.5	28.4	80.8	0.0	40.2	37.4	6.5	0.2	69.3	53.5	14.3	66.1	26.1
Sm	0.8	93.6	67.0	45.2	39.1	3.7	96.1	84.6	97.7	97.9		92.7	96.9	95.9	96.0	93.7	94.6	92.7	84.1	25.3	85.9	0.0	61.6	34.8	7.2	0.2	74.3	52.7	12.8	65.1	28.6
Eu	0.0	94.9	51.1	42.4	32.2	5.7	94.0	72.6	91.8	94.3	92.7		94.3	90.7	96.4	96.9	92.0	95.5	84.4	33.5	70.7	3.0	38.5	37.1	6.2	0.7	65.9	52.8	5.3	49.2	27.0
Gd	0.9	92.6	66.5	43.7	35.9	8.0	96.8	84.6	98.0	98.3	96.9	94.3		96.6	95.6	95.9	93.6	94.6	78.3	34.4	80.0	0.5	40.2	40.1	8.0	0.4	72.3	54.5	11.1	66.2	32.1
Tb	0.8	93.1	67.4	34.9	44.6	7.7	96.7	84.4	97.5	97.7	95.9	90.7	96.6		96.0	95.7	95.7	94.5	79.7	31.6	79.4	0.0	48.3	38.8	2.7	0.3	65.6	57.7	16.7	67.2	28.3
Dy	0.1	98.4	57.3	37.4	42.8	5.2	96.3	78.3	94.6	96.6	96.0	96.4	95.6	96.0		98.4	96.8	98.3	88.9	33.6	75.0	0.8	54.4	36.3	4.1	0.0	66.8	57.0	11.8	57.2	27.8
Ho	0.0	96.9	55.8	38.5	41.4	8.3	96.3	74.7	94.3	95.6	93.7	96.9	95.9	95.7	98.4		97.0	97.5	81.6	37.3	72.6	0.7	60.5	36.8	4.9	0.0	64.3	54.7	12.6	55.9	30.6
Er	0.1	96.9	60.5	37.1	41.7	2.8	95.7	76.4	94.4	95.3	94.6	92.0	93.6	95.7	96.8	97.0		95.7	80.4	35.2	75.4	0.0	63.8	32.0	6.7	0.1	63.5	53.5	21.0	60.3	26.8
Yb	0.2	97.0	53.0	31.0	32.5	3.6	96.2	75.7	93.0	95.2	92.7	95.5	94.6	94.5	98.3	97.5	95.7		85.4	39.5	67.1	0.5	44.1	34.8	5.8	0.5	61.1	52.6	12.0	54.5	21.5
Lu	1.6	87.8	47.4	38.4	39.5	2.5	82.1	71.0	78.5	82.5	84.1	84.4	78.3	79.7	88.9	81.6	80.4	85.4		19.2	63.9	1.2	49.8	20.7	0.9	0.1	57.6	55.3	7.5	45.1	15.2
Pb	11.9	35.3	16.2	3.1	11.6	1.9	27.0	16.0	25.7	28.4	25.3	33.5	34.4	31.6	33.6	37.3	35.2	39.5	19.2		14.8	14.3	9.1	26.7	9.1	2.4	19.3	37.8	2.7	19.1	34.1
Th	3.3	68.9	82.1	64.5	44.3	3.4	75.3	85.6	84.4	80.8	85.9	70.7	80.0	79.4	75.0	72.6	75.4	67.1	63.9	14.8		0.0	92.9	22.1	7.8	0.0	86.1	57.2	11.8	77.3	27.6
U	23.0	0.6	1.2	0.3	0.6	0.4	0.2	0.2	0.1	0.0	0.0	3.0	0.5	0.0	0.8	0.7	0.0	0.5	1.2	14.3	0.0		25.5	11.3	0.2	3.5	5.7	11.4	56.6	0.3	9.3
Al_2O_3	3.5	46.7	58.1	55.6	62.8	0.5	44.7	51.8	52.7	40.2	61.6	38.5	40.2	48.3	54.4	60.5	63.8	44.1	49.8	9.1	92.9	25.5		3.8	35.9	5.0	59.7	0.2	35.1	81.8	10.7
CaO	21.1	36.5	13.6	0.1	14.5	9.9	32.3	19.0	34.0	37.4	34.8	37.1	40.1	38.8	36.3	36.8	32.0	34.8	20.7	26.7	22.1	11.3	3.8		0.0	0.0	19.5	15.3	0.3	16.8	53.2
MgO	0.0	4.2	6.2	13.9	8.5	15.7	6.5	4.4	7.3	6.5	7.2	6.2	8.0	2.7	4.1	4.9	6.7	5.8	0.9	9.1	7.8	0.2	35.9	0.0		68.5	11.4	0.4	3.2	4.6	0.0
Na_2O	1.0	0.1	0.3	0.3	27.9	43.6	0.1	0.0	0.2	0.2	0.2	0.7	0.4	0.3	0.0	0.0	0.1	0.5	0.1	2.4	0.0	3.5	5.0	0.0	68.5		1.6	3.5	4.0	0.0	4.8
K_2O	1.0	59.2	76.2	52.4	21.9	1.4	61.7	77.0	72.2	69.3	74.3	65.9	72.3	65.6	66.8	64.3	63.5	61.1	57.6	19.3	86.1	5.7	59.7	19.5	11.4	1.6		65.2	1.7	76.6	21.5
Fe_2O_3	0.1	52.2	63.4	24.8	39.4	4.1	46.6	61.7	52.3	53.5	52.7	52.8	54.5	57.7	57.0	54.7	53.5	52.6	55.3	37.8	57.2	11.4	0.2	15.3	0.4	3.5	65.2		2.4	66.9	16.6
MnO	13.7	13.2	21.4	7.5	14.8	0.9	17.4	14.7	15.7	14.3	12.8	5.3	11.1	16.7	11.8	12.6	21.0	12.0	7.5	2.7	11.8	56.6	35.1	0.3	3.2	4.0	1.7	2.4		17.2	1.5
TiO_2	8.7	50.0	94.9	64.9	43.8	2.3	59.3	87.2	70.4	66.5	65.1	49.7	66.4	67.6	57.3	55.2	60.3	54.5	45.1	19.1	77.3	0.3	81.8	16.8	4.6	0.0	76.6	66.9	17.2		13.7
P_2O_3	8.6	30.2	14.8	16.6	53.2	32.4	23.4	14.5	25.3	26.1	28.6	27.0	32.1	28.3	27.8	30.6	26.8	21.5	15.2	34.1	27.6	9.3	10.7	53.2	0.0	4.8	21.5	16.6	1.5	13.7	

Carcaillet et al., Electronic Table B

Correlations between major and trace elements in the host rock. Correlation coefficients are calculated using simple linear regressions. When the coefficient is larger than 70, the field is shown in grey, and the intensity of the grey is correlated to the R value.

a) Calculations include all measurements from Table 1 b) Calculations include all measurements from Table 1 but those for sample C15

Element	Uncertainty		a			b		
	Average	Maximum	Coefficient of regresssion R	Slope s (%/m)	Total concentration change Δt (%)	Coefficient of regresssion R	Slope s (%/m)	Total concentration change Δt (%)
Al_2O_3	-	22	0.59	-13.64	-137.08	0.51	-11.32	-113.72
Th	10	19	0.51	-6.62	-66.54	0.63	-9.08	-91.29
Nb	6	8	0.56	-5.49	-55.16	0.59	-6.36	-63.91
Zr	3	6	0.67	-5.30	-53.25	0.75	-6.52	-65.51
TiO_2	-	10	0.55	-4.06	-40.82	0.68	-5.45	-54.80
La	3	6	0.41	-4.91	-49.35	0.70	-8.69	-87.33
Ce	3	6	0.57	-6.14	-61.75	0.72	-8.42	-84.59
Pr	3	11	0.45	-5.85	-58.79	0.70	-9.72	-97.68
Nd	2	6	0.37	-4.87	-48.90	0.68	-9.14	-91.88
Sm	7	14	0.38	-5.06	-50.81	0.62	-8.76	-88.03
Eu	9	14	0.30	-3.83	-38.46	0.59	-7.66	-76.98
Gd	4	12	0.39	-4.39	-44.16	0.64	-7.65	-76.90
Tb	6	11	0.40	-5.08	-51.00	0.69	-9.03	-90.79
Dy	5	14	0.34	-3.58	-35.98	0.63	-6.82	-68.57
Ho	5	12	0.36	-3.68	-36.98	0.66	-6.87	-69.07
Er	5	11	0.43	-4.07	-40.85	0.67	-6.67	-67.04
Yb	8	12	0.37	-3.54	-35.61	0.63	-6.21	-62.45
Lu	7	16	0.35	-2.94	-29.56	0.56	-5.01	-50.31
Y	2	6	0.30	-2.61	-26.25	0.59	-5.23	-52.53
Ba	3	4	0.46	-3.88	-39.03	0.46	-3.88	-39.03
Sr	2	3	0.42	-0.93	-9.33	0.49	-1.18	-11.88
CaO	-	4.5	0.19	0.08	0.80	0.10	0.04	0.43
MgO	-	4	0.10	0.23	2.35	0.06	-0.13	-1.33
Cs	5	10	0.29	-3.35	-33.62	0.46	-5.75	-57.74
K_2O	-	5	0.42	-2.96	-29.78	0.51	-3.92	-39.41
Li	5	11	0.09	0.62	6.18	0.40	0.06	0.56
Na_2O	-	9	0.43	2.61	26.21	0.33	2.14	21.50
Fe_2O_3	-	3	0.46	-2.56	-25.77	0.53	-3.25	-32.69
P_2O_3	-	7	0.04	-0.30	-3.05	0.17	-1.48	-14.87
Pb	3	6	0.02	-0.06	-0.61	0.23	-0.81	-8.18
U	3	7	0.29	2.15	21.57	0.43	3.34	33.56
MnO	-	7	0.49	4.24	42.61	0.70	6.25	62.80

Regression parameters for the concentrations versus scarp height plots.
Mean and maximum uncertainties on concentrations are reported. R is coefficient of regression, s the slope of the regression in %/m, and t the total concentration change over the whole scarp height H, in % (t= s x H). Negative (positive) slopes indicate a concentration decrease (increase) as one goes upscarp.
a) Regressions are calculated from all measurements listed in Table 1.b) Regressions are calculated from all measurements listed in Table 1, but those for the C15 sample.

Carcaillet et al.. Electronic Table C

	Na_2O	MgO	Al_2O_3	SiO2	P_2O_5	SO_3	K_2O	TiO_2	MnO	Fe_2O_3
Na_2O		35.9	49.7	58.3	5.1	20.4	28.9	40.5	40.7	44.8
MgO	35.9		0.4	0.5	16.4	1.0	0.2	1.0	22.7	2.2
Al_2O_3	49.7	0.4		88.1	4.1	67.6	60.6	48.4	29.0	54.1
SiO_2	58.3	0.5	88.1		0.1	54.0	65.6	74.3	39.3	79.7
P_2O_5	5.1	16.4	4.1	0.1		16.3	0.6	7.4	1.2	10.2
SO_3	20.4	1.0	67.6	54.0	16.3		76.1	22.7	32.0	27.7
K_2O	28.9	0.2	60.6	65.6	0.6	76.1		46.4	47.5	51.9
TiO_2	40.5	1.0	48.4	74.3	7.4	22.7	46.4		29.2	89.5
MnO	40.7	22.7	29.0	39.3	1.2	32.0	47.5	29.2		32.7
Fe_2O_3	44.8	2.2	54.1	79.7	10.2	27.7	51.9	89.5	32.7	

Correlation coefficients between major elements in the coating (from Table A). The coefficients were calculated using simple linear regressions. When the coefficient is larger than 70, the field is shown in grey, and the intensity of the grey is correlated to the R value.

Carcaillet et al., Electronic Table D

	Wave 5		Wave 4		Wave 3		Wave 2	
	Base (-0.35 m) T_r = 4.85 ka	Top (1.25 m) T_r = 1.85 ka	Base (1.95 m) T_r = 1.85 ka	Top (3.85 m) T_r = 0.70 ka	Base (4.45 m) T_r = 0.70 ka	Top (6.65 m) T_r = 3.10 ka	Base (7.15 m) T_r = 3.10 ka	Top (9.2 m) T_r = 1.50 ka
	Concentration peak (%)	Concentration peak (%)	Concentration peak (%)	Concentration peak (%)	Concentration peak (%)	Concentration peak (%)	Concentration peak (%)	Concentration peak (%)
Sr	-	-	-	-	-	-	-	-
Y	46.1	37.8	64.1	45.5	27.2	38.4	52.1	46.3
Zr	69.3	11.1	19.1	27.5	9.3	4.5	30.4	10.9
Nb	-	-	24.5	56.5	34.9	11.2	73.2	46.8
Cs	-	46.3	46.8	52.7	-	-	85.3	42.8
Ba	-	-	-	-	-	-	-	-
La	60.0	44.4	88.8	57.7	41.6	47.2	45.2	55.6
Ce	85.0	28.5	52.9	39.9	30.2	31.2	45.1	53.9
Pr	85.3	55.6	90.6	60.3	39.2	46.2	49.5	59.5
Nd	80.0	50.3	86.4	66.8	41.0	51.0	50.4	61.8
Sm	91.1	67.7	100.3	79.6	43.8	48.1	60.7	58.7
Eu	54.0	48.3	81.6	58.4	51.3	61.7	69.3	84.0
Gd	70.8	41.4	85.5	58.4	28.6	33.9	54.4	67.2
Tb	79.2	45.1	90.8	57.6	19.7	40.7	48.6	52.3
Dy	61.1	47.3	68.2	46.9	31.8	40.2	58.3	59.2
Ho	49.1	39.9	68.8	38.8	26.4	35.1	55.8	56.0
Er	56.7	41.5	66.7	39.4	28.7	41.6	51.8	35.2
Yb	52.4	35.5	67.1	36.3	34.1	40.9	48.7	55.5
Lu	42.5	34.1	43.3	51.3	42.5	38.5	53.3	52.1
Pb	-	-	16.9	2.9	-	-	29.8	21.6
Th	107.3	84.1	65.1	66.1	15.6	28.1	67.3	41.4
U	5.5	5.9	-	-	-12.5	13.1	61.7	90.8
Li	30.0	15.4	-	-	49.7	59.1	4.7	25.9
Al_2O_3	-	-	-	-	-	-	-	-
CaO	-	-	-	-	-	-	-	-
MgO	5.8	9.0	5.8	2.6	13.0	4.2	-	-
Na_2O	17.7	16.1	-	-	44.5	41.9	-	-
K2O	67.8	36.0	20.9	17.9	24.4	11.1	50.0	41.0
Fe_2O_3	-	-	4.6	7.2	-	-	54.2	35.1
MnO	-	-	-	-	8.0	14.0	-3.9	62.6
TiO_2	76.4	10.3	20.1	12.7	4.7	10.4	30.0	18.5
P_2O_3	34.1	41.9	51.3	64.8	-	-	51.3	48.1

Amplitudes of the concentration peaks at transition zones between earthquake slip zones.
Data are presented and 'waves' defined in Figure 6b. 'Base' and 'top' are for the two peak-concentrations that bound each 'wave'. The residence times (Tr) over which the peak-concentrations have built up are indicated. Elements having concentrations higher than 46% (average overall value) are highlighted in grey.

Carcaillet et al., Electronic Table E

Elements	R coefficient for model of Fig. 9 (%)	R coefficient for linear regression (%)
Y	90.61	58.51
La	89.55	69.91
Ce	85.58	71.60
Pr	92.25	69.99
Nd	92.38	67.68
Sm	94.04	62.31
Eu	92.83	58.79
Gd	92.74	63.91
Tb	90.57	69.07
Dy	91.99	63.10
Ho	91.88	66.07
Er	92.11	67.15
Yb	89.14	62.68
Lu	84.28	55.96
R_{min}	**84.28**	**55.96**
$R_{average}$	**90.71**	**64.77**
R_{max}	**94.04**	**71.60**

Best-fit coefficients (R) obtained (for REE-Y) using the model shown in figure 9 (left column) compared to values calculated with a simple linear regression (right column).

Carcaillet et al., Electronic Table F